Edited by
Tetyana Baydyk

ENERGY SYSTEMS AND RESOURCES: OPTIMISATION AND RATIONAL USE

Collective monograph

Technology® Center

2024

UDC 621.311
E54

Published in 2024
by TECHNOLOGY CENTER PC®
Shatylova dacha str., 4, Kharkiv, Ukraine, 61165

E54

Authors:
Edited by **Tetyana Baydyk**
Maksym Kovzel, Olga Nosko, Tetyana Baydyk, Masuma Mammadova, Ernst Kussul, Airam Curtidor, Yurii Sniezhkin, Zhanna Petrova, Vadym Paziuk, Viacheslav Mykhailyk, Tetiana Korinchevska, Kateryna Samoilenko, Igor Kozlov, Vyacheslav Kovalchuk, Viacheslav Miliev, Mykola Holovin, Serhii Vistiak, Olexiy Kozlov, Natalia Dunaievska, Taras Shchudlo, Ihor Beztsennyi, Dmytro Bondzyk, Yevhen Miroshnychenko
Energy systems and resources: optimisation and rational use: collective monograph. – Kharkiv: TECHNOLOGY CENTER PC, 2024. – 192 p.

This monograph is a complex scientific and applied work covering the most important directions in the field of sustainable energy, materials science and environmental safety. The studies and recommendations presented in it have practical significance and can be used for further development of scientific and technological solutions in this field.
The results presented in the monograph can be useful in the development of new solutions for the energy industry, in the design of renewable energy systems, in the sphere of waste utilisation and in the issues of reducing the environmental impact of industrial facilities. The obtained data and recommendations are intended for a wide range of specialists, including engineers, developers, scientists, designers, as well as undergraduate and postgraduate students of technical areas of training.
Figures 88, Tables 41, References 147 items.

This book contains information obtained from authentic and highly regarded sources. Reasonable efforts have been made to publish reliable data and information, but the author and publisher cannot assume responsibility for the validity of all materials or the consequences of their use. The authors and publishers have attempted to trace the copyright holders of all material reproduced in this publication and apologize to copyright holders if permission to publish in this form has not been obtained. If any copyright material has not been acknowledged please write and let us know so we may rectify in any future reprint.
The publisher, the authors and the editors are safe to assume that the advice and information in this book are believed to be true and accurate at the date of publication. Neither the publisher nor the authors or the editors give a warranty, express or implied, with respect to the material contained herein or for any errors or omissions that may have been made.
Trademark Notice: product or corporate names may be trademarks or registered trademarks, and are used only for identification and explanation without intent to infringe.

DOI: 10.15587/978-617-8360-02-3
ISBN 978-617-8360-02-3 (on-line)

Cite as: Baydyk, T. (Ed.) (2024). Energy systems and resources: optimisation and rational use. Kharkiv: TECHNOLOGY CENTER PC, 192. doi: http://doi.org/10.15587/978-617-8360-02-3

9 786178 360023

Copyright © Author(s) 2024
This is an open access paper under the Creative Commons Attribution-NonCommercial-NoDerivatives 4.0 International License (CC BY-NC-ND 4.0)

AUTHORS

CHAPTER 1

MAKSYM KOVZEL
PhD, Associate Professor, Forensic Expert
Dnipropetrovsk Scientific Research Forensic Center of the MIA of Ukraine
ORCID: https://orcid.org/0000-0001-5720-1186

OLGA NOSKO
PhD, Associate Professor, Dean
Faculty of Quality and Material Engineering
Institute of Industrial and Business Technologies Ukrainian State University of Science and Technologies
ORCID: https://orcid.org/0000-0002-5749-7578

CHAPTER 2

TETYANA BAYDYK
Doctor of Technical Sciences, Professor,
Investigator Titular C
Department of Micro and Nanotechnology
Institute of Applied Sciences and Technology
National Autonomous University of Mexico
ORCID: https://orcid.org/0000-0002-3095-2032

MASUMA MAMMADOVA
Doctor of Technical Sciences, Professor, Head of Department
Department of Number 11
Institute of Information Technologies
ORCID: https://orcid.org/0000-0002-2205-1023

ERNST KUSSUL
Doctor of Technical Sciences, Professor,
Investigator Titular C, Head of Group
Department of Micro and Nanotechnology
Institute of Applied Sciences and Technology
National Autonomous University of Mexico
ORCID: https://orcid.org/0000-0002-2849-2532

AIRAM CURTIDOR
Department of Micro and Nanotechnology
Institute of Applied Sciences and Technology
National Autonomous University of Mexico
ORCID: https://orcid.org/0000-0002-7388-1385

CHAPTER 3

YURII SNIEZHKIN
Doctor of Technical Sciences, Professor, Acting Head of the Institute, Academician of NAS of Ukraine
Institute of Engineering Thermophysics of NAS of Ukraine
ORCID: https://orcid.org/0000-0002-9049-3392

ZHANNA PETROVA
Doctor of Technical Sciences, Senior Researcher
Department of Mass Transfer in Heat Technologies
Institute of Engineering Thermophysics of NAS of Ukraine
ORCID: https://orcid.org/0000-0001-7385-8495

VADYM PAZIUK
Doctor of Technical Sciences, Associate Professor
Department of Mass Transfer in Heat Technologies
Institute of Engineering Thermophysics of NAS of Ukraine
ORCID: https://orcid.org/0000-0002-4955-1941

VIACHESLAV MYKHAILYK
PhD, Senior Researcher
Department of Mass Transfer in Heat Technologies
Institute of Engineering Thermophysics of NAS of Ukraine
https://orcid.org/0000-0003-2712-1382

TETIANA KORINCHEVSKA
PhD, Senior Researcher
Department of Mass Transfer in Heat Technologies
Institute of Engineering Thermophysics of NAS of Ukraine
ORCID: https://orcid.org/0000-0002-6638-4743

KATERYNA SAMOILENKO
PhD, Senior Researcher
Department of Mass Transfer in Heat Technologies
Institute of Engineering Thermophysics of NAS of Ukraine
ORCID: https://orcid.org/0000-0002-5169-4466

CHAPTER 4

IGOR KOZLOV
Doctor of Technical Sciences, Professor
Department of Nuclear Power Plants
Odesa Polytechnic National University
ORCID: https://orcid.org/0000-0003-0435-6373

VYACHESLAV KOVALCHUK
PhD, Associate Professor
Department of Nuclear Power Plants
Odesa Polytechnic National University
ORCID: https://orcid.org/0000-0001-8696-4414

VIACHESLAV MILIEV
Graduate student
Department of Nuclear Power Plants
Odesa Polytechnic National University
ORCID: https://orcid.org/0009-0000-2289-2490

MYKOLA HOLOVIN
Graduate student
Department of Nuclear Power Plants
Odesa Polytechnic National University
ORCID: https://orcid.org/0009-0005-2534-2239

SERHII VISTIAK
Graduate student
Department of Nuclear Power Plants
Odesa Polytechnic National University
ORCID: https://orcid.org/0000-0001-8696-4414

OLEXIY KOZLOV
Graduate student
Department of Nuclear Power Plants
Odesa Polytechnic National University
ORCID: https://orcid.org/0000-0002-1834-6902

CHAPTER 5

NATALIA DUNAIEVSKA
Doctor of Technical Sciences, Professor, Director
Thermal Energy Technology Institute of the National
Academy of Sciences of Ukraine
ORCID: https://orcid.org/0000-0003-3271-8204

TARAS SHCHUDLO
PhD, Senior Researcher
Department of Solid Fuel in Energy
Thermal Energy Technology Institute of the National
Academy of Sciences of Ukraine
ORCID: https://orcid.org/0000-0002-2754-2032

IHOR BEZTSENNYI
PhD, Senior Researcher
Department of Solid Fuel in Energy
Thermal Energy Technology Institute of the National
Academy of Sciences of Ukraine
ORCID: https://orcid.org/0000-0001-6536-5121

DMYTRO BONDZYK
PhD, Senior Researcher
Department of Solid Fuel in Energy
Thermal Energy Technology Institute of the National
Academy of Sciences of Ukraine
ORCID: https://orcid.org/0000-0003-3123-1971

YEVHEN MIROSHNYCHENKO
PhD, Researcher
Department of Solid Fuel in Energy
Thermal Energy Technology Institute of the National
Academy of Sciences of Ukraine
ORCID: https://orcid.org/0000-0003-2487-6886

ABSTRACT

The monograph "Energy systems and resources: optimisation and rational use" is devoted to topical issues in the field of energy, materials science and sustainable development, including the study of magnetic field effect on silicon microstructure, development of innovative designs of solar concentrators, use of solid domestic waste in the energy balance of Ukraine, as well as the prospects and technologies of co-combustion of coal and biomass at thermal power plants.

In 1 Section "Magnetic treatment of semiconductor silicon", within the framework of research on the influence of magnetic field on the microstructure of silicon grown by the Czochralsky method (Cz-Si), doped with elements Al, Mg, Cu, Fe, Zr, Hf, the influence of these impurities on the interaction energy of silicon atoms in the crystal lattice is considered for the first time. It is found that doping with elements reducing the interaction energy leads to an increase in defects during magnetic treatment for 240 hours, while 720 hours of treatment reduces their number.

In 2 Section "Support frame of solar concentrator with flat triangular mirrors" of the monograph is devoted to the development of improved designs of solar concentrators used in the field of green energy. The research is aimed at reducing production costs and increasing efficiency by reducing the number of metal elements and introducing automated assembly processes. The developed new design with fewer elements contributes to cheaper production and faster assembly process. The prototypes can find wide application in agriculture, organic waste recycling and energy supply of residential buildings within the concept of "green" buildings.

In 3 Section "Technological aspects of producing refuse derived fuel" special attention is paid to the issues of involvement of solid domestic waste in the energy balance of Ukraine by creating alternative solid fuel (RDF - refuse derived fuel). The kinetics of convective drying of RDF of different compositions depending on temperature and speed of the heat carrier is investigated. Drying coefficients, rates of thermal decomposition of organic and mineral substances, as well as calorific value of RDF are determined. The results obtained are the basis for the development of energy-efficient RDF production technologies to reduce dependence on fossil fuels.

The 4 Section "Choice optimization of the type of energy resource for the region" considers the current state and prospects of the energy complex of Ukraine. Based on the analysis of available energy resources, the methodology of selection and justification of priority fuels for regional energy supply is proposed. Environmental aspects of utilisation of traditional resources such as coal, oil, gas and nuclear fuel are considered, as well as the possibilities of transition to alternative energy sources.

The 5 Section "Scientific and technical solutions for implementing biomass combustion at coal-fired TPP in Ukraine" is devoted to the development of technologies for co-combustion of coal and biomass, which is a promising direction for reducing emissions of harmful substances, diversifying fuel sources and improving combustion conditions at thermal power plants. The technologies

of biomass combustion and gasification are considered, experimental studies of co-combustion of gas coal and biomass are carried out, thermal calculations of boiler plants using ANSYS FLUENT are performed. Recommendations for implementation of these technologies at Ukrainian TPPs were developed.

Thus, the results presented in the monograph are an important contribution to the solution of urgent problems in the field of sustainable energy, material science and environmental safety. The monograph will be useful for engineers, researchers, designers and specialists working in the field of energy, waste processing and development of "green" technologies.

KEYWORDS

Silicon, magnetic field, doping, crystal lattice defects, solar concentrators, alternative energy, production automation, municipal solid waste, refuse-derived fuel, thermal decomposition, energy efficiency, co-firing, biomass, greenhouse gas emissions, energy balance, convective drying, environmental safety, crystalline structure, phase transformations, computer modeling.

CIRCLE OF READERS AND SCOPE OF APPLICATION

This monograph is a complex scientific and applied work covering the most important directions in the field of sustainable energy, materials science and environmental safety. The studies and recommendations presented in it have practical significance and can be used for further development of scientific and technological solutions in this field.

The results presented in the monograph can be useful in the development of new solutions for the energy industry, in the design of renewable energy systems, in the sphere of waste utilisation and in the issues of reducing the environmental impact of industrial facilities. The obtained data and recommendations are intended for a wide range of specialists, including engineers, developers, scientists, designers, as well as undergraduate and postgraduate students of technical areas of training.

CONTENTS

List of Tables ix
List of Figures xi

Introduction 1

1 Magnetic treatment of semiconductor silicon 3
1.1 Earlier research findings and relevant literature review 5
1.1.1 Crystallochemical peculiarities of semiconductor silicon 5
1.1.2 Phase transformations in semiconductor silicon 6
1.1.3 Martensitic transformation mechanisms in silicon 11
1.1.4 General problems on magnetic field effect on "nonmagnetic" substances 12
1.1.5 The nature of Nernst-Ettingshausen effect 17
1.1.6 Magnetoplastic effect in diamagnetic crystals 18
1.2 Materials and methods of the study 23
1.2.1 Study materials 23
1.3 Microstructures of the samples before and after the magnetic field treatment 25
1.4 The sample microhardness values before and after treating with the magnetic field 37
1.5 The physical parameters of the samples before and after treating with the magnetic field 46
Conclusions 49
References 51

2 Support frame of solar concentrator with flat triangular mirrors 54
2.1 Literature review and problem statement 56
2.1.1 Existed prototypes of solar concentrators 57
2.1.2 Applications of solar concentrators 61
2.2 The aim and objectives of the study 62
2.3 Materials and methods 63
2.3.1 Object and hypothesis of the study 63
2.3.1.1 First model 63
2.3.1.2 Number of mirrors 65
2.3.2 Materials 65
2.3.3 Methods 66

2.3.3.1 Geometric model of solar concentrator ... 66
2.3.3.2 Calculation of number of structural elements ... 67
2.3.4 Software ... 68
2.4 New structure of solar concentrator with flat triangular mirrors ... 68
2.4.1 Reducing the number of structural elements ... 68
2.4.2 Calculation of structural elements ... 70
2.5 Discussion ... 71
Conclusions ... 72
References ... 73

3 Technological aspects of producing refuse derived fuel ... 76
3.1 Analytical review and analysis ... 77
3.1.1 Municipal solid waste and fuel from it ... 77
3.1.2 Technologies of obtaining RDF/SRF ... 79
3.2 Study of regularity of RDF convective drying ... 83
3.2.1 Preparation of municipal solid waste for drying ... 83
3.2.2 Research of drying modes of RDF ... 85
3.2.3 Research of heat and mass exchange processes during drying RDF ... 89
3.3 RDF thermal analysis ... 91
3.3.1 Research technique for thermal decomposition of RDF ... 92
3.3.2 Results of the derivatographic studies of RDF ... 94
Conclusions ... 102
References ... 102

4 Choice optimization of the type of energy resource for the region ... 106
4.1 State and prospects for the development of the energy sector of Ukraine ... 107
4.1.1 Hydropower ... 109
4.1.2 Wind power ... 110
4.1.2.1 Disadvantages of modern wind power plants ... 112
4.1.3 Solar energy ... 112
4.1.3.1 Disadvantages of solar energy ... 115
4.1.4 Bioenergy ... 116
4.1.4.1 Advantages and disadvantages of bioenergy ... 120
4.1.5 Thermal power ... 121
4.1.6 Nuclear energy ... 125
4.2 Methodology for substantiating the choice of the type of energy resource for the region ... 127
4.2.1 Comprehensive assessment of efficiency indicators of energy resources 128
4.2.1.1 Analysis of existing comprehensive assessments ... 131

4.2.1.2 Environmental pollution indicators and their standardization 132
4.2.1.3 Combined normalization of resource efficiency and environmental pollution indicators 133
4.2.2 Results of polluting capacity assessment 134
4.2.3 Using a complex indicator for resource selection 134
Conclusions 138
References 139

5 Scientific and technical solutions for implementing biomass combustion at coal-fired TPP in Ukraine 144
5.1 Coal and solid biofuel co-firing technologies 148
5.1.1 Existing biomass and coal co-firing technologies 148
5.1.2 Current biomass research 150
5.2 Experimental study of joint pulverized combustion of gas coal and biomass 152
5.3 Verification of the obtained results by performing engineering calculations using the normative method 158
5.4 Calculation of co-firing of coal with biomass for selected schematic solutions of the biomass feed system to the boiler fuel tank 163
5.4.1 Initial conditions for modeling co-firing 163
5.4.2 Main results of modeling in the mode without pellet input 166
5.4.3 Main results of modeling in the mode with the introduction of pellets 169
5.5 Recommendations for the use of co-firing of coal and biomass at Ukrainian TPPs 172
References 173

LIST OF TABLES

1.1	Properties of the studied silicon crystals	23
1.2	Temperatures of phase transformation for doped silicon and the dedicated thermal expansion coefficient values	33
1.3	Physical parameters and mechanical properties of the doped silicon samples before and after exposing to direct-current magnetic field	47
2.1	Parameters of the parabolic concentrator	66
3.1	Classification system for solid recovered fuels	79
3.2	Brief description of key technologies of waste processing	80
3.3	Composition of RDF (100 g)	84
3.4	RDF composition	94
3.5	Thermal characteristics of experimental fuel	95
3.6	Temperature ranges, proportions of decomposed organic substances and average rates of RDF decomposition	95
3.7	Derivatograms of thermal decomposition of RDF samples and their description	96
4.1	Global electricity production in 2022 by resource type, according to British Petroleum	107
4.2	Promising directions and levels of development of renewable energy sources in Ukraine until 2030	108
4.3	Average monthly level of solar radiation (solar constant) in Ukrainian cities (kWh/m2/day). Average over the last 22 years	114
4.4	Energy potential of biomass in Ukraine	119
4.5	Summary indicators of the Roadmap for the development of bioenergy in Ukraine by 2050	120
4.6	Emissions of pollutants during the operation of a 1000 MW thermal power plant	121
4.7	Comparison of the TPP and NPP operation with a capacity of 1000 MW for one year of operation	122
4.8	Average annual emissions of radionuclides from a thermal power plant, Bq/GWh	123
4.9	Specific activity of the main radionuclides in coal, slag and ash in Bq/kg	123
4.10	Average emissions of the main radionuclides, the density of contamination of the territory and the RN concentration in the air per 1 GWh in the area of the nominal TPP location	124
4.11	Specific emissions of atmospheric pollution (g/kWh) from the combustion of organic fuels (according to the International Institute for Applied Systems Analysis, Vienna)	124
4.12	Gross emissions (thousand tons/year) and fuel consumption for a 1000 MW TPP	124

4.13	List of substances emitted by heat and power enterprises when operating on various types of fossil fuels	125
4.14	Annual emissions from a 1000 MW fossil fuel TPP	125
4.15	Main categories of energy resources	128
4.16	Algorithm for constructing a comprehensive assessment of the efficiency of systems	130
4.17	Factors reflecting the applicability of the resource	130
4.18	Groupings and types of pollution indicators	133
4.19	Electricity production and pollution by region and resource (%)	136
5.1	Coal consumption in different regions of the world (2023)	145
5.2	Co-firing technologies in the corresponding furnaces. Advantages and disadvantages	149
5.3	Sieving of biomass prepared for combustion	154
5.4	Results of technical analysis of fuel samples	154
5.5	Results of elemental analysis of fuel samples of the combustible mass and chlorine content of fuel samples	155
5.6	Main parameters of the boiler operation	159
5.7	Fuel chamber characteristics	159
5.8	Zonal calculation of the fuel chamber	162
5.9	Boundary conditions on the walls of the zones	165
5.10	Input component parameters assigned to one burner	165
5.11	Characteristics of gas coal and pine pellets	166

LIST OF FIGURES

1.1 Dependence diagram between a gradual change in the crystal physical properties within a magnetic field (with a time constant t_1) and a relaxation after the magnetic field removal (with a time constant t_2): a relative change in a physical value of Dl/l is marked with a vertical arrow 13

1.2 Dependence between time t_1 and magnetic strength (H) for some substances. The approximation described in this publication is marked with a continuous line 14

1.3 The dependence between the relative value of property changes in solid bodies ($\Delta l/l$): *a* – the magnetic energy per unit volume ($\chi_m H_2/2$); *b* – time t_1 for some substances. The approximation described in this publication is marked with a continuous line 16

1.4 Dependence between the average edge dislocation pathlength (L) in NaCl:Ca crystals upon the direct magnetic field induction (B_0): exposure time of 15 min 21

1.5 Schematic illustration of the process sequence in the complexes of point defects within the magnetic field: on the energy scale of E complex 22

1.6 Microstructures of Cz-Si samples: *a* – initial state, ×500; *b, c, d* – after 240 hours of exposing to direct-current magnetic field, ×400; *e, f* – after 720 hours of exposing to direct-current magnetic field, ×400 25

1.7 Microstructures of Cz-Si samples doped with Al: *a* – initial state, ×500; *b, c, d, e* – after 240 hours of exposing to direct-current magnetic field, ×400; *f* – after 720 hours of exposing to direct-current magnetic field, ×400 27

1.8 Microstructures of Cz-Si samples doped with Cu: *a* – initial state, ×500; *b, c* – after 240 hours of exposing to direct-current magnetic field, ×400; *d* – after 720 hours of exposing to direct-current magnetic field (sample No. 1), ×400; *e, f* – after 720 hours of exposing to direct-current magnetic field (sample No. 2), ×400 28

1.9 Microstructures of Cz-Si samples doped with Zr: *a* – initial state, ×500; *b, c* – after 240 hours of exposing to direct-current magnetic field, ×500; *d, e, f* – after 720 hours of exposing to direct-current magnetic field, ×400 29

1.10 Microstructures of Cz-Si samples doped with Hf: *a* – initial state, ×500; *b, c, d* – after 240 hours of exposing to direct-current magnetic field, ×400; *e, f* – after 720 hours of exposing to direct-current magnetic field, ×400 30

1.11 Microstructures of Cz-Si samples doped with Mg: *a* – initial state, ×1000; *b* – after 240 hours of exposing to direct-current magnetic field, ×400; *c, d* – after 720 hours of exposing to direct-current magnetic field, ×400 31

1.12 Microstructures of Cz-Si samples doped with Fe: *a* – initial state, ×500; *b, c* – after 240 hours of exposing to direct-current magnetic field, ×400; *d, e, f* – after 720 hours of exposing to direct-current magnetic field, ×400 32

1.13 Diffractogram of Cz-Si sample (initial state) 34
1.14 Diffractogram of Cz-Si sample (B = 0.4 T) 35
1.15 Diffractogram of Cz-Si sample (B = 1.2 T) 36
1.16 Line profile (511) before the magnetic field action and after it: *a* – initial state; *b* – 0.4 T; *c* – 1.2 T 36
1.17 Microhardness graphs for Cz-Si(Al) samples: *a* – after 240 hours of exposing to direct-current magnetic field; *b* – after 720 hours of exposing to direct-current magnetic field 37
1.18 Microhardness per the structural units for Cz-Si(Al) samples (in the initial state, after 240- and 720-hour exposition to direct-current magnetic field) 38
1.19 Microhardness graphs for Cz-Si(Hf) samples: *a* – after 240 hours of exposing to direct-current magnetic field; *b* – after 720 hours of exposing to direct-current magnetic field 39
1.20 Microhardness values per the structural units of Cz-Si(Hf) samples (in the initial state, after 240 and 720 hours of exposing to direct-current magnetic field) 39
1.21 Microhardness graphs for Cz-Si(Cu) samples: *a* – after 240 hours of exposing to direct-current magnetic field; *b, c* – after 720 hours of exposing to direct-current magnetic field 40
1.22 Microhardness per the structural units of Cz-Si(Cu) samples (in the initial state, after 240- and 720-hour exposition to direct-current magnetic field) 41
1.23 Microhardness graphs for Cz-Si(Mg) samples: *a* – after 240 hours of exposing to direct-current magnetic field; *b* – after 720 hours of exposing to direct-current magnetic field 41
1.24 Microhardness per the structural units for Cz-Si(Mg) samples (in the initial state, after 240 and 720 hours of exposing to direct-current magnetic field) 42
1.25 Microhardness graphs Cz-Si(Fe) samples: *a* – after 240 hours of exposing to direct-current magnetic field; *b* – after 720 hours of exposing to direct-current magnetic field 43
1.26 Microhardness per the structural units of Cz-Si(Fe) samples (in the initial state, after 240 and 720 hours of exposing to direct-current magnetic field) 43
1.27 Microhardness graphs of Cz-Si(Zr) samples: *a* – after 240 hours of exposing to direct-current magnetic field; *b, c* – after 720 hours of exposing to direct-current magnetic field 44
1.28 Microhardness per the structural units of Cz-Si(Zr) samples (in the initial state, after 240 hours and 720 hours of exposing to direct-current magnetic field) 45
1.29 Microhardness graphs of Cz-Si samples: *a* – after 240 hours of exposing to direct-current magnetic field; *b, c* – after 720 hours of exposing to direct-current magnetic field 45
1.30 Microhardness per the structural units of undoped silicon in the initial state, after 240 and 720 hours of exposing to direct-current magnetic field 46
1.31 Dependence between the time span of the current minority-carriers and the average microhardness of the samples: *a* – initial state; *b* – after 240 hours of exposing to direct-current magnetic field; c – after 240 hours of exposing to direct-current magnetic field 48

2.1 Residential power plant: *a* – parabolic solar concentrators are collocated in special zone; *b* – solar concentrators are combined in the roof of TES and powerhouse 57
2.2 Solar concentrators from Ripasso Energy 58
2.3 Example of solar concentrator from Solarflux 59
2.4 Solar concentrator from ZED 59
2.5 Solar concentrator from EuroDish 60
2.6 The scheme of combining solar energy with agricultural plant 62
2.7 First structure project 64
2.8 Support structure frame of the first prototype: *a* – four mirrors collocated on the structure; *b* – concentration of solar energy in focal point 64
2.9 Prototype with the first structure model 65
2.10 Model of solar concentrator with parameters 66
2.11 Triangle ABC of solar concentrator 68
2.12 The second structure model: *a* – structure from parallel bars; *b* – one zone with screws (black points) 69
2.13 Scheme of screw connection for mirrors 69
2.14 Structure with mirrors 70
2.15 The concentrator with the second structure model 70
3.1 RDF production technology 80
3.2 Morphological composition of MSW for large cities of Ukraine 82
3.3 Average morphological composition of combustible solid waste, which can be raw materials for RDF 82
3.4 Effect of heat carrier temperature on the kinetics of the RDF drying process: V=2.5 m/s, d=10 g/kg dry air, δ=15 mm, mixture No. 1: 1, 1′ – 80 °C; 2, 2′ – 100 °C; 3, 3′ – 120 °C 86
3.5 Influence of heat carrier temperature on RDF drying speed V=2.5 m/s, d=10 g/kg dry air, δ=15 mm, mixture No. 1: 1 – 80 °C; 2 – 120 °C 86
3.6 The influence of the heat carrier speed on the kinetics of the RDF drying process t=120 °C, d=10 g/kg dry air, δ=15 mm, mixture No. 1: 1, 1′ – 2.5 m/s; 2, 2′ – 1.5 m/s 87
3.7 Influence of the composition of mixture (1, 2, 3) on the kinetics of the RDF drying process t=120 °C, V=2.5 m/s, d=10 g/kg dry air, δ=15 mm: 1 – mixture No. 1; 2 – mixture No. 2; 3 – mixture No. 3 88
3.8 Influence of the composition of the mixture (1,4) on the kinetics of the RDF drying process t=120 °C, V=2.5 m/s, d=10 g/kg dry air, δ=15 mm: 1 – mixture No. 1; 2 – mixture No. 4 88
3.9 Change in the temperature coefficient depending on the moisture content of the material and the heat carrier temperature during the RDF drying process V=2.5 m/s, d=10 g/kg dry air, δ=15 mm, mixture No. 1: 1 – 80 °C, 2 – 100 °C, 3 – 120 °C 89

3.10 Change of Rebinder criterion depending on material humidity and heat carrier temperature during RDF drying V=2.5 m/s, d=10 g/kg dry air, δ=15 mm, mixture No. 1: 1 – 80 °C, 2 – 100 °C, 3 – 120 °C 90

3.11 Change in heat flux from material humidity and temperature of the heat carrier in the process of drying RDF V=2.5 m/s, d=10 g/kg dry air, δ=15 mm, mixture No. 1: 1 – 80 °C, 2 – 100 °C, 3 – 120 °C 91

3.12 Block diagram of the modernized derivatograph "Q-1000" 93

3.13 Conditional thermal effects (CTE) and net calorific value Q_n^d of RDF samples 101

4.1 Hydropower potential of small rivers of Ukraine 109

4.2 Wind energy potential in Ukraine 111

4.3 Installed wind power capacity by regions of mainland Ukraine in the first half of 2021, MW 111

4.4 Solar energy potential in Ukraine 113

4.5 Duration of sunshine hours 113

4.6 Methods of energy production from biomass 118

4.7 Primary energy supply from biofuels 118

4.8 Environmental pollution index by power plants depending on the energy resource 134

4.9 Acceptability index values for energy resources 135

4.10 The value of the environmental conservation index 136

4.11 Concordance coefficient 137

4.12 Environmental pollution index by power plants depending on the energy resource for electricity production in the world and Ukraine 137

5.1 Variants of biomass co-firing at power plants: direct, indirect and parallel combustion 148

5.2 Experimental unit 153

5.3 Temperatures in the reactor in the modes of co-firing of gas coal dust and crushed pellets: *a* – pine; *b* – wheat straw; *c* – sunflower husk; *d* – sunflower husk of the 2nd series 156

5.4 Conversion degree of a mixture of gas coal and different types of biomass depending on the proportion of biomass in the mixture 156

5.5 Concentration of nitrogen oxide at the outlet depending on the biomass proportion 157

5.6 Sketch of the fuel chamber of the TP-87 boiler 160

5.7 Combustion chamber diagram with zones 161

5.8 Geometry of the calculation area – TP-87 fuel boilers 164

5.9 Temperature fields in sections along burners 3 – 10 (*a*), along burners 1 – 12 (*b*) and along the z axis (*c*) 166

5.10 Coke burnout intensities (a) and volatiles output (b) in the section along burners 3 – 10. White field – exceeding the upper limit of the scale 167

5.11 Comparison of mass-average temperatures at the zone outlet based on the results of numerical modeling with the data of the zone-by-zone calculation using the normative method 167

5.12 Comparison of heat flux densities in the walls of zones according to the results of numerical modeling with the data of zone-by-zone calculations using the normative method 168
5.13 Distribution of coke burnout intensity by fuel height according to the results of numerical modeling and according to the data of the zone calculation by the normative method 169
5.14 Temperature fields in the mode with the introduction of 10 % pine pellets in sections along the burners, 3 – 10 (*a*), 1 – 12 (*b*) and along the *z* axis (*c*) 170
5.15 Effect of pellet introduction on mass average temperatures at the zone outlet
5.16 Coke burnout intensities of coal (*a*) and pellets (*b*), as well as the intensity of volatile coal (*c*) and pellet output (*d*) in the cross section of burners 3 – 10. White field – exceeding the upper limit of the scale 170
5.17 The effect of the size of particles introduced into the pellets on the efficiency of burning coal coke and pellets 171

INTRODUCTION

Modern global challenges in the field of energy, ecology and resource conservation require a systematic approach and search for innovative solutions aimed at improving energy efficiency, introduction of renewable energy sources and rational use of natural resources. The rapid depletion of traditional fuels such as coal, oil and gas leads to the need to develop new technologies that ensure stable energy supply with minimal environmental impact. In addition, increasing volumes of industrial and domestic waste, as well as increasingly stringent environmental requirements for enterprises, create additional challenges for the energy sector and industry as a whole.

In this regard, studies aimed at developing new materials, technologies and approaches to the organisation of energy systems that could ensure high efficiency and environmental safety are becoming relevant. This monograph is devoted to a comprehensive study of some of the most important areas in the field of materials science, alternative energy and sustainable development, which are of strategic importance for modern industry and energy.

The following key issues are discussed in detail in the monograph:

– the influence of a magnetic field on the microstructure of silicon grown by the Czochralsky method (Cz-Si) doped with the elements Al, Mg, Cu, Fe, Zr, and Hf. For the first time in scientific practice the study of structural changes of silicon under the influence of magnetic field and the influence of various impurities on its crystal lattice is carried out. The research shows that these elements differently affect the interaction energy of silicon atoms in the lattice and behave differently under the influence of a magnetic field. The results may be useful for the production of semiconductor materials with improved characteristics, which is critical for microelectronics and solar energy;

– development of innovative designs of solar concentrators. The work explores the issues of improving the technological efficiency and reducing the production cost of solar concentrators, which plays a key role in the development of alternative energy. The existing designs have been analysed and new solutions have been proposed, aimed at reducing the weight of structural elements, reducing assembly costs and increasing the ease of operation. The developed prototypes of solar concentrators can be widely applied in agriculture, in power supply systems of residential buildings and in organic waste recycling processes;

– utilisation of municipal solid waste (MSW) in the energy balance of Ukraine. One of the most important directions of sustainable development is the processing and utilisation of waste for its further use as an alternative energy source. In this paper the physical and chemical properties of RDF (refuse-derived fuel) - an alternative solid fuel produced from combustible components of MSW are investigated. The kinetics of drying, thermal decomposition and calorific value of RDF of different compositions were analysed. The obtained data can contribute to the development of energy-efficient technologies of RDF production and its effective application at thermal power plants;

– analysis of the state and prospects of development of the energy complex of Ukraine. An important part of the monograph is the analysis of the structure of the energy balance of the country, identification of key problems and proposals to improve the current situation. The issues of using traditional energy resources, such as coal, oil, gas and nuclear fuel, as well as the prospects of transition to renewable energy sources are considered. A methodology for selecting optimal energy strategies for different regions, taking into account environmental and economic factors, is propose;

– co-firing of coal and biomass as a way to reduce harmful emissions. The work is aimed at the development of coal and biomass co-combustion technologies, which allows to reduce CO_2, SO_2 and NOx emissions, diversify fuel sources and increase the sustainability of energy systems. The basic principles of co-combustion are investigated, heat engineering calculations are performed, and experiments on co-combustion of gas coal and biomass are carried out. Recommendations for the introduction of technologies at TPPs have been developed, which can contribute to the improvement of energy efficiency and environmental safety.

Modern methods and approaches, including X-ray diffraction analysis, thermogravimetric analysis, computer modelling in ANSYS FLUENT software packages, as well as experimental methods of measuring and controlling the characteristics of materials were used in the research within the framework of this work.

The results presented in the monograph can be useful in the development of new solutions for the energy industry, in the design of renewable energy systems, in the sphere of waste utilisation and in the issues of reducing the environmental impact of industrial facilities. The obtained data and recommendations are intended for a wide range of specialists, including engineers, developers, scientists, designers, as well as undergraduate and postgraduate students of technical areas of training.

Thus, this monograph is a complex scientific and applied work covering the most important directions in the field of sustainable energy, materials science and environmental safety. The studies and recommendations presented in it have practical significance and can be used for further development of scientific and technological solutions in this field.

DOI: 10.15587/978-617-8360-02-3.CH1

Maksym Kovzel, Olga Nosko
© The Author(s) 2024. This is an Open Access chapter distributed under the terms of the CC BY-NC-ND license

CHAPTER 1

MAGNETIC TREATMENT OF SEMICONDUCTOR SILICON

ABSTRACT

The current publication reports on the magnetic field influence on the microstructure of Cz-Si doped with Al, Mg, Cu, Fe, Zr, Hf. The point is that these dopants have different effects on the interaction energy of silicon atoms in its crystal lattice and differently behave under magnetic field treatment. In this context, the problem of silicon processing is first time addressed.

It is established that the dopants (Al, Mg, Cu, Fe), which decrease the energy of atom interaction within the crystal lattice of silicon, lead to the increase in the defects of the silicon structural units after 240 hours of magnetic field treatment while 720 hours produce the decrease in the quantity of such defects.

Cz-Si doped with Zr, Hf (these dopants increase the interaction energy of the silicon crystal lattice) experiences the decrease in the quantity of defects in the structural units starting from 240 of exposing to the magnetic field.

By means of X-ray diffraction technique, the occurrence of new peaks on the scattering angles of 90–92 degrees has been detected, that is due to Si_{FCC} lattice distortion and the formation of Si orthorhomic alongside with it. This indicates phase transformations in the samples of semiconductor silicon during magnetic treatment at room temperature.

KEYWORDS

Semiconductor silicon, complex doping, interaction energy, phase transformations, dislocation density, twins, magnetic field treatment, microhardness, specific electrical resistivity, charge minority-carrier lifetime.

Commonly, power engineering for energy production has always been posed as the principle industry of any developed country. To provide energy independence is one of the strategic tasks to address in modern Ukraine's economy development. The promising way how this task can be solved is in maximizing the strategic balance by enhancing the energy share from the own energy

resources. The urgency of this problem in Ukraine determines the need for the development of the alternative energy forms based on renewable sources alongside with the energy saving.

Back in 1990, the world's developed countries initiated transition stage to the new energy sources. The environmentally-friendly attitude is among the features of this stage, i.e. it strives to reduce environmental pollution and to minimize carbon dioxide and sulfur dioxide emissions. Expected that during the next two or three decades, the mankind is to introduce ecologically-friendly renewable energy sources into everyday life, primarily wind power and solar power. Ignoring these tendencies threats with ecological disasters of the future and is able make the entire life on earth endangered.

Moreover, pursuing the target of achieving European Integration, Ukraine sets the strategic goal of rapid implementation for the energy produced from the renewable energy sources. Thus, solar power is the most promising direction of such kind in Ukraine, where there is a high potential due to the country's geographical position in the terrestrial latitudes with good solar radiation intensity. The latter implies that the photovoltaic equipment can be used throughout the year. Further, the high-performance operating time in the northern areas makes up 5 months (May to September), while in the southern areas it is 7 months (April to October). However, the solar power economic features require careful further study. According to experts, the operating cost of the electrical power generated by the solar modules will reduce by 5 times during the next 10 or 15 years.

Taking into account the above stated necessity of solar engineering development, silicon, as a constituent of solar cells, draws the close attention of the scientists. In particular, thermal stability of silicon crystal properties is one of the basic parameters of semiconductor quality and at the same time it is the very factor that determines the resistance of microelectronic devices to degradation at elevated temperatures and expands the area of their operation. Furthermore, thermal stability of silicon crystals is essential for manufacturing microelectronic devices, since crystals are exposed to high temperatures in many technological processes that often irretrievably deteriorate properties of primary crystals.

The topical character of the study is determined by the need to reveal the degradation regularities in silicon physical properties and the means of their further control, as well as by the necessity to develop semiconductor devices based on silicon with stable parameters.

The manufacturing processes and operation of semiconductor devices are known to be followed by thermal and radiation effects that cause the changes in the physical properties of both in semiconductors and the devices based on them. However, there are rigorous specifications to the manufactured semiconductor devices concerning stability of their parameters under various radiation and thermal operating conditions. The potentially productive ways of control over silicon physical parameter degradation are in its thermal treatment, doping and processing within a magnetic field. Today there is a growing demand for monocrystalline silicon for photo-emissive converters from both foreign and domestic companies. The circle of scientific interests of the global research community continues to be focused on solar cell manufacturing techniques from cheap silicon that can be represented by polycrystalline silicon of low-purity ("dirty"), thin films of amorphous silicon of polycrystalline type and other semiconductors.

Considering the full-scale opportunities for the silicon and the dedicated equipment, the need for the sufficiently high level of readiness should be provided, which enables the rapid and efficient growth of modern solar power in Ukraine.

The first section of the current publication contains the literature review on the regularities in semiconductor silicon structure formation and properties, as well as the modern views and opinions on phase transformations and martensitic transformation mechanisms that occur in semiconductor silicon. The contemporary publications targeting the problem of the magnetic field effect on the semiconductor silicon structure and properties have been reviewed. This analysis enables outlining the character of the further studies and the stages of the topical scientific and technical task to be solved for the current research: for the present publication we set the task to develop the complex resource-saving technology and energy saving solution for production of semiconductor silicon with enhanced physical and mechanical properties by influencing its liquid and solid forms physically and chemically with the objective to expand the areas of its application.

The second section provides the data on the material and the research techniques. The object of the research is monocrystalline semiconductor silicon samples (Cz-Si) grown by Czochralski method, both in undoped version and doped with single elements of B, Sn, Ge, Hf, Zr, and with the complexes of B-Sn and B-Mo, ranging from $2 \cdot 10^{-4}$ to $8.7 \cdot 10^{-2}$ at % in the initial state, after they have been exposed to the complete heating-cooling cycle, the thermal treatment regimes and the weak direct current magnetic field effect.

In the third section the structure peculiarities formed under the magnetic field effect for both the undoped Cz-Si samples and the Cz-Si doped with Al, Mg, Cu, Fe, Zr, and Hf have been analysed, with the focus on the difference in the dopant effects on the silicon atom interaction energy within silicon crystal lattice. During the magnetic treatment at room temperature, the phase transformations have been detected in semiconductor silicon samples via X-ray diffraction technique.

In the fourth section we report on the magnetic treatment effect on the microhardness values of doped Cz-Si structural units.

The fifth section reveals physical parameters and mechanical properties of the doped and undoped silicon samples before and after magnetic field treatment with the induction of 66 mT.

1.1 EARLIER RESEARCH FINDINGS AND RELEVANT LITERATURE REVIEW

1.1.1 CRYSTALLOCHEMICAL PECULIARITIES OF SEMICONDUCTOR SILICON

Silicon is an element of IVB subgroup of the periodic system, the atomic number of 14, an electron configuration of $1S^2 2S^2 P^6 3S^2 P^2$. Silicon atoms possess four valence electrons and form a diamond-type or a zinc blende type of the crystal lattice with covalent bonds and coordination number of 4 at room temperature, when silicon behaves as a typical semiconductor.

Silicon has high specific melting point and its density increases when transformed from a solid state to a liquid one [1].

Under atmospheric pressure silicon is a covalent substance with strong semiconductor properties. Interatomic bonds are defined by means of tetrahedral symmetry and have sp^3 hybrid composition. All 4 silicon atom bonds are equivalent and equally saturated.

In [1–3], it is shown that silicon undergoes the semiconductor-metal transition during melting, while at high pressure (~12 hPa) [2] there has been detected the transition from purely covalent structure (K=4) of a diamond to bcc tetragonal covalent metal structure within silicon (as the white tin type) and then (~16 hPa) the transition to the typical body-centered cubic metallic structure (K=8).

The publications [1–4] suggest that the transition to metallic state (when melting the elements belonging to IVB group (germanium and silicon) as well as compounds of AIIIBV and AIIBIV types etc.) is related to the disruption in homopolar bond space system and to the separation of many free electrons; the latter form a new configuration with electron density of higher symmetry [3].

Silicon melting causes the sharp increase in its conductivity which value becomes equal to the liquid metal conductivity value. It should be noted, that conductivity alteration is connected to the rearrangement from the "diamond structure" of a solid state to denser packing peculiar to the "metallic state" that occurs when melting these substances of short range ordering; this process is confirmed by the density increase factor that to some extent reflects the structural changes. According to the X-ray investigation data, it has been proved that the structure change occurs in many semiconductors with diamond structure (including silicon) when in a liquid state. During melting silicon coordination number increases from 4 to 6.

1.1.2 PHASE TRANSFORMATIONS IN SEMICONDUCTOR SILICON

It is peculiar of silicon to have high specific fusion heat as well as density increase during transition from a solid state to a liquid state [5, 6]. Fusion entropy of silicon is considerably higher than that of pure metals that is why its value is greatly affected by the process related to the electron delocalization at the solid-liquid transition. The electron component is connected to the chemical bond type change (mainly from covalent bonds to metallic ones) during melting that is followed by the marked increase of free electron concentration [6].

For the substances that become highly metallized at melting, solid-liquid transition is followed by disruption in the sp^3-hybrid homopolar bond space system, by detachment of four valence electrons and their transition to the free state and by major changes of the short range ordering and atom vibrational spectrum [7–9].

A distinguishing feature of the first-order phase transitions in silicon (by that we mean melting and crystallization) is the change of the free electron number and the important role of the electron component is in this transition. Apparently, at the temperature and the pressure change, allotropic transformation can be followed by the free electron number alteration.

The data on phase transitions in the solid polymorphic type of silicon are given in the publications [6–8]. Polymorphic closely-packed metallized modifications of silicon are formed at high pressure [7]. At the pressure of 12 hPa and the temperature of 20 °C, the phase transition SiI→SiII has been detected by means of resistometric investigation and X-ray analysis [8]. A notable dependence has been revealed for the SiI→SiII phase transition on the shift components of load, pressure and the holding-pressure time of the sample. Due to this, the transition continues at 2–3 hPa. SiII phase is reported as one having metallic conductivity. The inverse transition SiII→SiI has not been detected.

After subjecting SiII samples to certain pressure, there have been revealed 2 modifications of Si (SiIII and SiIV) by X-ray analysis under atmospheric conditions. Heating SiIII within 200–600 °C causes its lattice rearrangement and, consequently, there occurs SiIV modification with the hexagonal wurtzite-type structure. Under additional pressures, SiIV behaves as a metastable phase. Two assumptions have been suggested concerning SiIII: it either can be a stable phase under 12 hPa at 20 °C with a body-centered cubic lattice, or it is a transition phase from SiII of tetragonal structure when pressure is removed. Under the pressure of 12 hPa, SiII phase transforms into superconductive state if $T=6.7$ K [11].

In [9–11], the temperature dependence of some semiconductor silicon properties has been described, particularly, thermal expansion coefficient, hardness, lattice parameter, electrical properties at atmospheric pressure in the range from $T=20$ °C to $T<T_{melting}$. During phase transitions, semiconductor silicon undergoes discontinuous change of thermal, volumetric, mechanical and electrical properties due to the transition from one crystalline state into another. Establishing the property-temperature and property-pressure dependences allows revealing phase transition.

Normally, phase transition develops with a high rate, however, this behaviour is true only for certain regions. Being conditioned by the size and the number of a new phase regions that are formed per unit time, the volume rate of transformation is low in many cases, though the region formation rate is very high.

The volume rate of the transformation is taken into account in [9] for the studies on temperature dependence in silicon properties when heated at the rate of ≤5 °C/min. These studies on semiconductor silicon properties reveal the monotonic dependence.

The abnormal character of the temperature dependence of the sample linear dimensions shows that there are different silicon phases at certain temperatures due to formation of which the registered changes occur.

In [10], the following phase transitions in silicon at heating are described. The general conclusion based on the ultrapure silicon research data is that these phase transitions can be observed in the local crystal volumes during heating with the rate of less than 5 °C/min:

(I) within 250–350 °C $Si_{FCC}\rightarrow Si_{ORTHORHOMBIC}$;

(II) within 680–700 °C $Si_{ORTHORHOMBIC}\rightarrow Si_{BCC}$;

(III) within 1150–1200 °C $Si_{BCC}\rightarrow Si_{HCP}$;

(IV) within 1420 °C $Si_{HCP}\rightarrow P$.

Low-temperature transformations (I and II) have low ΔH values and can be referred as phase transitions that cause lattice atom shears at small distances. In this case we observe shear transformations that are based on the ordered lattice rearrangement. The lattices of both modifications are combined or adjacent while the shear transition starts heterogeneously. The nuclei appear in the areas with the dedicated dislocation nodes (the order growth rate is 10^3 m/sec). Polymorphic transformation rate is especially high in defect-free crystals. Phase transition III is accompanied by high thermal effect, so hyperthermal transformation in silicon is a first-order phase transition and it occurs due to the total rearrangement of the lattice. The specific feature of a first-order phase transition is the presence of interfaces that is why the transitions of this type lead to the fundamental crystal structure rearrangement.

The calorimetric analysis of the ultrapure semiconductor silicon [11] reveals that the phase transition is blurred and this phenomenon can be explained by as below:

– formation of polymorphic modifications with closely adjacent lattices;

– irregular distribution of impurity atoms within the crystals, namely O_2, H_2, C;

– irregular distribution of defects.

Considering the above stated, it can be suggested that when heating semiconductor silicon, its crystal lattice is proved to become denser before $T_{melting}$, conditioned by the degree of bond directions and followed by the transition to the metallic state. The transition of covalent crystals to the metallic state can be obtained regardless of the lattice disruption type and the techniques to influence the crystals.

The transition mechanism of the covalent crystals to the metallic state at various ways of the lattice excitement is the same: there occurs electron subcrystalline structure alteration, particularly, the sp^3-hybrid bond disruption is followed by the band gap narrowing and the corresponding increase in the number of charge carriers [11, 12].

The transition from the covalent bonding to the metallic one is carried out due to electron motion from the "coupled" state in the valance band to the "antibonding" conduction band, that leads to the decrease in the shear resistance of diamond lattice [12].

The experiment shows that at heating semiconductors, the transition from the semiconductor to the metal begins at the temperature considerably lower than $T_{smelting}$. It is interesting to note, that this temperature is not the same for the crystals obtained by different techniques [13]. The transition occurs due to the sequential lattice rearrangement from less dense to denser by the shear or shear-diffusion mechanism and is followed by the change in the correlation between the covalent component and the metal component of the chemical bond. In other words, in silicon there occurs direct and reverse martensitic transformation on its exposure to the different factors.

The most important feature of the diffusionless transformations is the concerted migration of large atomic groups during the new phase crystal growth. According to Kurdyumov, "Martensitic transformation is a regular lattice rearrangement in which the adjacent atoms do not interchange their places but only shear relative to each other at a distance which does not exceed the interatomic one" [14].

All the martensitic transformations without any exception have certain features conditioned by the following:

1) the cooperative character of atom migration during the crystal growth;

2) transformations in anisotropic elastic medium.

The crystals of the martensitic phase appear and reach their finite sizes at small-time intervals. The increase in the amounts of new phases takes place mainly due to the formation of new crystals, however, in some alloys there can be observed discontinuous growth of previously formed plates. The martensite crystals usually have a shape of a double convex lens and are twinned formations with a twining plane that coincides with the lens symmetry plane. Similar to twinning, such martensite crystal shape is explained by the elastic strain effect that occurs in the surrounding matrix during the growth of the new phase crystals.Theoretically, the analogy between twinning and diffusionless transformations is so due, that many authors regard twinning as a special case of diffusionless transformation during which the substance structure remains unchanged [15, 16]. Twinning can occur both with the change of the shape and without it (for instance, quartz). By analogy, diffusionless phase transformations can be subdivided into two groups:

1) diffusionless phase transformations that change the shape;

2) diffusionless phase transformations that do not lead to the change of the shape.

The transformation accompanied by the shape change is the one, during which there occurs primary macroscopic deformation; the transformation without such a change in the shape is the one, at which there is only "secondary" deformation. Thus, martensitic transformations are the diffusionless transformations accompanied by shape change. The diffusionless transformations with no shape change are more common for the crystals with complex structure, chiefly, for molecular crystals. These transformations, in case of preserving the atom migration cooperative character, can be deprived of many peculiar to martensitic transformations features related to the shape change.

In combination with the elastic medium effect on the growing crystal, the macroscopic shear, that follows martensitic transformations, causes the "elastic" martensite crystal formation. This phenomenon is analogous to elastic twinning. The martensite crystal growth takes place due to regular atom migration to new dislocations, so that the adjacent atoms of the initial lattice remain adjacent in the new lattice as well. On the separation interface of the two phases, there is one lattice which continuously transforms into the other, i.e. there is a coherent bonding between the lattices of the initial phase and the new one. With the crystal size increase, the elastic strains on the interface surface of the two phases also increase; eventually, these strains lead to plastic deformation and, consequently, to coherence violation between the two lattices and the crystal growth character alteration.

When covalent crystals are heated to the critical values at certain temperature due to the increase in the antiphase oscillation amplitude, there occurs covalent bond breakdown and the localized pairs of electrons in them become collective, that, in its turn, predetermines transition to the metallic state.

The transition of covalent crystals to the metallic state can be achieved irrespectively to the lattice excitement and the techniques of influence to which the crystal is exposed to: heating, high laser irradiation, radiation and magnetic exposure, high pressure, explosive treatment, etc.

Moreover, the mechanism of the covalent crystal transition to the metallic state is the same whatever the techniques of the lattice excitement: electron subcrystalline structure changes, namely the sp^3-hybrid bond disruption is followed by the band gap narrowing and, consequently, by the increase in the charge carriers quantity [17, 18]. The concentration of the charge carriers in InSb solid phase even at the temperature of ~420 °C reaches $0.3 \cdot 10^{21}$ cm^{-3} while in InSb liquid phase at $T_{melting}$ it is $N_t = 5 \cdot 10^{21}$ cm^{-3} [18]. The same results have been obtained in [17] for semiconductor silicon: $N_t = 1.0 \cdot 10^{25}$ cm^{-3} at the temperature of ~727 °C, that corresponds to metallic state.

The transition from the covalent bonding to the metallic one takes place due to transferring of electrons from the "coupled state" in "antibonding" conductive area, that leads to the decrease in the shear resistance of the diamond lattice [19].

The problem of heating which initiates the transition of semiconductor into metal starting at the temperature much lower than the melting temperature (different for different crystals) [13] is relevant to [17, 18] and finds its further explanation as given below. The gradual rearrangement of the lattice into the denser one by the shear or shear-diffusion mechanism is followed by the correlation change between the covalent and metal chemical bond components. For instance, in Si, Ge, and InSb crystals there occurs direct transformation or reverse martensitic transformation depending on the influence produced. According to the general regularities of semiconductor property changes within the range of 0.16–0.20 $T_{melting}$, the atoms in the crystal lattice interact via the covalent bond pattern while within 0.2–0.8 $T_{melting}$, heterodesmic covalent metal bonding occurs and eventually at the temperature higher than 0.8 $T_{melting}$ the metallic bonding is predominantly observed. The revealed regularity correlates with the idea of alteration of covalent crystal heat capacity at heating [20].

The classical theories tell that at the absolute zero of temperature, all atoms in the crystal are motionless and the potential energy of their interaction is minimal. At quite low temperatures atoms are supposed to have small oscillation, at that, the kinetic energy value of the atom oscillation should be small as compared to their interaction energy. With the temperature and oscillation amplitude increase, the atom interaction energy increases as well. At the temperature increase by 1 degree, the value of the oscillation energy absorbed determines the so called oscillating temperature, and, at first approximation, heat capacity (harmonious oscillator). However, when heated under conditions of constant pressure, the thermal expansion of a solid occurs during which the phenomenon grows into a more complicated character. The oscillation of the atom and its shift from the initial state of equilibrium generate the forces that affect the oscillation of the adjacent atoms. A small difference in a phase that can occur at any certain period of time leads to the fact that the atoms do not possess rigidly fixed middle positions to be independent of the adjacent atoms. Moreover, since all the interacting atoms of a solid body take part in the oscillating process, this process cannot have a single frequency. The general energy of the crystal does not change at a constant temperature,

but the energy of each atom changes chaotically in the course of time. Thus, when explaining the temperature drive of the heat capacity phenomenon at the elevated temperatures, one should take into account the higher (anharmonic) expansion terms of the potential energy decomposition by shearing.

1.1.3 MARTENSITIC TRANSFORMATION MECHANISMS IN SILICON

The first instance of martensitic transformation in Si was observed under influence of the compressive loads in the temperature range of 400–700 °C within the region of indentation trace left by the diamond indenter [21]. It was assumed that there are the possible mechanisms of martensitic transformations in silicon, particularly the formation of hexagonal diamond phase with cubic twinning. The martensitic transformation occurs because a structure becomes thermodynamically unstable [14]. It is usually followed by the change of the shape that is manifested through the emergence of narrow plates within the compressed matrix. Due to this, and also as a result of cooperative diffusionless reaction, the martensitic transformation sufficiently adds to the strain energy. Thus, in order to initiate the transformation of this kind, it is necessary to apply sufficient affecting forces. Such forces of the martensitic transformation provide the absence of diffusion processes and can be induced in two ways, namely by accelerated cooling and by high degree of strain. Considerable supercooling leads to the emergence of quite strong affecting forces.

The crystallography of martensitic transformation has macroscopic nature as it describes the crystallography before and after the transformation but not the further process of the latter.

Crossing of twins is the most characteristic model of martensitic transformation in Si. Each twin is formed based on the differences in the mobility of partial dislocations within Si. This phenomenon is conditioned by the difference in glissile activation energy for both head dislocations and partial dislocations of the split screw dislocation and it increases at higher temperature. According to this model, twinning in Si requires three factors as following:

– the presence of an axial segment of a screw dislocation,

– the effect of shear stress on a dislocation segment in a primary plane and a crossed plane,

– medium temperatures.

In monocrystal of Si, the martensitic transformation takes place within the temperature range of 250–700 °C. Direct and reverse martensitic transformation occur in Si and they depend on the nature of its properties when being exposed to heating and cooling, due to which there can be observed some kind of hysteresis of martensitic transformation temperature interval.

By the origin, five types of twins can be distinguished:

a) concretion at random collision;

b) parallel lamination of molecules on a twin nucleus;

c) deposit of molecules on a large crystal formed in a twinning position;

d) transition from one modification to the other;

e) due to mechanical action.

The more symmetric the crystal structure is, the less likely is the twin formation. In crystals with low symmetry, different types of twinning can occur. Apparently, the formation of various types of twins is due to the lattice symmetry decrease during $Si_{FCC} \rightarrow Si_{ORTHORHOMBIC}$ phase transformation within Si samples that have been exposed to thermal treatment in the temperature range of 250–550 °C. Twinning is hardly observed during thermal treatment in the region of coexistence of $Si_{FCC} \rightarrow Si_{BCC}$ (750 °C).

Only shear stresses can affect twinning. Twin boundary energy during twin formation is of secondary importance. As the crystal form preserves while twinning, small distortions can be observed in the transition section. This section has a structure similarity to that of the high-temperature modification, while the twin boundary movement resembles the movement of a phase boundary at polymorphic transformation. During the closed loop of polymorphic transformations in single crystals of pure substances, a regular crystallographic direction of high-temperature grain modification is preserved; the latter is formed respectively to the primary single crystal. Moreover, in the microstructure, the changes occur connected with the new grain growth that is the result of phase transformations [15, 22]. The grains have almost similar crystal-lattice orientation, and when exposed to X-ray diffraction technique, such aggregation reveals itself as a single crystal; the same process is observed when growing monocrystalline silicon [22].

Thus, the development of two-dimensional crystal boundaries in monocrystalline silicon and the presence of two-dimensional conductivity are related to the formation of the shear phase transitions and twin boundaries.

The martensitic crystal formation not only leads to the crystal lattice type change, but also to plastic deformation of both the new phase and the matrix. The plastic deformation develops due to the slip of twinning. Such redundant or accommodative deformation is an integral part of martensitic transformation and provides minimum energy of elastic distortion on the invariant surface of phase interfaces. The elastic resizing of the crystal can be observed under compressive stresses or tensile stresses. Similar to twinning, the formation of martensitic crystals may be caused by the parent phase strains. The strain helps to carry out transformation by 100 %.

1.1.4 GENERAL PROBLEMS ON MAGNETIC FIELD EFFECT ON "NONMAGNETIC" SUBSTANCES

During the last 30 years there have been published over 200 studies on the effect of magnetic field with induction of 0.1–30 T and exposure time in the range of 10^{-6}–10^{6} sec on various properties of "nonmagnetic" substances (polymers, dielectric materials), semiconductors and metals [23–26]. In some cases, the magnetic field effect on some properties is more or less pronounced. For instance, in ionic crystals magnetic field affects the spin-dependent reactions between paramagnetic defects [23–27]. However, there are many examples described when the external phenomenological effects of placing the samples in the magnetic field are very similar to those presented in [23–27]. Nevertheless, the required conditions of spin-dependent reaction

occurrence are often neglected. For example, magnetic field affects the properties of metals: the microhardness values of aluminium, bronze, bismuth, etc. but during the short time of a spin reaction totally excludes the magnetic field effect on spin-dependent reactions; the influence of the properties of polymers is observed if they do not contain spin particles. Moreover, in the scientific papers it is discussed that the magnetic field has certain effects on the "aged" crystals where there are neither processes, nor reactions, therefore the magnetic field has nothing to affect. Hard to imagine that those "unpredictable" spin-dependent reactions which require meeting of a number of experimental conditions and have the chance of about a few per cent to produce the effects in chemistry [27], could occur without providing special conditions and take place in all types of the substances wherein they are reported to act as a main technique to explain the magnetic effects. Irrespectively of the fact that a lot of scientists a priori attribute a "spin-dependent" origin to the mentioned effects, they often find it difficult to identify the type of the particles with a spin. All these make perform the further studies aimed at revealing general (rather than spin-dependent) reasons why the thermodynamically weak magnetic field has an effect on the state and properties of solids. The carried out generalizing analysis on the experimental data delivered by the various scientists and addressing the physical properties of a wide range of substances regardless of their response (i.e. the physical property of a substance that has been studied in the publications) allow determining the phase of a gradual physical property change in a magnetic field and the phase of subsequent relaxation of this property after removing of the magnetic field (**Fig. 1.1**).

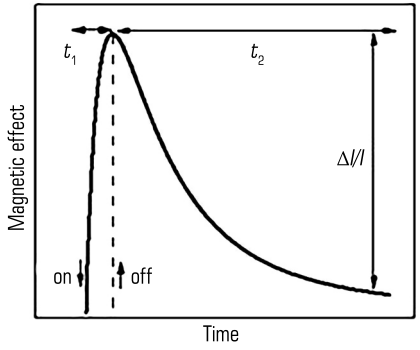

Fig. 1.1 Dependence diagram between a gradual change in the crystal physical properties within a magnetic field (with a time constant t_1) and a relaxation after the magnetic field removal (with a time constant t_2): a relative change in a physical value of $\Delta l/l$ is marked with a vertical arrow
Source: [27]

The duration of these phases (t_1 and t_2 respectively) is a universal quantitative characteristic for a number of magnetic effects. Another invariant value which can be analysed regardless

of both the measurement technique and the type of physical properties sensitive to the magnetic field is the relative value change of this property in saturation – $\Delta I/I$ (**Fig. 1.1**). By *I* we mean all the values described scientifically, whose changes under the magnetic field effect have been reported by the scientists (microhardness, dislocation pathlength, luminescence spectrum intensity, photoelectronic spectrum intensity, initial dislocation stress, electric conductivity, yield value, internal friction amplitude, etc.).

The dependence of time (t_1) on the magnetic strength in given in **Fig. 1.2**. It is obvious that regardless of the substance type and the research technique, t_1 value is subjected to a certain dependence: it reduces with the magnetic field (H) increase, i.e. magnetic induction process speeds up as the magnetic field increases. This is expected for one type of substance, but the demonstrable regularity in **Fig. 1.2** (that allows to discuss the universal dependence of $t_1(H)$ for various substances) suggests the assumption about the integral character of magnetic field physical effects on the substance properties.

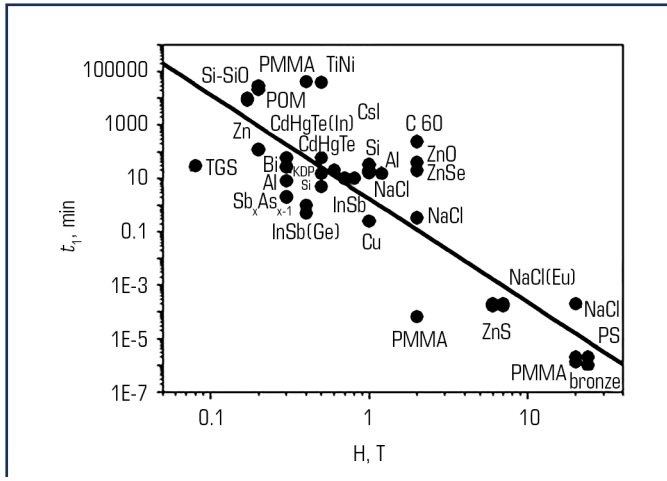

Fig. 1.2 Dependence between time t_1 and magnetic strength (H) for some substances. The approximation described in this publication is marked with a continuous line
Source: [27]

It would be natural to assume that in the magnetic field, there occur forces that affect the crystal lattice while the development of stresses changes the other properties of substances. In this case, the spread of $t_1(H)$ dependence could be explained by the difference in magnetic sensibility χ_m of solids under study. There are certain attempts to build $t_1(\chi_m H^2/2)$ dependence, where $\chi_m H^2/2$ is the magnetic field energy of the unit volume, which does not permit eliminating the spread. This indicates that the macroscopic magnetization of the substances under analysis is irrelevant for the observed effects, and the main impact on them is apparently produced

by the structure defects. In **Fig. 1.2**, the approximation of $t_1(H)$ is marked with a continuous line in double logarithmic coordinates with a linear function of $y=A+B\cdot x$, where $y=\lg t_1$, $x=\lg H$. From the approximation results, the function of $t_1=t_0/H^B$ with the parameters of $t_0=2$ min, $B=-3.9\pm0.3$ T can be drawn. Thus, the universal function is written as $t_1=t_0/H^4$. The paired measures, including the 4th-order ones, often occur in spin chemistry where the processes are governed by Δg spin contamination technique in a magnetic field [27].

Time (t_2) does not depend on the magnetic field. In thermodynamics, $t_1=t_2$ equation is applied to inverse processes. Further, if a magnetic field excites solids and transfers its energy to them, time (t_1 and t_2) are to be in a linear relation. The relaxation of an excited state should occur with the same invariable of time as the transition to excited state within the magnetic field. This is true for various processes, such as magnetization and demagnetization, chemical change in the potential with its postreduction, etc. The analysis reveals that there is no connection between t_1 and t_2 that means that the process is with the time invariable of t_2 that is often called relaxation and is in fact of a different origin. This process is represented by further transformations of the solid body defects subsystems that take place in the process with a time invariable of t_1. The attempts to obtain $t_2(H)$ dependence have been unsuccessful as well. Such dependence does not exist since the following processes that have once been initiated by the magnetic field become insensitive to the further magnetic field action and its values. The dependence between a relative change of physical properties in saturation per the time of $\Delta I/I$ is shown in **Fig. 1.3**. It turns out that the effects under study can be classified into three groups 1 (**Fig. 1.3, *a***), provided that the value of $\Delta I/I$ is built up as a magnetic energy function of a crystal lattice unit volume ($\chi_m H^2/2$). Group 1 is different from the other two groups by $\Delta I/I$ value being almost independent of the magnetic field value. Moreover, group 1 mostly includes semiconductors and metals, while in groups 2 and 3, which are highly sensitive to $\chi_m H^2/2$ value, ionic crystals and other dielectric materials prevail (**Fig. 1.3, *a***).

By this characteristic, group 2 and group 3 can be united into a single group that includes dielectric materials, which magnetic effect value depends heavily on the magnetic energy ($\chi_m H^2/2$) or (as it has been stated above) on the magnetic field. In **Fig. 1.3**, the continuous lines point to the approximation of 1, 2 and 3 types of $\Delta I/I$ dependences on ($\chi_m H^2/2$): $y=A+B\cdot x$, $y=\Delta I/I$, $x=(\chi_m H^2/2)$.

For all the three groups of substances, the magnetic effect is in a linear relation with magnetic energy $\chi_m H^2/2$. When small values of the magnetic energy of $\chi_m H^2/2$ or the weak magnetic fields, the effect is almost the same (practically identical A coefficients) and close to 5 % for each dependence of 1, 2 and 3. In large magnetic fields, B coefficient creates a large difference between 1, 2 and 3 groups.

One should mention that in spin chemistry [27], most effects are achieved by saturation in relatively low values (~0.1 T) of the magnetic fields while at values of the magnetic fields shown in **Fig. 1.3**, there is no dependence detected on the magnetic field. Thus, the established classification of the substances into groups can indicate the fact that the magnetic effects influencing semiconductors are really conditioned by spin-dependent reactions between the structure defects,

while the strong magnetic fields can activate some other magnetic field mechanisms of action in dielectric material that have not been previously discussed.

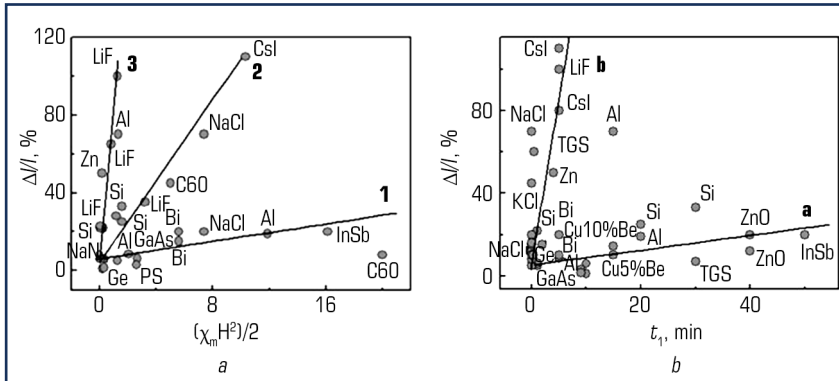

Fig. 1.3 The dependence between the relative value of property changes in solid bodies ($\Delta l/l$): *a* – the magnetic energy per unit volume ($\chi_m H^2/2$); *b* – time t_1 for some substances. The approximation described in this publication is marked with a continuous line
Source: [27]

From the above mentioned it can be obviously deduced that the magnetic effect value ($\Delta l/l$) is assumed to be related to the time (t_1) as it reflects time when waiting for the phenomenon to occur in a magnetic field and characterizes the kinetics of the change accumulation (that are induced by a magnetic field) in the crystal. **Fig. 1.3, *b*** shows $\Delta l/l(t_1)$ dependence that is also subdivided into *a* and *b* groups. Group *a* mostly includes semiconductors and metals while group *b* consists of dielectric materials. This fact emphases that there is a considerable difference in the mechanisms of the magnetic field effect on the physical properties of semiconductors and dielectric materials. **Fig. 1.3, *b*** shows the approximation of dependences $\Delta l/l(t_1)$ (marked with continuous lines) of *a* and *b* types per straight lines: $y=A+B\cdot x$, $y=\Delta l/l$, $x=t_1$ with the following parameters:

– for *a* line: $A=5.3\pm3.7$; $B=0.4\pm0.2$;

– for *b* line: $A=6.4\pm3.5$; $B=15.9\pm1.6$.

Group *b* embraces those substances, wherein the magnetic effect is in a linear relation with the time (t_1). Group *a* contains the substances with magnetic effect being independent of the time (t_1) that is expressed by a small value of *B* coefficient. The magnetic effect value ($\Delta l/l$) with short time (t_1) is almost the same (identical *A* coefficients) and close to 5 % for both *a* and *b* types of dependences.

The growing number in the publications to address the problem of a magnetic field effect on the properties of solids within the last few years allows revealing the number of general regularities for the solids:

1. Magnetic field induces the nonreversible transition to a new state after which the secondary processes occur causing sometimes the virtual crystal recovery and are perceived as "relaxation"

after being excited by a magnetic field. In fact, they are the consequences of the primary processes and are insensitive to further magnetic field effects and their values.

2. On average, for a wide range of substances (dielectric materials, metals and semiconductors), the time invariable to describe the time period of the transition into a new state decreases in its value with the magnetic field (H) increase according to the law of $t_1 = t_0/H^4$.

3. The relative change in the physical properties of solids under $\Delta l/l$ magnetic field effect in weak fields (~0.1–1 T) is the same for a wide range of substances and makes ~5 %. The influence of strong magnetic fields (3–30 T) is able to classify solids into two large groups in terms of their behaviour. Thus, the first group includes metals and semiconductors and there is $\Delta l/l$ dependence revealed on the magnetic field energy in such substance, while the second group mainly consists of dielectric materials in which $\Delta l/l$ shows strong dependence on the energy of a magnetic field per unit volume of a substance.

1.1.5 THE NATURE OF NERNST-ETTINGSHAUSEN EFFECT

Nernst-Ettingshausen effect or transverse effect is a thermomagnetic effect observed when a semiconductor with a temperature gradient is exposed to a magnetic field. This effect was discovered by Nernst and Ettingshausen in 1886, and in 1948 it was theoretically grounded by Sondheimer [28].

The nature of this effect is in the occurrence of the electric field (E) in a semiconductor and its direction is perpendicular to the temperature gradient vector (∇) and the magnetic induction vector (B), i.e. it is in the direction of the vector ($[\nabla T, B]$). If the temperature gradient and the magnetic induction are directed along X axis, then the electric field is parallel to Y axis. Therefore, there occurs the electric potential difference (u) between the points of a and b.

Both Nernst-Ettingshausen effect and Hall effect occur due to the flow divergence of charged particles caused by Lorentz force. However, there is the difference between them: Hall effect is responsible for the directed flow of particles resulted from the drift in the electric field, while in the case of Nernst-Ettingshausen effect, the same phenomenon is caused by diffusion.

The considerable difference between them is that unlike Hall constant, the sign of $q_{\perp}$ is independent of the charge carrier sign. Actually, during the drift in the electric field, the charge permutation causes the drift direction alteration, that changes the sign of Hall field.

In this case, the diffusion flow is directed from the heated end of the sample towards the cold one irrespectively to the particle charge sign. Therefore, the direction of the Lorentz force for positive and negative particles is mutually antithetic, but the direction of the electric charge flows in both cases is identical.

Longitudinal Nernst-Ettingshausen Effect.

The longitudinal Nernst-Ettingshausen effect is in the change of thermal electromotive force in metals and semiconductors under the magnetic field influence.

When the magnetic field is absent, the thermal electromotive force in electron semiconductor is defined by the difference between fast electron velocity components (drifting from the hot side) and slow electrons (drifting from the cold side) along the temperature gradient.

At the presence of the magnetic field, there is the change observed in the longitudinal components (along the temperature gradient) and transverse components (transverse to the temperature gradient) of the electron velocity, this change is dependent on the rotation angle of electron velocity in the magnetic field; the angle is defined by the time of free run of the electrons τ in metals or semiconductors.

If the time of the free run for slow electrons or electron holes (in a semiconductor) is greater than that for the fast electrons, then:

$$\upsilon_{1x}(H)/\upsilon_{1x}(0) > \upsilon_{2x}(H)/\upsilon_{2x}(0),$$

where $\upsilon_{1x}(H)$, $\upsilon_{2x}(H)$ – longitudinal components of velocities for slow electrons and fast electrons under magnetic field; $\upsilon_{1x}(0)$, $\upsilon_{2x}(0)$ – longitudinal components of velocities for slow and fast electrons when the magnetic field is absent.

The value of thermal electromotive force in a magnetic field (that is proportional to the difference of $\upsilon_{2x}(H) - \upsilon_{1x}(H)$) is higher than that when the magnetic field is absent at the difference of $\upsilon_{2x}(0) - \upsilon_{1x}(0)$; vice versa, if the time of free run for slow electrons is lower than that for the fast electrons, then the magnetic field presence decreases the thermal electromotive force.

In electron semiconductors, the thermal electromotive force increases within the magnetic field provided that there is the decrease in the time of free run τ under the increase in the electron energy (scattering at the acoustic phonons).

Within the same substances of electron semiconductors, the thermal electromotive force decreases under the magnetic field, if the time of free run τ increases with the increase in the electron energy (during the ionized impurity scattering) [29].

1.1.6 MAGNETOPLASTIC EFFECT IN DIAMAGNETIC CRYSTALS

In [30], was described the found and investigated decay of the particles from $CdCl_2$ impurity phase in monocrystalline matrix of NaCl (alkali-halide crystal) caused by magnetic field induction effect. Further, the structural changes started to appear in a few hours after the magnetic field induction treatment (the latency time) and lasted for several weeks. It has been revealed that the duration of the latency time and further structural changes are closely related to the "background" of the primary crystals. However, no physical model to explain these effects has been discussed in [30] and it is only stated that the magnetic field induction can affect the paramagnetic impurities which stabilise the quasi-equilibrium structure in primary crystals but cannot be controlled.

The direct magnetic field with the induction (0.5 T) causes the dislocation motion in NaCl and LiF crystals if no mechanical loads, thus changing the plastic properties of the sample. The established regularities of the magnetoplastic effect can be summarised as follows:

– the direction of the dislocation motion does not change during the magnetic field sign reversal (paired effect);

– the velocity of the dislocation motion is proportional to the square of the field induction and inversely proportional to the square root of paramagnetic center concentration within a crystal;

– dislocation pathlength tends to a constant value (saturation) depending upon the induction value of the magnetic field and the holding time for the crystals to spend within the magnetic field.

The paired nature of the magnetoplastic effect and its quadratic dependence on the induction value of a magnetic field imply the magnetostriction character of the phenomenon. To verify this assumption, the dedicated calibration measurement has been carried out to define the creep of NaCl samples at room temperature. At the load of ~30 kPa, the average dislocation pathlength during 5 minutes is similar to that of the magnetic field with 0.4 T induction holding (when without the load) during the same time. The revealed correlation should correspond to the magnetostriction constant of $m \sim \sigma/G \cdot B^2 \sim 4 \cdot 10^{-5}$ T^{-2}, where G is a shear modulus. However, the obtained value turns out to be several orders greater than the value of $m \leq 1.5 \cdot 10^{-9}$ T^{-2} obtained for these crystals independently.

The observed magnetoplastic effect can alternatively be explained as followings: the dislocation motion in the magnetic field occurs under the far-reaching internal stress field effects, while the magnetic field effect is narrowed to disconnecting of the dislocations from the local barriers (stoppers) through the spin-dependent electronic transitions in the magnetic field within the dislocation-impurity system.

The magnetoplastic effect, that has been evidenced by the chemical technique of double etching, necessitates the search for the similar effects in a wider range of experimental conditions, for instance: in a mode of active macrodeformation and creep, during microhardness measurement and electric dipole moment generated by the charged dislocations. These vast experiments have been carried out on the crystals of ZnS, Al, Bi, Si and InSb and C_{60} fullerite monocrystals and allow the following:

– to determine activation energy, reinforcement factor, yield point, creep rate and other magnetoplastic effect parameters as well as their dependence upon the effect produced by magnetic fields on the samples;

– to find out that the magnetic field affects these point defects of low-sensitivity which have less effective radii of interaction with the dislocations as compared to the point defects that are insensitive to the magnetic field effect;

– to reveal the magnetoplastic effect in a wide range of relative deformations ranging from ~10^{-7} to ~1 and to study this effect at different stages of macroplastic deformation;

– to establish the role of internal stresses within dislocation shears in magnetic fields when no external stresses.

The magnetic treatment of the dislocation-free crystals and the further detection of the motion in as-introduced dislocations in them reveal that within the subsystem of point defects there is the following phenomenon: the magnetically stimulated residual changes reduce the free pathlength of the dislocation under the magnetic field and increase them under conditions of mechanical load and the magnetic field absence. This difference as it has been noted earlier is conditioned in the crystals by the presence of the stoppers insensitive to the magnetic field along with magnetosensitive obstacles.

The first physical models of the magnetoplastic effect were based on the idea of the spin nature of the interaction between the dislocations and the paramagnetic point defects. Further, with the reference to this idea it was theoretically grounded, that the coeffect of the direct magnetic field and the pulsed magnetic field can cause resonance weakening of the crystals if the impulse frequency (ν) satisfies the condition of paramagnetic resonance, expressed by as given: $h\nu = g\mu_B B_0$ (h – Planck constant, g – factor of spectroscopic splitting, μ_B – Bohr magneton, B_0 – direct magnetic field induction).

Fig. 1.4 presents the dependence between the average edge dislocation pathlength and the magnetic field induction for various exposure modes. This dependence illustrates that at simultaneous exposure of NaCl:Ca (0.001 %) crystals to the magnetic fields, acting perpendicular each other, namely the direct current magnetic field and the ultrahigh-frequency magnetic field, there can be observed the maximum increase in the dislocation pathlength (L) at several discrete values of (B_0). Further, the "resonance" values of the induction correspond to $B_0 = h\nu/g\mu$, and the applied frequency of ultrahigh-frequency field is $\nu = 9.5$ GHz. Under these conditions, the resonance transitions occur between the splits from spin sublevels of electrons within the direct magnetic field and the effective factors of spectroscopic splitting $g_1 \approx 2$, $g_2 \approx 4$ and $g_3 \approx 6$, respectively.

For crystals with Eu impurities the dependence is even more complex (**Fig. 1.5**). Being obtained with the standard electron paramagnetic resonance spectrometer, the electromagnetic wave absorbance spectrum for NaCl crystals heavily doped with Eu shows the extrema.

By analysing the experimental data on the obtained magnetoplastic effects in diamagnetic crystals, there have been suggested the scheme of the probable mechanism how magnetic field effects on the evolution of metastable defect complexes. It is shown in **Fig. 1.5**.

The local minimum characterizes the profile of the elastic interaction between the constituents of the complex found in the metastable state. The solid line and the dotted lines that unite the complex constituents designate the covalent bonding in the equilibrium state and in the excited state: kT – thermally stimulated process, j – exchange integral, ΔE – exchange energy differences in S- and T-states of the complex, ν_i – frequency of transitions between absorption states that practically coincide with those in the weakening spectra, this indicates the fact that impurity ions are within the magnetosensitive complexes of defects.

According to the scheme (**Fig. 1.5**), the thermal fluctuations with the frequency (ν_1) excite the complex by covalent bonding stretching (or by changing configuration coordinates (r), such as bond angles) from the primary singlet S-state to the excited S-state. When the magnetic field does

not act, the complex, being exposed to the elastic forces from the crystal lattice, reverts to the original *S*-state due to prohibition for the complete spin that means that the complex is in dynamic equilibrium between *S*- and *S*-states.

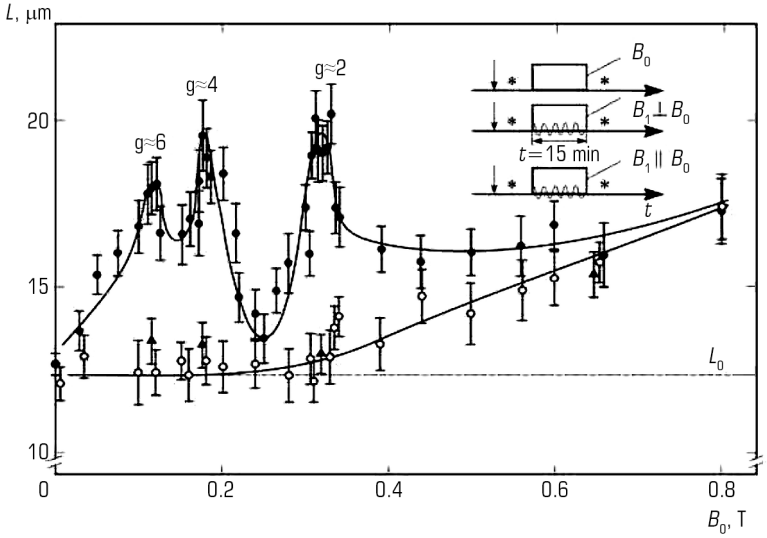

The related comments on the assignments:
○ – the absence of high-frequency current field (ν=9.5 GHz);
● – when exposed to the simultaneous action of high-frequency magnetic field and direct magnetic field in the configuration of $B_1 \perp B_0$, where B_1 – induction of the high-frequency magnetic field;
▲ – under simultaneous action of the high-frequency magnetic field and the direct magnetic field in the configuration $B_1 \parallel B_0$.

The dislocation pathlength (L_0), stipulated by the etching medium action, is shown with a shaded line for cases without external magnetic field.

The sequence of the procedures:
arrow – the inclusion of dislocations;
asterix – etching;
rectangle – exposing crystals to the magnetic field

Fig. 1.4 Dependence between the average edge dislocation pathlength (L) in NaCl:Ca crystals upon the direct magnetic field induction (B_0): exposure time of 15 min
Source: [30]

When there is a magnetic field, the prohibition is partially lifted, and the complex with $\nu_2=\mu_B B\Delta g/h$ frequency that has changed its multiplicity (Δg-mechanism of mixing states is the most probable under such conditions) evolves into a new electron *T*-state. Further, under influence

of the elastic forces from the crystal lattice there occurs reverse motion of nuclei. At that, the equilibrium R_T-state between them appears to be higher than that in the singlet *R*S-state, since the negative *J* value of exchange integrals causes the mutual repulsion of the complex constituents. Thus, with ν_3 frequency there occurs a relatively continuous triplet of *T*-state, in which the total energy of the complex constituent bonds is $\Delta E = 0.1–1$ eV, less than that in the *S*-state. The "dispersed" by this way complexes are less stable as compared to the initial ones, and the random motion of nuclei can cause either their decay with ν_4 frequency that is followed by the system escape from the local energy minimum and its further relaxation, or the restoration to the initial *S*-state with ν_5 frequency. Normally, the decay of the point defect complexes leads to the formation of weaker stoppers for the dislocations; that agrees with the experimental data on the weakening effect for the ionic crystals after they have been subjected to the magnetic fields.

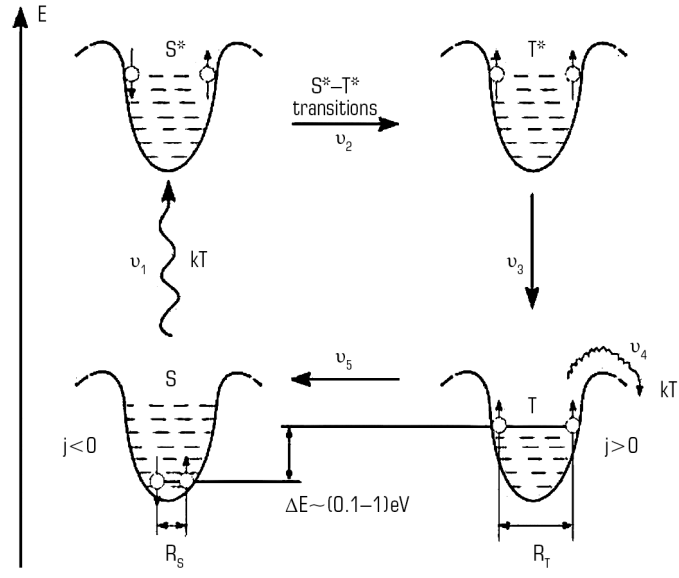

The related comments on the assignments:
S – continuous metastable singlet state of the complex;
S* – intermediate one excited by thermal fluctuations;
T* – intermediate excited triplet state, transition that is only possible in the presence of the magnetic field;
T – continuous metastable triplet state

Fig. 1.5 Schematic illustration of the process sequence in the complexes of point defects within the magnetic field: on the energy scale of *E* complex
Source: [30]

In other words it can be expressed as here: in the subsystem of the paramagnetic structural defects of the ionic crystals, spin-dependent magnetosensitive reactions are thought to considerably affect their plastic properties, while the kinetics of these reactions, according to the numerous tests, can be regulated by the weak constant fields and (what is even more efficient) by the pulsed magnetic fields.

1.2 MATERIALS AND METHODS OF THE STUDY

1.2.1 STUDY MATERIALS

In the current paper, there have been studied the samples of monocrystalline semiconductor silicon grown by Czochralski method (Cz-Si), both undoped version and doped with B, Sn, Ge, Hf, Zr, and the complexes of B-Sn and B-Mo ranging from $2 \cdot 10^{-4}$ to $8.7 \cdot 10^{-2}$ at % in initial state, after their exposure to the full heating-cooling cycle, various thermal treatment conditions and the weak direct magnetic field effect (refer to **Table 1.1**).

● **Table 1.1** Properties of the studied silicon crystals

No.	Sample characteristics (technique of preparing)	Oxygen content, atm/cm^3	Carbon content, atm/cm^3	Electric resistance at room temperature, ohm	Temperature ranges of variation lg(σ), lg(η), lg(μ) = *f*(1/*T*) from straight-line correlation							
					1		2		3		4	
					T_{start}	T_{end}	T_{end}	T_{end}	T_{start}	T_{end}	T_{start}	T_{end}
1	Float zone melting	$4\ 10^{14}$	$3\ 10^{15}$	1200	250	400	520	770	960	1005	1040	1150
2	Czochralski method, dislocation growth	10^{17}	10^{16}	25–50	260	380	770	860	960	1130	1170	1215
3	Czochralski method, dislocation-free growth	10^{17}	10^{16}	80–100	260	460	725	770	920	970	1090	1185
4	Cast polycrystalline	$2 \cdot 10^{17}$	$1.5\ 10^{18}$	0.3–3	220	320	432	555	730	918	1065	1180
5	"Raw" silicon trichlorosilane	–	–	1–20	210	350	650	750	920	960	1040	1190
6	"Raw" silicon monosilane	–	–	1–20	150	452	635	772	924	954	–	–

Source: [31]

1.2.2 METHODS OF THE STUDY

The chemical composition of the samples under analysis was determined by the spectroscopy performed at ARL-2400 testing facility.

The microstructure of the alloys was studied on the "Neophot-21" optical microscope. For revealing the general structure of semiconductor doped silicon, the samples were exposed to etching in $HF:H_2O:Cr_2O_3$ solution at the ratio of 3:3:1 with subsequent wash in the flowing water.

The temperature dependence of the thermal expansion coefficient of a semiconductor silicon was studied using the AD-80 dilatometer in the argon flow medium at the heating and cooling rate of 5 °C/min. The thermal expansion coefficient rate accuracy was 0.1 %.

The change in the solubility of doping elements (dopants) and their distribution between the structural constituents was studied by means of X-ray diffraction technique while the microhardness change was studied by means of the local X-ray spectrum analysis with MS – 46 microprobes and Camebax. XRD patterns of the alloys were recorded with DRON-3M diffractometer in k_α copper radiation. Aluminium of A999 grade and chemically pure silicon were used as reference standards. In order to determine the lattice parameters, the profiles of the diffraction extremum graphs (422) Si and (511) Si were recorded by means of the gravity center coordinate determination.

The microhardness of the modified silicon structural units was measured at PMT-3 testing facility under the load of 20 g. Each sample underwent from 36 to 76 measurements. In order to reveal the hidden regularities of silicon-based solid solution formation, the interval data imitating the distribution function [32] were used. For that purpose, the variation range of the characteristic was divided into n equal intervals and the number of cases in each interval was counted. The applied technique allowed taking into account and demonstrating silicon microhardness changes during doping.

XRD patterns of the alloys were recorded on DRON-3M diffractometer in k_α copper radiation. Chemically pure silicon was used as a reference substance.

The specific electric resistivity of doped Cz-Si was measured with 4-probe technique (the error was within of 2.5 %). The minority-carrier lifetime of charges was measured on the original testing facility for radiating heat kinetics measurement, the device built in V. Ye. Lashkaryov Institute of Semiconductor Physics of the National Academy of Sciences of Ukraine (Kyiv). The instrument accuracy was ±0.1 %.

The thermal treatment of the doped Cz-Si was performed in the laboratory in the chamber muffle kiln furnace of SNOL 2.5, 2.5/1.5. The desired temperature was maintained as accurate as ±0.5 °C by means of VRT-3 device. The temperature measurements were taken via chrome-aluminium thermocouples on R-4833 general-purpose instrument switched on according to the lattice network (the instrument accuracy of 0.05).

The magnetic treatment of the samples was carried out in the direct current magnetic field with induction of 0.066 T. The time periods of exposing for the samples were 10 and 30 days.

The measurements of the current minority-carrier lifetime after magnetic treatment were measured by the decay of the photoinduced current that occurred in the samples exposed to the GaAs light-emitting diode by means of SEMILABWT1000B device with the accuracy of ±0.1 %.

1.3 MICROSTRUCTURES OF THE SAMPLES BEFORE AND AFTER THE MAGNETIC FIELD TREATMENT

Fig. 1.6 shows the microstructures of Cz-Si samples in the initial state and after 240 and 720 hours of exposure in the direct magnetic field with the induction of 66 mT. The initial silicon microstructure is quite homogeneous with a low dislocation density (**Fig. 1.6, *a***).

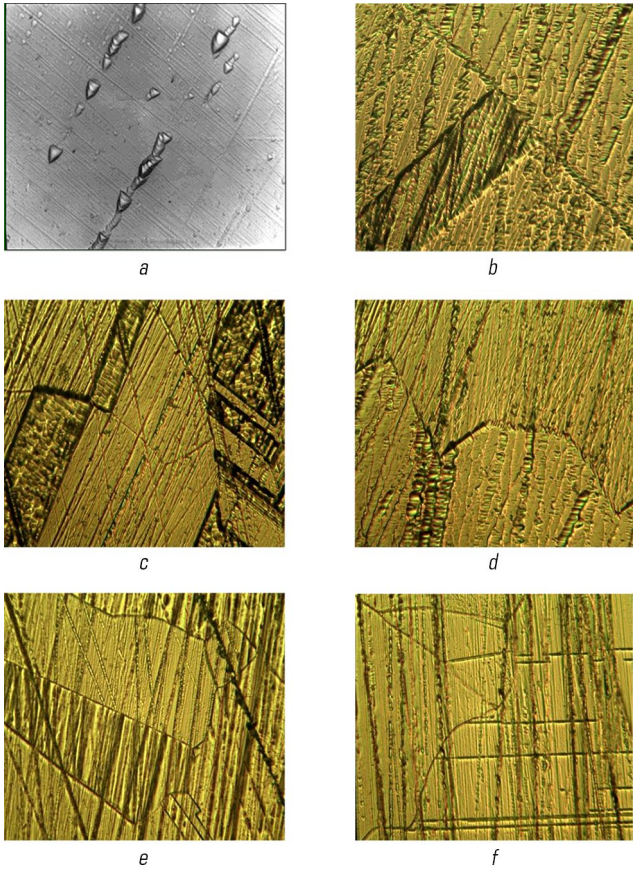

Fig. 1.6 Microstructures of Cz-Si samples: *a* – initial state, ×500; *b*, *c*, *d* – after 240 hours of exposing to direct-current magnetic field, ×400; *e*, *f* – after 720 hours of exposing to direct-current magnetic field, ×400
Source: [33–36]

240 hours of exposing to direct-current magnetic field for the monocrystalline silicon samples mean the worsening of their internal structures in terms of the significant increase in the quantity of their defects, namely the dislocation densities (**Fig. 1.6, *b–d***) and creating a great number of twins (**Fig. 1.6, *b*, *c***). However, the most interesting results revealed after the monocrystalline silicon treatment with the direct-current magnetic field are the formation of the polycrystalline silicon that is brought by the presence of a great number of grain boundaries.

The fact that the dislocation walls intersecting the grain boundaries just slightly change their directions or do not change them at all indicates that these boundaries are of the special type. The further exposing to the direct-current magnetic field has not influenced the sample microstructures except the grain sizes which become smaller (**Fig. 1.6, *e*, *f***).

The initial microstructures of the Cz-Si samples doped with aluminium (**Fig. 1.7, *a***) are characterized by rather high dislocation densities in the form of the pits after etching which form the chains. After 240 hours spent within the direct-current magnetic field (66 mT), the microstructures of the samples (**Fig. 1.7, *b–e***) show the considerable amounts of swirl-defects while the amounts of dislocations decrease to a certain degree. Etching of aluminium-doped Cz-Si samples allow to establish that 720 hours of exposing in the magnetic field result in a small quantity of single dislocations (**Fig. 1.7, *f***) and their chains in the samples but no swirl-defects have been found within such material.

The microstructures of Cz-Si samples doped with Cu are shown in **Fig. 1.8**. Initially, the samples had low densities of defects, which were mostly dislocation chains (**Fig. 1.8, *a***).

After 240 hours within the magnetic field, the sample microstructures exhibit some changes and the amount of dislocations reduces in them (**Fig. 1.8, *b*, *c***) while 720 hours of the mentioned treatment produce the effect of higher density of the chain-like dislocations in the microstructures of Si(Cu) samples as revealed after etching and comparing with the initial state (**Fig. 1.8, *e*, *f***).

In the microstructures of the Cz-Si samples doped with Zr (**Fig. 1.9**), rather high dislocation densities were found in the initial state, those dislocations were in the form of the separate pits from etching or their aggregations (**Fig. 1.9, *a***). After treating the samples with the direct-current magnetic field (B=66 mT) during the exposing time of 240 hours, the microstructures show a considerably lower number of dislocations (**Fig. 1.9, *b***). The metallographic analysis for the samples subjected to 720 hours of exposing in the magnetic field finds neither separate pits of etching nor dislocation aggregations (**Fig. 1.9, *c*, *d***), only the chains of dislocations have been revealed in these samples. In general, the microstructures have improved vs those of the samples subjected to 240 hours of exposing (this is also verified by the microhardness measurements).

In **Fig. 1.10**, we demonstrate the microstructures of Cz-Si samples doped with Hf. The microstructures of the initial samples have been characterized by rather high densities of dislocations and their regular arrangement along the certain crystallographic planes (**Fig. 1.10, *a***). Etching of the samples performed after 240 hours of the magnetic field action allows to reveal considerable quantities of swirl-defects while the dislocation densities decrease in them (**Fig. 1.10, *b–d***).

The notable changes are found in those sample microstructures which have undergone the magnetic field treatment during 720 hours. These changes can be described as follows: no swirl-defects and chains of dislocations like those revealed in the samples of 240-hour exposition; formation of large quantities of single dislocations like the pits from etching. Generally, the densities of the defects decrease in the samples of this type as compared against the samples with 240 hours of exposing.

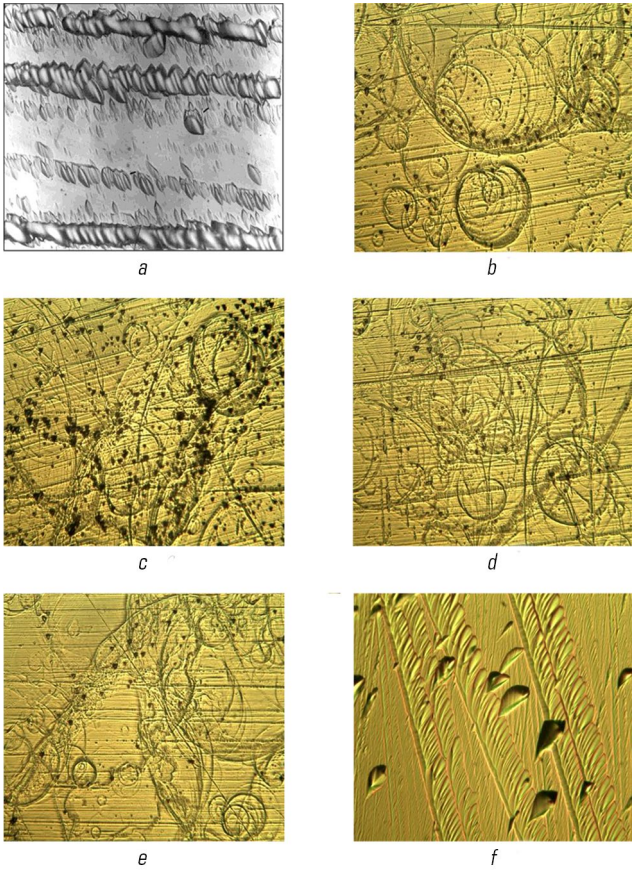

Fig. 1.7 Microstructures of Cz-Si samples doped with Al: *a* – initial state, ×500; *b*, *c*, *d*, *e* – after 240 hours of exposing to direct-current magnetic field, ×400; *f* – after 720 hours of exposing to direct-current magnetic field, ×400
Source: [33–36]

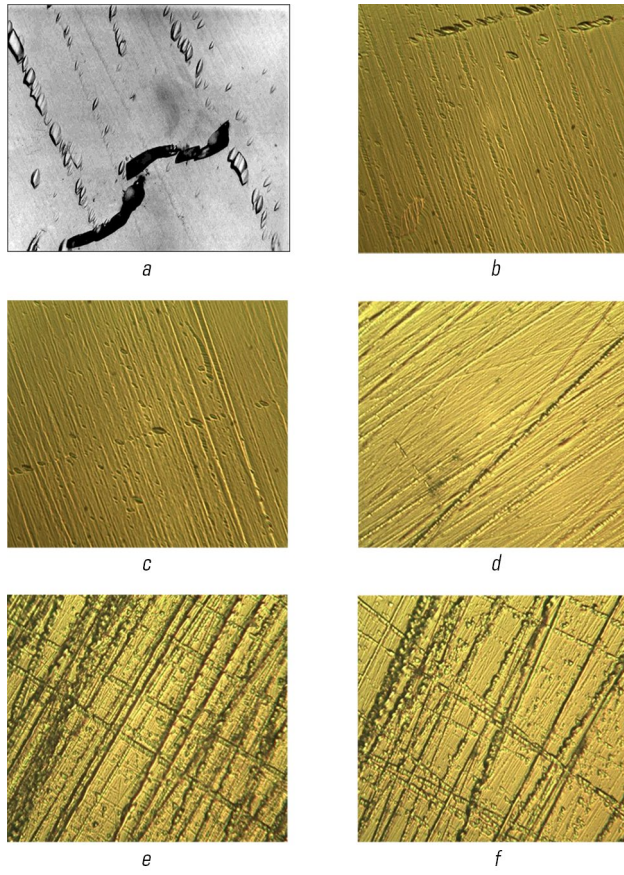

Fig. 1.8 Microstructures of Cz-Si samples doped with Cu:
a – initial state, ×500; *b*, *c* – after 240 hours of exposing to direct-current magnetic field, ×400; *d* – after 720 hours of exposing to direct-current magnetic field (sample No. 1), ×400; *e*, *f* – after 720 hours of exposing to direct-current magnetic field (sample No. 2), ×400
Source: [33–36]

In the structures of Cz-Si(Mg) samples held within the magnetic field during 240 hours (**Fig. 1.11, *b***), the considerable changes vs the initial state (**Fig. 1.11, *a***) have not been noted, however, 720 hours within the magnetic field give the rise of many single dislocations to appear in the samples, they are in the form of etching pits (**Fig. 1.11, *c*, *d***).

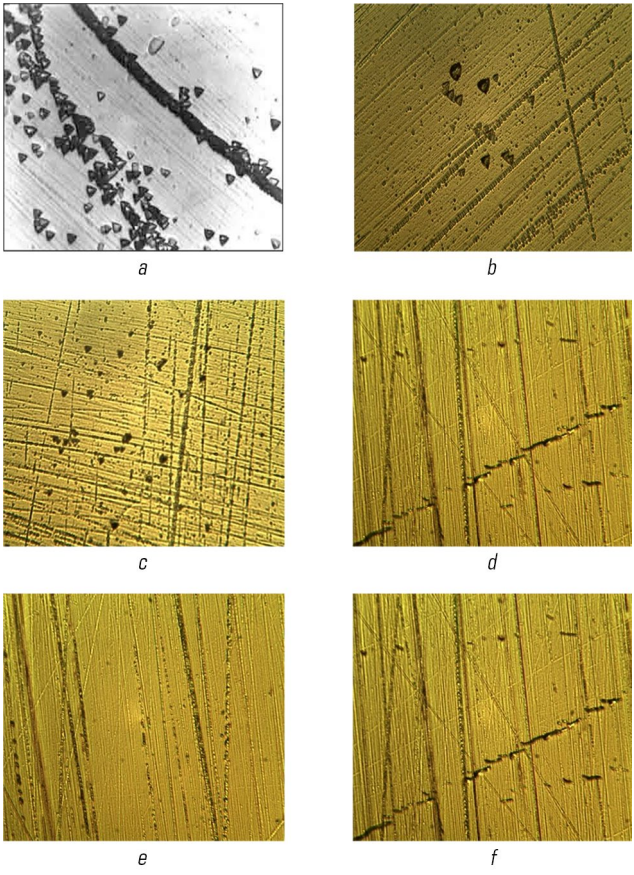

Fig. 1.9 Microstructures of Cz-Si samples doped with Zr: *a* – initial state, ×500; *b*, *c* – after 240 hours of exposing to direct-current magnetic field, ×500; *d*, *e*, *f* – after 720 hours of exposing to direct-current magnetic field, ×400
Source: [33–36]

The initial structures of Cz-Si-Fe samples (**Fig. 1.12, *a***) were with rather high densities of dislocations, arranged separately or in the form of chains. 240 hours of holding the samples within the magnetic fields enable preserving the single dislocations within the structures while the structures themselves exhibit no significant changes (**Fig. 1.12, *b, c***) in general. Further, the structures of the reported samples, which have spent 720 hours within the magnetic field, resemble their initial states, however the densities of the defects decrease (**Fig. 1.12, *d–f***).

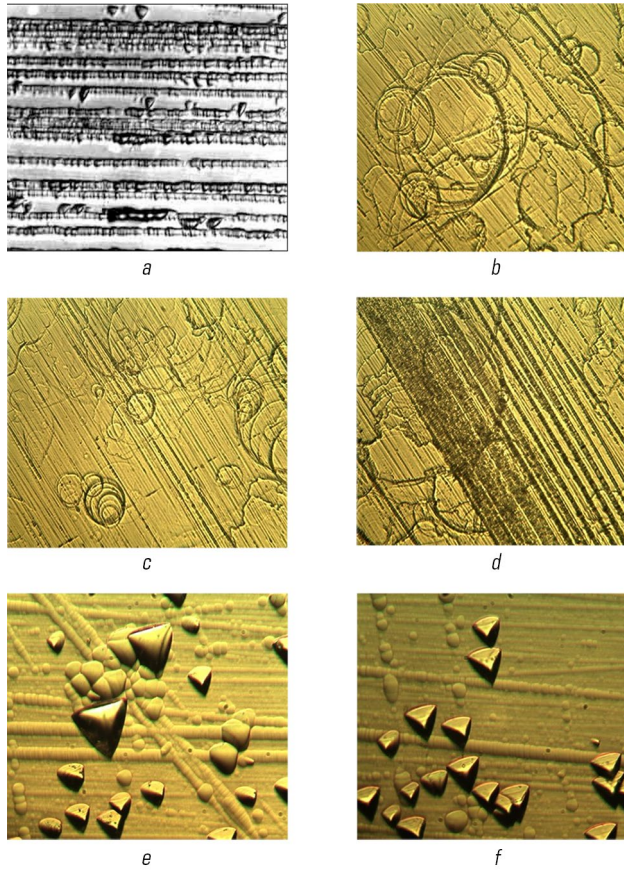

Fig. 1.10 Microstructures of Cz-Si samples doped with Hf: *a* – initial state, ×500; *b*, *c*, *d* – after 240 hours of exposing to direct-current magnetic field, ×400; *e*, *f* – after 720 hours of exposing to direct-current magnetic field, ×400
Source: [33–36]

The contemporary simulations promote the idea that magnetic field causes the spin-dependent degradation of the chemical bonds in the structural nanoclusters [37], formation of vacancy and oxygen sets (V-O, $Si_XV_YO_Z$), namely A-defects, which are able to result into the nuclei of two-dimensional defects such as dislocations [38]. The explanations on the phase transformation and the polycrystalline silicon formation in Cz-Si under the influence of the direct current magnetic field are not available in the contemporary science.

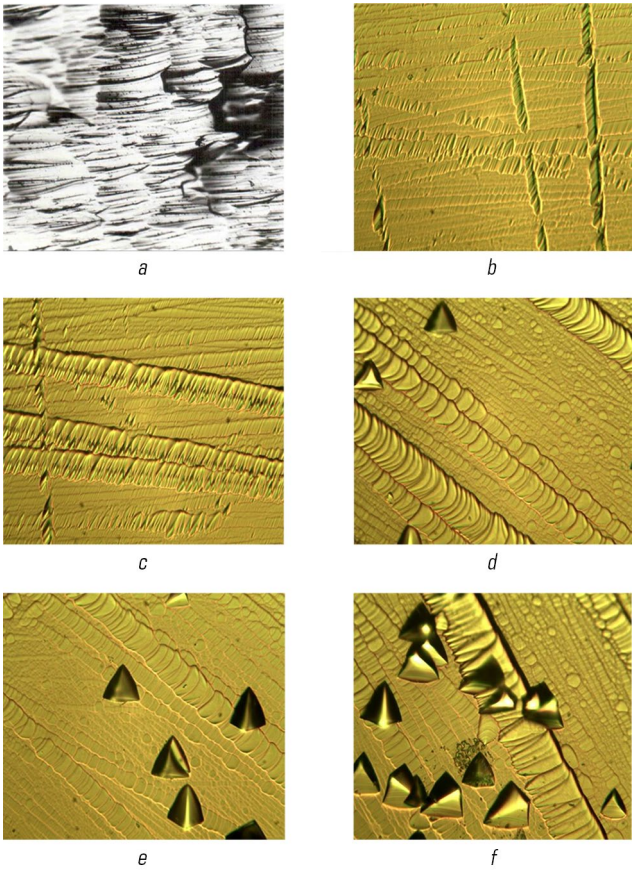

Fig. 1.11 Microstructures of Cz-Si samples doped with Mg: *a* – initial state, ×1000; *b* – after 240 hours of exposing to direct-current magnetic field, ×400; *c*, *d* – after 720 hours of exposing to direct-current magnetic field, ×400
Source: [33–36]

It can be assumed that the formation of polycrystalline silicon samples of undoped silicon is stipulated by those changes in the wave functions of the valency electron which have been produced by the direct-current magnetic field (this is confirmed by Larmor precession and the related Zeeman effect) and therefore the phenomenon is also promoted by the changes in the densities of the electron states in the space-and-time, that means the changes in the directions within which the covalent bindings occur. The rearrangement of covalent binding

orientations, in their turn, brings the changes in the crystal lattice type that means the phase transformation.

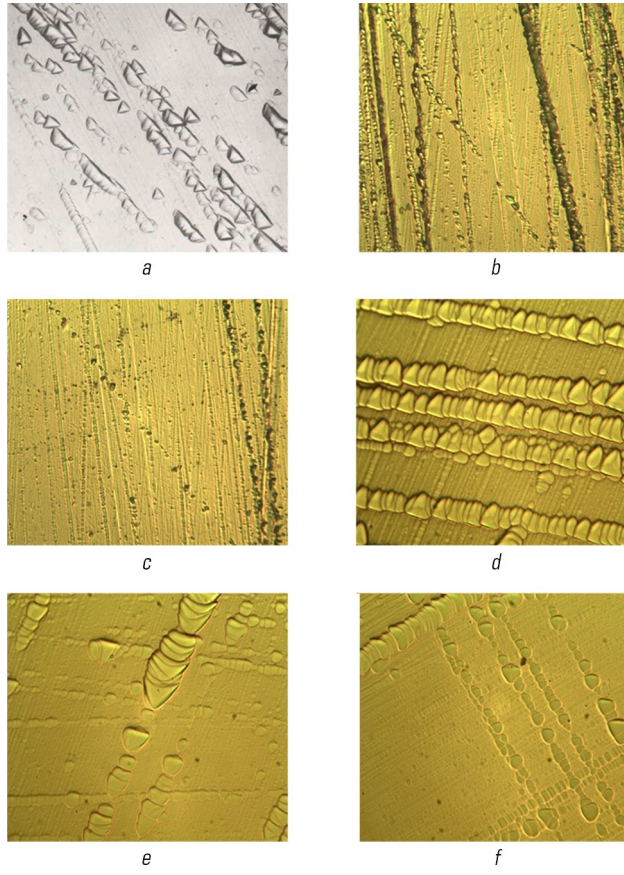

Fig. 1.12 Microstructures of Cz-Si samples doped with Fe: *a* – initial state, ×500; *b*, *c* – after 240 hours of exposing to direct-current magnetic field, ×400; *d*, *e*, *f* – after 720 hours of exposing to direct-current magnetic field, ×400
Source: [33–36]

The large number of twins formed within the structure might be assigned to the formation of silicon orthorhombic phase and silicon BCC_{III} phase with the shear pattern within the certain masses of the sample [1–4, 6]. In undoped silicon, the shear transformation of $Si_{FCC} \leftrightarrow Si_{ORTHORHOMBIC}$

occurs at the temperatures higher than 350 °C [39–43], in cases of the treatment in the magnetic field at the room temperature, this phenomenon is provoked only by the magnetic field influence. After 720 hours of exposing, there are no significant changes found in the sample structure. At this the measurements have shown the increase in the parameters of microhardness and specific electric resistance vs the samples which have been treated during 240 hours. This indicates the further proceeding of the phase transformation and the structure stabilization under the magnetic field effect.

Note that all the above-mentioned doping elements increase the critical temperatures for $Si_{FCC} \leftrightarrow Si_{ORTHORHOMBIC}$ and $Si_{ORTHORHOMBIC} \leftrightarrow Si_{BCCIII}$ (refer to **Table 1.2**). Moreover, the doping elements increase the thermodynamic stability of the closed packed phases of silicon to the magnetic field action (the magnetic field as well as the higher temperature add to the energy to the system). Furthermore, it might be assumed that the doping elements stabilise the high temperature phase of Si_{BCCIII}, thus eliminating low temperature shear-diffusion phase transformations as well as the formation of twins within the structure.

● **Table 1.2** Temperatures of phase transformation for doped silicon and the dedicated thermal expansion coefficient values

Cz-Si/doping elements	**Temperature/coefficient of thermal expansion °C/$\alpha \cdot 10^{-6} \cdot °C^{-1}$**		
	I $Si_{FCC} \leftrightarrow Si_{ORTHORHOMBIC}$	**II $Si_{ORTHORHOMBIC} \leftrightarrow Si_{BCC\ III}$**	**III $Si_{BCCIII} \leftrightarrow$ Sihcp**
Cz-Si	350/4.3	700/4.4	900/5.3
Cz-Si+Al	450/5.0	750/4.5	900/6.0
Cz-Si+Zr	500/4.5	–	850/4.7
Cz-Si+Hf	380/4.5	–	850/4.7

Source: [33–36]

Considering the influence of both the magnetic field and the doping elements on the energy of silicon interatomic bonds, it is difficult to make any assumptions since the most similar changes in the structures have been observed in the samples of Cz-Si(Al) and Cz-Si(Hf) after 240 hours and 720 hours of exposing to the magnetic field (refer to **Fig. 1.7, 1.10** respectively), despite the fact that aluminium drastically decreases the energy of silicon atom interaction while hafnium increases it greatly.

Further, the similar changes have been detected within the structures of Cz-Si(Cu) and Cz-Si(Fe) (**Fig. 1.8, 1.9**). At this, copper reduces the interaction energy of silicon atoms while iron does not bear influences on it.

In the samples of doped silicon, which has undergone magnetic field exposing during 240 hours, the increase in the defects of the inner structure can be explained via the changes in the wave functions of the electrons. Quite local is the change in the wave functions of electrons and the crystal lattice rearrangement is to provoke the breakage in covalent binding of those adjacent atoms, which wave functions will not have changed enough to meet the orientation changes of

covalent binding (the density of the electron states in the space-time). This local breakage of the atom binding is to cause the appearance of complete dislocations or partial ones together with the defects of atom packing.

The gradual decrease in both the density of the defects and the microhardness values of the structures in the samples of Si-Al, Si-Cu and Si-Zr after 720 hours spent in the magnetic field can be regarded as relevant to the structure stabilization during the time of quite long holding within the magnetic field as well as related to the decrease in the thermal capacity (enthalpy) of the system by means of annihilation of the certain portion of the structure defects. The same changes are observed in the samples during their annealing in the furnace [2].

Due to the commonly known property of aluminium to strongly decrease the energy of atom interaction in silicon, the easier shear-diffusion phase transformations within silicon occurs while hafnium influence is on the contrarily and drastically increases this energy that means slowing down the phase transformations and stabilizing the silicon structure of Si_{FCC} [31].

In order to identify the phases in the samples, which have been under the magnetic field treatment, the method of X-ray analysis have been applied. **Fig. 1.13** shows the diffractogram of Cz-Si sample in the initial state.

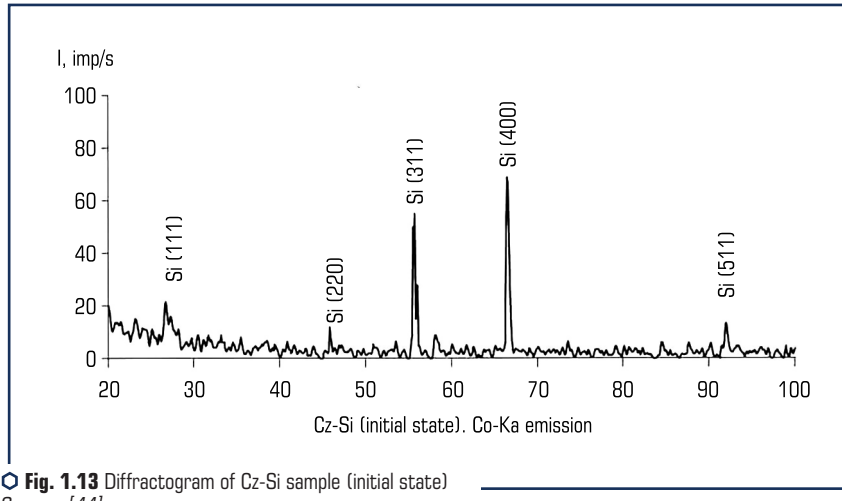

Fig. 1.13 Diffractogram of Cz-Si sample (initial state)
Source: [44]

In the initial state, Cz-Si in the diffractograms shows the reflections of FCC lattice, and line (400) possesses the maximal intensity at the scattering angles of less than 65 degrees (**Fig. 1.13**).

After treating the silicon samples with direct-current magnetic field of 0.4 T inductions, there have appeared the reflections at the scattering angles of 30–40 degrees (**Fig. 1.14**), which are interpreted as orthorhombic phase of silicon [45].

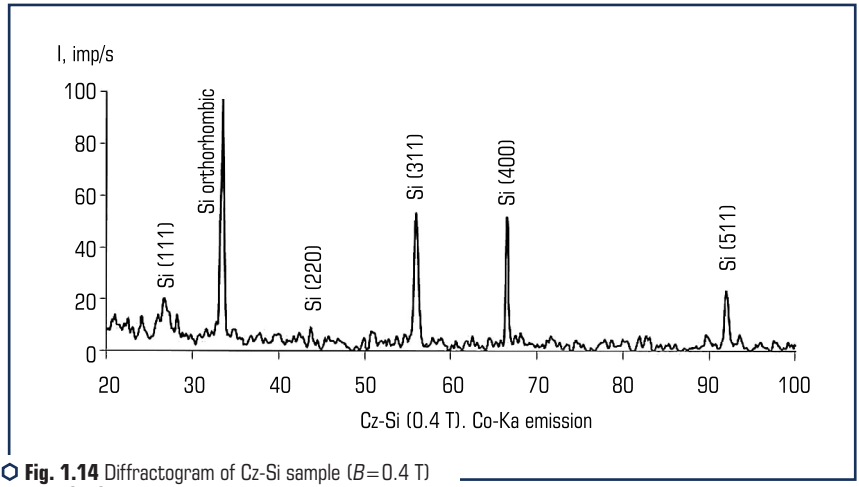

Fig. 1.14 Diffractogram of Cz-Si sample (B=0.4 T)
Source: [44]

The reflection intensityies for silicon with cubic close-packed lattice at angle of 65–70 degrees decrease after the magnetic field influence. It can be explained by phase transformation initiated in silicon, namely $Si_{FCC} \leftrightarrow Si_{ORTHORHOMBIC}$ [34] under the action of the direct current magnetic field with 0.4 T of induction.

Fig. 1.15 depicts that after treating the samples with the aggressive direct current magnetic field (B=1.2 T), there is the reduction in intensities of reflections in all the silicon phases and appears a considerable number of reflections from silicon oxide. This verifies the assumption of silicon surface activation with the direct-current magnetic field and enhancing its absorbing properties [46].

Furthermore, with the behaviour of this kind we confirm the assumption that the silicon phase structure stabilises under the action of direct magnetic field [33]. However, more detailed investigation on the line profile (511) evidences that additional phases are formed within the crystal array, and they possess the different type of the lattice.

In **Fig. 1.16**, the curves are presented to show the differential extrema (511) for the samples in the initial state and after treating with the magnetic field: B=0.4 T (*b*), 1.2 T (*c*). They have been obtained at the scattering angles of 90–92 degrees, which is the feature of silicon phase of cubic close-packed lattice [46].

The splits of the diffraction lines detect the presence of the distortions in the crystal lattices of Cz-Si samples. At this the split of the extremum (511) is to be assigned to overlapping of certain interferences of orthorhombic phase of silicon [41, 44, 45]. Further, the line splitting (511) increases with the increase in the induction of external magnetic field.

The splits of the differential extrema at the scattering angles of 90–92 degrees at higher values of external magnetic field induction evidence the presence of two phases in the silicon and

are relevant to the formation of $Si_{ORTHORHOMBIC}$ phase within this material array. The same is observed on the differential extremum split (511) at the scattering angles of 90–92 degrees after the silicon semiconductor heat treating at the temperature range of 280–450 °C, and it is assigned to the crystal lattice distortion of Si_{FCC} and formation of the certain quantity of $Si_{ORTHORHOMBIC}$ [47–48].

Eventually, the heat treatment of the silicon semiconductor gives greater splitting of the interference extremum (511) at increasing the annealing temperature from the range of 280–320 °C up to the range of 400–450 °C [48]. In the currently reported research, the significant splitting is observed at the increase of the external magnetic field induction from 0.4 T to 1.2 T. This evidences that the magnetic field and the heat treatment initiate the phase transformations of silicon.

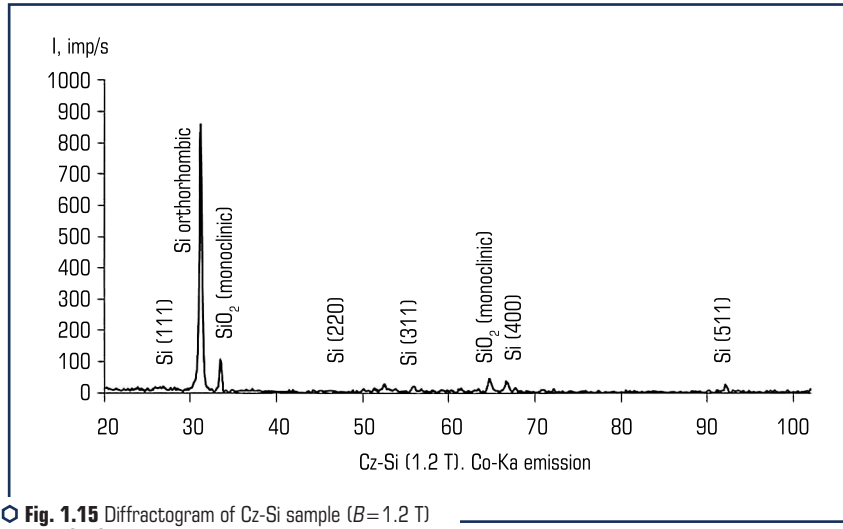

Fig. 1.15 Diffractogram of Cz-Si sample ($B = 1.2$ T)
Source: [44]

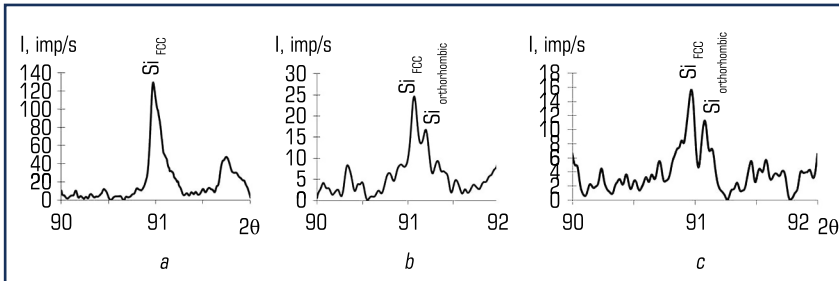

Fig. 1.16 Line profile (511) before the magnetic field action and after it: *a* – initial state; *b* – 0.4 T; *c* – 1.2 T
Source: [44]

1.4 THE SAMPLE MICROHARDNESS VALUES BEFORE AND AFTER TREATING WITH THE MAGNETIC FIELD

Magnetic field acting on Si sample has certain influence on the sample microhardness values. For the sake of the reader's swift reference we consider it is reasonable to summarise the revealed data on the microhardness change in similar patterns of representation as below.

In **Fig. 1.17**, the graphs present the microhardness values of the aluminium-doped silicon samples after 240 hours (**Fig. 1.17, *a***) and 720 hours (**Fig. 1.17, *b***) of exposing to direct-current magnetic field with the induction of 66 mT. The analysis performed for the graphs has revealed that the average microhardness of the sample matrices after 240 hours of exposition is 11000 MPa (the values vary within the range of 9000–14000 MPa), the dislocations areas demonstrate 12500 MPa (the variation range makes 11500–12500 MPa), the swirl-defect allow 10000 MPa of the value (within the range of 9000–16000 MPa).

The average microhardness per the structural units of the samples after 720 hours spent within the magnetic field becomes lower by 2500 and 950 MPa; for the matrix such change is within the range of 8500–10500 MPa while that of the dislocation areas is within the range of 9500–14000 MPa (swirl-defects have not been detected). These bring the conclusion that the ranges of the structural units' microhardness values undergo the considerable changes of decrease.

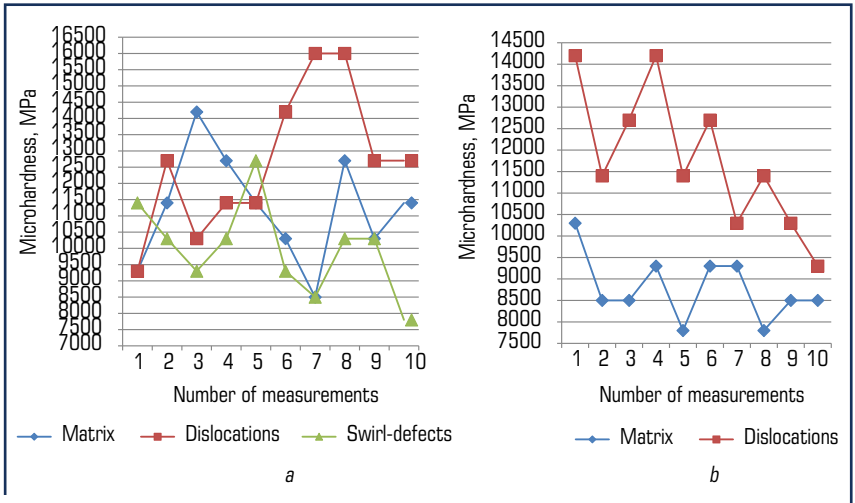

Fig. 1.17 Microhardness graphs for Cz-Si(Al) samples: *a* – after 240 hours of exposing to direct-current magnetic field; *b* – after 720 hours of exposing to direct-current magnetic field

Fig. 1.18 shows the average microhardness values per the structural units for Cz-Si(Al) samples both in the initial state and after 240- and 720-hour exposition to direct-current magnetic field.

As it can be deduced from the given bar graph, the sample microhardness values notably increase after 240 hours of exposing within the magnetic field vs the initial state of the samples. The further treating of the samples (720 hours) causes the gradual decrease in the microhardness values that is connected with the decrease in the defects of the silicon samples.

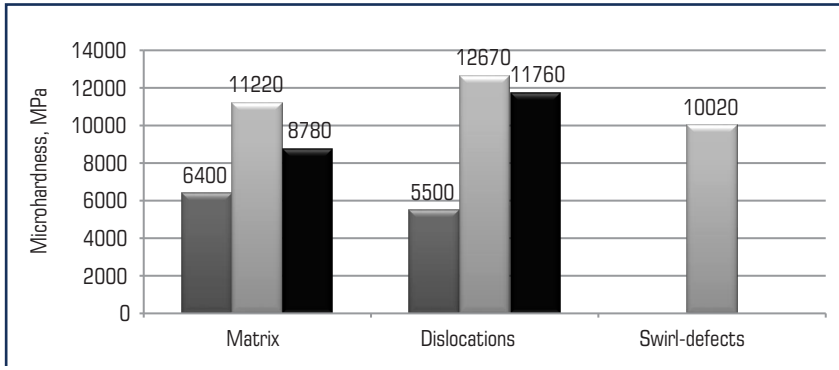

Fig. 1.18 Microhardness per the structural units for Cz-Si(Al) samples (in the initial state, after 240- and 720-hour exposition to direct-current magnetic field)

In **Fig. 1.19**, we demonstrate the microhardness graphs for Cz-Si(Hf) samples after they spent 240 and 720 hours within the magnetic field for the treatment. The average microhardness values of the structural units, which Cz-Si(Hf) samples possess after 240 hours and 720 hours of the mentioned holding, are as follows: 9000 MPa (variation range is 8500–10500 MPa) and 10400 MPa (with the variations within the range of 89500–12500 MPa) for the matrices, respectively; 12400 MPa (12500–14500 MPa) and 12700 MPa (12500–16500 MPa) for the dislocation areas.

Therefore, it follows that the increase in the holding time within the magnetic field results in higher range of the microhardness value variations that is probably connected with the increase in the defects. The microhardness parameter for swirl-defects has been revealed as much as 11000 MPa in the samples after 240-hour exposing while the etched samples of 720-hour exposing have not exhibited swirl-defects.

The microhardness average values per the structural units of Cz-Si(Hf) samples before and after the magnetic treatment are given in **Fig. 1.20**. These bar graphs show that the microhardness values gradually increase (but with slowing intensity) during further exposing to direct-current magnetic field.

In **Fig. 1.21**, we show the microhardness graphs for Cz-Si(Cu) after the action of the direct-current magnetic field. After 240 hours of magnetic field influence, the microhardness values for the matrix vary from 7100 MPa to 9500 MPa while those for the dislocation areas are within the range of 7700–11500 MPa. After 720 hours of holding, the microhardness values show

the variations from 5600 MPa to 9500 MPa for the matrix and from 6100 to 12700 MPa for the dislocation areas.

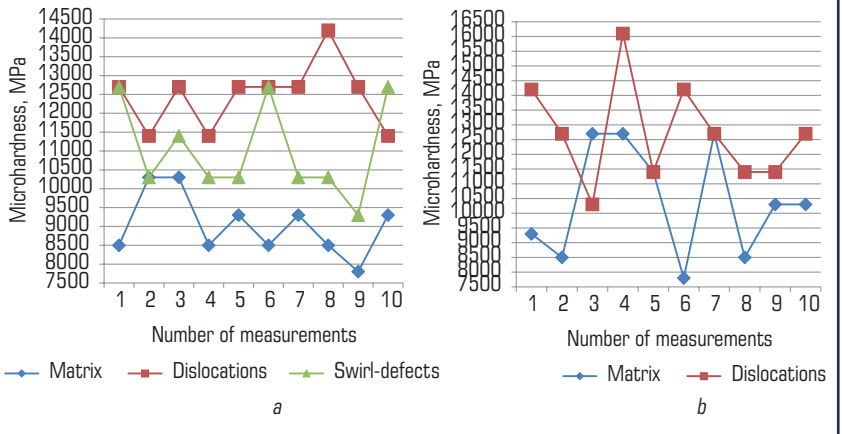

Fig. 1.19 Microhardness graphs for Cz-Si(Hf) samples: *a* – after 240 hours of exposing to direct-current magnetic field; *b* – after 720 hours of exposing to direct-current magnetic field

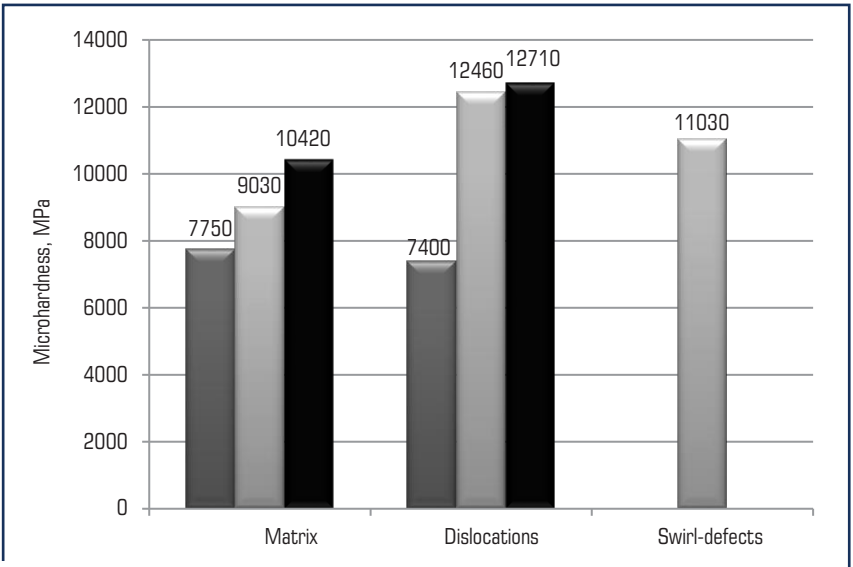

Fig. 1.20 Microhardness values per the structural units of Cz-Si(Hf) samples (in the initial state, after 240 and 720 hours of exposing to direct-current magnetic field)

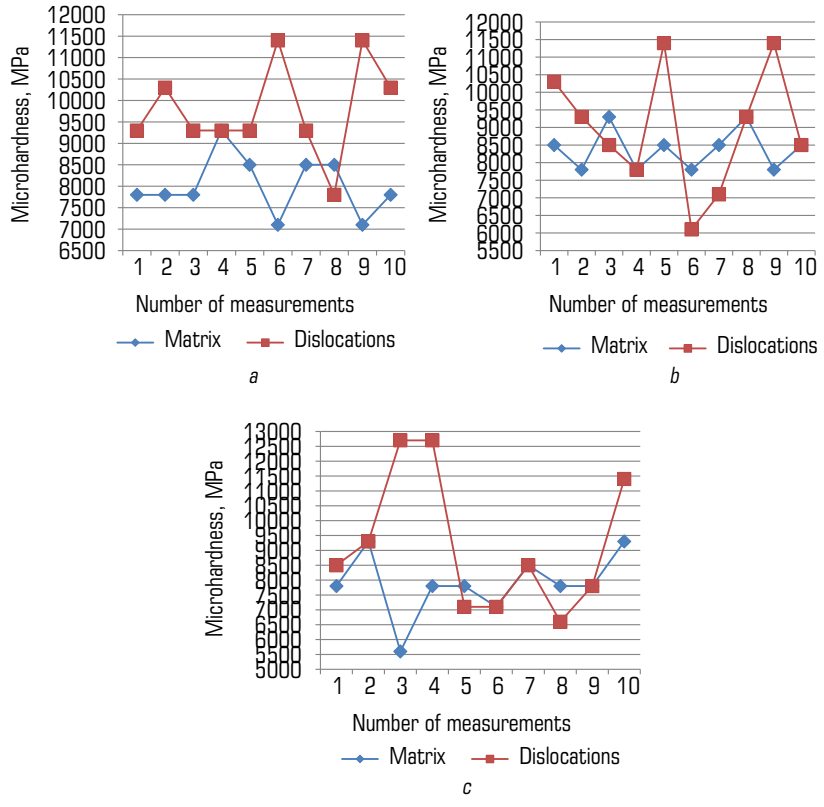

Fig. 1.21 Microhardness graphs for Cz-Si(Cu) samples: *a* – after 240 hours of exposing to direct-current magnetic field; *b*, *c* – after 720 hours of exposing to direct-current magnetic field

The average microhardness values per the structural units of Cz-Si(Cu) samples before and after the magnetic field treatment are shown in **Fig. 1.22**. Comparing with the initial state, the microhardness parameter increases by approximately 1400 MPa in the matrix and by approximately 3500 MPa for dislocations after 240 hours of the treatment. After 720 hours spent within the magnetic field, the microhardness values increase by 100 MPa more for the matrix, but the hardness of the dislocation zone decreases by 700 MPa.

In **Fig. 1.23**, the microhardness graphs of Cz-Si(Mg) samples are presented after their exposing for 240 and 720 hours within the magnetic field. The analysis of the graphs detects that after 240-hour treatment by the magnetic field, the microhardness values of the sample matrices vary from 7700 MPa up to 10300 MPa while those of the dislocation areas are within

10300–12700 MPa. After 720 hours of the magnetic field action, the microhardness values for the matrices vary 7700–11400 MPa, while for the dislocations they are 10300–12700 MPa.

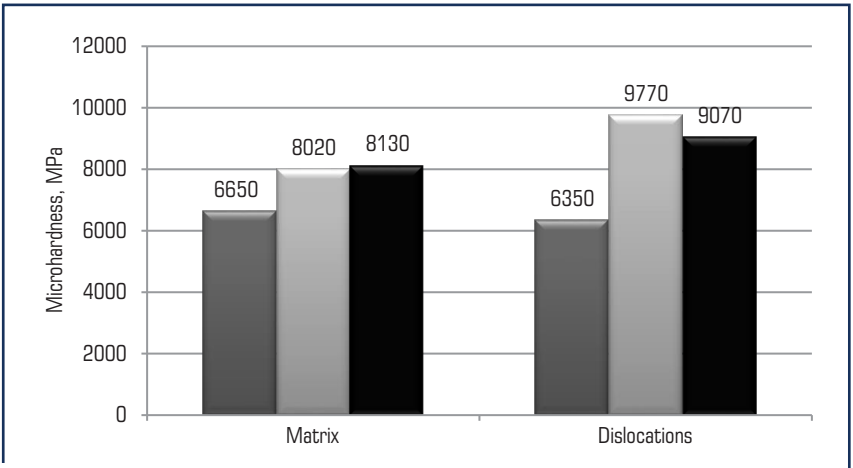

Fig. 1.22 Microhardness per the structural units of Cz-Si(Cu) samples (in the initial state, after 240- and 720-hour exposition to direct-current magnetic field)

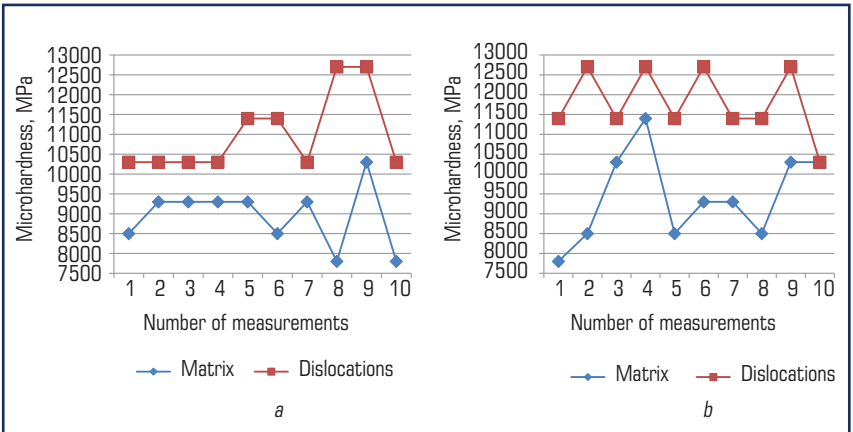

Fig. 1.23 Microhardness graphs for Cz-Si(Mg) samples: *a* – after 240 hours of exposing to direct-current magnetic field; *b* – after 720 hours of exposing to direct-current magnetic field

Fig. 1.24 presents the average values of microhardness per the structural units of Cz-Si(Mg) samples before and after treating with the direct-current magnetic field. This bar graph demonstrates that the microhardness values of the structural units increase during the time of exposing

samples within the magnetic field. After 240 hours of holding the samples, the values for the matrix microhardness increase on average as much as by 1800 MPa while in the dislocation zones such an increase is by 5000 MPa. The further treatment of the samples within the magnetic field leads to the greater microhardness values for the matrix by 500 MPa while the zone of the dislocations exhibits the increase by 800 MPa in this parameter.

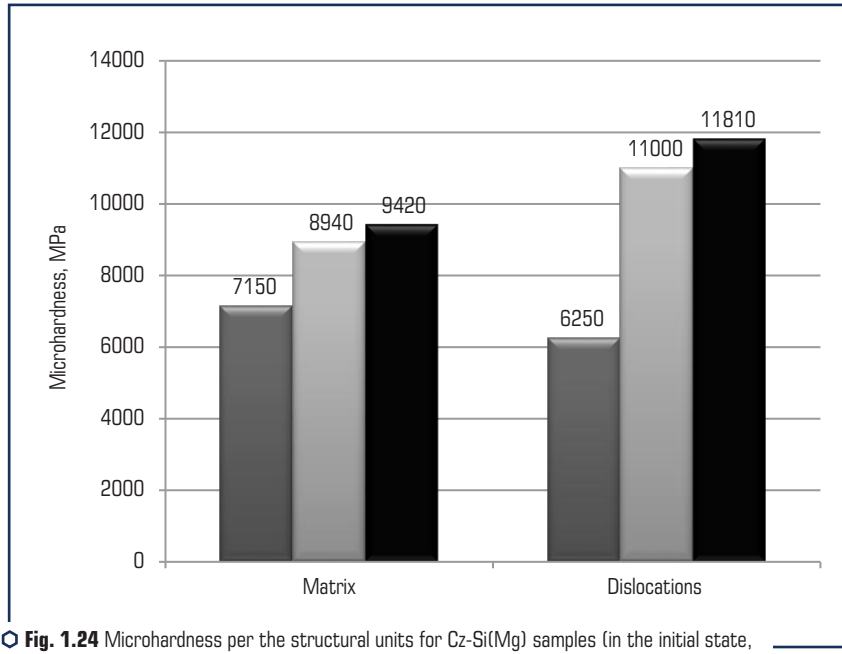

Fig. 1.24 Microhardness per the structural units for Cz-Si(Mg) samples (in the initial state, after 240 and 720 hours of exposing to direct-current magnetic field)

Fig. 1.25 reports on the microhardness graphs for Cz-Si(Fe) samples after 240 and 720 hours of their exposing within the magnetic field. The dedicated measurements on microhardness per the structural units have given the following results. After 240 hours of exposing, the matrix microhardness varies within the range of 7100–9300 MPa while the microhardness of the dislocations areas varies from 8500 to 12700 MPa. After 720 hours of exposing, the hardness for matrix is within 7100–8500 MPa and for the dislocations it is within 9300–14200 MPa.

For the average values of microhardness per the structural units of Cz-Si(Fe) samples before and after their treatment refer to **Fig. 1.26**. After 240 hours of exposing within the magnetic field, the microhardness of the matrix values grows by 1000 MPa and that of the dislocations by 4360 MPa. The further treatment causes the decrease in the matrix microhardness by 80 MPa but increase in the microhardness values of the dislocations areas by 1300 MPa.

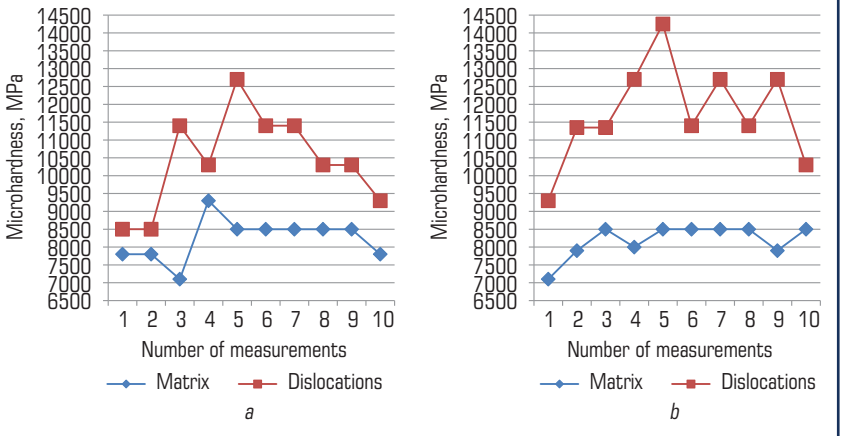

Fig. 1.25 Microhardness graphs Cz-Si(Fe) samples: *a* – after 240 hours of exposing to direct-current magnetic field; *b* – after 720 hours of exposing to direct-current magnetic field

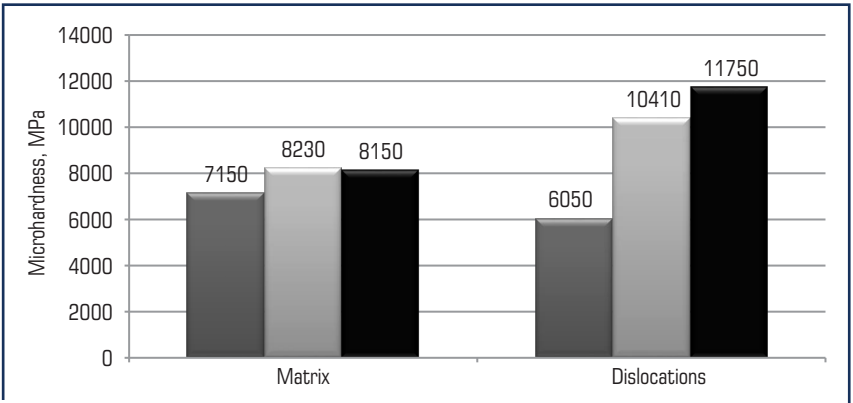

Fig. 1.26 Microhardness per the structural units of Cz-Si(Fe) samples (in the initial state, after 240 and 720 hours of exposing to direct-current magnetic field)

In **Fig. 1.27**, the microhardness average values are described graphically for the samples of Cz-Si(Zr) after 240 and 720 hours of their holding within the magnetic field. The analysis on the graphs shows that after 240 hours spent within the direct-current magnetic field, the matrix microhardness values vary within the range of 7100–14200 MPa while the dislocation areas have the range of 10300–16000 MPa for this parameter. After holding the samples during 720 hours for exposing, the matrix microhardness is 7100–11400 MPa but for the dislocation areas, it ranges within 8500–12700 MPa.

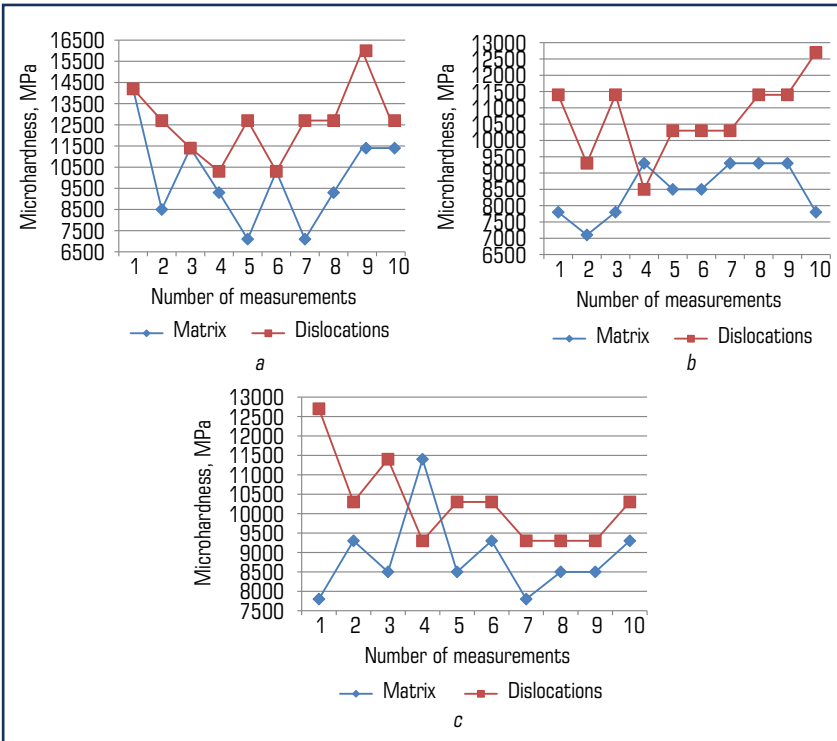

Fig. 1.27 Microhardness graphs of Cz-Si(Zr) samples: *a* – after 240 hours of exposing to direct-current magnetic field; *b*, *c* – after 720 hours of exposing to direct-current magnetic field

In **Fig. 1.28**, we report on microhardness values per the structural units of Cz-Si(Zr) samples before and after exposing to direct-current magnetic field. It is obvious from the bar graphs demonstrated that the microhardness values of the sample structural units increase after 240 hours of exposing within the magnetic field. The measurements after 720 hours of the treatment reveal that the microhardness values are smaller as compared with the values registered after 10 days of magnetic field treatment.

Fig. 1.29 represents the results of the microhardness measurements of the undoped silicon samples after their holding within the magnetic field during the period of 240 hours and 720 hours. The microhardness values of the sample matrices after 240 hours of treatment are 7400–12700 MPa, those of the dislocation areas are within the range of 7400–11400 MPa, the twin areas are 8500–16000 MPa. The microhardness values per the structural units after 720 hours of treating with the direct-current magnetic field are as follows: 8500–12700 MPa for matrix, 10300–14200 MPa for dislocation areas, 7000–14200 MPa for twins.

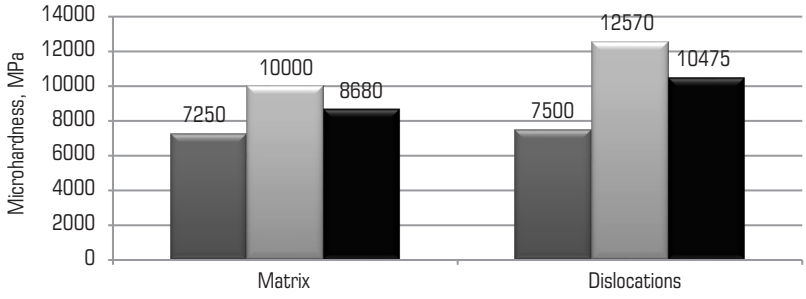

Fig. 1.28 Microhardness per the structural units of Cz-Si(Zr) samples (in the initial state, after 240 hours and 720 hours of exposing to direct-current magnetic field)

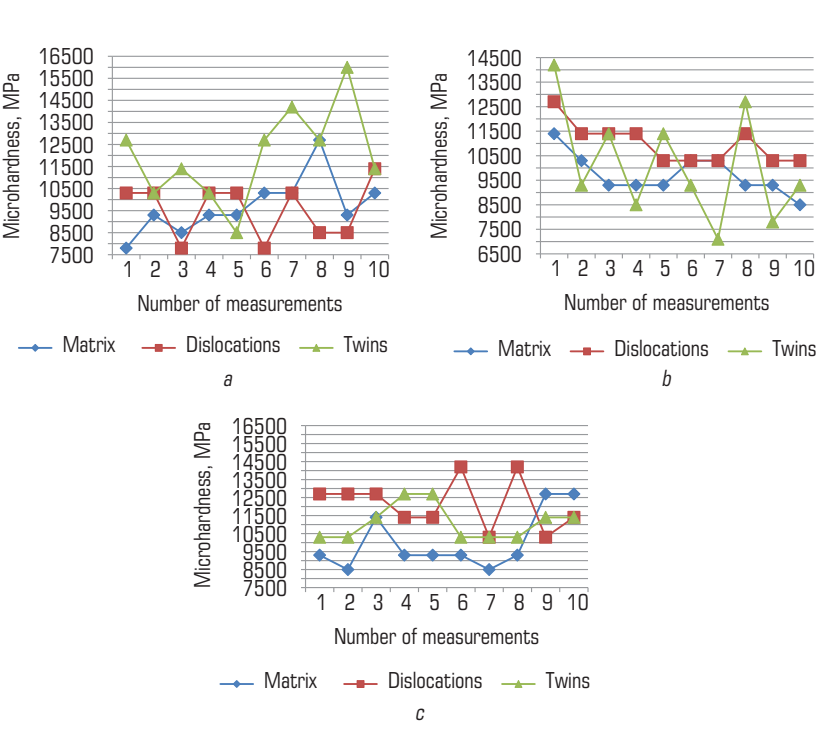

Fig. 1.29 Microhardness graphs of Cz-Si samples: *a* – after 240 hours of exposing to direct-current magnetic field; *b*, *c* – after 720 hours of exposing to direct-current magnetic field

The microhardness values per the structural units of undoped silicon samples before and after their treating with the magnetic field are reported in **Fig. 1.30**.

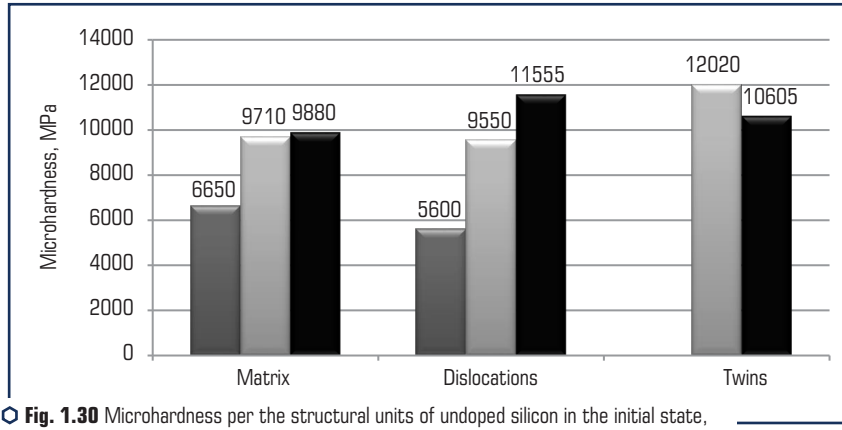

Fig. 1.30 Microhardness per the structural units of undoped silicon in the initial state, after 240 and 720 hours of exposing to direct-current magnetic field

After 240 hours spent within the magnetic field, the matrix microhardness values grow stronger by 3000 MPa, the dislocation area microhardness shows the increase by 3900 MPa, a large quantity of twins appears and their average microhardness is 12000 MPa. After 720 hours of holding within the magnetic field, the microhardness values go up for the certain structural units as given: within matrix – by 200 MPa, within the dislocation zones – by 2000 MPa; however the microhardness values of twins decrease by 1500 MPa.

1.5 THE PHYSICAL PARAMETERS OF THE SAMPLES BEFORE AND AFTER TREATING WITH THE MAGNETIC FIELD

Table 1.3 reports on the values of the physical parameters and the mechanical properties of the samples of both undoped and doped silicon before and after treating with the magnetic field induction of 66 mT.

In the initial state, the highest values of the specific electric resistance are possessed by Si-Zr sample, the lowest ones are the characteristics of the undoped silicon. The longest lifetime for the current minority-carriers is observed with the samples of the undoped silicon.

The date presented in the table evidence that there is a significant decrease observed in the values of the specific electric resistance and the life time for the current minority-carriers after the treating the samples of doped silicon within direct-current magnetic field. For the samples of undoped silicon, the decrease in the life time for the current minority-carriers is as great as several orders.

● **Table 1.3** Physical parameters and mechanical properties of the doped silicon samples before and after exposing to direct-current magnetic field

Sample	Properties	Initial State	240 hours of exposing	720 hours of exposing
Cz-Si	ρ, Ohm·cm	80–100	46–49	83–92
	t, μs	574	0.65	0.63
	Conduction type	P	p	P
	Hμ, MPa	6500	9500	9600
Cz-Si-Al	ρ, Ohm·cm	200–210	55–65	60–65
	τ, μs	12.1–12.5	0.40	0.32
	Conduction type	P	p	P
	Hμ, MPa	6800	10750	10320
Cz-Si-Hf	ρ, Ohm·cm	180–192	12.8–14.3	13.5–14.0
	τ, μs	148	23.08	28.11
	Conduction type	P	p	P
	Hμ, MPa	7750	10500	10900
Cz-Si-Cu	ρ, Ohm·cm	170–190	44.8–46.2	43.7–50.0
	τ, μs	134–138	16.32	14.55
	Conduction type	P	p	P
	Hμ, MPa	6900	10450	10700
Cz-Si-Zr	ρ, Ohm·cm	308–324	13.0–23.5	22.5–25.6
	τ, μs	228	93.3	69.57
	Conduction type	N	n	N
	Hμ, MPa	7900	11200	10300

Source: [33]

All the samples exhibit the drastic drop of the electric resistance after 240 hours of exposing to direct-current magnetic field, however some increase is observed in the values of this parameter with the further treatment by holding the samples in the magnetic field (Si-Cu behaved as an exception to this regularity). The sharp drops of the life times of the current minority-carriers are registered with all the samples after 240 hours of holding within the magnetic field, and they are followed by the further decrease if the holding time of 720 hours (however Si-Hf has been an exception).

In **Fig. 1.31**, we show the dependences between the life times of the current minority-carriers and the average microhardness for the undoped and the doped silicon samples before and after treating the samples with the direct-current magnetic field.

For the samples in their initial state, the dependence is discernible between the microhardness value and the life time of the current minority-carriers. After treating them with the magnetic field,

this dependence considerably weakens and the notable irregularities in it are found if we study the Si samples doped with Zr, Hf (**Fig. 1.31, *b, c***) and Mg (**Fig. 1.31, *c***).

Shortening the life time for the current minority-carriers can be explained as the relevance with that oxygen which the silicon surficial layers contain. As the publication reports [34], during the time when silicon is treated within the magnetic field, the oxygen content increases drastically in its surficial layers, the same is true for the ions of the alkaline metal (K^+, Na^+), hydroxyl groups and other radicals. This is related to the surface activation and enhancing its absorption ability under the influence of weak magnetic field.

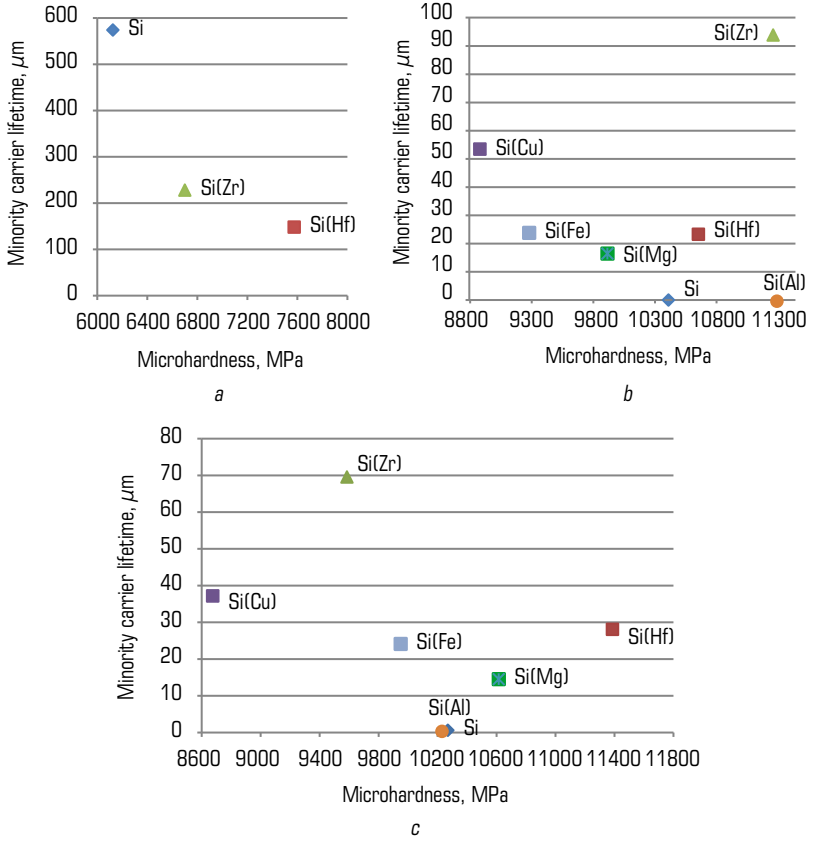

Fig. 1.31 Dependence between the time span of the current minority-carriers and the average microhardness of the samples: *a* – initial state; *b* – after 240 hours of exposing to direct-current magnetic field; *c* – after 240 hours of exposing to direct-current magnetic field

Apart from the oxygen in the principle state or the triplet state, the radical groups absorbed on the silicon surface also possess the ability of capturing the current carriers [33] and drastically decrease their lives in the free state.

Doping silicon with the elements of a greater affinity for oxygen (Zr, Hf, Al) permits the decrease in the influence of oxygen on the charge carrier life time by its binding. This is an assumable explanation for the reason why the samples doped with the mentioned elements have quite high values for the auxiliary charge carrier life time if the microhardness values are also high. The exception to this regularity is Si(Al).

CONCLUSIONS

1. The microstructure of the initial Cz-Si sample which is formed under the influence by the treatment within the magnetic field has been not studied before the research conducted for the current publication. The research reveals as follows:

– during 240 hours of exposing to the magnetic field, there is the significant increase in the number of the internal structure defects and the density of the dislocations as well as the formation of twins;

– during 720 hours of treating within the magnetic field, the polycrystalline silicon is formed with a large quantity of grain boundaries.

2. This research is the first time when it has been addressed to the problem of the magnetic field influences on the microstructure of Cz-Si doped with the elements which influence differently the energy of interaction between the silicon atoms within the crystal lattice, namely – Al, Mg, Cu, Fe, Zr, Hf.

With this publication, we show what influence produces the treatment within the magnetic field on Cz-Si doped with those elements which are able to decrease the interaction energy of silicon atoms (Al, Mg, Cu, Fe).

The data revealed can be summarized as follows:

– there is an increase in the quantity of the sample structural defects at exposing during 240 hours but their notable decrease is observed during 720 hours;

– Cz-Si doped with Zr and Hf, which increase the energy of interaction between the silicon atoms within the lattice, goes down significantly in the quantity of structural defects starting from at the point of 240 hours spent within the magnetic field.

3. By means of X-ray analysis conducted for the samples, which have been subjected to the magnetic field, it is registered that there are splits in the diffraction lines as well as the appearance of the new peaks at the scattering angles of 90–92 degrees. These phenomena are caused by the distortions of Si_{FCC} crystal lattice and forming $Si_{ORTHORHOMBIC}$ along with it. This evidences about the phase transformations in the samples of the semiconductive silicon when the magnetic treatment at the room temperature.

4. The study performed to address the problem of magnetic field influence on the microhardness of the doped Cz-Si has revealed as follows:

– the microhardness of Cz-Si doped with Al, Mg, Cu, Fe grows by 1.8–2.0 times at exposing both during 240 hours and 720 hours;

– the microhardness of Cz-Si doped with Zr, Hf grows by 1.5–1.8 times after exposing to the magnetic field during 240 hours while such values are higher by 1.2–1.5 times after 720 hours of exposition.

5. In this publication, the problem of the magnetic field treatment is first studied in terms of its influence on the physical properties of the doped Cz-Si, namely, its specific electric resistance (ρ, Ohm·cm), life time (τ, μs). It has been revealed as follows:

– 240 hours spent within the magnetic field decrease the specific electric resistance (ρ, Ohm·cm) of Cz-Si by 1.7–2.0 times while 720 hours of exposing decrease this parameter by 1.08;

– specific electric resistance (ρ, Ohm·cm) of Cz-Si Al, Cu decreases by 3.4 times at exposing within the magnetic field during the time period from 240 to 720 hours;

– for Cz-Si doped with Zr we observe the decrease in specific electric resistance values (ρ, Ohm·cm) by 18 times after 240 hours of the mentioned exposing and by 13.5 times at 720 hours of exposition;

– for Cz-Si doped with Hf, the specific electric resistance decreases by 13.5 times after 240 and 720 hours of exposing;

– the life time for minority-carriers of the charge (τ, μs) decreases 900 times within Cz-Si under conditions of both 240 and 720 hours of the magnetic field treatment;

– for Cz-Si doped with aluminium, the life time for minority-carriers of the charge decreases by 30 times when 240 hours of treatment while the decrease in 38 times is detected after 720 hours of exposing;

– for Cz-Si doped with copper, the life time for its minority-carriers of the charge decreases by 8–9 times both under 240 hours and 720 hours within the magnetic field;

– for Cz-Si doped with hafnium, the life time for its minority-carriers of the charge (τ, μs) decreases by 6 times at 240 hours and by 5 times at 720 hours of exposing;

– doping with zirconium enables sustaining the longest life times for its minority-carriers of the charge (τ, μs) vs those of the initial state: the life time for its minority-carriers of the charge experiences the shortening just by 2.4–3.2 after exposing within the magnetic field during 240 and 720 hours and they correspond to the values of 93.3 μs and 69.57 μs, respectively, compared against 0.63–0.65 of Cz-Si.

6. In this publication, we report on the development of the new complex production technology for silicon semiconductor. The technology includes the stages of silicon doping with the transition metals and rare earth metals, heat treatment at the temperatures of phase transformations and treating within the magnetic field at room temperature. These stages provide the enhanced set of the mechanical and the physical properties for Cz-Si products intended for devices.

REFERENCES

1. Glazov, V. M., Timoshina, G. G., Mikhailova, M. S. (1996). Printcipy legirovaniia kremniia dlia povysheniia ego termostabilnosti. Doklady Akademii Nauk, 347 (3), 352–355.
2. Taran, Yu. N., Glazov, V. M., Regel, A. R., Kutsova, V. Z., Koltsov, V. B., Timoshina, G. G. et al. (1991). Strukturnye prevrashcheniia pri nagreve monokristallov kremniia Fizika i tekhnika poluprovodnikov, 4 (25), 588–595.
3. Kol'tsov, V. B., Zubkov, A. M., Timoshina, M. I. (2002). Metodika issledovaniy elektrofizicheskikh svoystv monokristallov kremniya v shirokom intervale temperatur. Fizika poluprovodnikov i polumetallov. Saint-Petersburg.
4. Kozhitov, L. V., Botavin, V. V., Shepel, P. N., Timoshina, G. G., Timoshina, M. I. (2002). Issledovanie kinetiki raspada kremniia, legirovannogo perekhodnymi i redkozemelnymi elementami. Kremniy-2002. Novosibirsk, 129.
5. Novokhatskiy, I. A., Kisun'ko, V. Z., Ladyanov, V. I. (1985). Osobennosti proiavlenii razlichnykh tipov strukturnykh prevrashchenii v metallicheskikh rasplavakh. Izvestiya vuzov. Chernaya metallurgiya, 5, 1–9.
6. Kutsova, V. Z., Nosko, O. A., Timoshina, M. I. (2006). Alloying effect on structure and properties of semiconductor silicon. Proceeding of the International Conference Silicon 2006, 450–459.
7. Tonkov, E. Yu. (1988). Fazovye prevrashcheniia soedinenii pri vysokom davlenii. Vol. 1, 2. Moscow: Metallurgiya, 463, 356.
8. Kutsova, V. Z., Nosko, O. A., Timoshina, M. I. (2007). Vliianie legiruiushchikh elementov na strukturu, fazovyi sostav i svoistva poluprovodnikovogo kremniia. Kremniy-2007. Moscow: Gosudarstvennyy tekhnologicheskiy universitet "Moskovskiy institut stali i splavov", 109.
9. Glazov, V. M., Zemskov, B. S. (1967). Fiziko-khimicheskie osnovy legirovaniia poluprovodnikov. Moscow: Nauka, 372.
10. Klevan, O. S., Engh, T. A. (1995). Dissolved impurities and inclusions in FeSi and Si, development of a filter sampler. INFACON 7. Trondheim, 441–451.
11. Prikhodko, E. V. (1983). Metallokhimiia kompleksnogo legirovaniia. Moscow: Metallurgiya, 184.
12. Nesterenko, A. M., Uzlov, K. I., Kutsova, V. Z., Nyshchenko, A. N. (1988). Vliianie skorosti okhlazhdeniia na obrazovanie tverdykh rastvorov v sisteme Al-Si. Izvestiya AN SSSR, Metally, 2, 192.
13. Savitskiy, E. M., Burkhanov, S. S. (1967). Metallovedenie tugoplavkikh metallov i splavov. Moscow: Nauka, 324.
14. Liubov, B. Ia. (1969). Kineticheskaia teoriia fazovykh prevrashchenii. Moscow: Metallurgiia, 264.
15. Taran, Yu. N., Kutsova, V. Z., Uzlov, K. I., Falkevich, E. S. (1992). Shearing phase transformations in semiconductors. Proceeding of the International Conference 'Silicon 92', 88–95.
16. Milvidskiy, M. G., Osvenskiy, V. B. (1984). Strukturnye defekty v monokristallakh poluprovodnikov. Moscow: Metallurgiya, 256.

17. Glazov, V. M., Koltsov, V. B., Kutsova, V. Z., Taran, Yu. N., Timoshina, G. G., Uzlov, K. I., Falkevich, E. S. (1990). Issledovanie elektro-fizicheskikh svoystv kremniya v shirokom intervale temperatur. Elektronnaya tekhnika, 11.
18. Glazov, V. M., Kurbatov, V. A., Koltsov, V. B. (1985). Issledovanie effekta Kholla antimonidov Ga i In v tverdom i zhidkom sostoyanii. Fizika i tekhnika poluprovodnikov, 19 (4), 662–667.
19. Kopaev, Iu. V., Meniailenko, V. V., Molotkov, S. N. (1985). Neravnovesnye fazovye perekhody v kovalentnykh poluprovodnikakh pod vozdeistviem lazernogo izlucheniia. Fizika tverdogo tela, 27 (11), 3288–3294.
20. Landau, L. D., Lifshits, E. M. (1964). Statisticheskaia fizika. Moscow: Nauka, 568.
21. Tairov, Yu. M., Tsvetkov, V. F. (1980). Rost kristallov i politipizm karbida kremniya. Rost kristallov, 13, 104–111.
22. Taran, Yu. N., Kutsova, V. Z., Chervonyy, I. F., Shvets, E. Ya., Falkevich, E. S. (2004). Poluprovodnikovyy kremniy: teoriya i tekhnologiya proizvodstva. Zaporozhe: Zaporozhskaya gosudarstvennaya inzhenernaya akademiya, 344.
23. Alshits, V. I., Darinskaya, E. V., Koldaeva, M. V., Petrzhik, E. A.; Hirth, J. P. (Ed.) (2008). Magnetoplastic Effect in Nonmagnetic Crystals. Dislocations in solids. Amsterdam: Elsevier, 14 (86), 333–437. https://doi.org/10.1016/s1572-4859(07)00006-x
24. Alshits, V. I., Darinskaya, E. V., Koldaeva, M. V., Petrzhik, E. A. (2003). Magnetoplastic effect: Basic properties and physical mechanisms. Crystallography Reports, 48 (5), 768–795. https://doi.org/10.1134/1.1612598
25. Golovin, Yu. I. (2004). Magnitoplastichnost tverdykh tel (Obzor). Fizika Tverdogo Tela, 46, 769.
26. Morgunov, R. B. (2004). Spinovaia mikromekhanika v fizike plastichnosti. Uspekhi fizicheskikh nauk, 174, 131–153.
27. Buchachenko, A. L. (2013). Mass-Independent Isotope Effects. The Journal of Physical Chemistry B, 117 (8), 2231–2238. https://doi.org/10.1021/jp308727w
28. Zinenko, V. N., Sorokin, B. P., Turchin, P. P. (1983). Osnovy fiziki tverdogo tela. Moscow: Vysshaia shkola, 330.
29. Milnes, A. G., Feuch, D. L. (1972). Heterojunctions and Metall-Semiconductor Junctions. New York; London: Academic Press, 418. https://doi.org/10.1016/b978-0-12-498050-1.x5001-6
30. Zhitinskaya, M. K., Nemov, S. A., Svechnikova, T. E. (1997). Vliyanie neodnorodnostey kristallov Bi_2Te_3 na poperechnyy effekt Nernsta – Ettingsgauzena. Fizika i tekhnika poluprovodnikov, 31 (4), 441–443.
31. Chervonyi, I. F., Kutsova, V. Z., Pozhuiev, V. I., Shvets, Ye. Ya., Nosko, O. A., Yehorov, S. H., Voliar, R. M. (2009). Napivprovidnikovyi kremnii: teoriia i tekhnolohiia vyrobnytstva. Zaporizhzhia, 350.
32. Vapnik, V. N. (Ed.) (1984). Algoritmy i programma vosstanovleniya zavisimostey. Moscow: Nauka, 816.
33. Kutsova, V. Z., Nosko, O. A., Tutyk, V. A., Sulay, A. M. (2015). Struktura, mekhanichni ta elektrofizychni vlastyvosti monokrystalichnoho kremniiu pid diieiu postiinoho mahnitnoho polia. Metallurgicheskaya i gornorudnaya promyshlennost, 1, 73–79.

34. Kutsova, V. Z., Nosko, O. A., Sulay, A. M. (2014). Vliianie legirovaniia i termicheskoi obrabotki na strukturu i svoistva poluprovodnikovogo kremniia. Metallurgicheskaya i gornorudnaya promyshlennost, 6, 65–72.
35. Kutsova, V. Z., Nosko, O. A., Sulay, A. M. (2015). The structure, mechanical and electrophysical properties of monocrystalline silicon under influence of constant magnetic field. Ukrainian journal of mechanical engineering and materials science, 1 (1), 91–98.
36. Kutsova, V. Z., Nosko, O. A., Sulai, A. M. (2017). The influence of constant magnetic field on the structure and properties of monocrystalline silicon. Metaloznavstvo ta termichna obrobka metaliv, 2, 32–40.
37. Bonch-Bruevich, V. P., Kalashnikov, S. G. (1990). Fizika poluprovodnikov. Moscow: Nauka, 685.
38. Moss, T. S., Burrell, G. J., Ellis, B. (1973). Semiconductor opto-electronics. Butterworth-Heinemann, 441. https://doi.org/10.1016/c2013-0-04197-7
39. Kutsova, V. Z., Uzlov, K. Y., Khronenko, V. M. (1999). Temperaturnaya zavisimost' otnositel'nogo udlineniya sverkhchistogo kremniya. Metallurgicheskaya i gornorudnaya promyshlennost, 4, 72–74.
40. Taran, Iu. N., Kutcova, V. Z., Kovalchuk, M. G., Uzlov, K. I. (1988). Neodnorodnost beta-tverdogo rastvora v siluminakh. Metallovedenie i termicheskaia obrabotka metallov, 9, 33–37
41. Taran, Yu. N., Kutsova, V. Z. (2002). Fazovye prevrashcheniya i svoystva poluprovodnikovogo kremniya. Vysokochistye metallicheskie i poluprovodnikovye materialy. Kharkovskaya nauchnaya assambleya ISPM-8, 68–73.
42. Taran, Yu. M., Kutsova, V. Z., Nosko, O. A. (2002). Fazovi peretvorennia ta vlastyvosti napivprovidnykovoho kremniiu. Metaloznavstvo ta obrobka metaliv, 1–2, 59–65.
43. Taran, Yu. M., Kutsova, V. Z., Nosko, O. A. (2004). Semiconductor–Metal Phase Transitions. Uspehi Fiziki Metallov, 5 (1), 87–166. https://doi.org/10.15407/ufm.05.01.087
44. Kutsova, V. Z., Stetsenko, A. P., Mazochuk, V. F. (2017). Phase transformations in semiconductor silicon by the influence of magnetic field. Systemni tekhnolohii. Rehionalnyi mizhvuzivskyi zbirnyk naukovykh prats, 5 (112), 103–107.
45. Oranska, O. I., Gornikov, Yu. I., Gun'ko, V. M., Brichka, A. V. (2022). On the use of model diffraction profiles in the microstructure analysis of nanocrystalline metal oxides based on powder x-ray diffraction data. SURFACE, 14 (29), 148–158. https://doi.org/10.15407/surface.2022.14.148
46. Makara, V. A., Vasiliev, M. O., Steblenko, L. P., Koplak, O. V., Kuryliuk, A. M., Kobzar, Yu. L., Naumenko, S. M. (2009). Influence of Magnetic Treatment on the Microhardness and Surface Layers Structure of Silicon Crystals. Physics and Chemistry of Solid State, 10 (1), 193–198.
47. Nosko, O. A. (2006). Osobennosti struktury, fazovye prevrashcheniya legirovannogo kremniya i modifitsirovannykh zaevtekticheskikh siluminov i razrabotka sposobov povysheniya ikh svoystv [PhD dissertation]. Dnepropetrovsk, Ukraine.
48. Kutsova, V. Z. (1993). Teoriya i praktika upravleniya strukturoy i svoystvami liteynykh splavov na osnove alyuminiya i titana [Doctor's thesis]. Dnepropetrovsk, Ukraine.

DOI: 10.15587/978-617-8360-02-3.CH2

Tetyana Baydyk, Masuma Mammadova, Ernst Kussul, Airam Curtidor
© The Author(s) 2024. This is an Open Access chapter distributed under the terms of the CC BY-NC-ND license

CHAPTER 2

SUPPORT FRAME OF SOLAR CONCENTRATOR WITH FLAT TRIANGULAR MIRRORS

ABSTRACT

Green energy includes solar, wind, geothermal and other types of energy sources generation. The object of this research is solar concentrators. The problem to be solved is connected with the development of the structure frame, especially for solar concentrators with flat triangular or square mirrors that approximate a parabolic shape surface. The essence of the investigation is developing and producing several prototypes of solar concentrators that have low cost of materials but since the devices were assembled by hand, the cost their manufacture is quite high. Therefore, it is important to reduce cost through automation of solar concentrator production process. To obtain the better condition for future automation it is necessary to reduce the number of metal structural elements of solar concentrator. In this case the automation problem is simpler for its realization. The purpose of the research is to develop a new and improved design of the solar concentrator frame prototype, which should be technologically simpler than the previous one and lighter in weight. The study proposes a new frame structure design that contains fewer metal elements, is lighter than the previous one and is more convenient for the automatic assembly process. The development of improved solar concentrator design and structure can help to reduce the cost of assembly and to accelerate the solar concentrator assembly process. In case of massive production, they can be used in practice. The proposed solar concentrators can be used, in particular, for green buildings in rural areas, in reactors to accelerate the chemical process of processing organic waste, in agriculture in combination with agricultural fields. These solar concentrators are quite promising in combination with small thermal energy storage devices, with the help of which it is possible to create small power plants for green buildings that satisfy all the energy needs of residential buildings.

KEYWORDS

Solar energy, flat facet parabolic solar concentrator, thermal energy storage, support frame.

Energy consumption is growing all over the world due to new lifestyle trends in the form of the increasing use of electronic devices. Global energy consumption will grow nearly 50 % from 2018

through 2050, according to the U.S. Energy Information Administration (EIA) [1]. With the threat of global warming and the rising cost of energy, the trend towards the use of renewable and sustainable energy sources is becoming more and more popular.

The use of solar energy, for example, in Mexico or in Azerbaijan, has great potential, since these countries have good conditions for the development of this industry, which is expressed in the duration of sunny days, their number, as well as direct solar radiation on the surface [2]. Solar energy is the most powerful and affordable, as well as the use of solar energy is leading in renewable energy.

Solar power plants are designed to convert the energy of solar radiation into heat and electricity. There are the following types:

1) photovoltaic (PV) converters that are used to directly convert electricity through the photovoltaic effect [3, 4];

2) thermal concentrated solar power (CSP) that are designed to produce thermal energy for its further use or conversion into other types of energy. The mirrors and lenses are used in CSP to generate thermal energy.

Photovoltaic converters used semiconductors. The operation of the device is based on the emission of photoelectrons or the internal photoelectric effect. Currently, silicon-based photovoltaic modules (single-crystal and polycrystalline) are the most common type.

Solar concentrators are devices that capture incoming solar radiation and convert it into usable heat. This heat is transferred to the working liquid for transfer directly to the consumer, to a heat exchanger, or a heat engine (for example, Stirling or Ericsson engines) to generate electricity. The temperature level of the working liquid determines its energy performance, and the main factor is the mass flow rate of the working liquid. There are installations for the simultaneous production of electricity and hot water at the outlet.

Renewable energy has many aspects to develop. Solar, wind, geothermal energy and so on demand the special instruments and apparatus to generate electricity from different energy sources. So, industrial engineering and engineering design are very important to be developed. But not only engineering side of this problem is important. For example, the storage and transportation of renewable energy is very important too [5]. For this reason, the mathematical models are constructed to evaluate or optimize the renewable energy systems [6, 7]. In [7] the authors not only created the mathematical model but and applied the model to analyze energy storage and hydrogen production at renewable energy power plants in Japan in 2050.

It is important to integrate renewable energy sources for new housing developments to reduce demand for grid energy and carbon emissions [8]. Different technologies are oriented to include or to combine with green energy [9, 10]. An effective response to climate change is a rapid replacement of fossil carbon energy sources with green energy [10]. So, the target of decarbonization in the energy sector can be achieved. The intensification of the use of different renewable energy sources is essential for the fulfillment of the Paris Agreement or for achieving the goals of sustainable development [11].

So, green energy, and especially solar energy generation is very actual and important area of science and engineering. To create cheap and effective devices is a challenge for scientists.

2.1 LITERATURE REVIEW AND PROBLEM STATEMENT

Solar energy is one of the most accessible energy sources. Different countries actively develop the photovoltaic systems. For example, one of the leaders in these investigations is India [12]. Development and application of solar energy have been regarded by the government of India and common people, and they thought that solar photovoltaic energy can provide more energy in future compare to other renewable energies.

Not only photovoltaic systems are developed. Parabolic solar concentrators are developed [13]. The authors developed a system comprising external parabolic solar concentrators integrated with cylindrical vertical type sensible-based thermal energy storage (TES) tanks. Solar concentrators can generate thermal energy in the highest operating temperature range (≥300 °C) and can be used in solar thermal-energy applications in the industrial sector [14]. Parabolic dish concentrator converts 72 % of solar energy into usable heat [15]. With 50 % of global energy consumption in the form of heat, the market for thermal energy is vast.

The parabolic concentrators are expensive because of using large-area curved mirrors. A way to overcome these difficulties can be connected with plane mirror using. To reduce the cost, let's propose to use plane mirrors that have a cost 2–3 dollars for one square meter. For our task it is necessary only to cut them. Low cost parabolic solar concentrators based on multitude of small triangular flat mirrors that can approximate parabolic surfaces were developed [16]. These solar concentrators can be used for energy supply to residential houses [17]. Small scale residential power plant will contain flat facet parabolic solar concentrators, TES, and powerhouse hall. Let's present in **Fig. 2.1** two possible variants of their collocation. The system presented in **Fig. 2.1, *a***, is better when there are free areas or can combine the solar concentrators with agricultural fields [17]. The system presented in **Fig. 2.1, *b***, is better for economic surface using.

Parabolic solar concentrators can generate heat energy (approximately 300–400 °C) in the focal point and then can be accumulated in TES. Equipment for transformation of heat energy to electrical energy and middle/low temperature heat energy is situates in powerhouse hall. Middle/low temperature heat energy can be used for space and water heating (for example, hot water we can use for chemical reactors to accelerate the chemical process of organic waste processing [6]), for meal preparation, etc. Electrical energy is needed for illumination and electrical devices feeding.

Let's propose the design of solar concentrators and TES [6]. Flat facet solar concentrators were proposed in 80th years and the prototype of solar energy plant based on these concentrators was made in Australia, White Cliffs (1998) [18, 19]. After that many versions of flat facet solar concentrators were proposed, developed and patented.

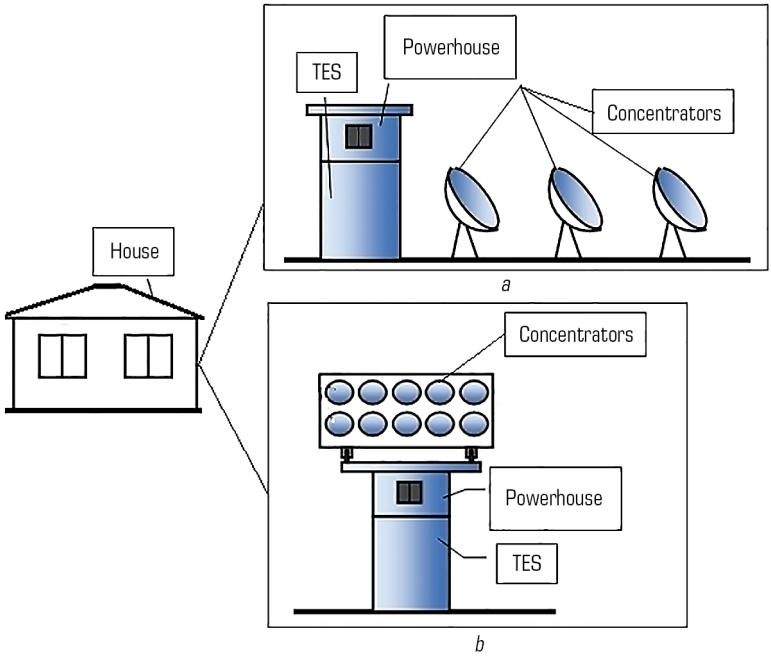

Fig. 2.1 Residential power plant: *a* – parabolic solar concentrators are collocated in special zone; *b* – solar concentrators are combined in the roof of TES and powerhouse

The main goal of these works is to decrease the cost of materials and labour needed for parabolic solar concentrator manufacture.

2.1.1 EXISTED PROTOTYPES OF SOLAR CONCENTRATORS

Last decade we developed several prototypes of flat facet concentrators and improved the methods of adjustment of parabolic surface [19–21]. It is possible to estimate the cost of concentrators near 20 or 30 USA dollars per square meter. This cost permits to supply all needed energy for the houses in countries with hot arid climate, for example, in Azerbaijan and Mexico. In countries with cold climate such as Ukraine and Canada solar energy can provide a significant part (sometimes more than half) of the energy consumed by a residential house. So, let's consider the possibility of using solar concentrators in different countries. In this regard, let's propose a brief analytical review of modern technologies of existing solar concentrators.

The proposed concentrator is useful in application both for remote consumers from engineering networks and for saving energy resources. A solar parabolic concentrator can be used with different receivers in focal point, for example, with the Stirling or Ericsson engines that can transform the thermal energy to electricity.

The parabolic concentrator with a spiral receiver for converting thermal energy and obtaining water at a temperature of 85 °C for domestic needs is described in different applications [22].

At present, among countries with low incomes, parabolic concentrators are popular, made with low characteristics, nevertheless, with a temperature suitable for heating water or cooking. Solar installations of this type are usually made from satellite parabolic antennas by coating them with a reflective surface. Solar parabolic cooking units are very popular in India, and the output characteristics are sufficient for cooking due to the scorching sun and climate [23]. In **Fig. 2.2** the solar concentrators from Repasso Energy are presented.



Fig. 2.2 Solar concentrators from Ripasso Energy
Source: [23]

The responsible for this project was the company Ripasso Energy. In the Kalahari Desert in South Africa two solar concentrators with diameter of 12 meters each were installed and that are synchronized thanks to a Stirling engine. Studies have shown that conventional solar panels can provide 15 percent of the energy they receive in electricity, but Ripasso has developed a device (solar concentrator) and has managed to double this amount to 34 percent, managing to generate 75 MW to 85 MW per hour that is enough to power an average of ten homes for a year [23, 24]. The solar concentrator of Ripasso is equipped with a mirror reflector with a total area of $S = \pi \cdot R^2 = 3.14 \cdot 6^2 = 113.04$ m^2, a giant disk rotates after the sun moving and constantly adjusts to extract the maximum solar energy. For comparison, producing this amount of electricity from coal burned in a Combined Heat and Power (CHP) plant releases 81 tons of CO_2 into the atmosphere.

Solarflux (USA), a company specializing in the production of parabolic solar concentrators, has developed a model, which converts 72 % of solar energy into usable heat [25]. The solar concentrator from Solarflux is presented in **Fig. 2.3**.

These characteristics were confirmed by tests conducted by the Center for Energy Research at Lehigh University in Pennsylvania, USA. Utilizing an innovative optical design and dual-axis tracking, the parabolic solar concentrator maximizes year-round solar energy capture. As a thermal concentrator, the full spectrum of solar irradiance is taken advantage of, and losses resulting from conversion into electricity are avoided. The solar concentrator had been designed from the ground up to minimize the Levelized Cost of Heat (LCOH) over the lifetime of the system. Built from environmentally resilient low-cost metal components, the concentrator is manufactured using proven techniques borrowed from the aerospace and automotive industries. With 50 % of global energy consumption in the form of heat, the market for thermal energy is vast. The parabolic solar concentrator of Solarflux provides a clean, inexpensive source of thermal energy for a wide range of applications, including industrial process heat, space heating and cooling, hot water, water desalination and purification, and remote and distributed power applications.

The Solar Invictus dish from ZED Solar (developed by AEDesign) is a parabolic concentrator with a diameter of 9 m. The total mass of the supporting structure is reduced to a minimum through the use of the structural properties of the mirrors [26, 27]. The solar concentrator from ZED solar is presented in **Fig. 2.4**.

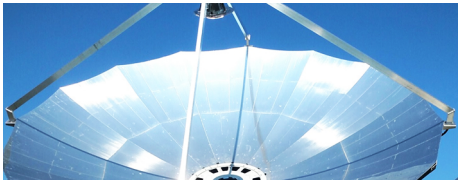

Fig. 2.3 Example of solar concentrator from Solarflux
Source: [25]



Fig. 2.4 Solar concentrator from ZED
Source: [26]

Conventional azimuth and elevation tracking, ZED Solar built its first two prototype dishes in Lahore, Pakistan in 2010 and 2012. The company delivered a prototype to Cleanergy in Omol, Sweden in 2012, 10 more prototypes for the Cleanergy pilot project in Dubai in 2014, and a prototype EOR steam receiver in Abdali, Kuwait in 2016. The size of this concentrator (9 meters) is sufficient large. It is difficult to install it, for example, in roof of the building. Such constructions require a lot of space.

In addition to the solar concentrator models described above, there are a dozen interesting ones, such as the EuroDish [28, 29], which have very good energy conversion rates. The solar concentrator from EuroDish is presented in **Fig. 2.5**.



Fig. 2.5 Solar concentrator from EuroDish
Source: [29]

Industrial designs can use various energy converters, however, it should be noted that most projects use a Stirling engine to convert to electrical energy. Within the Spanish-German project EuroDish, two new prototypes of a parabolic dish with a Stirling motor were designed and built, in which it was intended to act on the following aspects:

– reduction of the price of components by identifying elements of standard use in the industry;

– development of a new manufacturing system for the concentrator disk. Tensioned membrane technology has been abandoned and a 'composite' material and mold system has been used;

– improvement of the Stirling engine SOLO V161, especially those components used in the cavity that receives concentrated solar energy;

– development of a new optimized procedure for system assembly, using new special tools;

– remote control and monitoring through the WWW;

– testing of pre-commercial units as reference systems.

The most of the described and developed models are efficient and good for green energy. The main problem that we can see is connected with their production. The manual labor and manual assembly are the points that can elevate the cost of the product. So, it is very important to simplify the solar concentrator structure for future automation of these processes.

The models of solar concentrators developed in different countries are used for different applications. Critical point is the size of solar concentrators. Nine meters of diameter (for example, as Solar Invictus has) is large for some applications. If to want to install the solar concentrators in roofs of the buildings it is necessary to reduce the diameter of solar concentrators and its weight. The weight we can reduce decreasing the number of structural elements. The other critical point for all developed and discussed above models is that every prototype is a one-piece item. The manual labor elevates the cost of solar concentrator. Before automating the solar concentrator production process, it is necessary to simplify the solar concentrator structure.

2.1.2 APPLICATIONS OF SOLAR CONCENTRATORS

The tropical countries with high air humidity can be the other application area for solar concentrators. In this case it is possible to use solar powered dehumidifiers with hot air generated by solar concentrators. Special chemical substances can be used to eliminate the excessive humidity. Frequently they have active surfaces that can absorb the water vapour from the air. Sometimes the solutions are dangerous for human health or they can have corrosive properties. Sometimes it is necessary to regenerate the adsorption property of the substances. For this purpose, they need to be heated to high temperature. Solar concentrators can be used for hot air generation. Low cost flat facet solar concentrators are proposed for different applications, for example, for the dehumidification system and for the combination of solar concentrators and agricultural fields [19, 21, 30, 31]. This application was proposed as demonstrated in **Fig. 2.6**.

Low cost flat facet solar concentrators are proposed for different applications, for example, for the combination of solar concentrators and agricultural fields [30, 31].

The tropical countries with high air humidity can be the other application area for solar concentrators. In this case it is possible to use solar powered dehumidifiers [32, 33] with hot air generated by solar concentrators.

These solar concentrators can be used with small scale TES [6]. Using TES, it is possible to make power plants for green buildings. Small solar power plants can support all the energy demands of residential houses.

The most of the described and developed models are efficient and good for green energy. The main problem that it is possible to see is connected with their production. The manual labor and manual assembly are the points that can elevate the cost of the product. So, it is very important to simplify the solar concentrator structure for future automation of these processes.

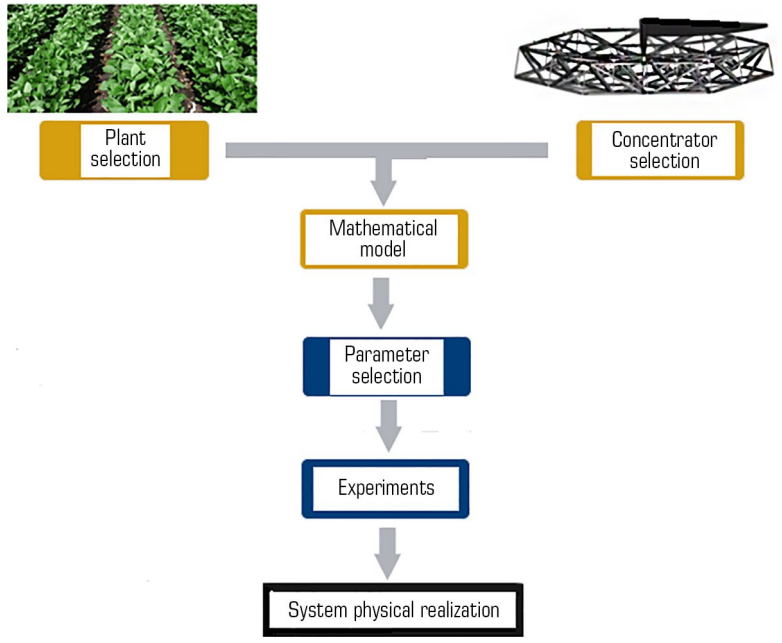

Fig. 2.6 The scheme of combining solar energy with agricultural plant

The models of solar concentrators developed in different countries are used for different applications. Critical point is the size of solar concentrators. Nine meters of diameter (for example, as Solar Invictus has) is large for some applications. If we want to install the solar concentrators in roofs of the buildings it is necessary to reduce the diameter of solar concentrators and its weight. The weight we can reduce decreasing the number of structural elements. The other critical point for all developed and discussed above models is that every prototype is a one-piece item. The manual labor elevates the cost of solar concentrator. Before automating the solar concentrator production process, it is necessary to simplify the solar concentrator structure.

2.2 THE AIM AND OBJECTIVES OF THE STUDY

The aim of the study is the development of a new structure frame prototype of solar concentrator. This will make it possible to propose new structure (support frame) of the solar parabolic concentrator with reduced cost, less weight, and better conditions for automatic production.

To achieve this aim, the following objectives are accomplished:

– give the essence and critical review the possibilities for improving the first model;

– consider the possibility to decrease the number of metal structural elements and respectively the weight of the whole structure of solar concentrator and propose the improved design with connections of metal elements with mirror triangular elements.

2.3 MATERIALS AND METHODS

Research methods are based on an analytical research method and computer simulation using the SolidWork software.

The SolidWork program was used to design 3D models of the studied parts and the whole model of solar concentrator prototype.

Scientific novelty is the development of an improved support structure of a solar parabolic concentrator. A major role in this work has the possibility to simplify the support frame of solar concentrator to collocate the flat mirrors.

2.3.1 OBJECT AND HYPOTHESIS OF THE STUDY

The object of research is the solar concentrator. The main hypothesis of the study is connected with the simplification of the frame structure of solar concentrator with flat triangular mirrors. The methods that were used are computer simulation and physical prototyping.

2.3.1.1 FIRST MODEL

The first models of solar concentrator prototypes were developed, manufactured and described in our publications [16, 20]. The support structure of the solar concentrator is presented in **Fig. 2.7**.

The structure contains horizontal top aluminium bars, vertical bronze bars, diagonal aluminium bars and horizontal low aluminium bars. Horizontal top bars are connected as triangular cells that are the base for triangular mirrors.

The solar concentrator structure has a hexagonal shape, i.e. it has six external sides. The structure has aluminum triangles to have possibility to collocate the plane triangular flat mirrors: one mirror for one triangle. In total this prototype has 24 cells for 24 mirrors.

In **Fig. 2.8, *a*,** there are four mirrors collocated and fixed on the support structure.

In **Fig. 2.8, *b*,** the first prototype is presented in complete form with all triangular mirrors and with concentrated solar light in focal point.

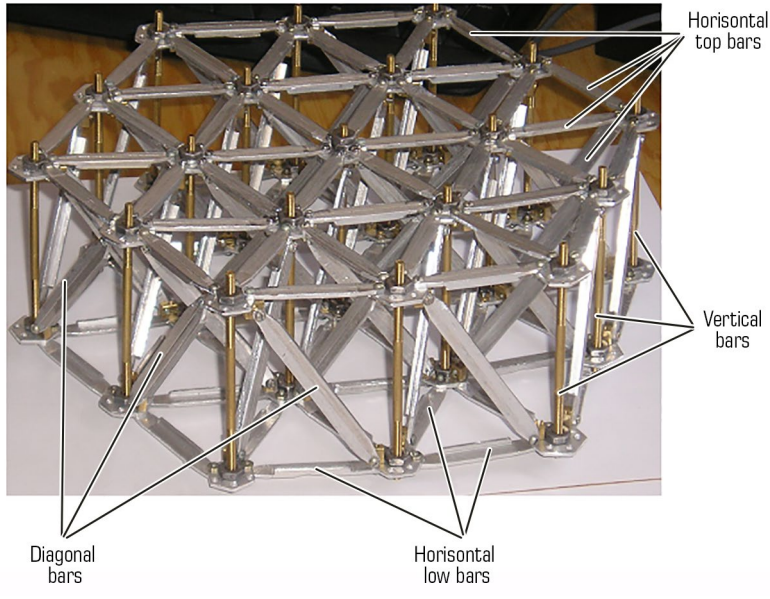

Fig. 2.7 First structure project
Source: [16]

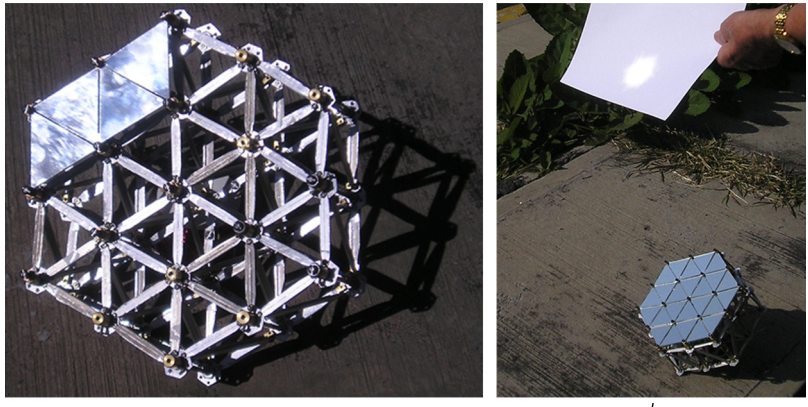

a *b*

Fig. 2.8 Support structure frame of the first prototype: *a* – four mirrors collocated on the structure; *b* – concentration of solar energy in focal point

2.3.1.2 NUMBER OF MIRRORS

In common case it is possible to calculate the number of mirror N using the following equation:

$$N = \left(6 \cdot n^2\right) - 6, \tag{2.1}$$

where n – the number of layer. In the next paragraph, let's explain this formula in more detail. Several prototypes of one meter of diameter were made. In these prototypes we did not place the mirrors in the center (minus 6 mirrors). This hole is used for collocate the gauge with parabolic edge to adjust all screws to obtain the parabolic surface curve [16, 20].

In **Fig. 2.9**, the solar concentrator prototype is presented that contains six layers and in accordance with equation (2.1) contains 210 flat mirrors. This structure was patented in USA, Spain and Mexico. In this case we used the same principle: one cell for one flat mirror.

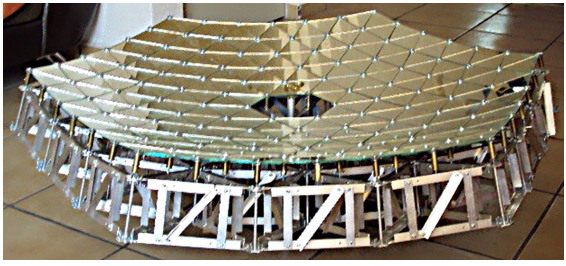

Fig. 2.9 Prototype with the first structure model
Source: [20]

The main disadvantage is the large number of elements in the structure. Let's use aluminum, which is lightweight, but the number of elements complicates the assembly of the device.

The assumptions made in the work are following: it is possible to reduce number of structural metallic elements without loss of structural strength; with reducing of number of elements we can do the structure lighter than previous structure. Simplifications adopted in the work are connected with idea that we can use structural elements of the previous prototype as basic elements of the structure of solar concentrator.

2.3.2 MATERIALS

The materials that were used in the study are metallic components for support frame. It was used aluminum bars (**Fig. 2.7–2.9**). The structure in this case is sufficiently light and firm.

Before constructing the prototypes, it is possible to simulate the elements and structure of solar concentrator using SolidWork.

2.3.3 METHODS

As method that was used in the study is a geometrical model of solar concentrator. It was selected the diameter of solar concentrator 1.6 meters. With calculations using this model it was demonstrated the possibility to obtain sufficient thermal energy with proposed solar concentrators.

2.3.3.1 GEOMETRIC MODEL OF SOLAR CONCENTRATOR

This part presents the mathematical description of the model. The sketch of solar concentrator is drawn in the SolidWorks software environment (**Fig. 2.10**).

The main parameters are shown in the **Table 2.1**.

We want to explain the values from the **Table 2.1**. They were obtained for our prototype of solar concentrator. The concentrator contains $N=210$ flat mirrors, which have a triangular shape with size of one side L_1 (**Fig. 2.10**) [6].

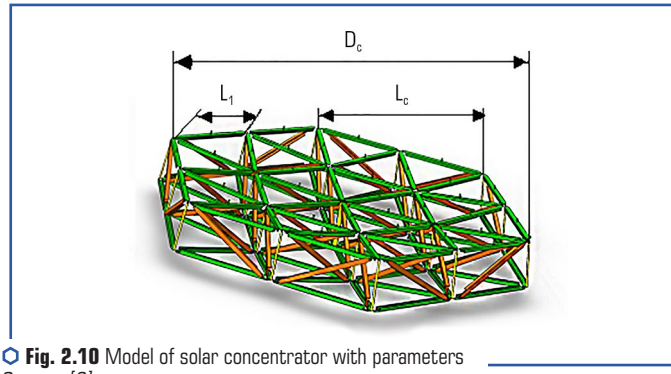

Fig. 2.10 Model of solar concentrator with parameters
Source: [6]

Table 2.1 Parameters of the parabolic concentrator

Parameter name	Value	Unit
Concentrator diameter (D_c)	1.6	m
Size of a mirror side (L_1)	0.13	m
Solar constant (kW per square meter) (C_s)	1.361	kW/m^2

The surface area of the parabolic concentrator can be calculated using equation:

$$A_c = \frac{\pi D_c^2}{4} = \frac{3.14 \cdot 2.56}{4} = 2.01\,\text{m}^2. \tag{2.2}$$

The power of the concentrator with this area is possible to present as:

$$W_C = N \cdot L_1^2 \cdot C_S \cdot \frac{t_M}{24} \cdot \eta_C \cdot \frac{\sqrt{3}}{4} = 210 \cdot 0.13^2 \cdot 1361 \cdot \frac{7}{24} \cdot 0.7 \cdot \frac{\sqrt{3}}{4} = 2091.53\ \text{W}, \tag{2.3}$$

where W_C – the concentrator power; N – the number of mirrors; L_1 – the size of a mirror side; C_S – the solar constant (amount of energy that reaches 1 square meter of the earth) (C_s= =1.361 kW/m^2) [34]; t_M – the number of hours (average) with the direct sun (not diffuse), for example, in Mexico, 7 hours of sunlight per day; η_C – the concentrator efficiency (η_C=0.7).

Satellites have directly measured the amount of energy arriving at Earth from the Sun as sunlight. Although this value varies slightly over time, it is usually very close to 1,361 watts of power per square meter (1.4 kW).

The concentrator contains N=210 flat mirrors, which have a triangular shape with size of one side L_1 (**Fig. 2.8**) [6]. So, there is concentrator power (W_C) more than 2 kW that is sufficient to built a system with thermal energy storage and use it for chemical reactor heating.

2.3.3.2 CALCULATION OF NUMBER OF STRUCTURAL ELEMENTS

To calculate the number of structural elements we present schematically part of solar concentrator structure. We can on the base of every external side (side L_C in **Fig. 2.10**) demonstrate the triangular zone that begins from outside line to the central point of solar concentrator structure. One triangle it is schematically presented in **Fig. 2.11**. The one triangle corresponds to triangle ABC (in this case AB=L_c).

We can on the base of every side demonstrate the triangle that begins from outside line to the central point of solar concentrator structure. We want to consider one triangle as it is schematically presented in **Fig. 2.11**. The one triangle corresponds to triangle ABC (in this case AB=L_c).

It is possible to see the triangle ABC (magenta colour), where point C is the central point of structure of solar concentrator and near this point we begin to place four triangular mirrors. Triangle ABC is 1/6 part of the solar concentrator structure (for this reason in equation (2.1) let's multiply by 6). There are seven lines which are parallel to AB line (blue colour). So, every zone has 49 triangular mirrors. In total, there is the solar concentrator with 288 mirrors (49*6–6=294–6=288 mirrors) if we do not include six mirrors in center of the solar concentrator structure.

Every mirror is collocated on cell from three upper aluminum bars that are connected with three vertical bars with other three lower aluminum bars. To make the system from bars

tough three diagonal bars were added. So, every cell includes 12 bars. If the structure contains 288 mirrors so it is necessary to construct it 3456 metal bars.

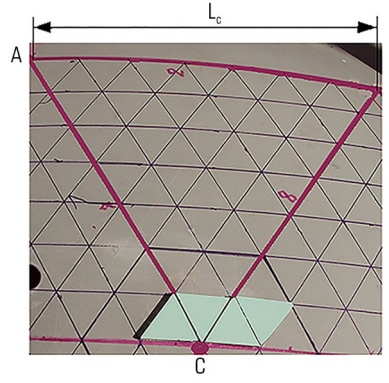

Fig. 2.11 Triangle ABC of solar concentrator

In the first type of structure every triangular mirror has the support cell for every mirror (**Fig. 2.7, 2.8**). Every vertex of the triangle has a fixing screw.

The problem of this prototype is complexity of the solar concentrator structure (**Fig. 2.10**) and large number of structural metal elements for automatic assembly.

Next, let's look at the frame improvements of the prototype of solar concentrator.

2.3.4 SOFTWARE

The methods that were used in the study are simulating of the support structure using SolidWork. After that the hardware as prototypes of solar concentrators were made to validate the proposed solutions. At the first stage we used SolidWork software to simulate the the 3D models of structure of solar concentrator.

2.4 NEW STRUCTURE OF SOLAR CONCENTRATOR WITH FLAT TRIANGULAR MIRRORS

2.4.1 REDUCING THE NUMBER OF STRUCTURAL ELEMENTS

The second structure of the support frame was developed after the model described in Section 2.3.1.1. New structure is presented in **Fig. 2.12**. Instead of triangular cells for every mirror

it was proposed to have parallel bars in every zone of structure to collocate several mirrors. As for the first prototype and for the second prototype the structure has six zones (hexagon shape); so, the structure in the both cases have six external sides. In **Fig. 2.12, *a*** is presented the structure from parallel bars. In **Fig. 2.12, *b*** one zone with screws (black points) that are used to fix the triangular mirrors. The same scheme is used for all six triangular zones of concentrators [35].

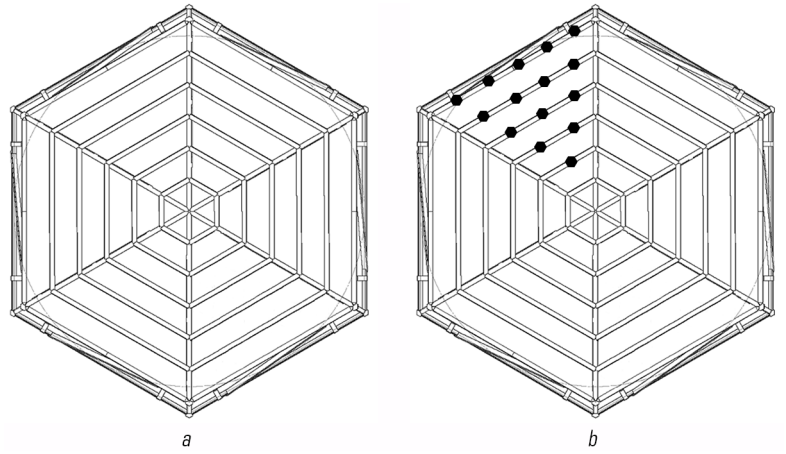

Fig. 2.12 The second structure model:
a – structure from parallel bars; *b* – one zone with screws (black points)

In **Fig. 2.13**, let's present the scheme of screw connection for mirrors with metallic elements that we use. This connecting node contains distance ring; washer (to protect mirror) and screw.

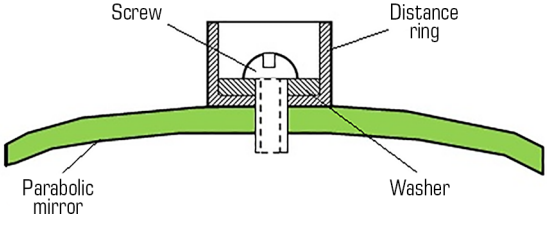

Fig. 2.13 Scheme of screw connection for mirrors

For the first model the number of metal structural elements has been calculated in case of seven parallel lines in every zone (**Fig. 2.9**). It was 3456 aluminium bars.

2.4.2 CALCULATION OF STRUCTURAL ELEMENTS

If to analyze the second model with seven lines we decrease by 56 the number of metal elements (in **Fig. 2.12** we demonstrate only six lines in every zone). In **Fig. 2.14**, let's present the structure with mirrors in one zone.

The total number of triangular mirrors *N* we can calculate as in equation (2.1). But the number of horizontal top bars, vertical bars, diagonal bars and horizontal low bars (**Fig. 2.7**) will decrease significantly.

In **Fig. 2.15**, let's present the simulation of the solar concentrator structure with flat triangular mirrors with new support frame.

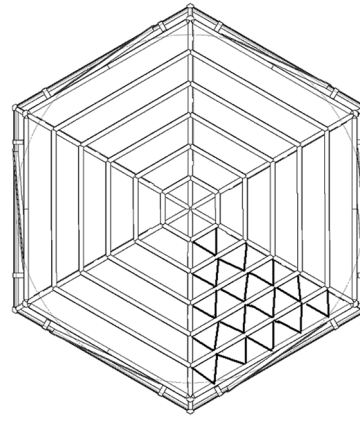

Fig. 2.14 Structure with mirrors

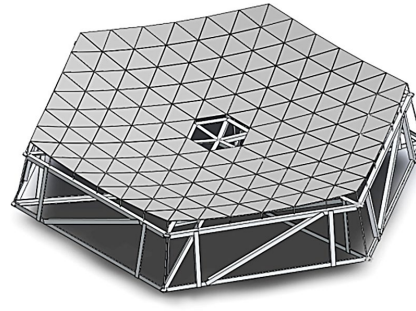

Fig. 2.15 The concentrator with the second structure model

For example, it is possible to analyze the situation with horizontal top bars. Number of bars in the center of prototype is not changed: six radial bars and six perimertric bars. In total, there are 12 bars in the center with length of triangular size *a*. With every new line the gain will be more significant. The primer line after center in the first prototype (**Fig. 2.9**) had $K_1=(7-1\cdot6=36$ bars with length of triangular size *a*.

In new version (**Fig. 2.12, 2.14**) line 1 has $K_2=(2\cdot6)l=12l+2a$ bars, where $l=2a$. If the first line has bar with length (*a*) the second line has the size of (2*a*). And every new line will have the size (*n*·*a*), where *n* is the number of lines.

It is possible to imagine the prototype with two lines. In this case for the first prototype $K_1=(11-2)\cdot6=54$ bars. For the second prototype $K_2=(3\cdot6)l+2a=18l+2a$ bars with length ($l=3a$).

If the frame has three lines for the first prototype $K_1=(15-3)\cdot6=72$ bars. For the second prototype $K_2=(4\cdot6)l+2a=24l+2a$ bars with length ($l=4a$) and so on.

This reducing of number of bars is described only for horizontal top bars. But if the vertical, diagonal and horizontal low bars analyzed too, the savings will be greater. In total, if for the first prototype it was said about thousands of structural elements, then in this new case it is only about tens elements.

If the structure contains six or seven lines in one zone, there is the solar concentrator from one to two meters of diameter. It is not heavy and can be carried, transported and installed in different places. The advantage of new model is less consumption of metal bars. So, in this case the solar concentrator will be light in comparison with the weight of previous one.

2.5 DISCUSSION

It was proposed the geometrical model of solar concentrator and the results of calculations with this model (equations (2.2) and (2.3)) demonstrated that it is possible to build solar concentrator with 1.6 meters of diameter to obtain sufficient energy for heating. Due to its small size and weight the concentrator can be easily transported and installed. This solar concentrator is possible to install on the roofs of the buildings as TV antennas.

The main result that was obtained is a development of new support structure for prototype of solar concentrator. New support structure (support frame) of a solar parabolic concentrator was developed to reduce the number of structural elements, and as consequence of this, to reduce the cost and make construction lighter and easier to automatic assembly (**Fig. 2.12, 2.14**).

This prototype, in comparison with the first model developed earlier (**Fig. 2.7, 2.8**), contains less metal elements in the structure. It is not necessary to construct the cell for every triangular mirror from metal elements as it was made in the first prototype. For mirror supporting is sufficient to have horizontal bars as it is presented in **Fig. 2.12, 2.14**.

Green energy is a future of energetic development. So, any contribution to the technological aspects of this solar energy capture process is very important.

It was developed and described new frame of solar concentrator prototype in what the parabolic surface was approximated by triangular plane mirrors. After analysis of the first model of solar concentrator the possibilities for its improving were found. The first prototypes are presented in **Fig. 2.7, 2.8**. For the comparison the new structure is presented in **Fig. 2.12, 2.14**. The new structure has advantages compared to the previous version. For example, fewer structural elements that allows for easier assembly process. Fewer automation steps result in shorter build times. Also, in this case, the prototype structure becomes lighter. It is easier to transport and install this compact solar concentrator prototype with diameter of 1.6 meters.

This new structure is more convenient for automation of the assembly process of solar concentrators in future.

The parabolic solar concentrators provide a clean, inexpensive source of thermal energy for a wide range of applications, including industrial process heat, space heating and cooling, hot water, water desalination and purification, and remote and distributed power applications.

The proposed solar concentrators can be used directly to produce heat energy. To produce electrical energy, it is necessary to use Stirling thermal motor or Ericsson motor in focal point to convert heat energy to electricity.

The proposed solar concentrators can be used for different applications, for example, for green buildings in rural areas, or for chemical reactors to accelerate the chemical process of organic waste processing. Other application is to use solar concentrators in combination with agricultural fields. These solar concentrators can be used with small scale TES. Using TES, it is possible to make power plants for green buildings. Small solar power plants can support all the energy demands of residential houses.

The limitations of the study that must be taken into account when trying to apply in practice are connected with necessity to develop or to adapt existing sun tracking system, which can increase the efficiency of solar concentrator system. It is important to investigate as well as in further theoretical studies of solar concentrator systems to improve their structure and work.

CONCLUSIONS

1. In comparison with existed models of solar concentrators it was proposed the concentrator from one meter of diameter to two meters of diameter that is less than it is known from literature (for example, 9 meters). It was demonstrated with geometrical model that diameter of 1.6 meters is sufficient to produce thermal energy. The number of structural elements was more than three thousand elements.

2. The new model of support frame of solar concentrator was proposed. The result is a decreased number of structural metal elements. New design of frame structure is presented which contains less metal elements and it is lighter in comparison with previous one and more convenient for automatic assembly process. Instead of thousands of structural elements as for the first prototype in this case we are talking about several tens. The disadvantage is connected with the size of elements. For the

first concentrator all elements are unified; there are only three types. For the second solar concentrator there are different elements with different sizes but there are much fewer of them. The cost of the both types of concentrators is small because of using the flat triangular mirrors. With this investigation the cost of solar concentrator can decrease even more. It was proposed the scheme of screw connection for mirrors with metallic elements. This connection method is safe and reliable.

FINANCING

This research was partly supported by the project UNAM-DGAPA-PAPIIT IT 102320.

ACKNOWLEDGMENTS

We thank Dra. Graciela Velasco Herrera for their comments on the text of this article and the master's and PhD students that help us in different aspects of investigation.

REFERENCES

1. Market Overview (2021). Energy Information Administration (EIA). International Energy Agency (IEA). Available at: https://www.solarflux.co/markets/
2. Kussul, E., Baydyk, T., Mammadova, M., Rodriguez Mendoza, J. L. (2022). Solar concentrator applications in agriculture. Energy facilities: management and design and technological innovations. Kharkiv: PC TECHNOLOGY CENTER, 177–207. https://doi.org/10.15587/978-617-7319-63-3.ch5
3. Renewable energy solutions. Suncatcher Energy. Available at: https://suncatcherenergy.com/ Last accessed: 12.01.2024
4. Solar Energy for Homes, Businesses, and Farms. Suncatcher Solar. Available at: https://suncatchersolar.com/ Last accessed: 12.01.2024
5. Kousksou, T., Bruel, P., Jamil, A., El Rhafiki, T., Zeraouli, Y. (2014). Energy storage: Applications and challenges. Solar Energy Materials and Solar Cells, 120, 59–80. https://doi.org/10.1016/j.solmat.2013.08.015
6. Kussul, E., Baydyk, T., Curtidor, A., Herrera, G. V. (2023). Modeling a system with solar concentrators and thermal energy storage. Problems of Information Society, 14 (2), 15–23. https://doi.org/10.25045/jpis.v14.i2.02
7. Harada, K., Yabe, K., Takami, H., Goto, A., Sato, Y., Hayashi, Y. (2023). Two-step approach for quasi-optimization of energy storage and transportation at renewable energy site. Renewable Energy, 211, 846–858. https://doi.org/10.1016/j.renene.2023.04.030

8. Gil, G. O., Chowdhury, J. I., Balta-Ozkan, N., Hu, Y., Varga, L., Hart, P. (2021). Optimising renewable energy integration in new housing developments with low carbon technologies. Renewable Energy, 169, 527–540. https://doi.org/10.1016/j.renene.2021.01.059
9. Erdiwansyah, Mahidin, Husin, H., Nasaruddin, Zaki, M., Muhibbuddin. (2021). A critical review of the integration of renewable energy sources with various technologies. Protection and Control of Modern Power Systems, 6 (1). https://doi.org/10.1186/s41601-021-00181-3
10. Heard, B. P., Brook, B. W., Wigley, T. M. L., Bradshaw, C. J. A. (2017). Burden of proof: A comprehensive review of the feasibility of 100% renewable-electricity systems. Renewable and Sustainable Energy Reviews, 76, 1122–1133. https://doi.org/10.1016/j.rser.2017.03.114
11. Sebestyén, V. (2021). Renewable and Sustainable Energy Reviews: Environmental impact networks of renewable energy power plants. Renewable and Sustainable Energy Reviews, 151 (6), 111626. https://doi.org/10.1016/j.rser.2021.111626
12. Sahoo, S. K. (2016). Renewable and sustainable energy reviews solar photovoltaic energy progress in India: A review. Renewable and Sustainable Energy Reviews, 59, 927–939. https://doi.org/10.1016/j.rser.2016.01.049
13. Pranesh, V., Velraj, R., Kumaresan, V. (2022). Experimental investigations on a sensible heat thermal energy storage system towards the design of cascaded latent heat storage system. International Journal of Green Energy, 20 (1), 63–76. https://doi.org/10.1080/15435075.2021.2023879
14. Tiwari, G.N., Tiwari, A., Shyam (2016). Solar Concentrator. Handbook of Solar Energy. Theory, Analysis and Applications. Springer, 247–291. https://doi.org/10.1007/978-981-10-0807-8_6
15. Crider, J. (2024). Clean Technika, Solarflux FOCUS Parabolic Dish Concentrator Converts 72 % Of Solar Energy Into Usable Heat. Available at: https://cleantechnica.com/2021/08/05/solarflux-focus-parabolic-dish-concentrator-converts-72-of-solar-energy-into-usable-heat/
16. Kussul, E., Baidyk, T., Makeyev, O. et al. (2007). Development of Micro Mirror Solar Concentrator. The 2-nd IASME/WSEAS International Conference on Energy and Environment (EE'07), Portoroz (Portotose), 294–299. Available at: https://www.wseas.org/multimedia/books/2007/energy-and-environment-2007.pdf
17. Baydyk, T., Kussul, E., Bruce, N. (2014). Solar chillers for air conditioning systems. Renewable Energy and Power Quality Journal, 1 (12), 223–227. https://doi.org/10.24084/repqj12.290
18. Change the World We Live In. Available at: http://www.anzses.org Last accessed: 15.23.2023
19. Johnston, G. (1998). Focal region measurements of the 20m2 tiled dish at the Australian National University. Solar Energy, 63 (2), 117–124. https://doi.org/10.1016/s0038-092x(98)00041-3
20. Kussul, E., Makeyev, O., Baidyk, T., Blesa, J. S., Bruce, N., Lara-Rosano, F. (2011). The Problem of Automation of Solar Concentrator Assembly and Adjustment. International Journal of Advanced Robotic Systems, 8 (4). https://doi.org/10.5772/45685

21. Kussul, E., Baydyk, T., Mammadova, M., Rodriguez, J. L. (2022). Development of a model of combination of solar concentrators and agricultural fields. Eastern-European Journal of Enterprise Technologies, 6 (8 (120)), 16–25. https://doi.org/10.15587/1729-4061.2022.269106
22. Temirlan, E. (2022). Design and study of solar spiral receivers using computer simulation [Master degree thesis].
23. Luvela, M. (2015). Solar Stirling Engine Efficiency Records Broken by Ripasso Energy. Available at: https://www.greenoptimistic.com/solar-stirling-engine-ripasso/#:~:text=They%20have%20designed%20a%20Solar,the%20solar%20energy%20into%20electricity
24. Pane, C. (2023). Is this the world's most efficient solar system? Inhabitat. Available at: https://inhabitat.com/this-solar-power-system-converts-twice-as-much-of-the-suns-energy-as-existing-technology/
25. Highly Efficient Solar Thermal Energy Technology (2021). Available at: https://www.solarflux.co/product/
26. ZED Solar Limited (2016). Available at: https://zedsolar.com/
27. Solar Invictus 53E. Parabolic Tracking Solar Concentrator for Use with a Stirling Engine AEDesign. Available at: https://www.aedesign.com.pk/energySolarInvictus53E.html
28. El Disco Stirling EuroDish de la Escuela Superior de Ingenieros de Sevilla, https://biblus.us.es/bibing/proyectos/abreproy/4801/fichero/3.+Cap%C3%ADtulo+1.pdf
29. EuroDish. Available at: https://www.psa.es/es/instalaciones/discos/eurodish.php
30. Mammadova, M., Baydyk, T., Kussul, E. (2022). Solar concentrators in combination with agricultural fields: Azerbaijan and Mexico. 10. European Conference on Renewable Energy Systems. Istanbul, 342–348.
31. Baydyk, T., Mammadova, M., Kussul, E., Herrera, G., Curtidor, A. (2022). Assessment of the impact of the combination of crops with solar concentrators on their productivity. Problems of Information Society, 13 (1), 11–18. https://doi.org/10.25045/jpis.v13.i1.02
32. Hamed, A. M. (2003). Desorption characteristics of desiccant bed for solar dehumidification/humidification air conditioning systems. Renewable Energy, 28 (13), 2099–2111. https://doi.org/10.1016/s0960-1481(03)00075-2
33. Solar Energy Dehumidification Experiment on the Citicorp Center Building (1997). Final Report Prepared for NSF, Energy Laboratory, Massachusetts Institute of Technology, Report No. MIT-EL 77-005, 176.
34. Solar constant. Available at: https://en.wikipedia.org/wiki/Solar_constant Last accessed: 07.01.2024
35. Baydyk, T., Mammadova, M., Velasco, G., Kussul, E. (2024). Improvement of solar concentrator structure. Eastern-European Journal of Enterprise Technologies, 2 (8 (128)), 38–45. https://doi.org/10.15587/1729-4061.2024.301538

DOI:10.15587/978-617-8360-02-3.CH3

Yurii Sniezhkin, Zhanna Petrova, Vadym Paziuk,
Viacheslav Mykhailyk, Tetiana Korinchevska, Kateryna Samoilenko
© The Author(s) 2024. This is an Open Access chapter distributed under the terms of the CC BY-NC-ND license

CHAPTER 3

TECHNOLOGICAL ASPECTS OF PRODUCING REFUSE DERIVED FUEL

ABSTRACT

The involvement of municipal solid waste in the energy balance of Ukraine is one of the important ways of replacing fossil fuels and solving environmental problems related to the disposal of waste in proving ground and landfills.

The purpose of the research is to find a rational composition of an alternative solid fuel for burning in cogeneration power plants and an energy-efficient technology for its production.

The object of research is alternative solid fuel (RDF – refuse derived fuel) based on combustible components of municipal solid waste.

The kinetics of convective drying of RDF of different composition depending on the temperature and rate of heat carrier was investigated. The relative and kinetic coefficients of drying, generalized drying rates for each drying period and the calculated duration of the drying process for different compositions of RDF were determined.

The thermal decomposition of various refuse derived fuel mixtures was investigated using thermal analysis methods. Temperatures of dehydration, thermal decomposition of organic and mineral substances are determined. Data were obtained on the content of water, organic and mineral substances, and ash in RDF of various compositions. The rates of thermal destruction in different phases of heating were calculated, the kinetics of decomposition and heat generation during the thermal decomposition of organic substances were compared. The calorific value of RDF of different composition was determined by the method of calorimetry.

KEYWORDS

Municipal solid waste, technology, RDF, drying, thermal analysis, calorific value of solid fuel.

Among the technologies of energy use of municipal solid waste, the most common and one of the most effective is the technology of burning this waste in cogeneration plants with the production of electrical and thermal energy.

Obtaining highly efficient composite fuels based on solid household waste is of considerable scientific interest as it requires the development of appropriate energy-saving technologies.

Analysis of technological stages of RDF (refuse derived fuel) production showed that all stages of production are energy consuming. The drying stage is characterized by particularly high energy consumption. Drying processes account for about 40–50 % of the total energy consumption, and in cases of drying municipal solid waste (MSW) with high humidity, the consumption increases to 70 %. Low energy efficiency is characteristic of the stages of raw material preparation, which affects the energy efficiency of production in general and the cost of fuel.

Therefore, research and identification of factors influencing the processes of raw material preparation and drying will improve the quality of fuel and ensure a sustainable year-round production cycle. Study of methods for preparing raw materials for drying and modeling the kinetics of dehydration in drying machines will allow to develop ways and directions of energy saving.

Increasing the calorific value of composite fuel based on MSW requires combining components, the physical and chemical properties of which are not sufficiently studied. Combustion of RDF also requires knowledge of kinetics of thermal decomposition of components and generation of heat.

The analysis of the results of research into various aspects of the proposed technology for burning fuel from municipal solid waste in cogeneration plants indicates the need to carry out a complex of research to components of this technology and, above all, technologies for obtaining RDF and its burning.

Simultaneously with the involvement of municipal solid waste in the energy industry, environmental problems related to the disposal of waste in proving ground and landfills, which leads to catastrophic pollution of air, soil, surface and groundwater, will be solved. Due to the expected decrease in the number of proving ground and landfills, the volume of greenhouse gas emissions will decrease.

3.1 ANALYTICAL REVIEW AND ANALYSIS

3.1.1 MUNICIPAL SOLID WASTE AND FUEL FROM IT

Incorrectly utilized municipal solid waste (MSW) harms the environment and human health, and also takes up too much land.

Traditional methods of disposal and treatment of MSW include landfill, incineration and biological treatment. However, these methods have certain disadvantages [1, 2]. Even well-planned and managed landfills can become problematic from an environmental and public perception perspective [3]. The European Commission requires reductions in landfilling to prevent or reduce negative impacts on the environment, including pollution of surface water, groundwater, soil and air, as well as the global environment, including the greenhouse effect [4].

One of the perspective and important ways to solve this problem is to use municipal solid waste as fuel.

Fuel from waste (RDF) – this is an alternative solid fuel that contains the combustible part of household or industrial harmless waste remaining after the separation of secondary raw materials [5]. Secondary raw materials usually make up 20–40 mass % of MSW [6]. The ratio of RDF production to MSW is about 24 %, which means that only 240 kg of RDF can be extracted from one ton of municipal waste [7]. RDF is a cheaper fuel than conventional fossil fuels, and the higher calorific value of dried RDF depends on the composition of the components and ranges from 17–25 MJ/kg. The composition mainly includes polymer materials that cannot be recycled, paper, cardboard, textiles, packaging waste, wood waste, etc. [8]. Unlike direct MSW incineration, RDF incineration has higher efficiency due to higher calorific value and less negative impact on the environment.

One of the main indicators that limit the use of RDF is greenhouse gas emissions. When coal to replace on RDF, the water content should be less than 15 %. In this case, the net emission reduction is 0.4 tons of CO_2/ton of coal [9]. In most cases, RDF is co-fired with biomass to reduce the total amount of recorded CO_2 emissions, as biomass is considered carbon neutral [10, 11].

Such fuel is usually used in cement furnace, boilers and for electricity production [5]. Electric power stations and cement plants burn RDF mainly by blending it with coal or biomass [19, 20, 21]. According to reports [12], in Europe, between 30 % and 60 % of fossil and alternative fuels have been replaced by RDF in cement and waste processing plants. In 2015, RDF consumption in Europe was 12 million tons [13]. Other energy carriers, such as fuel oil and gases, are obtained from RDF through pyrolysis and gasification processes [14].

If the fuel passes the test and meets the requirements set forth in the DSTU EN 15359 [15], it is classified as a solid recovered fuels (SRF). The standard states that SRF is produced from non-hazardous waste. Raw materials for fuel can be industrial waste, municipal solid waste, industrial waste, commercial waste, construction and demolition waste, sewage sludge, etc. The goal of producing solid recovered fuel is to use it to produce energy with the highest possible energy efficiency. This is facilitated by a clearly defined system of classification and specification.

The classification system is based on three main characteristics – economic (lower calorific value), technical (chlorine content) and environmental (mercury content). The characteristics are chosen to give the interested party an immediate but simplified view of the fuel in question. Only fuel derived from non-hazardous waste that meets European SRF standards can be classified as SRF.

The classification (**Table 3.1**) for SRF is based on limit values for three important fuel characteristics:

a) average value of lower calorific value (ar);

b) average value of chlorine content (d);

c) median and 80th percentile for mercury content (ar).

Each characteristic is divided into 5 classes. For the SRF must be assigned a class number from 1 to 5 for each characteristic. The combination of class numbers makes up the class code. The features are of equal importance, so no class number defines the code. The classes were defined as a tool for the identification and pre-selection of SRF.

Table 3.1 Classification system for solid recovered fuels

Classification characteristic	Statistical measure	Unit	Classes				
			1	2	3	4	5
Net calorific value (NCV)	Mean	MJ/kg (ar)	≥25	≥20	≥15	≥10	≥3
Chlorine (Cl)	Mean	% (d)	≤0.2	≤0.6	≤1.0	≤1.5	≤3
Mercury (Hg)	Median 80th percentile	mg/MJ (ar) mg/MJ (ar)	≤0.02 ≤0.04	≤0.03 ≤0.06	≤0.08 ≤0.16	≤0.15 ≤0.30	≤0.50 ≤1.00

*Note: *Median is a number that "divides" "in half" an ordered collection of all sample values, i.e. the average value of a variable characteristic, which is in the middle of a series arranged in ascending or descending order of the characteristic.*
***Percentile is the value that a given random variable does not exceed with a fixed probability given as a percentage. Thus, the n-th percentile is the same as n/100*

3.1.2 TECHNOLOGIES OF OBTAINING RDF/SRF

Fuel from waste is obtained according to the requirements of the end user. According to the composition, RDF is divided into two types – those that don't contain organic wastes and those that contain it. In the production of the first type of RDF, metals and inert substances are removed from municipal solid waste, and the organic fraction is screened and composted. A product with a high calorific value is obtained, which mainly consists of plastic, paper and textiles [16]. Another type of RDF is made from the same residual waste composition, but includes organics that become part of the RDF through a process of "biostabilization" or "biodrying". This process allows the organics to go through a partial composting process without adding moisture. Since composting is an exothermic process, the heat from partial composting dries out the material and oxidizes the decaying organic fraction while keeping the other organic matter intact. Then this biostabilized material is mechanically processed through several grading steps to achieve the specific size required to produce the desired RDF. The level of mechanical processing depends on the fuel specifications for the combustion technology used by the RDF end user [16, 17].

In terms of physical characteristics, RDF can be manufactured as bulk or granular materials [17]. This depends on several factors, including the proximity of the production unit to the final consumer, the need to store the material before its use and the type of power system of the incineration facility [16].

Municipal solid waste processing technologies with the production of RDF can be conditionally divided into four groups according to the characteristics of the raw materials (**Table 3.2**) [18]. Given the number of potential products, the type of specific technology used to convert solid waste into RDF may vary from one location to another [19].

Technologies for the direct production of RDF/SRF include the following main stages: sorting, grinding, separation, mixing, drying, granulation and packaging. In general, the technological scheme of fuel production from waste is presented in **Fig. 3.1** [20].

Table 3.2 Brief description of key technologies of waste processing [18]

Features \ Production technology	Clean material recovery facility	Dirty material recovery facility	Mechanical biological treatment	Mechanical heat treatment
Feedstock	Mixed/Commingled recyclables (Municipal & Commercial)	Mixed Residual Waste (Mainly C&D municipal & commercial waste)	Mixed putrescible residual waste (mostly municipal)	Mixed residual wastes (Municipal and Commercial)
Product/outputs	– Separated recyclable materials: paper, cardboard, plastics, glass, steel and aluminum. – Glass fines for potential further processing. – Light residuals-potential RDF. – Residual to landfill	– Separated recyclable materials including paper, cardboard, plastics, glass, steel, aluminum, masonry product, soil, timber. – RDF. – Residuals to landfill	– Low grade soil amendment/compost. – Recyclable material including rigid plastics, steel and aluminum. – RDF. – Residuals to landfill	– Organic rich fiber-low grade soil amender, fuel. – RDF from inorganic fraction-to thermal process. – Recyclables (low grade)

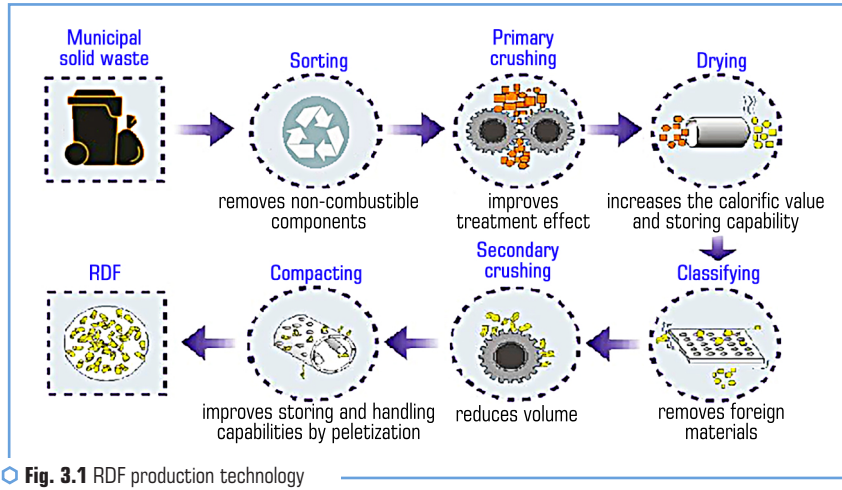

Fig. 3.1 RDF production technology

The steps and necessary equipment for the production of RDF are given below [17]:

1. *Waste reception, sampling, manual sorting and bag opening area:* MSW arriving by appropriate transport is unloaded for sampling, manual sorting of large components and transported to bag opening machines.

2. *Sorting* includes the separation of municipal solid waste into biodegradable, glass, textiles, paper, plastic, leather and rubber, metals and other hazardous municipal solid waste, as well as

inert materials. Secondary raw materials are extracted, which are then processed. The main components used in the production of RFD include directly combustible materials.

3. *Primary crushing:* the two-shaft primary crusher is designed for crushing residual waste to a size of less than 100 mm.

4. During *drying*, the material is dehydrated. This can happen both under the influence of solar radiation and in special dryers. This process increases the calorific value of the material, reduces the mass, and also increases the ability to store fuel for a long time.

5. A rotary drum is used *to separate* the material by size. Separation usually occurs in two or more stages of the process. This is done by passing the waste through drum screens, most often roller drums with different hole sizes. At various stages of processing, conveyor belts are attached to conveyor belts and positioned at an angle to allow oversized materials to pass over them. Remaining material is thrown onto the conveyor belt, which transports the material for further processing.

Magnetic separators are used to remove any metals from remaining material. The device uses eddy currents that create a powerful magnetic field that makes separation possible. The eddy current separator is applied to a conveyor belt that transports a layer of mixed waste. At the end of the conveyor belt is an eddy current rotor.

Fans on the air separation stage are used to create a column of air moving upwards. Light materials are blown up, and dense materials fall. Air carrying lightweight materials such as paper and plastic bags enters a separator where these items fall out of the air stream. The quality of separation at this stage depends on the strength of air currents and the method of introducing materials into the column. Moisture content is also critical, as water can weigh down some materials or cause them to stick together.

6. The two-roller secondary chopper is designed for *secondary crushing* of material to a thickness of less than 50 mm. After that happens finer crushing to an RDF particle size of less than 25 mm.

7. *The compacting* of material is intended for the production of fuel pellets with a diameter of 16–25 mm by extrusion. The crushed material is fed into the granulator by gravity. The roller pushes the material through holes of the die and extrudes the material. The knife under the press die can adjust the size of the granules. Then the granules are cooled on a cooling conveyor and sent to storage.

The choice of municipal solid waste processing technology directly depends on the characteristics of the waste. The defining characteristics are the morphological, fractional and chemical composition, density, heat of combustion and moisture content of municipal solid waste [11]. These characteristics depend on the place and time of waste generation. The average annual morphological composition for large cities of Ukraine is presented in **Fig. 3.2** [22].

The largest share is food waste, which has high moisture content and low calorific value, so it is not recommended to use it for the production of RDF. If the non-combustible components to separate, it is possible to predict the composition of fuel that can be obtained in large cities of Ukraine. In this case, RDF can contain polymer materials, paper and cardboard, textiles, wood, leather and rubber (**Fig. 3.3**).

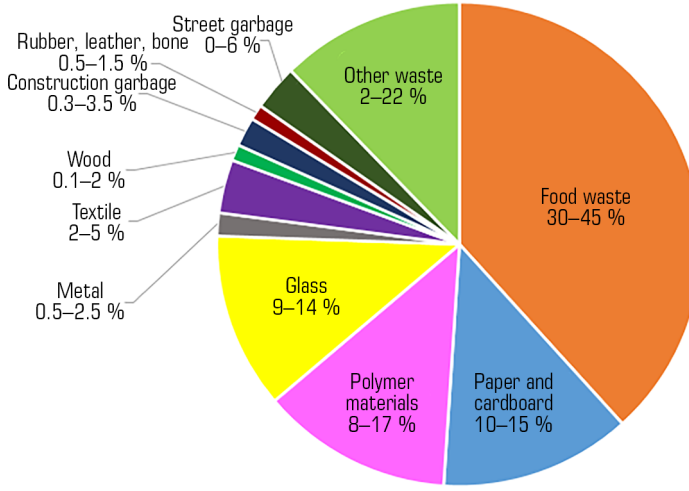

Fig. 3.2 Morphological composition of MSW for large cities of Ukraine

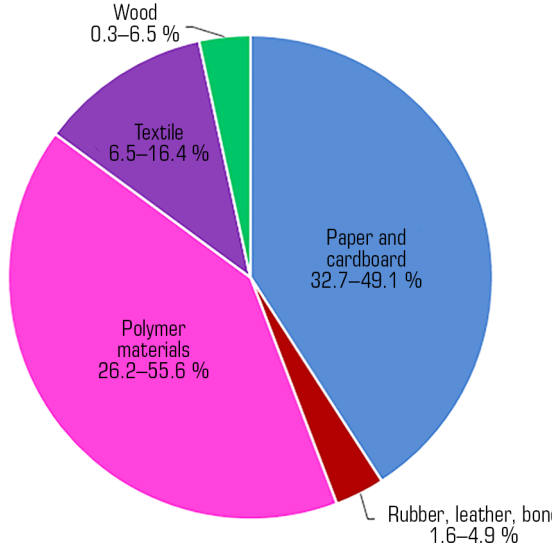

Fig. 3.3 Average morphological composition of combustible solid waste, which can be raw materials for RDF

Analysis of technological stages of RDF production showed that all stages of production are energy consuming. The drying stage is characterized by particularly high energy consumption. Drying processes account for about 40–50 % of the total energy consumption, and in cases of drying municipal solid waste with high humidity, the consumption increases to 70 %. Low energy efficiency is characteristic of the stages of raw material preparation, which affects the energy efficiency of production in general and the cost of fuel. Thus, about 10–20 % of the total energy consumption is spent on crushing.

Granulation is the final stage of solid fuel production and 10–30 % of total energy is spent on its implementation. Granulation costs depend on the physico-mechanical and physico-chemical properties of the fuel components, pressure and temperature in the compaction zone. Due to the insufficient amount of experimental data on the physico-chemical and physico-mechanical properties of municipal solid waste, there may be energy overspending during the production of fuel from this type of raw material.

Therefore, research and identification of influencing factors on raw material preparation and drying processes will improve fuel quality and ensure a stable year-round production cycle. The study of methods of preparing raw materials for drying and modeling the kinetics of dehydration in drying devices will allow to develop ways and directions of energy saving.

Increasing the calorific value of composite fuel based on MSW requires combining components, the physical and chemical properties of which are not sufficiently studied. Combustion of RDF also requires knowledge of kinetics of thermal decomposition of components and generation of heat.

The efficiency of using RDF is determined by obtaining its characteristics during the combustion process. The results of the thermal analysis, as well as the determination of the calorific value, are important.

3.2 STUDY OF REGULARITY OF RDF CONVECTIVE DRYING

3.2.1 PREPARATION OF MUNICIPAL SOLID WASTE FOR DRYING

1. The composition of municipal solid waste in Ukraine was analyzed, among which RDF was allocated (40 % of the total mass of waste). The main components are highlighted: wood, textile materials, polymer materials, paper, cardboard, leather, rubber, bones.

2. 4 types of mixtures are made from 5 groups of materials, including: wood (5 – 23 %), textile materials (12 – 16 %), polymer materials (25 – 50 %), paper, cardboard (25 – 50 %), leather, rubber, bones (3 – 4 %) (**Table 3.3**).

3. The initial moisture content of the obtained mixtures was determined, which is from 5 to 6 %, which depends on the composition.

4. The mixtures were dried to a completely dry mass at a coolant temperature of 150 °C and duration of 4 hours for the subsequent uniform moistening of these mixtures.

Table 3.3 Composition of RDF (100 g)

The name of the component RDF	Composition of mixtures, %/g			
	I mixture	II mixture	III mixture	IV mixture
Wood (pine)	23	5	5	5
Textile materials (cotton, synthetic fabrics)	12	15	16	16
Polymer materials (PET bottles, polyethylene film)	31	40	50	25
Paper, cardboard	31	37	25	50
Skin, rubber, bones	3	3	4	4

5. Before conducting research, it is possible to determine the initial moisture content of RDF. The RDF mixture is placed into boxes and dried in a laboratory dryer for 5 hours at a temperature of 105 °C. After drying, the boxes are removed from the laboratory dryer and placed in a desiccator to cool for 15–30 minutes. Cooled boxes with material are weighed in a closed state on scales.

The moisture content of the material relative to the mass of the dry substance is calculated as a percentage:

$$W = \frac{m_2 - m_3}{m_3 - m_1} \cdot 100\ \%, \tag{3.1}$$

where m_1 – mass of the empty box (with a lid), g; m_2 – mass of the box with the research sample before drying, g; m_3 – mass of the box with research sample after drying, g.

6. Research on the drying of RDF samples begins with setting the drying mode on a convective stand [23], then the sample is placed on a grid of scales in the drying chamber, and a computer program for collecting and processing information is turned on, which continuously records the time and change in the mass of the sample, the heat carrier temperature and the temperature in the middle of sample.

7. After drying, RDF samples are removed from the drying chamber and analyzed for quality characteristics and the final moisture content of the material is determined according to item 5 and formula (3.1).

8. After determining the absolutely dry mass of the sample, the computer program determines the current moisture content of the material W during drying and calculates and plots drying curves and drying rates: $W=f(\tau)$, $dW/d\tau=f(W)$.

9. The characteristics are calculated using a specially developed program "Sooshka".

10.1. Kinetic of the drying process:

$$W(t) = \frac{G(t) - G_{a.d.}}{G_{a.d.}} \cdot 100\ \%, \tag{3.2}$$

where $G(t)$ – calculations of mass of sample, g; $G_{a.d.}$ – absolutely dry mass, g.

10.2. The drying speed is determined:

$$N = \frac{dW}{d\tau}. \tag{3.3}$$

10.3. The drying temperature coefficient is an estimate of the derivative of the average temperature of the sample from the moisture content:

$$b = \frac{dt_{aver}}{dU}, \tag{3.4}$$

where $U = W/100$ – moisture content of the sample, %; $t_{aver.}$ – calculated as the average value of the temperature calculation on the surface and in the sample material, °C.

10.4. Rebinder number is equal to the ratio of the amount of heat expended to heat the body to the amount of heat to evaporate moisture in an infinitesimally small period of time:

$$Rb = \frac{c}{r} b, \tag{3.5}$$

where c – specific heat capacity of the material, kJ/(kg·°C); r – specific heat of phase transformation, kJ/kg.

10.5. The heat flux per unit surface of the sample is calculated from the ratio:

$$q(\tau) = rg\left(\frac{dU}{d\tau}\right)(1 + Rb), \tag{3.6}$$

where $g = G_{a.d.}/S_m$ – the ratio of the mass of absolutely dry body to the surface of the material.

10.6. The heat transfer coefficient is determined by the formula:

$$\alpha = \frac{1000 \cdot q(\tau)}{t - \theta}, \tag{3.7}$$

where t – heat carrier temperature; θ – sample temperature.

3.2.2 RESEARCH OF DRYING MODES OF RDF

The study of drying modes is carried out with the determination of the influence of the following factors: the heat carrier temperature (80–120 °C), the speed of movement of the heat carrier (1.5–2.5 m/s) and the composition of the mixture (No. 1–4).

The influence of heat carrier temperature on the kinetic of the drying process. When the temperature of the heat carrier increases from 80 to 120 °C, the drying duration is accelerated by 56 %.

eating of the material in a layer of 15 mm to the final temperature takes place within 10–15 minutes. The material at a heat carrier temperature of 80 °C heats up to a temperature of 78.8 °C, at a temperature of 100 °C – 98.9 °C, at a temperature of 120 °C – 119.8 °C (**Fig. 3.4**).

The process of drying municipal solid waste is in 2 stages: a period of heating up to the maximum drying speed and a period of falling drying speed (**Fig. 3.5**).

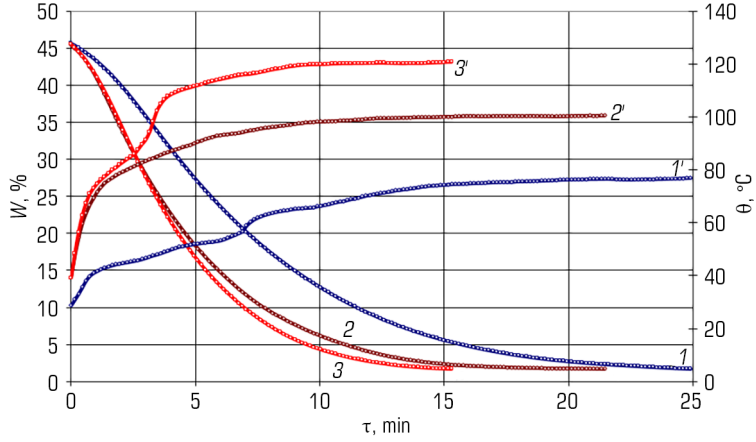

Fig. 3.4 Effect of heat carrier temperature on the kinetics of the RDF drying process: V=2.5 m/s, d=10 g/kg dry air, δ=15 mm, mixture No. 1: 1, 1′ – 80 °C; 2, 2′ – 100 °C; 3, 3′ – 120 °C

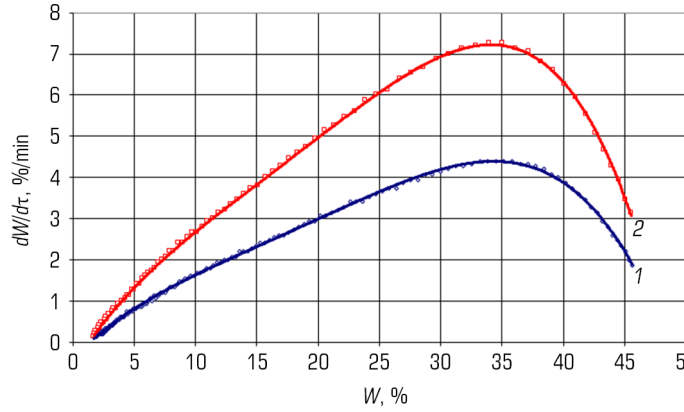

Fig. 3.5 Influence of heat carrier temperature on RDF drying speed V=2.5 m/s, d=10 g/kg dry air, δ=15 mm, mixture No. 1: 1 – 80 °C; 2 – 120 °C

To compare the effect of coolant temperature on the drying speed of RDF mixtures, heat carrier temperatures of 80 and 120 °C were selected. The maximum drying speed increases by 1.82 times when the heat carrier temperature increases (**Fig. 3.5**).

The influence of the heat transfer speed on the kinetics of the drying process. Conducted studies of the effect of temperature on the kinetics of drying process showed that increasing the heat carrier temperature to 120 °C significantly intensifies the drying process. Therefore, the effect of the speed of movement of the heat carrier on the kinetics of the drying process is carried out at a temperature of the heat carrier of 120 °C. To compare the speeds of movement of heat carrier, speeds of 1.5 and 2.5 m/s were selected.

Increasing the heat carrier speed from 1.5 to 2.5 m/s reduces the drying time by 6 minutes or by 38 %. The heating temperature of the material at a heat carrier speed of 1.5 m/s is 115 °C, which is 4.8 °C lower than the heat carrier speed of 2.5 m/s (**Fig. 3.6**).

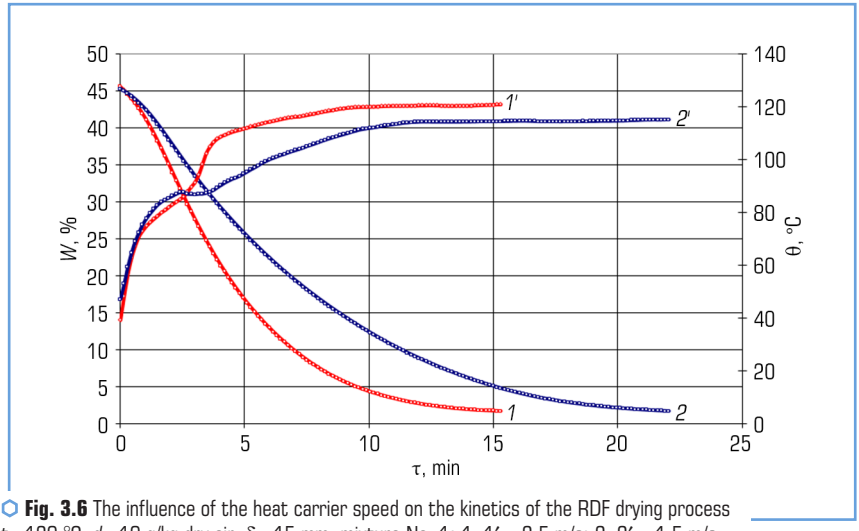

Fig. 3.6 The influence of the heat carrier speed on the kinetics of the RDF drying process t=120 °C, d=10 g/kg dry air, δ=15 mm, mixture No. 1: 1, 1′ – 2.5 m/s; 2, 2′ – 1.5 m/s

The influence of the RDF mixture composition on the kinetics of drying process. According to **Table 3.3**, there are 4 types of RDF mixtures that can significantly affect the kinetics of the drying process.

To study the kinetics of the drying process, it is possible to choose the drying mode studied earlier: coolant temperature 120 °C, coolant movement speed 2.5 m/s.

The analysis of the influence of the composition of RDF mixture on the kinetics of the drying process showed that it is appropriate to separate the comparison of mixtures No. 1, 2, 3 and No. 1, 4. The duration of drying of mixtures No. 1, 2, 3 (with the content of polymeric materials

from 31 to 50 %) is 16 minutes, but the heating of the material occurs in different ways, which is connected with the composition of solid fuel. Thus, the final heating temperature of mixture No. 1 is 119.8 °C, mixture No. 2 is 116.7 °C, and mixture No. 3 is 117.6 °C (**Fig. 3.7**).

The influence of mixtures No. 1, 4 (with cardboard content from 31 to 50 %) on the kinetics of the drying process was also analyzed (**Fig. 3.8**). When changing mixtures from No. 1 to No. 4, the duration of drying increases by 28 %.

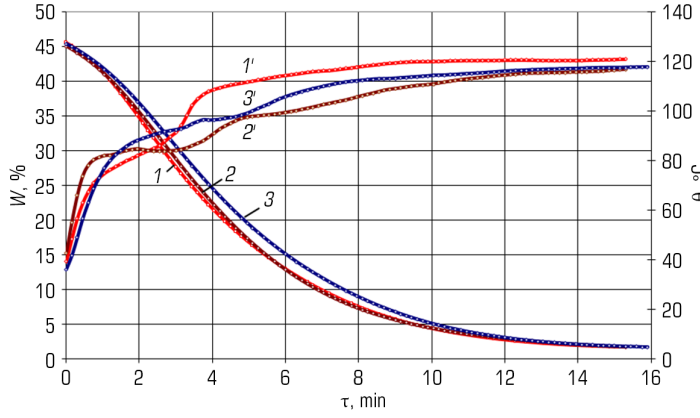

Fig. 3.7 Influence of the composition of mixture (1, 2, 3) on the kinetics of the RDF drying process t=120 °C, V=2.5 m/s, d=10 g/kg dry air, δ=15 mm: 1 – mixture No. 1; 2 – mixture No. 2; 3 – mixture No. 3

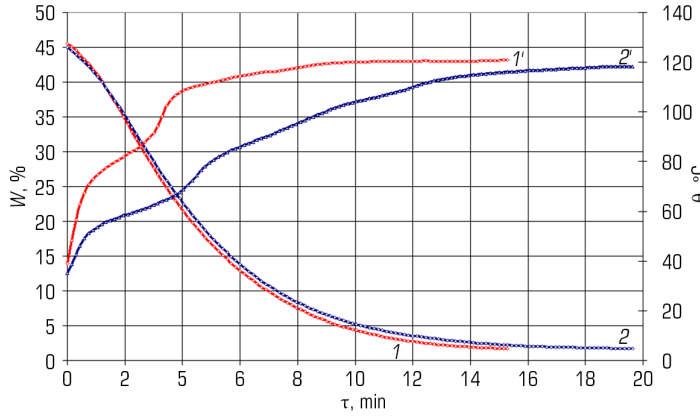

Fig. 3.8 Influence of the composition of the mixture (1,4) on the kinetics of the RDF drying process t=120 °C, V=2.5 m/s, d=10 g/kg dry air, δ=15 mm: 1 – mixture No. 1; 2 – mixture No. 4

3.2.3 RESEARCH OF HEAT AND MASS EXCHANGE PROCESSES DURING DRYING RDF

The kinetics of heat exchange during drying can be fully revealed by the data of the kinetics of moisture exchange.

Value of magnitude $d\bar{t}/d\bar{W}$ determines the change in the average temperature of the dried material per unit of change in its average humidity over an infinitesimally small period of time and is called the drying temperature coefficient:

$$b = \frac{d\bar{t}}{d\bar{W}}. \tag{3.8}$$

Magnitude b is a function of integral humidity $b = f\left(\bar{W}\right)$.

Based on the ratio of RDF heating and moisture evaporation, as can be seen from **Fig. 3.9**, the most appropriate drying mode is 100 °C.

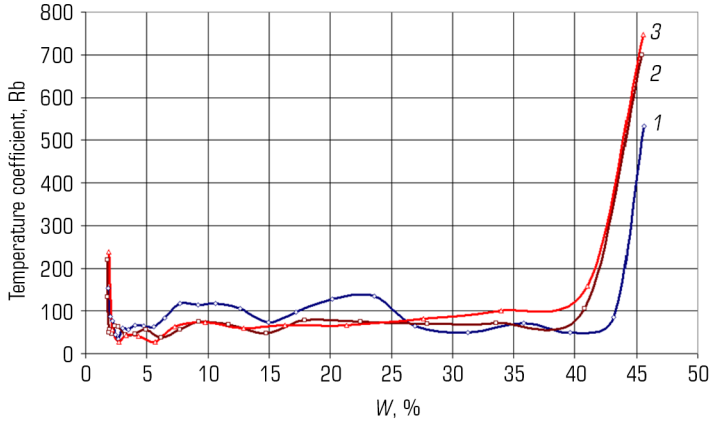

Fig. 3.9 Change in the temperature coefficient depending on the moisture content of the material and the heat carrier temperature during the RDF drying process V=2.5 m/s, d=10 g/kg dry air, δ=15 mm, mixture No. 1: 1 – 80 °C, 2 – 100 °C, 3 – 120 °C

General variable $b\left(\bar{c}/r\right)$ is an integral characteristic of the kinetics of the drying process. It determines the ratio heat amount of the heating of the material during drying and to the evaporation of moisture in an infinitesimally small period of time. This basic drying criterion is called the Rebinder number:

$$Rb = b\frac{\bar{c}}{r} = \frac{\bar{c}}{r}\left(\frac{d\bar{t}}{d\bar{W}}\right). \tag{3.9}$$

Rebinder criterion (**Fig. 3.10**) shows that heat is spent on heating the material at the beginning of RDF drying, then drying occurs with simultaneous heating and evaporation of moisture from the material to a moisture content of 3 %. At a humidity of 3 %, heat is inefficiently used, as the material is heated sharply with a decrease in the evaporation of moisture from the material.

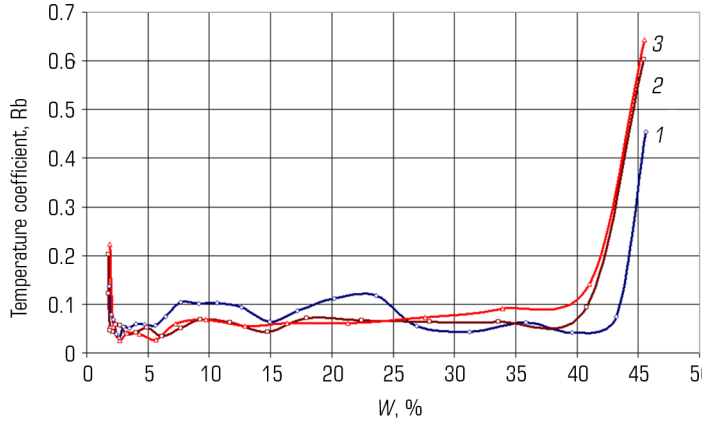

Fig. 3.10 Change of Rebinder criterion depending on material humidity and heat carrier temperature during RDF drying V=2.5 m/s, d=10 g/kg dry air, δ=15 mm, mixture No. 1: 1 – 80 °C, 2 – 100 °C, 3 – 120 °C

The heat supplied to the material is spent on heating the material and on the evaporation of moisture. The density of the heat flow spent on evaporation is calculated by the intensity of moisture exchange $m(\tau)$ from the equation:

$$q_{evap} = rm(\tau) = rg\frac{d\bar{W}}{d\tau}. \quad (3.10)$$

The heat flow density for heating the material is determined by the ratio:

$$q_{heat} = cg\frac{d\bar{t}}{d\bar{\tau}}, \quad (3.11)$$

where c – heat capacity of the material.

In accordance with the law of conservation of energy, the specific heat flow per unit surface of the body is equal to:

$$q(\tau) = rg\frac{d\bar{W}}{d\tau} + \bar{c}g\frac{d\bar{t}}{d\tau} = gr\frac{d\bar{W}}{d\tau}\left[1 + \frac{\bar{c}}{r}\frac{d\bar{t}}{d\bar{W}}\right]. \quad (3.12)$$

The heat flux density reaches its maximum value when the material is heated to the maximum value (**Fig. 3.11**). During the removal of moisture from the material, the heat flux density decreases.

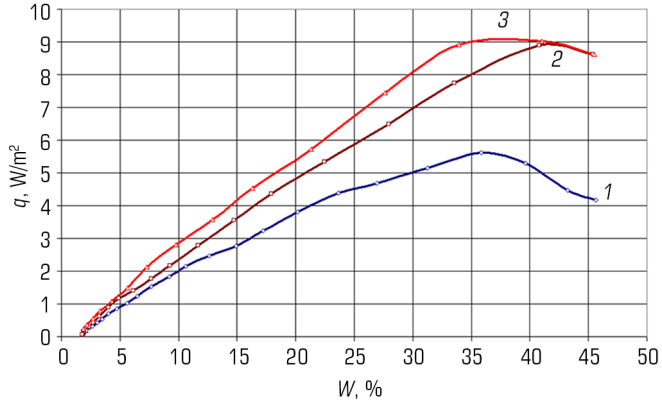

Fig. 3.11 Change in heat flux from material humidity and temperature of the heat carrier in the process of drying RDF V=2.5 m/s, d=10 g/kg dry air, δ=15 mm, mixture No. 1: 1 – 80 °C, 2 – 100 °C, 3 – 120 °C

The main conclusions based on the results of the experiments:

1. When the heat carrier temperature increases from 80 to 120 °C, the duration of drying decreases by 56 %.

2. Increasing the speed of heat carrier from 1.5 to 2.5 m/s at a temperature of 120 °C reduces the drying time by 6 minutes or by 38 %.

3. When changing the composition of the RDF mixture with a high content of polymer materials from 31 to 50 % to the RDF mixture with a high content of paper and cardboard from 31 to 50 %, the drying time increases by 28 %.

4. The study of heat and mass exchange processes during drying of RDF, in particular the temperature coefficient, the Rebinder number and the change in heat flow from the moisture content of the material when the temperature of the heat carrier changes from 80 to 120 °C, indicated the feasibility of drying above 100 °C. The maximum value of the heat flow at modes 100, 120 °C has a value of 9 W/m^2, which is 1.63 times higher than the drying mode 80 °C.

3.3 RDF THERMAL ANALYSIS

The efficiency of using RDF is ultimately determined during the combustion process. However, it is possible to predict fuel characteristics with the results of thermal analysis. Thermogravimetry

and differential thermal analysis contribute to expanding knowledge on the kinetics of thermal destruction and heat generation [24].

Research into the RDF characteristics is actively carried out around the world [11, 25, 26, etc.]. However, there are problems associated with quality assurance and accurate determination of the thermal characteristics of the fuel due to its heterogeneous composition. Also, fuel from waste of different composition has different kinetics of thermal destruction [11, 25–27]. Therefore, each type of RDF requires a study of thermal characteristics to predict its quality.

Combustion of RDF also requires a comprehensive study of its thermotechnical characteristics, in particular, the investigation of physicochemical properties, kinetics of thermal decomposition of the components and heat generation.

3.3.1 RESEARCH TECHNIQUE FOR THERMAL DECOMPOSITION OF RDF

Derivatography is one of the most informative methods of studying the thermal decomposition of solid fuels. It makes it possible to determine the stages and temperature ranges of decomposition, the type of thermal effects and the depth of structural and chemical transformations of the fuel.

The derivatography, which combines thermogravimetry (TG) with classical differential thermal analysis (DTA), has found wide application in scientific research. It allows obtaining information about the behavior of individual substances and composites under conditions of programmed heating. Qualitative and quantitative assessment of the processes occurring during heating of samples is carried out using the curves of changes in sample temperature (T), its mass (TG), differential thermogravimetry (DTG), which is a derivative of the TG, and DTA curve. The DTA curve represents the temperature difference between the sample and the inert material in the form of the difference in thermoelectromotive forces of thermocouples. It allows one to identify the thermal processes occurring in the sample when it is heated. The temperature of the peaks of thermal effects (DTA) is higher than the temperature of the corresponding maximums of the rate of mass change (DTG) due to the existing thermal resistance of the sample material and the crucible walls.

Thermogravimetric studies were carried out in a derivatograph "Q-1000" manufactured by MOM (Hungary), modernized at the Institute of Engineering Thermophysics of the NAS of Ukraine. The block diagram of a modernized derivatograph for studying the thermal destruction of solid fuels is shown in **Fig. 3.12**.

The derivatograph consists of a furnace, a scales unit, measurement and information processing units. The set temperature is maintained in furnace 1 using programmer 2 and controlled by thermocouple 3. A scales unit includes analytical scales 4 with devices for changing sensitivity and absorbing vibrations. A hollow ceramic rack 5 is suspended on one side of the scales rocker, the upper end of which is inserted into the furnace.

In the upper part, the rack has a comb with built-in junctions from two differential thermocouples. The first (working) thermocouple is designed to measure the temperature of the sample (T) during

the heating process. A crucible with an inert substance is placed on the junction of the second thermocouple. The temperature difference between the sample and the inert substance is registered in the form of a differential electromotive force (DTA).

The electromagnetic coil of the device 7 and the ferrite rod of the device 8 are placed on the other side of the scales rocker. Device 8 is made in the form of a differential transformer with a ferrite rod in the middle, designed to register the change in the mass of the sample (TG). Device 7 consists of an electromagnetic coil in the form of a frame, which is suspended in the field of a permanent magnet. In the frame, a voltage is generated proportional to the rate of change of the mass of the sample (DTG) when moving in a uniform magnetic field.

Information about the change in mass and temperature of the sample is sent to the analog-to-digital converter 11 and transmitted to the personal computer 13 using the interface converter 12.

Control of the collection and processing of information from the derivatograph "Q-1000" was carried out using the "Derivatograph" computer application program created in the Delphi programming language.

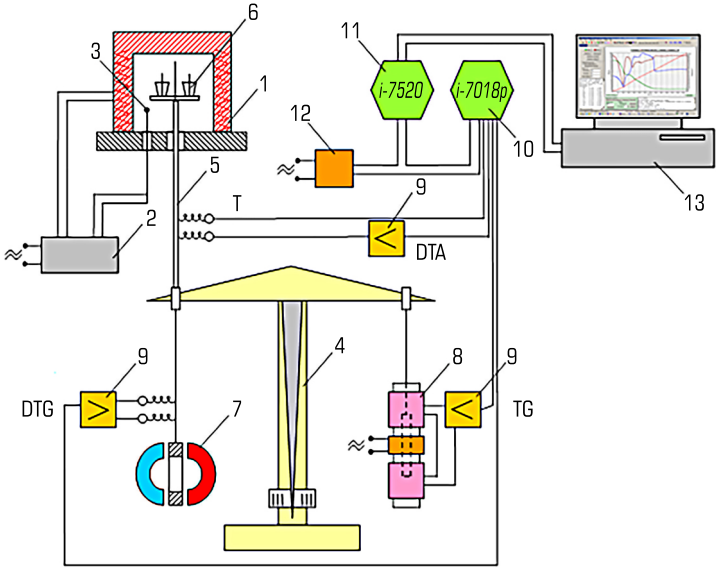

1 – furnace; 2 – temperature programmer in the furnace;
3 – thermocouple of temperature control in the furnace; 4 – scales;
5 – ceramic rack; 6 – sample; 7 – device for measuring the rate of moisture removal;
8 – device for measuring the change in mass of the sample; 9 – signal amplifier;
10 – analog-to-digital converter; 11 – interface converter; 12 – power supply; 13 – computer

Fig. 3.12 Block diagram of the modernized derivatograph "Q-1000"

All materials (combustible components of MSW) were stored for a long time in the laboratory at a relative humidity of 40 % and a temperature of 20 °C. Before the study, they were crushed to a particle size of ≤0.5 mm. Almost all samples had equilibrium moisture content.

The thermal decomposition of the samples was studied by heating them from ambient temperature to 1000 °C at a constant rate (7.4 K/min) with a scale resolution of 0.5 mg. Fuel samples weighing 50–70 mg were placed into an open conical platinum crucible. Destruction took place under static conditions of a gas environment in the zone of thermal decomposition reactions, that is, in a gas atmosphere formed during the thermal decomposition of organic substances in the absence of air movement in the area of the crucible.

3.3.2 RESULTS OF THE DERIVATOGRAPHIC STUDIES OF RDF

Eight variants of experimental RDF were made based on the results of studies carried out using methods of thermal and thermogravimetric analysis of MSW components and data on the average morphological composition of combustible solid waste, which can be a raw material for RDF (**Fig. 3.3**). RDF samples were made by mixing the components in the required ratio (**Table 3.4**).

According to the research results, data on the change in temperature (T) and mass of the sample (TG), rate of mass change (DTG) and heat generation (DTA) were obtained during the heating process. Processing and analysis of the obtained data made it possible to determine the temperature ranges of dehydration, thermal decomposition of organic and mineral substances, moisture and ash content of the samples (**Table 3.5**).

Temperature ranges, proportions and average rates of decomposition of organic substances of the fuel were calculated (**Table 3.6**). The analysis of the obtained data makes it possible to estimate the kinetics of thermal destruction of organic substances.

Table 3.4 RDF composition

RDF sample	RDF components, %					
	cardboard	polyethylene film	polyethylene terephthalate (PET) bottle material	fabric	genuine leather	pine wood
A	50	26	0	16	3.5	4.5
B	37	40	0	15	3.5	4.5
C	36	0	41	15	3.5	4.5
D	25	25	25	16	4	5
E	47	39	0	7	3.5	3.5
F	29	31	0	13	4	23
G	0	50	0	20	10	20
H	50	50	0	0	0	0

Table 3.5 Thermal characteristics of experimental fuel

RDF sample	Water removal		Thermal decomposition				Ash content, % DM
			organic substances		mineral substances		
	range, °C	moisture content, %	range, °C	content, % DM	range, °C	content, % DM	
A	23–166	6.28	166–530	91.32	530–1000	3.81	4.87
B	20–166	4.69	166–538	92.69	538–1000	3.58	3.73
C	20–165	5.31	165–573	93.66	573–1000	2.95	3.39
D	23–164	4.13	164–560	92.73	560–1000	2.37	4.90
E	23–156	4.78	156–536	91.02	536–1000	4.41	4.57
F	20–165	5.17	165–534	92.79	534–1000	3.69	3.52
G	23–154	4.51	154–544	95.92	544–1000	2.19	1.89
H	23–157	3.81	157–534	90.54	534–1000	4.73	4.73

Note: DM – dry matter

Table 3.6 Temperature ranges, proportions of decomposed organic substances and average rates of RDF decomposition

RDF sample	First stage			Second stage			Third stage			Average rate of decomposition, % DM/min
	range, °C	proportion, % DM	decomposition rate, % DM/min	range, °C	proportion, % DM	decomposition rate, % DM/min	range, °C	proportion, % DM	decomposition rate, % DM/min	
A	166–352	43.99	1.87	352–470	38.05	2.41	470–530	9.28	0.96	1.86
B	166–353	35.67	1.52	353–476	46.27	2.87	476–538	10.75	1.06	1.86
C	165–351	31.56	1.30	351–457	41.45	3.06	457–573	20.65	1.22	1.71
D	164–351	27.45	1.12	351–455	45.25	3.54	455–560	20.03	1.27	1.75
E	156–355	36.99	1.48	355–477	44.44	2.78	477–536	9.59	0.98	1.79
F	165–357	41.47	1.71	357–463	37.61	2.72	463–534	13.71	1.22	1.88
G	154–336	30.13	1.29	336–487	56.33	2.89	487–544	9.46	1.0	1.84
H	157–361	35.73	1.39	361–472	42.44	2.90	472–534	12.37	1.21	1.79

The resulting derivatograms of thermal decomposition of RDF samples and their description are presented in **Table 3.7**. Derivatograms show T, TG, DTG and DTA profiles during sample heating. All samples are characterized by a three-stage destruction accompanied by endothermic and exothermic effects. Dehydration takes place at the first stage, thermal decomposition of organic substances at the second stage, and decomposition of mineral substances at the third stage (**Table 3.5**).

The calorific value was determined according to the standard technique for solid fuels [28–30].

Table 3.7 Derivatograms of thermal decomposition of RDF samples and their description

RDF A	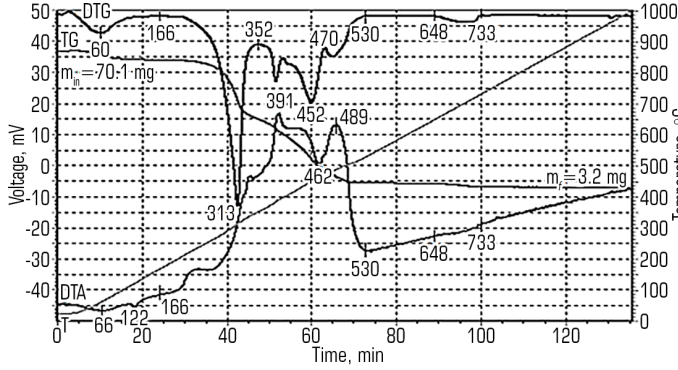
RDF A description	Dehydration occurs in the range of 23–166 °C. The moisture content of the sample is the highest among all fuel samples due to the high content of cardboard. The thermal decomposition of organic substances occurs in three stages differing in the decomposition rate and thermal effects. Decomposition of 43.99 % DM occurs in the range of 166–352 °C at a rate of 1.87 % DM/min (**Table 3.6**). At the same time, heat generation is constantly increasing. At this stage, the maximum decomposition rate was registered at a temperature of 313 °C. The decomposition rate increases to 2.41 % DM/min in the second stage (352–470 °C) due to polyethylene. The intense emission of gases outside the crucible leads to heat loss, which is registered on the DTA curve in the form of an endothermic peak with a maximum at 463 °C. The decomposition of organic substances is completed at the third stage in the range of 470–530 °C. A further increase in temperature causes the decomposition of mineral substances. Sample mass loss (TG and DTG curves) and heat absorption (DTA curve) are observed at temperatures of 648–733 °C. This is a consequence of the thermal dissociation of calcium carbonate in the cardboard. The ash content of RDF A is 4.87 % DM, and the determined net calorific value is 23.03 MJ/kg
RDF B	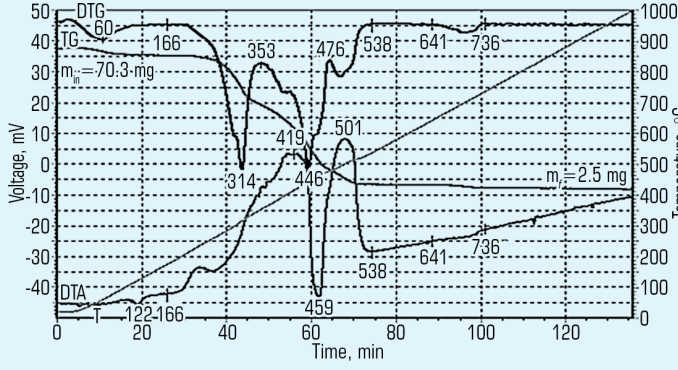
RDF B description	Dehydration of RDF B ends at 166 °C, as for RDF A, after which the stage of decomposition of organic substances begins (**Table 3.5**). This stage is also characterized by three stages of decomposition (**Table 3.6**). At the first stage (166–353 °C), 35.67 % DM is removed at a rate of 1.52 % DM/min. At the second stage (353–476 °C), the intensity of decomposition increases 1.9 times due to the high content of polyethylene film in the fuel. In the range of 419–501 °C, a strong endothermic peak

Continuation of Table 3.7

	is registered on the DTA curve, which was observed during the decomposition of the polyethylene sample. At the third stage (476–538 °C), the intensity of decomposition of organic substances decreases. Increasing the polyethylene film content and decreasing the cardboard content in RDF B causes changes in the nature of the destruction of organic substances. The impact of polyethylene as a fuel component becomes more noticeable and causes a powerful release of decomposition products. At the same time, the net calorific value of RDF B increases to 27.01 MJ/kg compared to RDF A due to the contribution of the net calorific value of polyethylene film (42.56 MJ/kg)
RDF C	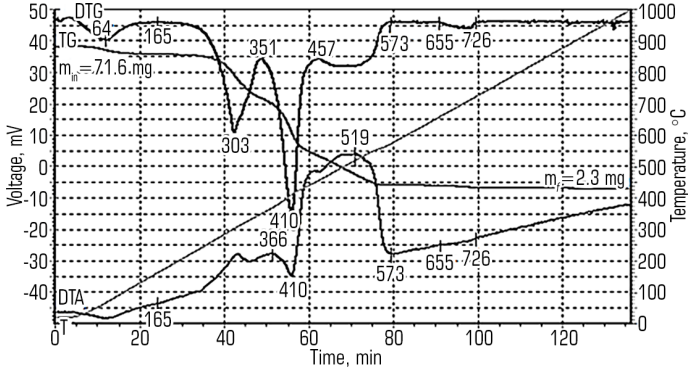
RDF C description	The thermal decomposition of RDF C, in which PET bottle material was added instead of polyethylene film, is generally similar to RDF B. Water is removed in the range of 20–165 °C (**Table 3.5**). A slight increase in heat release is observed (DTA curve) at the first stage of decomposition of organic substances (165–351 °C). At the second stage, intense destruction is observed – the rate of decomposition increases by 2.4 times (**Table 3.6**) and reaches a maximum at 410 °C. Against the background of general heat generation, a small endothermic peak indicates a slight release of gaseous decomposition products outside the crucible. In the range of 457–573 °C (third stage), the rate of decomposition decreases and completely stops when reaching 573 °C (DTG and DTA curves). Thermal dissociation of calcium carbonate in cardboard is registered in the range 655–726 °C (DTG and DTA curves). The calorific value of fuel is reduced to 18.85 MJ/kg due to the replacement of polyethylene film with material from a PET bottle in the composition of RDF C
RDF D	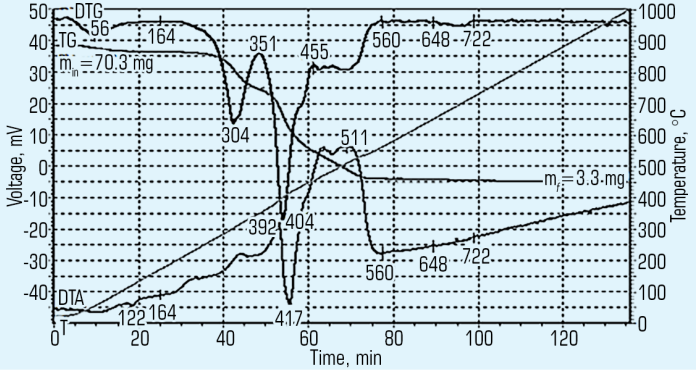

Continuation of Table 3.7

RDF D description	The thermal decomposition of the RDF D occurs according to the decomposition patterns of RDF C. The moisture content of RDF D is 4.13 % due to the low content of cardboard (**Table 3.5**). The stages of decomposition of organic substances differ significantly in decomposition rates (**Table 3.6**). A high content of polymer materials (50 %) causes an increase in the rate of decomposition in the second stage (351–455 °C) and the formation of a significant amount of gaseous products. These products escape the sample and cause a large heat loss, reflected as an endothermic peak in the DTA curve appears as an endothermic peak on the DTA curve with a maximum at 417 °C. The destruction of organic substances ends at 560 °C and is accompanied by a decrease in heat generation. The calorific value of this fuel is 24.60 MJ/kg
RDF E	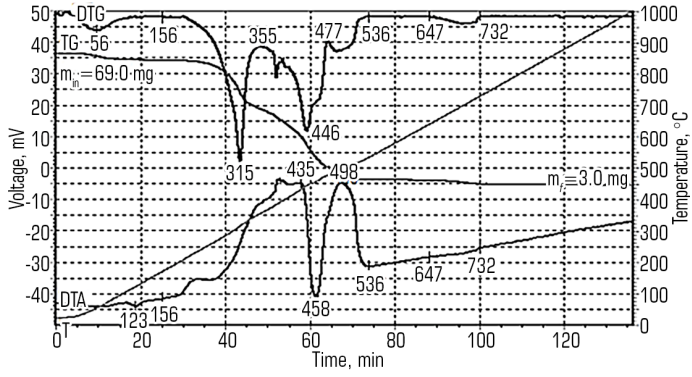
RDF E description	Water removal ends earlier by 8–10 °C compared to previous fuel samples (**Table 3.5**). The decomposition of organic substances occurs in three stages, as for all experimental fuel samples. The highest intensity is characteristic of the second stage due to the high content of polymer components. Decomposition of 44.44 % DM occurs at a rate of 2.78 % DM/min. In the range of 435–498 °C, an endothermic peak is registered on the DTA curve with a maximum at 458 °C. It is a consequence of heat loss due to the formation of a significant amount of gaseous products leaving the sample location. The destruction of organic substances ends at 536 °C. The net calorific value of the fuel is 26.46 MJ/kg due to the high content of polyethylene film
RDF F	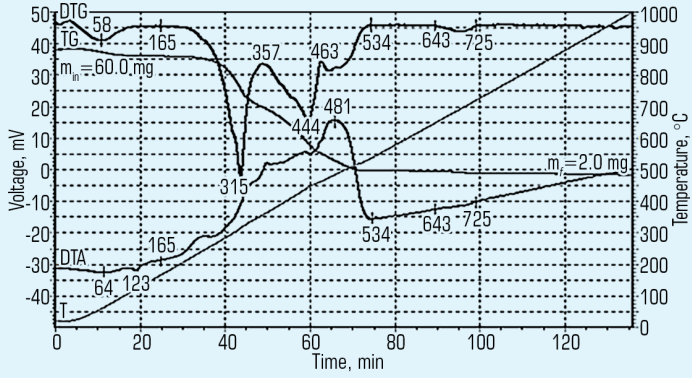

Continuation of Table 3.7

RDF F description	Water is removed from RDF F in the temperature range of 20–165 °C, after which the organic substances of RDF fuel decompose in three stages (**Table 3.5**). In the first and third stages, a slightly lower rate of decomposition is observed than in the second (**Table 3.6**), which is a consequence of deeper destruction processes in the second stage and the influence of the kinetics of polyethylene film decomposition. Heat generation increases in the second stage and reaches its maximum at 481 °C (DTA curve). In this case, the endothermic peak accompanying the formation of gaseous substances is not observed. Thermally unstable mineral substances degrade in fuel components in the range of 534–1000 °C with the formation of simpler molecules. The ash content is determined to be 3.52 % DM. The process of calcium carbonate dissociation was observed in the range of 643–725 °C. The net calorific value of this fuel composition is 25.22 MJ/kg
RDF G	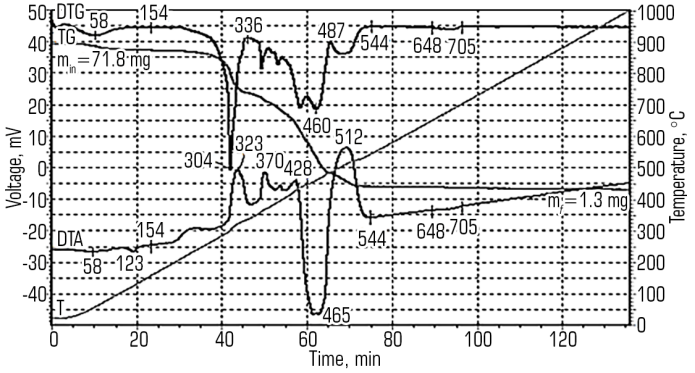
RDF G description	Water removal occurs in the narrowest range of all samples (23–154 °C) due to the absence of cardboard in the composition. The decomposition of organic substances is accompanied by intense gas formation, as evidenced by three endothermic peaks (323–370, 370–428, 428–512 °C) of different intensity. Most organic substances is removed at a rate of 2.89 % DM/min in the second stage of decomposition. The lowest content of mineral substances (2.19 % DM) and ash content (1.89 % DM) is observed in RDF G among all experimental fuel samples due to the absence of cardboard in the fuel composition. The selected fuel composition provided the highest calorific value – 30.82 MJ/kg
RDF H	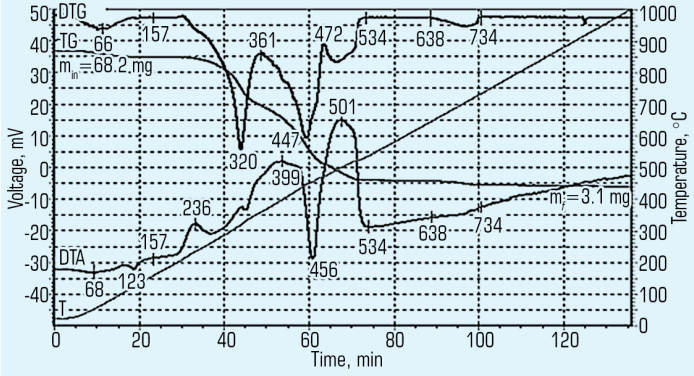

Continuation of Table 3.7

RDF H description	RDF H contains cardboard and polyethylene film in equal proportions and has the lowest moisture content (3.81 %). The destruction of organic substances occurs according to the patterns characteristic of the above fuel samples, in particular RDF B and RDF E. The net calorific value of the fuel sample is 28.89 MJ/kg

The analysis of the obtained data makes it possible to compare the destructive processes occurring in the fuel when it is heated to 1000 °C. Dehydration of all RDF samples is completed at a temperature of 154–166 °C (**Table 3.5**). The lowest temperature of the dehydration completion (154 °C) is found in the RDF G sample, which does not contain cardboard. RDF A has a narrower range of decomposition of organic compounds (364 K). This is explained by the presence of a significant amount of cardboard in the composition, the decomposition of which is completed earlier by 23 K than polyethylene and by 79 K than PET. The widest range (408 K) is registered in RDF C, which has the highest PET content. The highest values of the average rate of decomposition have RDF A, B and F, which do not contain PET. It follows from this that an increase in the PET content in fuel causes an expansion of the temperature range of decomposition and a decrease in the overall rate of the decomposition of organic substances.

DTA profiles (**Table 3.7**) indicate that for RDF containing only polyethylene polymers (**Table 3.5**), the release of gaseous substances occurs with an endothermic peak located in the range of 456–465 °C. The same behavior and a similar maximum of the endothermic peak (459 °C) were observed during the decomposition of polyethylene film. The PET presence in the fuel accelerates the release of gaseous substances. The maximum of the endothermic peak is registered at 410 °C (RDF C) and 417 °C (RDF D). In PET, this maximum was registered at 418 °C.

Determination of the calorific value Q_n^d of experimental fuel compositions showed (**Fig. 3.13**) that the highest calorific value is for RDF G, which does not contain cardboard, and the lowest is for RDF C, which does not contain polyethylene film.

Conditional thermal effects (CTE) of thermal decomposition of organic substances were also determined using the "Derivatograph" application program (**Fig. 3.13**). CTE was calculated as the area between the DTA curve and the most likely estimated DTA baseline divided by the mass of the organic substances of the sample. The baseline is a straight line connecting the points of complete dehydration and completion of heat release. The area under the curves of exothermic thermal effects was determined by the trapezoidal method using the "Derivatograph" program.

According to the obtained data, RDF E has the highest value of the specific thermal effect, and RDF D has the lowest value. As it is possible to see, this does not correspond to the results for determining the lower calorific value (**Fig. 3.13**). This confirms the assumption that the registered endothermic peak (DTA curves) underestimates the CTE value due to the loss of heat of thermal decomposition due to the emission of gaseous substances outside the crucible. Therefore, more accurate research results, namely a determined net calorific value of samples, should be taken into account when assessing the thermal characteristics of multicomponent RDF.

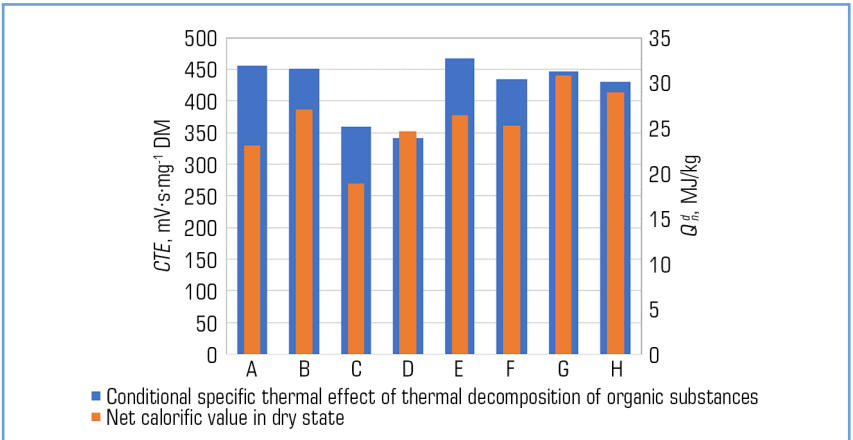

Fig. 3.13 Conditional thermal effects (CTE) and net calorific value Q^d_n of RDF samples

Thermal analysis of experimental RDF based on combustible components of the MSW showed that the temperature of the drying agent should be such as to prevent overheating of the material above the temperature of its complete dehydration during convective drying. This measure will prevent ignition of RDF in the dryer.

The following conclusions can be drawn from the results of experimental studies:

1. The thermal decomposition of RDF was investigated using thermal analysis methods in the range of 20–1000 °C. Temperatures characterizing different stages of destruction, moisture and ash content of samples, rate of thermal decomposition of organic substances, conditional thermal effect and calorific value were determined.

2. It was established that the high polyethylene content in RDF leads not only to a high calorific value of the fuel, but also to a powerful release of volatile thermal decomposition products. This improves combustion kinetics. Polyethylene terephthalate also intensively emits gaseous products during thermal decomposition. However, increasing the polyethylene terephthalate content reduces the calorific value of the fuel due to its significantly lower calorific value compared to polyethylene. Therefore, it is better to send PET products to recycling as much as possible at the stage of waste sorting.

3. Destruction of cardboard does not cause emissions of harmful compounds. However, it should be taken into account that a high content of cardboard causes an increased ash content of the fuel. It was established that the ash content can vary in the range of 1.8–16 % DM for different samples of paper and cardboard. In addition, it is necessary to take into account the presence of chalk in them. Because the decomposition of chalk requires additional energy at sufficiently high temperatures.

Based on the obtained data, it is possible to recommend the presented compositions RDF A and F, which satisfy the conditions set for fuel, as well as RDF B, D and E while ensuring the neutralization of harmful emissions.

CONCLUSIONS

1. Analysis of technological stages of RDF production shows that all stages of production are energy consuming. The consumption is especially large for drying processes. They account for about 40–50 % of total energy consumption. The consumption increases up to 70 % in cases of drying MSW with high moisture content.

Increasing the calorific value of composite fuel based on MSW requires combining components whose thermal properties have not been sufficiently studied. RDF combustion also requires knowledge of the kinetics of thermal decomposition and heat generation.

2. The kinetics of convective drying of RDF of different compositions was studied depending on the temperature (80–120 °C) and the rate of the heat carrier (1.5–2.5 m/s). The drying time is reduced by 56 %, and the maximum drying rate increases by 1.82 times when the heat carrier temperature increases from 80 to 120 °C. Increasing the rate of the heat carrier from 1.5 to 2.5 m/s reduces the drying time by 38 % at a temperature of the heat carrier of 120 °C. The drying time increases by 28 % when the RDF composition changes from the content of polymer materials (31–50 %) to the content of paper and cardboard (31–50 %).

3. The study of heat and mass transfer during drying of fuels, in particular the temperature coefficient, Rebinder number and heat flow, depending on the moisture content of fuels at constant temperatures, showed the feasibility of drying at higher temperatures.

4. RDF was studied in the range of 20–1000 °C using thermogravimetry and differential thermal analysis methods. It is shown that the thermal decomposition of organic substances is staged in RDF. The stages differ in both temperature ranges and decomposition rates.

5. Based on the obtained data, it is possible to recommend the compositions RDF A and F, which satisfy the conditions set for fuel, as well as RDF B, D and E while ensuring the neutralization of harmful emissions.

6. It would be rational to have the maximum amount of polymers, especially polyethylene, in the fuel based on the calorific value and kinetics of thermal decomposition of experimental RDF. However, in practice, the polymer content in the fuel will be determined by the air emission treatment system of a particular energy enterprise.

REFERENCES

1. Daskalopoulos, E., Badr, O., Probert, S. D. (1997). Economic and Environmental Evaluations of Waste Treatment and Disposal Technologies for Municipal Solid Waste. Applied Energy, 58 (4), 209–255. https://doi.org/10.1016/s0306-2619(97)00053-6
2. Clark, R. M. (1981). Resource recovery planning and management. Ann Arbor, Mich: Ann Arbor Science, 167.

3. Pinto, F., André, R. N., Carolino, C., Miranda, M., Abelha, P., Direito, D. et al. (2014). Gasification improvement of a poor quality solid recovered fuel (SRF). Effect of using natural minerals and biomass wastes blends. Fuel, 117, 1034–1044. https://doi.org/10.1016/j.fuel.2013.10.015
4. Council Directive 1999/31/EC on the landfill of waste (1999). FAOLEX Database. Food and Agriculture Organization of the United Nations. Available at: https://faolex.fao.org/docs/pdf/eur38106.pdf Last accessed: 13.06.2023
5. Haykiri-Acma, H., Kurt, G., Yaman, S. (2016). Properties of Biochars Obtained from RDF by Carbonization: Influences of Devolatilization Severity. Waste and Biomass Valorization, 8 (3), 539–547. https://doi.org/10.1007/s12649-016-9610-5
6. Hernandez-Atonal, F. D., Ryu, C., Sharifi, V. N., Swithenbank, J. (2007). Combustion of refuse-derived fuel in a fluidised bed. Chemical Engineering Science, 62 (1-2), 627–635. https://doi.org/10.1016/j.ces.2006.09.025
7. Nath, K. J. (1999). Solid waste management in the present Indian perspective. Annual Conference. Jönköping.
8. Seo, M. W., Kim, S. D., Lee, S. H., Lee, J. G. (2010). Pyrolysis characteristics of coal and RDF blends in non-isothermal and isothermal conditions. Journal of Analytical and Applied Pyrolysis, 88 (2), 160–167. https://doi.org/10.1016/j.jaap.2010.03.010
9. Nakajima, Y., Matsuyuki, M. (1981). Utilization of waste tires as fuel for cement production. Conservation & Recycling, 4 (3), 145–152. https://doi.org/10.1016/0361-3658(81)90018-7
10. Yang, Y., Liew, R. K., Tamothran, A. M., Foong, S. Y., Yek, P. N. Y., Chia, P. W. et al. (2021). Gasification of refuse-derived fuel from municipal solid waste for energy production: a review. Environmental Chemistry Letters, 19 (3), 2127–2140. https://doi.org/10.1007/s10311-020-01177-5
11. Zajemska, M., Magdziarz, A., Iwaszko, J., Skrzyniarz, M., Poskart, A. (2022). Numerical and experimental analysis of pyrolysis process of RDF containing a high percentage of plastic waste. Fuel, 320, 123981. https://doi.org/10.1016/j.fuel.2022.123981
12. Lecture "RDF from municipal solid wastes" by Dirk Lechtenberg (2018). Eggersmann. YouTube. Available at: https://www.youtube.com/watch?v=MwT3IepTFag Last accessed: 18.09.2023
13. The European Cement Association (2015). Markets for solid recovered fuel. Data and Assessments on Markets for SRF. Brussels: CEMBUREAU.
14. Sarquah, K., Narra, S., Beck, G., Awafo, E. A., Antwi, E. (2022). Bibliometric Analysis; Characteristics and Trends of Refuse Derived Fuel Research. Sustainability, 14 (4), 1994. https://doi.org/10.3390/su14041994
15. DSTU EN 15359:2018. Solid renewable fuel (2019). Technical characteristics and classes (EN 15359:2011, IDT).
16. Fichtner, K. (2023). Management of municipal solid waste in Metro Vancouver-A comparative analysis of option for management of waste after recycling. AECOM. Available at: http://

www.metrovancouver.org/services/solidwaste/planning/Thenextsteps/SDD_3_AECOM_FULL_REPORT.pdf Last accessed: 15.08.2023
17. Srivastava, H. (2023). Market analysis & literature review on refuse derived fuel (RDF) from residual waste. UBC Sustainability Scholar. Available at: https://sustain.ubc.ca/sites/default/files/2021-053_Market%20Analysis%20&%20Literature%20Review_Srivastava.pdf Last accessed: 10.11.2023
18. Resource recovery technology guide (2018). Sustainability Victoria. Available at: https://assets.sustainability.vic.gov.au/susvic/Guide-Waste-Resource-Recovery-Technology-Guide.pdf Last accessed: 14.11.2023
19. Rogoff, M. J., Screve, F. (2019). Energy From Waste Technology. Waste-To-Energy, 29–56. https://doi.org/10.1016/b978-0-12-816079-4.00003-7
20. Shukla, P., Srivastava, R. K. (2022). Comparative study of coal and refuse derived fuel – produced from municipal solid waste in Rewa city (M.P.). International journal of innovative research in technology, 9 (4), 745–751. Available at: https://ijirt.org/master/publishedpaper/IJIRT156793_PAPER.pdf
21. Kobzar, S. H., Topal, O. I., Haponych, L. S., Holenko, I. L. (2020). Investigation of Co-firing for Fuel Derived from Municipal Solid Waste in a Model Combustion Chamber. Èlektronnoe Modelirovanie, 42 (6), 72–90. https://doi.org/10.15407/emodel.42.06.072
22. Bulyandra, O., Haponych, L., Golenko, I., Topal, O. (2020). Prospects of the use of fuel from municipal solid waste at TPP of sugar factories. Scientific Works of National University of Food Technologies, 26 (3), 137–146. https://doi.org/10.24263/2225-2924-2020-26-3-16
23. Paziuk, V. M., Petrova, Zh. O., Tokarchuk, O. A., Polievoda, Yu. (2021). Special aspects of soybean drying with high seedling vigor. University. Pjlstehnica of Buharest Scientific Bulletin, Series D, 83 (2), 327–336.
24. Li, X., Ma, B., Xu, L., Hu, Z., Wang, X. (2006). Thermogravimetric analysis of the co-combustion of the blends with high ash coal and waste tyres. Thermochimica Acta, 441 (1), 79–83. https://doi.org/10.1016/j.tca.2005.11.044
25. Kaniowski, W., Taler, J., Wang, X., Kalemba-Rec, I., Gajek, M., Mlonka-Mędrala, A. et al. (2022). Investigation of biomass, RDF and coal ash-related problems: Impact on metallic heat exchanger surfaces of boilers. Fuel, 326, 125122. https://doi.org/10.1016/j.fuel.2022.125122
26. Sever Akdağ, A., Atimtay, A., Sanin, F. D. (2016). Comparison of fuel value and combustion characteristics of two different RDF samples. Waste Management, 47, 217–224. https://doi.org/10.1016/j.wasman.2015.08.037
27. Gug, J., Cacciola, D., Sobkowicz, M. J. (2015). Processing and properties of a solid energy fuel from municipal solid waste (MSW) and recycled plastics. Waste Management, 35, 283–292. https://doi.org/10.1016/j.wasman.2014.09.031
28. DSTU ISO 1928:2006. (2008). Solid mineral fuels. Determination of the highest heat of combustion by the method of combustion in a calorimetric bomb and calculation of the lowest

heat of combustion (ISO 1928:1995, IDT). To replace GOST 147-95 (ISO 1928-76). Kyiv: Derzhspozhivstandard of Ukraine, 40.

29. EN ISO 21654:2021. (2021). Solid recovered fuels – Determination of calorific value. Replaces EN 15400:2011.
30. Skliarenko, E., Vorobiov, L. (2023). Technique for determining the heat of combustion in the production of fuel from solid municipal waste with preferred characteristics. SWorldJournal, 1 (20-01), 11–20. https://doi.org/10.30888/2663-5712.2023-20-01-008

DOI: 10.15587/978-617-8360-02-3.CH4
Igor Kozlov, Vyacheslav Kovalchuk, Viacheslav Miliev,
Mykola Holovin, Serhii Vistiak, Olexiy Kozlov
© The Author(s) 2024. This is an Open Access chapter distributed under the terms of the CC BY-NC-ND license

CHAPTER 4

CHOICE OPTIMIZATION OF THE TYPE OF ENERGY RESOURCE FOR THE REGION

ABSTRACT

The work is devoted to a close analysis of the state and prospects for the development of the energy complex of Ukraine. The aim of the study is to develop a methodology for selecting and substantiating the predominant type of energy resources for energy supply of regions.

The state of use of available energy resources, their share in the total volume of energy production is clarified. The advantages and disadvantages of available resources in connection with their impact on the environment are considered.

It is proved that the predominant amount of energy is produced using traditional fossil and produced resources: coal, oil, gas and nuclear fuel. Energy production traditionally follows the availability of resources in the region and the need for energy, which creates an uneven concentration of industry and its accompanying environmental impact.

The use of a complex indicator for assessing the efficiency of types of energy resources and the impact of their use on the state of the environment is proposed. A methodology for using the proposed complex indicator to substantiate the energy strategies of regions is developed.

KEYWORDS

Energy resource, hydropower, wind power, solar power plants, bioenergy, thermal power, nuclear power, efficiency and pollution index, energy strategies, regions.

In the modern world, energy is the basis for the development of basic industries that determine the progress of social production.

According to British Petroleum in 2022 [1]. 29,165.1 TWh of electricity were produced in the world. Among the main sources of electricity generation by type of resource are: oil – 728.6 TWh (2.5 %); gas – 6,631.4 TWh (22.7 %); coal – 1,031.2 TWh (35.4 %); nuclear – 2,679.0 TWh (9.2 %); hydro – 4,334.2 TWh (14.9 %); renewable – 4,204.3 TWh (14.4 %); other – 270.5 TWh (0.9 %) (**Table 4.1**).

According to Reuters, the Energy Institute's Statistical Review of World Energy in 2023 [2] reports that total global primary energy consumption reached a historic high of 620 exajoules (EJ) (620 1018 J), and emissions exceeded 40 gigatons of CO_2 for the first time. Fossil fuel use in 2023 increased by 1.5 % to 505 EJ, accounting for 81.5 % of total energy consumption, down 0.5 % from 2022. Oil consumption in 2023 exceeded 100 million barrels per day for the first time in history.

Table 4.1 Global electricity production in 2022 by resource type, according to British Petroleum

Place of production		Oil	Gas	Coal	Nuclear	Hydro	Renewable	Other	Total
Worldwide	TWh	728.6	6,631.4	10,317.2	2,679.0	4,334.2	4,204.3	270.5	29,165.1
	%	2.5	22.7	35.4	9.2	14.9	14.4	0.9	–
European Union	TWh	43.9	556.2	461.2	608.6	276.9	801.7	63.5	2,812.0
	%	1.6	19.8	16.4	21.6	9.8	28.5	2.3	–
Ukraine	TWh	0.5	7.2	24.8	62.1	11.1	7.0	–	112.7
	%	0.4	6.4	22.0	55.1	9.8	6.2	–	–

Source: [1]

Total electricity generation in 2023 grew by 2.5 %, slightly higher than the 2.3 % increase in the previous year. Renewable fuel generation (excluding hydropower) increased by 13 % to a new record high of 4,748 terawatt-hours (TWh). The share of renewable energy sources in the total energy balance excluding hydropower was 8 %, compared to 7.5 % in the 2022 report.

Including hydropower, renewable energy sources account for 15 % of the global balance. The record growth in renewable generation was driven by increases in wind and solar capacity: in 2023, the capacity growth in these two categories was 67 % higher than in 2022.

The 2 % increase in emissions (over 40 gigatons of CO_2) in 2023 is due to more intensive consumption of oil and coal, while gas consumption has remained stable.

This figure is expected to increase to 3.3 % in 2024 due to the improvement of the global economic outlook [3].

By 2030, the global demand for electricity may amount to 33,275 TWh [4]. The Ministry of Energy and Coal Industry predicts an increase in electricity consumption in Ukraine by 86 % by 2030 to 280 billion kWh [5].

4.1 STATE AND PROSPECTS FOR THE DEVELOPMENT OF THE ENERGY SECTOR OF UKRAINE

According to the Energy Strategy of Ukraine [6], the share of renewable energy sources in the structure of electricity production by 2030 will be 13 %.

The main directions of development of RES until 2030 (**Table 4.2**) and further prospects are:

– use of wind energy and hydropower for electricity production;

– use of solar and geothermal energy – for electricity and heat production;

– utilization of biomass waste, solid household waste, etc. – by burning or obtaining biogas for heat and electricity production.

Table 4.2 Promising directions and levels of development of renewable energy sources in Ukraine until 2030

Indicators	Production of thermal and electrical energy from renewable sources in 2020–2030			
	2020		2030	
	MTOE	%	MTOE	%
Wind energy	1.00	6.97	2.15	9.95
Photovoltaics	0.01	0.07	0.03	0.14
Small hydropower	0.48	3.36	0.65	3.01
Large hydropower	5.6	39.06	6.53	30.23
Solar thermal collectors	0.7	4.88	1.28	5.93
Bioenergy	6.3	43.93	10.13	46.9
Geothermal energy	0.247	1.73	0.83	3.84
TOTAL	14.34	100	21.6	100

In 2022–2024, the entire Ukrainian energy sector found itself in the epicenter of a full-scale war, therefore, the information component of the performance indicators of electricity production subsectors in the materials provided is based on data from the pre-war period (until 2022).

In 2021, the share of electricity generated from renewable energy reached 8.1 % or 12.8 TWh, of which 56 % was due to solar radiation, 33 % to wind energy, almost 8 % to biomass and biogas combustion, and 3 % to small hydropower [7].

Thus, in 2021, all RES power plants produced 12,804 million kWh [7] of clean electricity, which exceeded last year's figures by 1,941.9 million kWh or 17.8 %:

– Ukrainian wind power plants produced 3,866 million kWh or 614.4 million kWh more compared to 2020, which is 2.9 7 % of total electricity production;

– solar power plants produced 7,670 million kWh or 4.8 %, which is 1,065.4 million kWh more than the amount of electricity produced in the same period of 2020;

– small hydropower plant generation increased by 56.1 million kWh, reaching 276 million kWh or 0.17 % of the total balance;

– Ukrainian bioenergy plants generated 992 million kWh or 0.6 %, which is 206 million kWh more than the previous year's production level.

4.1.1 HYDROPOWER

In 2019, in the Unified Energy System (UES) of Ukraine, with a total capacity of all generating sources of 52.7 million kW and a total production of 154 billion kWh, the capacity of hydroelectric power plants (HPPs) and pumped storage power plants (PSPPs) amounted to 12 % of the total capacity, and the production without small HPPs amounted to 7.87 billion kWh (5.1 % of the total production) [8, 9], including:

1) large HPPs of the Dnipro and Dniester cascades (taking into account the first stage of the reconstruction of the Dnipro cascade HPP), respectively:

– Dnipro cascade HPP (capacity 3.92 million kW, production 9.42 billion kWh);

– Dniester cascade HPP (capacity 0.74 million kW, production 1.01 billion kWh);

2) small hydroelectric power plants (Tereblia-Rikska on the Tereblia River, Oleksandrivska on the Southern Bug River) with a total capacity of 0.041 million kW and a production of 0.23 billion kWh;

3) small hydroelectric power plants (SHPs up to 10 MW) with a total capacity of 0.1 million kWh and a production of about 0.3 billion kWh (according to the existing classification, small hydroelectric power plants (SHPs) include hydroelectric power plants with a capacity of 1 to 10 MW, mini hydroelectric power plants – from 200 to 1000 kW, and micro hydroelectric power plants – no more than 200 kW).

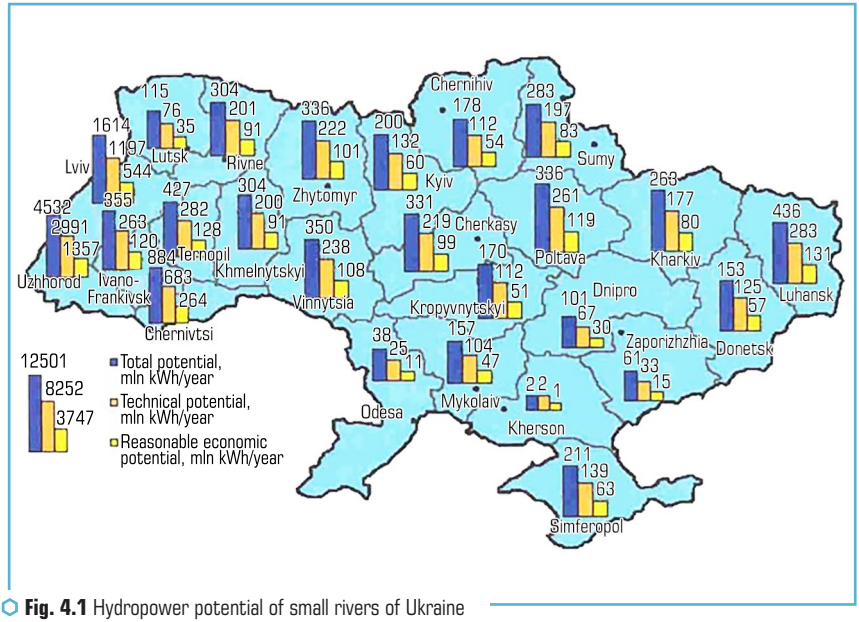

Fig. 4.1 Hydropower potential of small rivers of Ukraine

The total installed capacity of pumped storage power plants (PSPPs) (in turbine mode) is 1.5 million kW, production – 1.5 billion kWh, including:

– Kyiv PSPP (capacity – 0.23 million kW, production –0.226 billion kWh);

– three units of Dniester PSPP (capacity – 0.97 million kW, production –1.02 billion kWh);

– two units of Tashlyk PSPP (capacity – 0.3 million kW, production –0.23 billion kWh).

According to the Institute of Renewable Energy of the National Academy of Sciences of Ukraine, the hydropower potential of small rivers is about 12.5 billion kWh, which is about 28 % of the total hydropower potential of all rivers in Ukraine [10]. The potential by region of Ukraine is shown in **Fig. 4.1** [11].

The main disadvantage of the construction of SHPPs is the threat of disrupting the natural state of the ecological system.

Environmental protection. Potentially, the construction of hydropower facilities changes the landscape and land use conditions, ecological chains in the relevant rivers, water temperature and quality, affects biodiversity, can lead to increased greenhouse gas emissions as a result of intensification of organic compound decomposition processes, etc.

4.1.2 WIND POWER

For Ukraine, wind power plants (WPPs) are a new industry, their contribution to energy supply is currently not significant (6.97 % in the overall structure of electricity production in Ukraine, **Table 4.1**), and while it is in its infancy.

According to the draft of the updated Energy Strategy, Ukraine has significant potential for the development of wind power. The most promising areas for its development are the southern and southeastern regions of the country, where the average wind speed exceeds 5 meters per second (see the areas shaded in brown and red in **Fig. 4.2**).

Most often, to ensure the economic efficiency of WPP construction, the minimum required average annual wind speed should be 2.0–4.5 m/s. To reliably ensure the efficient operation of WPP, the average annual wind speed should be in the range from 5 m/s to 25 m/s [12].

At the end of 2021, the total capacity of the wind energy sector in mainland Ukraine reached 1,672.9 MW [7]. Installed wind energy capacity by regions of mainland Ukraine in the first half of 2021, MW is shown in **Fig. 4.3** [13].

It should also be noted that in the first half of 2021, 73 new wind turbines with a total capacity of 278.4 MW were put into operation in three regions of Ukraine [13]:

– the first stage of the Dniester WPP with a total capacity of 40 MW in the Odessa region;

– the first stage of the Zaporizhzhia WPP with a total capacity of 98 MW in the Zaporizhzhia region;

– the second stage of the Syvash WPP with a total capacity of 140.4 MW in the Kherson region.

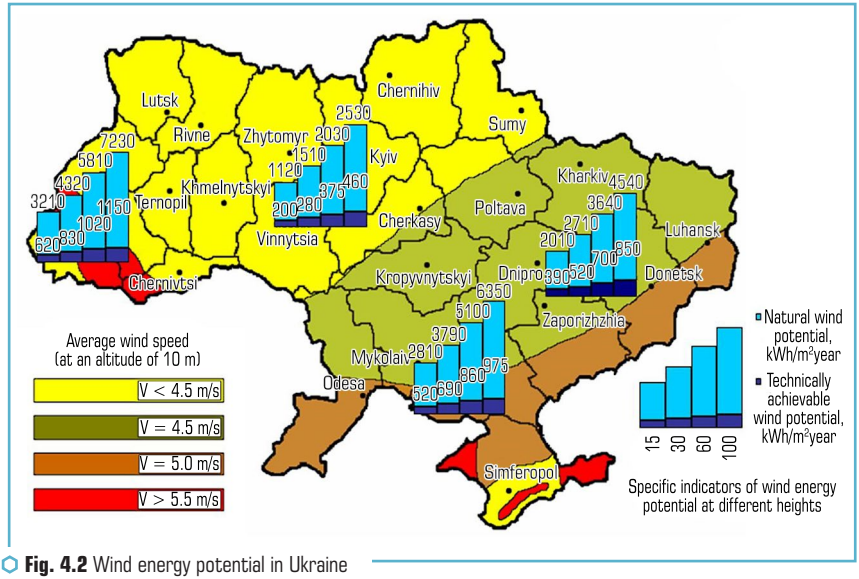

Fig. 4.2 Wind energy potential in Ukraine

Source: [11]

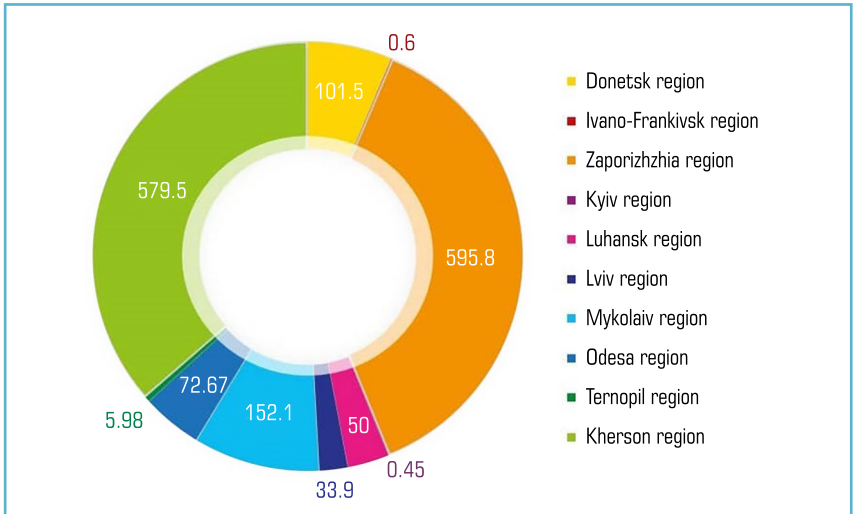

Fig. 4.3 Installed wind power capacity by regions of mainland Ukraine in the first half of 2021, MW

Source: [13]

4.1.2.1 DISADVANTAGES OF MODERN WIND POWER PLANTS

Along with the obvious advantages of wind power plants (autonomy, available energy resource, etc.), one cannot fail to note the characteristic disadvantages [14]:

1. Instability and wind dependence. It is impossible to accurately predict how much electricity will be received in a certain period of time, and in the absence of wind, energy production will completely cease.

2. High construction cost. Installation of a plant capable of producing 1 MW of electricity is more than 1 million USD.

3. Interference with radio communications and telecommunications. The operation of wind power plants causes signal distortion.

4. Change in the natural landscape.

5. Large area required to install an entire generator unit.

6. Danger to living creatures. The blades of turbines that constantly rotate pose a potential threat to certain species of living organisms, in particular, birds. For example, according to statistics, such turbines are the cause of the death of about 5 birds per year.

7. Noise pollution (up to 50 decibels at a distance more than 1 km). The noise created by «windmills» causes concern not only for wildlife, but also for people living near such structures.

8. The emergence of dangerous infrasound with a frequency of 6–7 Hz, which causes vibration.

9. Low energy output. Wind generators are much smaller in rank than other sources of electricity. Wind turbines are inefficient at high loads.

4.1.3 SOLAR ENERGY

Solar energy is one of the new types of energy production based on renewable sources, in particular, solar energy. The main goal is to convert solar radiation into other technological types of energy.

In Ukraine, as of the end of the first half of 2021, the total installed capacity of solar power plants (SPPs) is 7284 MW, including:

– 6,351 MW – solar power plants;

– 933 MW – household SPPs.

The main determining factors in the use of solar energy are the intensity of solar radiation (**Fig. 4.4**) and the duration of sunshine hours (Fig. 4.5).

Solar radiation intensity is the power of the Sun's radiation per unit surface area, measured in watts per square meter (W/m^2).

To calculate the amount of solar radiation that is converted into thermal energy, it is also necessary to take into account the duration of radiation (**Fig. 4.5**). The total energy of solar radiation is the power for a selected period of time, measured as watt-hours (W·h). The period can be taken as: day, month, year, etc.

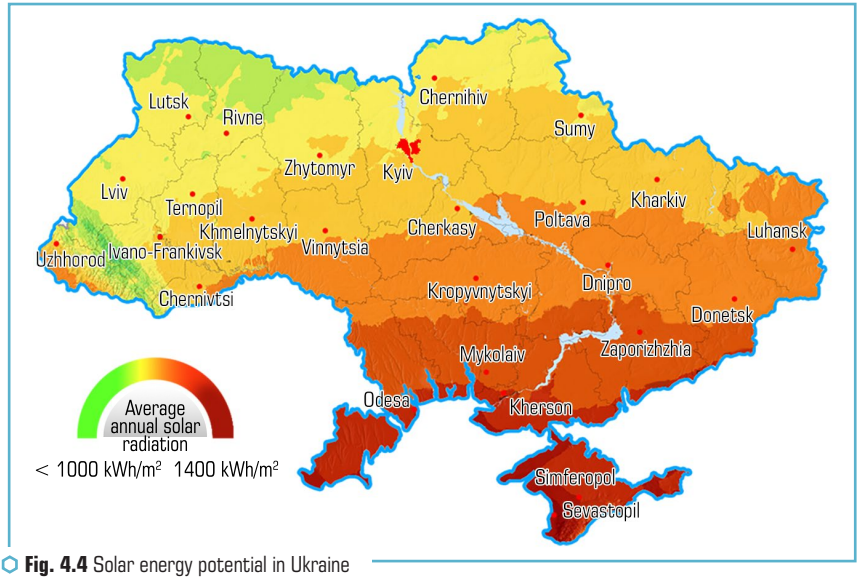

Fig. 4.4 Solar energy potential in Ukraine

Source: [15]

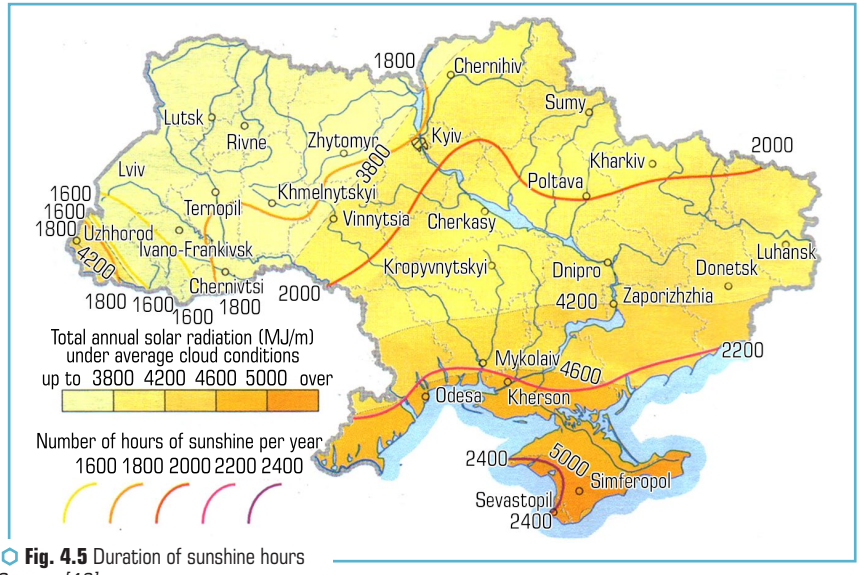

Fig. 4.5 Duration of sunshine hours

Source: [16]

The maximum daily total solar radiation in Ukraine is about 8 kWh/m^2 in the summer. Sometimes on a sunny winter day, the total solar radiation can reach a value of up to 3 kWh/m^2.

The total average annual solar radiation in the territory of Ukraine, according to long-term observations, varies from 1,000 kWh/(m^2) in the northern and central parts of the country to 1,350 kWh/(m^2) in the Crimean Peninsula and the southern part of the Odesa region. For the convenience of analysis, these calculations were divided into 4 zones.

All southern regions of Ukraine are located in the first and second zones; more than half of the country's territory is located in the third zone, the fourth zone is the least favorable for the use of solar energy.

The highest value of solar radiation in the first zone is 1350 kWh/km^2 per year, and the lowest is in the fourth zone 1000 kWh/km^2 per year. In the second and third zones, these values are, respectively, 1250 kWh/km^2 and 1150 kWh/km^2 per year. In general, the territory of Ukraine belongs to the zone of medium solar intensity. The average monthly level of solar radiation for Ukrainian cities is given in **Table 4.3** [17].

Table 4.3 Average monthly level of solar radiation (solar constant) in Ukrainian cities (kWh/m^2/day). Average over the last 22 years

Regions / Months	January	February	March	April	May	June	July	August	September	October	November	December	Average
1	2	3	4	5	6	7	8	9	10	11	12	13	14
Simferopol	1.27	2.06	3.05	4.30	5.44	5.84	6.20	5.34	4.07	2.67	1.55	1.07	3.58
Vinnytsia	1.07	1.89	2.94	3.92	5.19	5.3	5.16	4.68	3.21	1.97	1.10	0.9	3.11
Lutsk	1.02	1.77	2.83	3.91	5.05	5.08	4.94	4.55	3.01	1.83	1.05	0.79	2.99
Dnipro	1.21	1.99	2.98	4.05	5.55	5.57	5.70	5.08	3.66	2.27	1.20	0.96	3.36
Donetsk	1.21	1.99	2.94	4.04	5.48	5.55	5.66	5.09	3.67	2.24	1.23	0.96	3.34
Zhytomyr	1.01	1.82	2.87	3.88	5.16	5.19	5.04	4.66	3.06	1.87	1.04	0.83	3.04
Uzhhorod	1.13	1.91	3.01	4.03	5.01	5.31	5.25	4.82	3.33	2.02	1.19	0.88	3.16
Zaporizhzhia	1.21	2.00	2.91	4.20	5.62	5.72	5.88	5.18	3.87	2.44	1.25	0.95	3.44
Ivano-Frankivsk	1.19	1.93	2.84	3.68	4.54	4.75	4.76	4.40	3.06	2.00	1.20	0.94	2.94
Kyiv	1.07	1.87	2.95	3.96	5.25	5.22	5.25	4.67	3.12	1.94	1.02	0.86	3.10
Kropyvnytskyi	1.20	1.95	2.96	4.07	5.47	5.49	5.57	4.92	3.57	2.24	1.14	0.96	3.30
Luhansk	1.23	2.06	3.05	4.05	5.46	5.57	5.65	4.99	3.62	2.23	1.26	0.93	3.34
Lviv	1.08	1.83	2.82	3.78	4.67	4.83	4.83	4.45	3.00	1.85	1.06	0.83	2.92
Mykolaiv	1.25	2.10	3.07	4.38	5.65	5.85	6.03	5.34	3.93	2.52	1.36	1.04	3.55
Odesa	1.25	2.11	3.08	4.38	5.65	5.85	6.04	5.33	3.93	2.52	1.36	1.04	3.55

Continuation of Table 4.3

1	2	3	4	5	6	7	8	9	10	11	12	13	14
Poltava	1.18	1.96	3.05	4.00	5.40	5.44	5.51	4.87	3.42	2.11	1.15	0.91	3.25
Rivne	1.01	1.81	2.83	3.87	5.08	5.17	4.98	4.58	3.02	1.87	1.04	0.81	3.01
Sumy	1.13	1.93	3.05	3.98	5.27	5.32	5.38	4.67	3.19	1.98	1.10	0.86	3.16
Ternopil	1.09	1.86	2.85	3.85	4.84	5.00	4.93	4.51	3.08	1.91	1.09	0.85	2.99
Kharkiv	1.19	2.02	3.05	3.92	5.38	5.46	5.56	4.88	3.49	2.10	1.19	0.9	3.26
Kherson	1.30	2.13	3.08	4.36	5.68	5.76	6.00	5.29	4.00	2.57	1.36	1.04	3.55
Khmelnytskyi	1.09	1.86	2.87	3.85	5.08	5.21	5.04	4.58	3.14	1.98	1.10	0.87	3.06
Cherkasy	1.15	1.91	2.94	3.99	5.44	5.46	5.54	4.87	3.40	2.13	1.09	0.91	3.24
Chernihiv	0.99	1.80	2.92	3.96	5.17	5.19	5.12	4.54	3.00	1.86	0.98	0.75	3.03
Chernivtsi	1.19	1.93	2.84	3.68	4.54	4.75	4.76	4.40	3.06	2.00	1.20	0.94	2.94

Note: according to NASA

In most cases, the average annual solar radiation intensity level of 11–12 kWh/m^2 is sufficient for the construction of a solar power plant to be economically feasible.

Based on the intensity of solar radiation, which is the main factor determining the power of a photovoltaic cell, the SPP parameters are calculated. The electrical power (N, W) for a solar power plant with photovoltaic cells is determined by the formula [18]:

$$N = \eta_{PV} \cdot F_{PV} \cdot I, \quad (4.1)$$

where η_{PV} – efficiency of photovoltaic converters (0.12–0.17); F_{PV} – total area, m^2; I – solar radiation intensity, W/m^2.

4.1.3.1 DISADVANTAGES OF SOLAR ENERGY

The existing advantages of solar energy (silence, autonomy, available energy resource, etc.) are reduced by significant disadvantages.

Intermittent cycle. Dependence on weather and time of day. Energy can only be generated during the day in clear weather. In adverse weather conditions (cloudy weather), solar panels simply do not work, which leads to a sharp reduction in the production of electricity by SPPs.

Low power per square meter. One of the most important parameters of electricity is the average power density per square meter (m^2), which is measured in W/m^2 and the amount of energy that can be obtained from a unit of area. For solar energy, this figure is on average 170 W/m^2, this value is greater than for all used renewable energy sources, but compared to traditional energy

sources (oil, coal, gas, nuclear energy), this figure is much lower. Which leads to an increase in the area of solar panels for the production of 1 kW of energy.

Impact on the ecosystem. Solar vacuum power plants are equipped with mirrors with precise focus. If a bird falls into the focus of the mirrors, it dies instantly. According to some sources, one bird dies every two minutes above large solar installations.

Environmental pollution. Solar energy as a source is the most environmentally friendly type of energy. But for its production it is necessary to produce solar panels, during the production and utilization of which greenhouse gases are emitted into the atmosphere, and chemical compounds containing: lead, cadmium, gallium, arsenic, etc. [18], which are dangerous for the environment and humans.

4.1.4 BIOENERGY

Bioenergy is a branch of the global energy industry based on the production and use of biofuels based on the use of biomass, including the following technologies: direct combustion and pyrolysis of wood fuel and solid household waste; biogas technologies; production of liquid biofuels for vehicles.

Biomass is biologically renewable substances of organic origin that undergo biological decomposition (wastes from agriculture (crop and livestock farming), forestry and technologically related industries, as well as the organic part of industrial and household waste).

The main sources of biomass for use in energy purposes can be divided into primary and secondary (waste).

Primary sources are biomass of trees, shrubs, some perennial grasses, algae. For these purposes, special "energy plantations" of fast-growing crops in natural conditions such as willow, poplar, reed, corn, oats, sorghum and others are created for their direct use as biofuel in power plants of thermal power plants, in boiler rooms, etc.

Secondary sources include:

– waste from the forestry, woodworking and pulp and paper industries, agricultural waste – residues of primary biomass (straw, husks of grain crops, oilseed cake) and waste from livestock and poultry farming (manure, litter);

– industrial liquid waste from industrial production (food industry, sugar industry, winemaking, etc.);

– municipal waste from urban treatment plants and landfills.

Depending on the sources and properties of organic raw materials, various technologies for its transformation and energy use are possible. The simplest classification divides the initial raw materials into "dry" (for example, wood waste) and "wet" (for example, livestock farm effluents). For the use of dry biomass, thermochemical technologies (direct combustion, gasification, pyrolysis) are most effective. For wet biomass, biochemical processing technologies with the production of biogas (anaerobic decomposition of organic raw materials) or liquid biofuels (alcoholic fermentation processes, etc.) are used.

Solid fuels include: firewood and their new modifications: fuel granules and briquettes, including pellets, which are pressed products from wood waste (sawdust, chips, bark, substandard wood, logging residues), straw, agricultural waste (sunflower husks, nut shells, manure), etc.

As a result of the application of modern thermochemical and biotechnologies, the energy stored in biomass is converted into biofuel, heat and electricity.

The most common types of biomass used as raw materials for obtaining fuel and using it to produce electricity or heat include:

– straw, corn stalks, sunflower; husks and other waste from processing sunflower, grain and other agricultural crops, etc. (in the processing process, granules (pellets), briquettes are obtained);

– annual and perennial plant biomass, energy plants (energy willow, sorghum, miscanthus, millet, etc.);

– wood, its waste and products of its processing (in the processing process, granules, pellets, briquettes are obtained);

– livestock and poultry waste;

– vegetable crop waste and their processing;

– plant waste from the food industry, peat;

– fruit biomass, etc.

For energy production, solid biomass is used, as well as liquid and gaseous fuels obtained from it: biogas, biodiesel, bioethanol [19].

Biomass can also be used for energy purposes by direct combustion (wood, straw, sewage sludge), as well as in the processed form of liquid (rapeseed oil esters, alcohols, liquid pyrolysis products) or gaseous biofuels (biogas from agricultural and crop waste, sewage sludge, solid household waste, gasification products of solid fuels) (**Fig. 4.6**).

Renewable energy production is rapidly developing in most European countries and the USA.

The annual growth of biomass in the world is estimated at 200 billion tons in terms of dry matter, which is energy equivalent to 80 billion tons of oil.

During 2021, 992 million kWh of "green" electricity was produced in Ukraine from biomass and biogas, which is 7.7 % of the total electricity production from renewable sources in 2021 [20]. According to the Ministry of Energy, bioenergy in Ukraine as of 2021 operated with a total capacity of 275.9 MW [20].

The steady trend of increasing biomass energy production observed in Ukraine indicates its desire to comply with global trends in the development of alternative energy. In terms of resources, the presence in the country of powerful agricultural and forestry enterprises, with a favorable climate and large areas of free land suitable for traditional agricultural production creates all the necessary prerequisites for an increase in the share of biofuels produced from biomass. The agrarian orientation of the economy of our state determines the state's special interest in the priority development of the bioenergy complex, the foundation of which will be built in agriculture. Over the past 20 years, the supply of primary energy from biomass and biofuels in the world has increased by

a third and is about 11 % of the total primary energy supply (TPES), or almost 70 % of TPES from renewable sources. The supply of primary energy from biofuels and waste reached 4.241 million tons of oil equivalent in 2020, which replaces about 5.2 billion m^3 of natural gas (**Fig. 4.7**) [21].

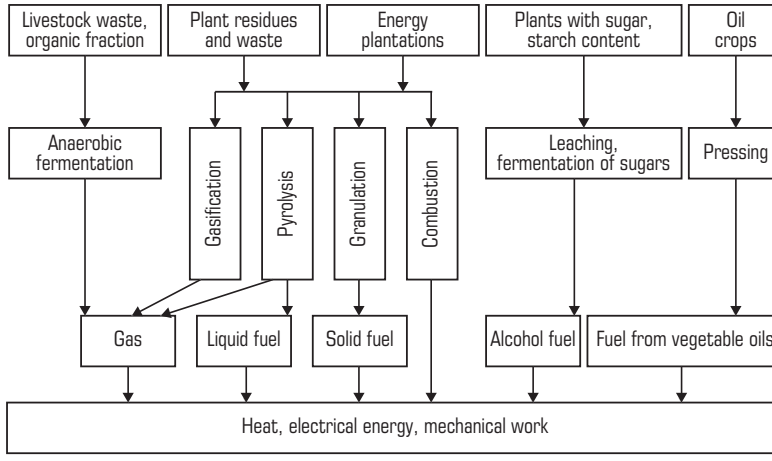

Fig. 4.6 Methods of energy production from biomass
Source: [19]

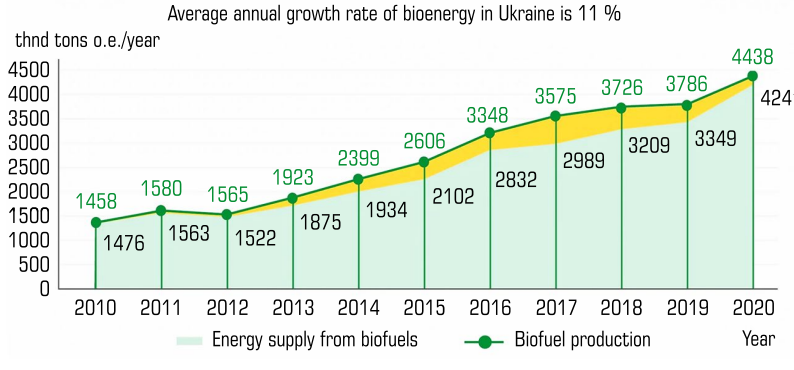

Fig. 4.7 Primary energy supply from biofuels

Ukraine has a large potential of biomass available for energy production, which is a good prerequisite for the dynamic development of the bioenergy sector. The economically feasible energy

potential of biomass in the country is about 20–25 MTOE per year. The main components of the potential are agricultural waste (straw, corn stalks, sunflower stalks, etc.) – more than 11 MTOE per year (according to 2015 data) and energy crops – about 10 MTOE per year. At the same time, agricultural waste is a real part of the biomass potential, and data on energy crops reflect the amount of biomass that can be obtained by growing these crops on free land in Ukraine. It should be noted that this process has been actively developing in the last few years.

Every year in Ukraine, about 2 million tons of biomass of various types are used for energy production. Wood accounts for the highest percentage of use of economically feasible potential – 80 %, while for other types of biomass (except for sunflower husks) this figure is an order of magnitude lower. The least actively (at the level of 1 %) is the energy potential of straw of grain crops and rapeseed (**Table 4.4**) [22].

Table 4.4 Energy potential of biomass in Ukraine

Biomass type	Theoretical potential, million tons	Part available for energy production, %	Economic potential, MTOE
Cereal straw	32.8	30	3.36
Rapeseed straw	4.9	40	0.68
By-products of corn production (stalks, cobs)	46.5	40	3.56
By-products of sunflower production (stalks, baskets)	26.9	40	1.54
Secondary agricultural residues (sunflower husks)	2.4	100	1.00
Wood biomass (fuel wood, logging residues, wood processing waste)	8.8	96	2.06
Wood biomass (deadwood, wood from protective forest belts, waste from pruning and uprooting of perennial agricultural plantations)	8.8	45	1.02
Biodiesel (from rapeseed)	–	–	0.39
Bioethanol (from corn and sugar beets)	–	–	0.82
Biogas from waste and by-products of the agricultural and industrial complex	2.8 billion m^3 CH_4	42	0.99
Biogas from solid waste landfills	0.6 billion m^3 CH_4	29	0.14
Biogas from wastewater (industrial and municipal)	0.4 billion m^3 CH_4	28	0.09
Energy plants:			
– willow, poplar, miscanthus	11.5 billion m^3 CH_4	100	4.88
– corn (for biogas)	3.0 billion m^3 CH_4	100	2.57
Peat	–	–	0.40
Total	–	–	23.10

Source: [22]

The potential for "total primary energy supply from biofuels and waste" by 2050 is given in **Table 4.5** [22].

Table 4.5 Summary indicators of the Roadmap for the development of bioenergy in Ukraine by 2050

Year	Installed capacity		Biofuel consumption*, MTOE	Natural gas displacement, billion m^3	Gasoline and diesel displacement, million tons	CO_2 emissions reduction, million tons per year
	MWt	MWel				
2020	8,206	202	3.77	4.34	0.17	8.90
2025	12,276	844	5.83	6.35	0.25	14.31
2030	19,087	1,846	8.57	9.11	0.39	21.35
2035	30,237	2,804	12.01	12.62	0.50	30.37
2040	39,338	3,609	15.13	15.77	0.67	38.66
2045	45,351	4,299	17.64	17.98	0.96	45.79
2050	49,655	5,230	20.28	19.92	1.23	54.40

Source: [22]

4.1.4.1 ADVANTAGES AND DISADVANTAGES OF BIOENERGY

The main advantages of bioenergy [23] are the utilization of organic waste, reducing environmental pollution. Biofuels are made from various raw materials, such as manure, crop waste and plants grown specifically for fuel. These are renewable resources that are unlikely to run out in the near future. Biofuels reduce greenhouse gas emissions. In addition, when growing crops for biofuels, they partially absorb carbon monoxide, which makes the biofuel system even more sustainable.

Biofuels are quite easy to transport, they have stability and a fairly high "energy density", they can be used with minor modifications to existing technologies and infrastructure.

The **disadvantages** of biofuels [23] include:

– limitations in regional suitability (in some areas it is simply impossible to grow biofuel crops, for example in areas with a cold or arid climate);

– water use – the less water used to grow crops, the better, as water is a limited resource;

– food security (too much biofuels can lead to famine). The problem with growing crops for fuel is that they will take up land that could be used to grow food;

– destruction of animal habitats and the risk of environmental change due to the use of fertilizers and pesticides when growing biofuel crops (most often monocultures for ease of cultivation).

4.1.5 THERMAL POWER

The main part of the electricity in the world as of the end of 2021 is produced at thermal power plants (TPPs). This is followed by hydroelectric power plants (HPPs) and nuclear power plants (NPPs) (**Table 4.1**) [1].

Thermal power plants. Coal, black oil, gas, and oil shale are usually used as fuel for thermal power plants. Fossil fuels are non-renewable resources. According to many estimates, coal on the planet will last for 100–300 years, oil for 40–80 years, and natural gas for 50–120 years.

It is known that thermal power plants are decisive in water and oxygen consumption, as well as in thermal pollution. A typical TPP with a capacity of 2 million kW consumes 18,000 tons of coal, 2,500 tons of black oil, and 150,000 m^3 of water daily. 7 million m^3 of water are used daily to cool the exhaust steam at thermal power plants, which leads to thermal pollution of the cooling reservoir. The following are emitted with the products of fuel combustion (of the total amount): ~30 % of solid aerosol particles, ~60 % of sulfur oxides (SO_2) and nitrogen oxides (NO_x), as well as the main share of CO_2 as a determining factor in the greenhouse effect, which leads to climate warming.

The impact of the energy sector on the environment strongly depends on the type of fuel used. The most "clean" fuel is natural gas, which produces the least amount of substances that pollute the atmosphere when burned. This is followed by oil (black oil), hard coal, brown coal, shale, peat.

As mentioned above, many by-products are formed during the combustion of fuel. When burning coal, a significant amount of ash and slag is formed. Most of the ash can be captured, but not all. All exhaust gases are potentially harmful, even water vapor and carbon dioxide CO_2. These gases absorb infrared radiation from the Earth's surface, and some of it is reflected back to the Earth, creating the so-called "greenhouse effect". If the level of CO_2 concentration in the Earth's atmosphere increases, global climate change may occur.

When fuel is burned, heat is generated, some of which is released into the air, leading to thermal pollution of the atmosphere. This, ultimately, entails an increase in the temperature of water and air basins, melting glaciers, etc. This, ultimately, causes an increase in the temperature of water and air basins, melting glaciers, and similar phenomena. In turn, an increase in temperature can cause profound climate changes throughout the Earth.

The effect of a large number of solid particles entering the atmosphere can be equally catastrophic. **Tables 4.6, 4.7** provide quantitative data on various substances formed during the operation of a typical 1000 MW thermal power plant using organic fuel [24].

Table 4.6 Emissions of pollutants during the operation of a 1000 MW thermal power plant

Contaminant	SO_x, t	N_xO_x, t	CO_2, t	CO, t	Solid particles, t	Radioactivity*, Bq	Flue gases, GJ	Heat of condensation, GJ
Per year	1 100	350	72 500	94	300	259	1 350	4 050

*Note: *Radioactivity is mainly caused by the radium isotopes ^{235}Ra and ^{238}Ra. Data are given for coal. For oil, this figure is 50 times lower*

Table 4.7 Comparison of the TPP and NPP operation with a capacity of 1000 MW for one year of operation

Parameters	TPP	NPP
Fuel demand	3.5 million tons of coal	1.5 tons of enriched uranium (or 1 thousand tons of uranium ore)
CO_2 emissions	10 million m^3	Does not release
SO_2 and other acid rain emissions	More than 400 thousand tons	Does not release
Solid waste	100 thousand tons of ash	About 2 tons (radioactive!)

TPPs are characterized by high radiation and toxic pollution of the environment. This is due to the fact that ordinary coal and its ash contain trace impurities of uranium and a number of toxic elements in much higher concentrations than the earth's crust.

The impact of energy on the environment strongly depends on the type of fuel used. The most "clean" fuel is natural gas, which produces the smallest amount of substances that pollute the atmosphere when burned. This is followed by oil (black oil), hard coal, brown coal, shale, peat.

As mentioned above, many by-products are formed during the combustion of fuel. When burning coal, a significant amount of ash and slag is formed. Most of the ash can be captured, but not all. All exhaust gases are potentially harmful, even water vapor and carbon dioxide CO_2. These gases absorb infrared radiation from the Earth's surface and some of it is reflected back to Earth, creating the so-called "greenhouse effect". If the CO_2 concentration in the Earth's atmosphere increases, global climate change may occur.

During coal combustion, most of the uranium, thorium and their decay products are released from the original coal matrix and distributed between the gas and solid fractions. Almost 100 % of the radon present is converted to the gas phase and is released with the flue gases [25].

In addition to flue gases, the main sources of radionuclides entering the environment during coal combustion at power plants include the removal of coal particles from open coal storage sites (coal drift) and ash dumps [26]. During combustion, most of the mineral fraction of coal melts and forms a glassy ash residue, a significant portion of which remains in the form of slag. Heavy particles are trapped in the ash, but the lightest part of the ash, the so-called "fly ash", is carried along with the gas flow into the power plant pipe. The specific efficiency of ash-carryover increases with increasing dispersion.

Highly dispersed ash is practically not captured by equipment for cleaning TPP gases [27], so flue gases are the main source of pollution from power plants.

The total emission of radionuclides at coal-fired power plants, on average, is about $1.33 \cdot 10^{10}$ Bq per 1 GW. **Table 4.8** shows the average annual emissions of radionuclides from US TPPs according to [28] per 1 GWh.

It is seen that the main share is contributed by radon isotopes, which in total give $1.2 \cdot 10^{10}$ Bq per GWh of electricity.

Table 4.8 Average annual emissions of radionuclides from a thermal power plant, Bq/ GWh

Radionuclide	Bq/ GWh	Half-life period
^{220}Rn	$4.07 \cdot 10^{9}$	55,6 s
^{222}Rn	$8.14 \cdot 10^{9}$	3.8 days
^{238}U	$5.55 \cdot 10^{7}$	4.5 billion years
^{234}U	$5.55 \cdot 10^{7}$	245 thousand years
^{226}Ra	$4.44 \cdot 10^{7}$	1600 years
^{218}Po	$1.41 \cdot 10^{8}$	3 minutes
^{214}Pb	$1.41 \cdot 10^{8}$	27 minutes
^{214}Po	$1.41 \cdot 10^{8}$	0,00016 s
^{210}Pb	$1.41 \cdot 10^{8}$	22 years
^{210}Po	$1.41 \cdot 10^{8}$	138 days
^{216}Po	$8.88 \cdot 10^{7}$	0.15 s
^{212}Pb	$8.88 \cdot 10^{7}$	11 years
^{40}K	$1.96 \cdot 10^{8}$	1.3 billion years

The isotope ^{210}Pb accumulates in ash especially intensively due to thermochemical processes, so that its concentration increases by 5–10 times [29]. It is known that lead and its compounds are toxic. In particular, when entering the body, lead accumulates in bones, causing their destruction. **Table 4.9** presents typical ratios of concentrations of the main radionuclides in coal, slag and fly ash according to [30].

Fly ash emitted into the air poses a great danger due to its ability to spread over considerable distances and penetrate human lungs. Fine fractions of fly ash are enriched with various harmful substances. In addition to radionuclides, they contain heavy metals and trace elements Co, V, Cu, Zn, Cr, Ni, Cd, As, Be [31]. For example, in soils located in the zone of influence of TPPs, concentrations of vanadium up to 110 mg/kg, beryllium – up to 15–50 mg/kg of dry soil were observed [32].

Table 4.9 Specific activity of the main radionuclides in coal, slag and ash in Bq/kg

Isotope	Coal	Slag	Fly ash
^{238}U	9–31	56–185	70–370
^{226}Ra	7–25	20–166	85–281
^{232}Th	9–19	59	81–174
^{40}K	2–130	230–962	233–740

The dispersion of pollution with flue gases occurs over large areas, since TPP emissions into the atmosphere are carried out at an altitude of 100–300 m.

The average emissions of the main radionuclides, the density of contamination of the territory and their retention in the atmosphere in the area of the nominal average TPP location, according to [29], are presented in **Table 4.10**.

Specific emissions of harmful substances with TPP flue gases and exhaust gases of gas turbine plants when using different fuels are given in **Table 4.11**.

Gross emissions and fuel consumption for a 1000 MW TPP are given in **Table 4.12**.

Table 4.10 Average emissions of the main radionuclides, the density of contamination of the territory and the RN concentration in the air per 1 GWh in the area of the nominal TPP location

Indicators	Radionuclides					
	^{226}Ra	^{228}Ra	^{210}Pb	^{210}Po	^{232}Th	^{40}K
Annual emission, 10^{10} Bq	1.96	1.11	8.14	7.40	1.96	19.61
Territory contamination density, 10^{7} Bq/km^2	38.85	9.25	114.70	70.30	–	388.5
Air concentration, 10^{-8} Bq/l	6.29	4.07	14.80	14.43	6.29	–

Table 4.11 Specific emissions of atmospheric pollution (g/kWh) from the combustion of organic fuels (according to the International Institute for Applied Systems Analysis, Vienna)

Emissions	Fuel type			
	Coal	Brown coal	Black oil	Natural gas
SO_2	6.0	7.7	7.4	0.002
NO_x	2.8	3.4	2.4	1.9
Solid particles	1.4	2.7	0.7	–
Fluorine compounds	0.05	1.11	0.004	–

Source: [33]

Table 4.12 Gross emissions (thousand tons/year) and fuel consumption for a 1000 MW TPP

Emissions	Type and annual fuel consumption		
	Natural gas ($1.9 \cdot 10^9$ m^3)	Black oil ($1.57 \cdot 10^6$ t)	Coal ($2.3 \cdot 10^6$ t)
SO_2	0.012	52.7 139,0	139.0
NO_x	12.0	22.0	21.0
CO	insignificant	0.08	0.21
solid particles	0.46	0.73	4.49
hydrocarbonates	insignificant	0.67	0.52

Note: Content: in black oil $S^p = 1.6$ %; in coal $S^p = 3.59$ %
Source: [33]

Substances emitted by heat and power enterprises when operating on various types of fossil fuels are given in **Table 4.13**.

Annual emissions from a 1000 MW fossil fuel TPP are presented in **Table 4.14**.

Table 4.13 List of substances emitted by heat and power enterprises when operating on various types of fossil fuels

Fuel type	Gaseous substances	Aerosols	Impurity elements
Coal	NO, NO_2, SO_2, SO_3, CO_2, HCl, HF, Hg (vapors), As(vapors) – The Donetsk deposit is very rich in arsenic., H_2S, NH_3	Fly ash, soot; formaldehyde, benzopyrene; ^{40}K, ^{226}Ra, ^{232}Th(thorium),	As, Cd, Pb, Ti, Cr, Na, Ni, V, Cu, Zn, Mn, Mo, Sb, SiO_2, Al_2O_3, TiO_2, NO_{3-}, SO_4^{2-}
Black oil	NO, NO_2, SO_2, SO_3, CO, CO_2, Hg (vapors), hydrocarbons	Ash (V_2O_5), formaldehyde, benzopyrene, soot (ash contains particles of unburned fuel, soot does not contain these particles)	As, Cd, Pb, Ti, Cr, Na, Ni, V, Cu, Zn, Mn, Mo, Sb – these particles are usually removed from the surface of boilers during cleaning
Gas	NO, NO_2, CO, CO_2, SO_2 traces, hydrocarbons	Hydrocarbons	–

Source: [33]

Table 4.14 Annual emissions from a 1000 MW fossil fuel TPP

Fuel type	Substance, t/year							
	NO_2	CO	SO_2	Solid particles	V_2O_5	Benzapyrene, $C_{20}H_{12}$	Formaldehyde HCOH	Total
Natural gas	13,888	14681	–	2	–	0.0009	–	28,564
Black oil	23,242	27,975	153,786	1,090	2,150	0.018	1,200	209,442
Coal (brown)	45,114	530,405	269,864	134,366	–	0.13	2,850	982,600

Source: [33]

4.1.6 NUCLEAR ENERGY

Nuclear energy is the most important subsector of the global energy industry. The low cost of electricity produced by NPPs represents serious competition to other types of power plants. Nuclear generation is 6 times cheaper than "green" and 3 times cheaper than thermal [34].

A clear advantage of NPPs is the absence of aerosol and greenhouse gas emissions into the atmosphere. According to the Intergovernmental Panel on Climate Change (IPCC) [35–37], greenhouse gas emissions from nuclear power over the entire life cycle are equal to 12 tons of CO_2 equivalent per GWh. For comparison: wind power plants – 11 t CO_2 equivalent per GWh, hydropower

plants – 24 t CO_2 equivalent per GWh, solar power plants – 48 t CO_2 equivalent per GWh, gas – 490 t CO_2 equivalent per GWh, coal – 820 t CO_2 equivalent per GWh. If to evaluate the planetary scale, the operation of all nuclear power plants in the world saves greenhouse gas emissions at the level of 2 billion tons of CO_2 equivalent per year, which is proportional to the absorption capacity of the entire forest massif of the planet. A positive factor is also material intensity.

Studies by the Joint Research Center (Jointresearchcenter) at the European Commission [38] show that nuclear power has the lowest specific material intensity compared to other low-carbon types of generation. For example, the metal content for the production of 1 MWh of electricity at NPP is 13 times less than in wind generation. It is also important that NPP requires a relatively small area: for example, 950 hectares of land are required to install a 1 GW WPP, and 28 hectares NPP of the same capacity. At the same time, NPPs provide a stable base load of networks, which does not depend on weather conditions, 24 hours a day, 7 days a week for at least 60 years.

NPPs emit very little CO_2 during their life cycle. The criterion for inclusion in the Taxonomy of electricity generation technology is emissions of less than 100 g/kWh. According to the JRC report [39], NPPs emit an average of 28 g/kWh of CO_2, which is comparable to the emissions of hydro and wind power plants, and even lower than that of solar panels, which have an average emission of about 85 g/kWh. The figures vary from source to source (for example, the ICPP 2014 report [40] gives average emissions for NPPs at 12 g/kWh and for industrial photovoltaics at 48 g/kWh), but the order and ratio are approximately the same. Emissions from gas and coal-fired plants are around 500 and 900 g/kWh, respectively.

According to the IAEA PRIS [41] as of January 1, 2024:

– there are 412 operating reactors in operation worldwide (excluding 25 reactors that have been shut down) with a gross installed capacity of 391,387 MW; 57 reactors are under construction;

– the total NPP number in the world with the status of operating reactors is 170 NPPs; with the status of operating reactors and suspended in operation – 179 NPPs.

Nuclear power can currently be considered as the most promising. This is due to both relatively large reserves of nuclear fuel and a gentle impact on the environment. The advantages also include the possibility of building NPP without being tied to resource deposits, since their transportation does not require significant costs due to small volumes. It is enough to note that 0.5 kg of nuclear fuel allows to get as much energy as burning 1000 tons of coal.

NPPs are safe, reliable and do not emit greenhouse gases, and therefore it is worth considering nuclear power as the most attractive industry for investment. On the other hand, it is impossible not to note the issues of volumes, cost of disposal and safety of radioactive waste produced, which require separate research. In addition, the article [42] discusses the risks of man-made disasters using the examples of events at the Three Mile Island NPP (1979), the Chernobyl NPP (1986), and Fukushima-1 (2011). Among the causes of accidents, errors and shortcomings in the design of the plants and the human factor are primarily highlighted. However, it is noted that after the mentioned events, the designs of nuclear power plants were revised in such a way as to ensure a significant increase in the safety of their operation.

Currently, small modular reactors (SMRs) [43], which produce electricity in the range of 10 to 300 MW [44–48], are considered particularly promising, offering more compact and cost-effective alternatives to conventional nuclear reactors. This makes them particularly attractive for use in smaller or remote locations.

The development of SMRs, which began in the 1970s, has accelerated significantly in recent years due to the increasing demand for clean energy sources and advances in technology. Key design features of SMRs that ensure their increased safety and efficiency compared to classic nuclear reactors include:

– optimized geometric arrangement of the reactor, which minimizes the possibility of accidents;
– application of passive safety systems that operate without external intervention in emergencies;
– simplicity of design to facilitate maintenance and repair.

Thus, SMRs open wide opportunities for the production of electricity, hydrogen and heat. They can be located both on land and in water. The SMR-160, designed as an advanced PWR-type SMR, has a thermal capacity of 525 MW and an electrical capacity of 160 MW [45].

The design includes robust passive safety systems to provide protection against design basis accidents, acts of sabotage or unintentional human actions. According to the Holtec development concept, the SMR-160 is designed for "safe abandonment" in design basis incident situations, allowing for safe dissipation of residual heat without the need for operator action. By combining fully passive safety systems with natural circulation in the primary circuit, the design is significantly simplified compared to classic NPPs, which contributes to the ease of its manufacture, construction and maintenance. The modular design of the SMR-160 involves the manufacture and assembly of key components in advance, which allows for a reduction in the construction time of each NPP – up to 24 months.

4.2 METHODOLOGY FOR SUBSTANTIATING THE CHOICE OF THE TYPE OF ENERGY RESOURCE FOR THE REGION

According to studies [49], any energy source is characterized by two parameters: energy density and speed of its transmission.

The product of these values is the maximum power that can be obtained from a unit of surface using the energy of this type.

For solar energy, this value in the near-Earth space is more than a kilowatt per square meter, and at sea level, taking into account losses in the atmosphere, a flow of 100–200 watts per square meter can actually be used. This flow is sufficient for life on the planet, but as the main source of energy for humanity it is extremely inefficient.

Similar problems limit the use of geothermal energy due to the heat-conducting properties of rocks.

Hydropower of river flows and the use of sea tides is no more than 5 % and is profitable only in mountainous areas, when there is a large potential energy per unit area of the reservoir.

The use of wind, also due to the insufficient density of the energy flow, turns out to be economically insufficiently justified.

Sources with high energy density – fuel cells – are characterized by a low rate of its transmission, so the real energy consumption does not exceed 200 W/m^2.

In addition, it is worth considering such an indicator as the installed capacity utilization factor (abbreviated as ICUF). It indicates the efficiency of the operation of electric power enterprises. It is calculated as the ratio of the arithmetic average capacity to the installed capacity of the electric power plant for a certain time interval [50]. Thus, if there are two power plants – nuclear and solar, with the same nominal capacity (720,000 MWh/month), the solar power plant will produce only 15–30 % of this value, since it directly depends on the sun. This indicator will be its ICUF.

Taking into account the above, there is a need to introduce the "General indicator for the selection and development of energy production taking into account the environmental component" of the Paris Agreement [51].

4.2.1 COMPREHENSIVE ASSESSMENT OF EFFICIENCY INDICATORS OF ENERGY RESOURCES

Analysis of the distribution and use of energy resources convincingly shows that energy production traditionally follows the availability of resources in the region and the need for energy. In this regard, an uneven concentration of industry and its accompanying environmental impact are created. To level the situation, it is necessary to have indicators that allow a comprehensive assessment of the possibilities of regions for the development of the economic sector, taking into account the availability of resources and minimal environmental impact.

In order to justify the choice of the preferred type of energy resource, using the example of the energy supply of the region (Odesa), the "Method of expert assessments of the use of energy resources (system efficiency)" was formed.

The most common energy resources are divided into two main categories: fossil and non-fossil [52] (**Table 4.15**).

Fossil resources are represented by hydrocarbons in various phase states.

Non-fossil resources, in turn, consist of renewable and manufactured resources.

Table 4.15 Main categories of energy resources

Fossil			**Non-fossil**						
			Renewable			**Manufactured**			
Coal, peat	Oil	Gas	Solar	Wind	Hydropower	Biogas	Household waste	Hydrogen	Nuclear

Fossil fuels – coal, natural gas and oil are the main sources of primary energy for thermal energy (thermal power).

In Ukraine, about 30 % of all electricity [53] is provided by thermal power. It works both on its own and on imported raw materials.

The operation of thermal power plants is accompanied by emissions of many greenhouse gases, the main of which are water vapor and carbon dioxide, which are formed during the combustion of all types of hydrocarbon fuels. The products of coal combustion and anthropogenic emissions of carbon dioxide accumulate in the atmosphere, contributing to the development of the greenhouse effect. The annual emission of CO_2 by all TPPs in the world is approaching 10 billion tons of carbon dioxide, accounting for about 30 % of all anthropogenic emissions of greenhouse gases into the atmosphere of the planet [54].

An important element of the study is the establishment of a comprehensive assessment of the efficiency indicators of the choice of the type of energy resource, favorable for electricity and heat supply in the conditions of a specific region.

To conduct such an assessment, the method of expert assessments [55] was used using a random number generator to form an information field about the values of the characteristics of energy resources and statistical processing of data on acceptable energy resources in the conditions of the regions under consideration.

The developed methodology was applied to analyze and form a number of preferences by type of energy resources of the large southern region of Ukraine – Odesa region.

The aim of the presented methodology is to form a comprehensive assessment of the degree of efficiency of electricity generation and pollution of the territories of energy production facilities based on the analysis of the values of the observed environmental indicators.

The methodology proposes two mutually complementary criteria, the resource preference index and the environmental preservation index, which evaluate a number of preferences of energy resources from the standpoint of accessibility and impact on the environment of a particular region.

To achieve the formulated aim, it is necessary to solve the following tasks:

– forming a list of observed indicators;

– forming limit or normalizing values of the observed indicators;

– consistent normalization according to permissible values, amounts of resources under consideration, and observed indicators.

The existing global trend provides for the preferential development of the use of non-fossil resources [56].

Each of the types of energy resources specified in (**Table 4.15**) is characterized by qualities, the totality of which in dimensionless form can be a criterion for making a decision on the preferential acceptability of using a particular resource.

The algorithm for constructing a comprehensive assessment of the efficiency of the system is the sequence of procedures is presented in **Table 4.16** [57].

Table 4.16 Algorithm for constructing a comprehensive assessment of the efficiency of systems

Stage	Procedure
Stage 1	Selection of a set of indicators characterizing the state of systems
Stage 2	Selection of reference systems by indicators
Stage 3	Assessment of intervals of partial indicators of system functioning
Stage 4	Average point estimate of values of temporary indicators of system functioning
Stage 5	Assessment of weighting coefficients for temporary indicators
Stage 6	Integral assessment of system functioning efficiency

Factors reflecting the applicability of the resource formed 6 groups, which include 27 indicators that have a positive (+) or negative (–) trend of change [57] (**Table 4.17**).

Table 4.17 Factors reflecting the applicability of the resource

No.	Group	Indicators		
1	2	3		
1	TECHNOLOGICAL FACTORS are variables related to the existence, availability and development of technology	1	+	Availability of the resource in the region
		2	–	Need to import resources
		3	+	Availability of delivery transport
		4	+	Availability, readiness
		5	+	Productivity
		6	+	Quality of the resources supplied
		7	+	Final carbon intensity of energy
2	ENVIRONMENTAL FACTORS are variables that are caused by the interaction of resources and the environment	8	–	Volume of waste
		9	–	Level of emissions in general
		10	–	Level of CO_2 emissions per TPES
		11	+	Waste recycling
		12	–	Waste disposal
		13	+	Safety of maintenance
3	RELIABILITY FACTORS are caused by the quality of service, the interaction of the system and the environment (technical, software, operational)	14	+	Reliability, failure
		15	+	Repairability
		16	+	Duration of operation
		17	+	Level of renewal of fixed assets
		18	+	Support of the life cycle of objects

Continuation of Table 4.17

1	2	3		
4	WEIGHT FACTORS are used to assess the need for space for implementation	19	–	Capital investments
		20	–	Dimensions
		21	–	Material intensity
5	TECHNICAL FACTORS include the need for resources for their own needs	22	–	Own energy consumption
		23	–	Consumption of reagents
		24	+	Possibility of utilization
6	INSTITUTIONAL FACTORS are related to management, regulation	25	+	Level of remuneration
		26	+	Quality of management
		27	+	Quality of personnel

4.2.1.1 ANALYSIS OF EXISTING COMPREHENSIVE ASSESSMENTS

The comprehensive approach is based on the formation of groups of indicators that reflect individual aspects of the state of the system. Siemens Corporation, together with the Economist Intelligence Unit, developed an expert methodology for a comprehensive assessment of cities, which includes eight groups of indicators:

1) greenhouse gas emissions;
2) energy consumption;
3) urban management;
4) transport;
5) water use;
6) waste and land use;
7) air quality;
8) environmental management, ensuring the reflection of all aspects of the functioning of the system.

For comparison, all indicators are normalized in a dimensionless form. The overall index is constructed as a quantitative sum of all groups, taking into account the weight assignment [57].

Similar expert assessments by international organizations Mercer Human Resource Consulting and The Blacksmith Institute [58] are also known in urban planning. Other indices for assessing the state of cities are constructed in a similar way.

For example, in the ecological safety of cities, the atmospheric pollution index, the threshold mass index of hazardous substances, the total hazard index of individual components polluting a particular biogeochemical environment (water, air and soil), etc. are used.

Indicators are estimated using the normalization of indicators. If the change intervals are known, the ratio is used for normalization:

$$I_i = \frac{p_i - p_{i,min}}{p_{i,max} - p_{i,min}}, \tag{4.2}$$

where p_i – the value of the i-th indicator for a certain object; $p_{i\,min}$, $p_{i\,max}$ – respectively, the minimum and maximum value of this indicator in the group of objects under study; I_i – the corresponding indicator.

When assessing surface water pollution, the water pollution index is often used:

$$I_{pw} = \frac{1}{6} \cdot \sum_{i=1}^{6} \frac{C_i}{MPC_i}, \tag{4.3}$$

where C_i – the values of the observed indicators; MPC_i – the maximum permissible concentrations of pollutants in water.

Integral indicators for assessment are determined by the relationship [59]:

$$I = \sum_{i=1}^{m} a_i \times I_i, \tag{4.4}$$

where I_i – indicators in the form of values of indicators that are normalized; a_i – weighting factors.

It seems effective to supplement relative indices with multi-stage normalization, which is used in [59]. Based on expert assessments, a reliable complex indicator for comparing the ecological load of the environment was obtained.

4.2.1.2 ENVIRONMENTAL POLLUTION INDICATORS AND THEIR STANDARDIZATION

The methodology presented below differs from that used in [57] by replacing expert assessments with monitoring control data or project documentation. To assess the pollution of territories, 6 groups were used, which contain 33 indicators (**Table 4.18**).

The technological group concentrates indicators that characterize the capabilities and needs of the analyzed systems. The environmental group includes a list of all possible undesirable impurities and their emission levels. The third group combines system reliability indicators. Other groups concentrate indicators of the general characteristics of the systems.

All available limit indicators are used as standardizing parameters: permissible limit values of the indicator (p_{max}; p_{min}), maximum permissible emissions (*MPE*) and maximum permissible concentrations (*MPC*).

The current values of the indicators are taken according to operational monitoring data or project technical documentation of the systems.

Table 4.18 Groupings and types of pollution indicators

No.	Type	No.	Type
1 – Technological		19	^{51}Cr
1	Productivity	20	Thorium
2	Energy consumption	21	Uranium
3	Water consumption as a reagent	22	Tritium into the atmosphere
4	Cooling water consumption	23	Suspensions
2 – Environmental (Emission level)		24	Tritium into the hydrosphere
5	Heat	25	Liquid waste
6	Water vapor	**3 – Reliability**	
7	CO_2 on TPES	26	Duration of operation
8	Carbon monoxide (CO)	27	Level of renewal of fixed assets,
9	NO_x	28	Quality of resources supplied
10	SO_x	29	Security of service
11	Hydrocarbons (5 20 %)	**4 – Technical**	
12	Inert radioactive gases	30	Own energy consumption
13	^{131}I	**5 – Institutional**	
14	$^{137}Cs_-$	31	Level of management
15	^{60}Co	**6 –Dimensions**	
16	^{90}Sr	32	Area occupied by the object
17	^{89}Sr	33	Territory of the region
18	^{54}Mn	–	–

4.2.1.3 COMBINED NORMALIZATION OF RESOURCE EFFICIENCY AND ENVIRONMENTAL POLLUTION INDICATORS

Normalization of current indicator values is performed in several stages.

The primary normalization of current indicator values was performed according to relations (4.2)–(4.4). If data on MPC were available, normalization was performed according to the relation:

$$I_i = \frac{C_i}{MPC_i}, \tag{4.5}$$

where C_i – the current values of the i-th indicator; MPC_i – the MPC value of the i-th indicator.

After the primary normalization, the individual indicator values are normalized by their sums for the systems being compared.

The obtained normalized indicator values are summed for each system and the obtained sums are normalized by their total sum.

4.2.2 RESULTS OF POLLUTING CAPACITY ASSESSMENT

Comparison of the polluting capacity of power plants using fossil resources, carried out according to the presented algorithm, confirmed the distribution of the latter by the degree of saturation of the environment with undesirable impurities (**Fig. 4.8**).

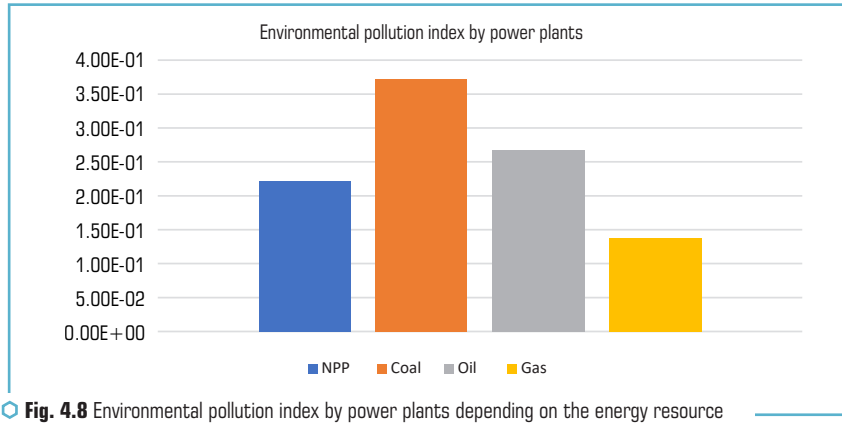

Fig. 4.8 Environmental pollution index by power plants depending on the energy resource

It should be noted that the initial data are of the most general nature without reference to specific objects.

The calculations adopted weighting factors in accordance with the recommendations [58, 60].

The results obtained are characterized by high stability, which indicates the stability of the methodology.

The maximum permissible value of the environmental pollution index by power plants is determined according to the given normalization scheme for its own values and is therefore equal to 1.

4.2.3 USING A COMPLEX INDICATOR FOR RESOURCE SELECTION

The environmental pollution index obtained according to the given methodology is a measure of the share of the maximum permissible relative pollution (**Fig. 4.9**).

The indicators of the environmental group, inherent in the nuclear resource and absent from the carbon group resources, neutralize the advantages of nuclear power plants with their quantity.

The indicators of the technological group and part of the environmental group, which are inherent in all types of resources, have the predominant values.

In the normalization process, the predicted pollution is reduced to unit productivity.

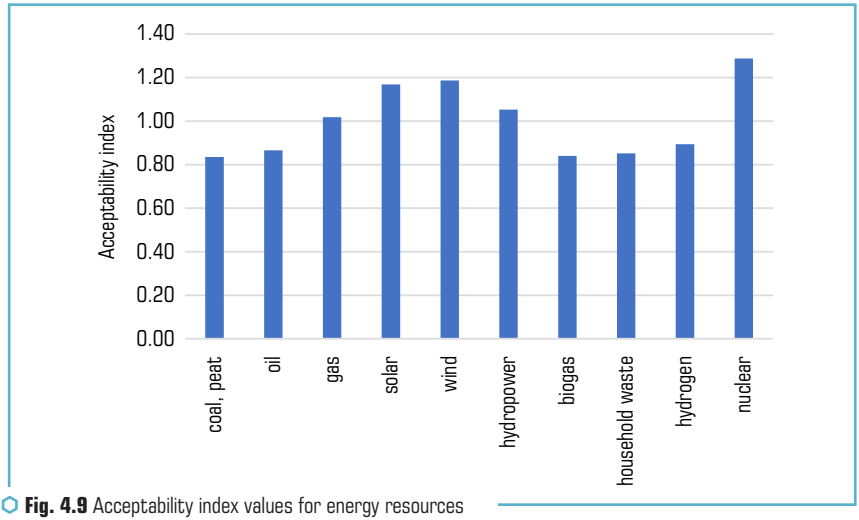

Fig. 4.9 Acceptability index values for energy resources

The lowest acceptability index values in the region under consideration are characteristic of traditional solid and liquid fossil resources, as well as for some resources made from waste and natural raw materials (0.8–0.9).

Fossil gas and hydropower are characterized by an acceptability index slightly higher than 1. Renewable resources (solar and wind energy) are distinguished by a noticeably higher index value (about 1.2). The most promising resource for the region was the nuclear energy resource, which reached an acceptability value of 1.3.

A comparison of the trends in the change in the acceptability index and the environmental protection index (**Fig. 4.10**) allows to note their synchronicity. At the same time, the module of the environmental protection index is slightly higher than the acceptability index for nuclear energy. The comparison made suggests that the acceptability of a particular energy resource for the region under consideration is largely regulated by the environmental characteristics of the resources.

The reliability of the results obtained when using the expert assessment method can be assessed by the degree of consistency of expert positions regarding each indicator using the Kendall concordance coefficient [61]:

$$W = \frac{12 \cdot S}{n^2 \cdot m \cdot \left(m^2 - 1\right)},$$

where S – the sum of the squares of deviations of all estimates of the ranks of each object of expertise from the average value; n – the number of experts; m – the number of objects of expertise.

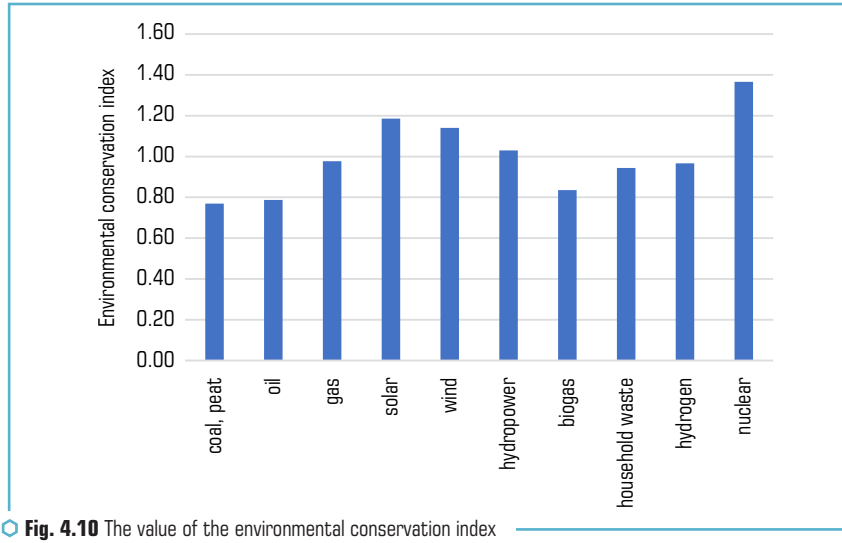

Fig. 4.10 The value of the environmental conservation index

The concordance coefficient (**Fig. 4.11**) varies in the range $0 < W < 1$, with the value $W = 0$ indicating complete disagreement, and $W = 1$ indicating complete unanimity.

For different indicators, the value of the concordance coefficient does not exceed 0.5. There is no specific trend in the change in the coefficient, which confirms the random nature of the data being analyzed.

This allows to extend the obtained patterns proportionally to the distribution of electricity production by type of resources (**Table 4.19**).

Table 4.19 Electricity production and pollution by region and resource (%)

Region	NPP	TPP		
		Coal	Oil	Gas
World	10.3/3.1	36.7/18.6	2.8/1	23.5/4.4
Ukraine	55/14.5	19.3/8.5	0.5/0.16	9.3/1.5

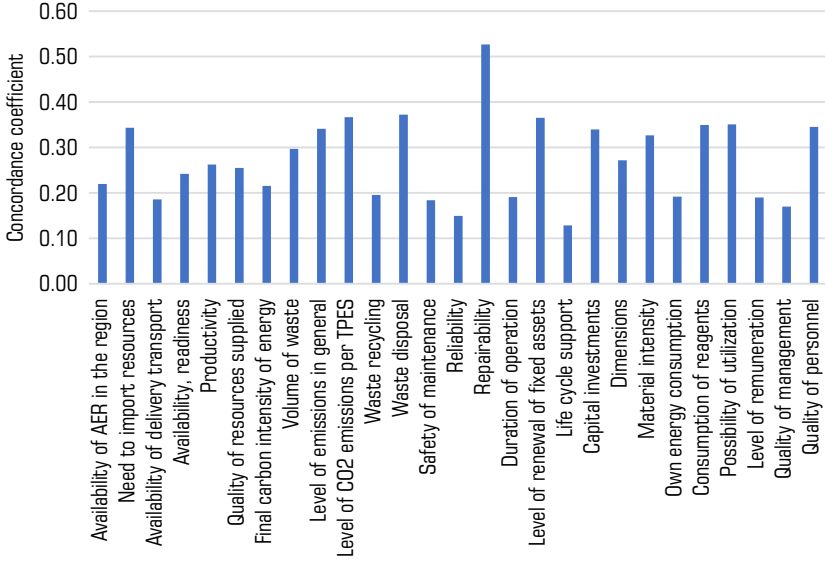

Fig. 4.11 Concordance coefficient

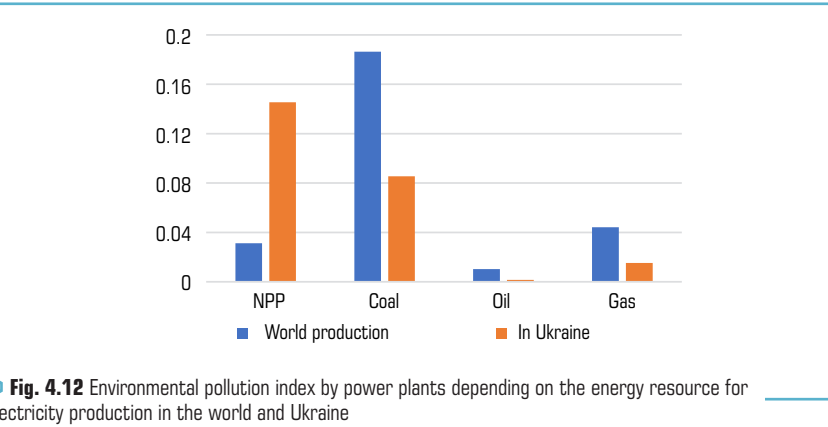

Fig. 4.12 Environmental pollution index by power plants depending on the energy resource for electricity production in the world and Ukraine

The results obtained differ in absolute values of acceptability for different types of resources and different methods. At the same time, the trends of change by resource are preserved.

CONCLUSIONS

Almost all types of energy resources are present in the energy complex of Ukraine. The overwhelming amount of energy is produced using traditional energy resources with a stable trend of using renewable resources.

Hydropower plants and pumped storage power plants produce up to 12 **%** of the total capacity. The use of the potential of small rivers is constrained by threats of disruption of the natural state of the ecological system.

Wind power plants are a new industry in the energy balance of Ukraine, its contribution to energy supply does not significantly exceed 1 **%** in the overall structure of electricity production with a tendency of gradual growth.

The development of the use of wind resources is constrained by characteristic disadvantages: wind dependence, noise pollution, impact on living organisms, change in the natural landscape.

The installed capacity of solar power plants is more than 7.5 GW and continues to grow, mainly in the southern regions, where solar insolation is longer.

The large potential of biomass available for energy production is a good prerequisite for the dynamic development of the bioenergy sector. The economically feasible energy potential of biomass in the country is about 20–25 MTOE per year.

The spread of solar power plants is restrained by: intermittent production mode, the need for storage, indirect impact on the environment, etc.

The spread of biomass potential is restrained by the need for a balance between food and industrial agriculture, the lack of effective waste processing technologies, etc.

The bulk of electricity in the world, and until recently in Ukraine, is produced at thermal power plants using fossil energy resources. Thermal power plants are decisive in the consumption of fossil resources, water and oxygen, as well as environmental pollution. The most "clean" fuel is natural gas, which produces the least amount of substances that pollute the atmosphere when burned. This is followed by oil (fuel oil), coal, brown coal, shale, peat.

Nuclear energy is the most important subsector of the global energy industry. The low cost of electricity produced by nuclear power plants represents serious competition to other types of power plants. Nuclear generation is 6 times cheaper than "green" and 3 times cheaper than thermal. Its clear advantage is the practical absence of aerosol and greenhouse gas emissions into the atmosphere throughout its life cycle.

Energy production traditionally follows the availability of resources in the region and the need for energy, which creates an uneven concentration of industry and its accompanying environmental impact. To level the situation, it is necessary to have indicators that allow for a comprehensive assessment of the opportunities of regions for the development of the economic sector, taking into account the availability of resources and minimal environmental impact.

An integrated approach is based on the formation of groups of indicators that reflect individual aspects of the state of the system.

Existing comprehensive indicators assess the efficiency of the used resource and its impact on the environment differently, as a result of which the detection of the impact of resource use on the environment is lost.

The proposed indicator is built on a monitoring study of 33 indicators, divided into 6 groups, reflecting the capabilities and needs of the analyzed systems.

The summaries of heterogeneous indicators are combined by normalization according to available limit indicators: permissible limit values of indicators, maximum permissible emissions and maximum permissible concentrations.

The proposed efficiency and pollution index consistently reflect the advantage of the resource for the region, taking into account technological, environmental, technical and other indicators.

The proposed efficiency and pollution index allows for independent justification of energy strategies of regions, taking into account their industrial, resource and environmental potentials.

REFERENCES

1. Statistical Review of World Energy (2023). Energy Institute. Available at: https://www.energyinst.org/__data/assets/pdf_file/0004/1055542/EI_Stat_Review_PDF_single_3.pdf
2. Harvey, R. (2024). Fossil fuel use, emissions hit records in 2023, report says. Reuters. Available at: https://www.reuters.com/business/environment/fossil-fuel-use-emissions-hit-records-2023-report-says-2024-06-19/
3. Yermolenko, H. (2023). Global electricity demand to grow by 3.3% in 2024. GMK Center. Available at: https://gmk.center/news/globalnyj-spros-na-elektroenergiju-v-2024-godu-vyrastet-na-3-3/
4. Heletukha, H. H., Zheliezna, T. A., Prakhovnik, A. K. (2015). Analiz enerhetychnykh stratehii krain YeS ta svitu i roli v nykh vidnovliuvanykh dzherel enerhii. Analitychna zapyska BAU № 13. Available at: https://uabio.org/wp-content/uploads/2020/04/uabio-position-paper-13-ua.pdf
5. Potreblenie elektroenergii v Ukraine k 2030 godu udvoitsya, - prognoz (2012). LB.ua. Available at: https://lb.ua/economics/2012/03/27/142943_potreblenie_elektroenergii.html
6. Pro skhvalennia Enerhetychnoi stratehii Ukrainy na period do 2030 roku (2013). Rozporiadzhennia Kabinetu Ministriv Ukrainy No. 1071-p. 24.07.2013. Available at: https://zakon.rada.gov.ua/laws/show/1071-2013-%D1%80#Text
7. Omelchenko, V. (2022). Ukraine's renewable energy sector before, during and after the war. Razumkov Centre. Available at: https://razumkov.org.ua/en/articles/ukraines-renewable-energy-sector-before-during-and-after-the-war
8. Zvit z otsinky vidpovidnosti (dostatnosti) heneruiuchykh potuzhnostei (2019). NPC «Ukrenergo». Available at: https://ua.energy/zvit-z-otsinky-vidpovidnosti-dostatnosti-generuyuchyh-potuzhnostej/
9. Landau, Yu. A. (2020). Analysis of the state and prospects of using hydropower resources in the development of the United power system (UES) of Ukraine. Hidroenerhetyka Ukrainy, 3–4, 16–21. Available at: https://uhe.gov.ua/sites/default/files/2020-12/8.pdf

10. Suchasnyi stan, problemy ta perspektyvy rozvytku hidroenerhetyky Ukrainy. Analitychna dopovid (2014). Natsionalnyi instytut stratehichnykh doslidzhen, 54.
11. Atlas enerhetychnoho potentsialu vidnovliuvanykh ta netradytsiinykh dzherel enerhii Ukrainy (2001). Natsionalna akademiia nauk Ukrainy, 41.
12. Solovev, A., Degtiarev, K. (2013). Vetrenaia vetrianaia energetika. Nauka i zhizn, 7, 42–47.
13. Yatseno, O. (2021). Nazvano oblasti Ukrainy, de naibilshe vitroelektrostantsii. EcoPolitic. Available at: https://ecopolitic.com.ua/ua/news/nazvano-oblasti-ukraini-de-najbilshe-vitroelektrostancij/
14. Palchevskaia, E. S., Kuimova, M. V. (2015). O preimushchestvakh i nedostatkakh vetroelektrostantsii. Molodoi uchenyi, 9 (89), 479–480.
15. Solar Service. Available at: https://solarservice.pro/karta-solnechnoj-aktivnosti-ukrainy
16. Renewable energy sector: Unlocking sustainable energy potential (2018). National Investment Council of Ukraine. Available at: https://publications.chamber.ua/Renewable%20energy%20sector.pdf
17. Surface meteorology and Solar Energy (2013). Available at: https://ntrs.nasa.gov/citations/20080012200
18. Labeish, V. G. (2003). Netraditsionnye i vozobnovliaemye istochniki energii, 79.
19. Babyna, O. M. (2018). The role of bioenergy in the development of agrarian sector of Ukraine. Black sea economic studies, 30–1, 28–32. Available at: http://www.bses.in.ua/journals/2018/30_1_2018/8.pdf
20. Omolchenko, V. (2022). Ukraine's renewable energy sector before, during and after the war. Razumkov Centre. Available at: https://razumkov.org.ua/en/articles/ukraines-renewable-energy-sector-before-during-and-after-the-war
21. Bioenerhetyka v Ukraini vzhe zamishchuie 5,2 mlrd kubometry pryrodnoho hazu (2021). Mirror of the Week. Available at: https://zn.ua/ukr/ECONOMICS/bioenerhetika-v-ukrajini-vzhe-zamishchuje-5-2-mlrd-kubometri-prirodnoho-hazu.html
22. Geletukha, G., Zheliezna, T., Matveev, Yu., Kucheruk, P., Kramar, V. (2020). Roadmap for bioenergy development in Ukraine until 2050. UABIO Position Paper № 26. Bioenergy Association of Ukraine. Available at: https://uabio.org/wp-content/uploads/2020/11/uabio-position-paper-26-en.pdf
23. Biopalyvo. Alternatyvna enerhetyka u sviti ta Ukraini (2016). Enerhiia pryrody. Available at: https://alternative-energy.com.ua/uk/vocabulary/біопаливо/
24. Shevchenko, V. V., Don, A. V., Kononova, T. G. (2019). Problems of modern electric power industry, ways of its development and estimation of electric power sources. Collection of works XVI International Scientific Conference «Science and Society», 61–73. https://doi.org/10.5281/zenodo.3892964
25. Radioactive Elements in Coal and Fly Ash: Abundance, Forms, and Environmental Significance. (1997). U.S. Geological Survey Fact Sheet FS-163-97. Available at: https://pubs.usgs.gov/fs/1997/0163/report.pdf

26. Maurichеva, T. S., Kiselev, G. P. (2006). Osnovnye polozheniia kolichestvennoi otsenki radioaktivnogo vozdeistviia ugolnykh TETS na okruzhaiushchuiu sredu. Vestnik Pomorskogo universiteta, 1 (9), 110.
27. Maurichеva, T. S. (2007). Kolichestvennaia otsenka postupleniia radionuklidov v okruzhaiushchuiu sredu pri rabote ugolnykh TETS na primere TETS-1 g Severodvinska. [Doctoral dissertation].
28. Study of Hazardous Air Pollutant Emissions from Electric Utility Steam Generating Units (1998). Final Report to Congress. Available at: https://www.epa.gov/airtoxics/combust/utiltox/eurtc1.pdf
29. Puchkov, L. A., Vorobev, A. E. (2000). Chelovek i biosfera: vkhozhdenie v tekhnosferu, 335.
30. Warner, F., Harrison, R. M. (1993). Radioecology after Chernobyl: Biogeochemical Pathways of Artificial Radionuclides. Wiley, 400.
31. Kovalenko, G., Piven, G. (2010). Environmental Risk for the Public Health from Releases from Thermal and Nuclear Power Plants of Ukraine. Nuclear and Radiation Safety, 4 (48), 50–56. https://doi.org/10.32918/nrs.2010.4(48).11
32. Kryshev, I. I. (2010). Ekologicheskaia bezopasnost iaderno-energeticheskogo kompleksa Rossii, 382.
33. V. A. Maliarenko, V. A., Kanilo, P. M. (2012). Incineration of organic fuels and ekologo-chemical safety. Energy saving. Power engineering. Energy audit, 11 (105), 30–37. Available at: http://eee.khpi.edu.ua/article/view/20805
34. Nuclear Power: Myth and Reality. Second Edition. (2010). Heinrich Boell Foundation, 352.
35. Novak, A. (2021). Razvitie atomnoi energetiki neobkhodimoe uslovie globalnoi klimaticheskoi povestki. Energeticheskaia politika, 9 (163), 6–11.
36. Technical assessment of nuclear energy with respect to the 'do no significant harm' criteria of Regulation (EU) 2020/852 ('Taxonomy Regulation') (2021). JRC Science for Policy Report. Available at: https://finance.ec.europa.eu/system/files/2021-03/210329-jrc-report-nuclear-energy-assessment_en.pdf
37. Core Writing Team, Pachaurim R. K., Meyer, L. A. (Eds.) (2014). Climate Change 2014: Synthesis Report. Contribution of Working Groups I, II and III to the Fifth Assessment Report of the Intergovernmental Panel on Climate Change. IPCC, Geneva, Switzerland, 151. Available at: https://www.ipcc.ch/site/assets/uploads/2018/02/SYR_AR5_FINAL_full.pdf
38. IAEA. The Power Reactor Information System (PRIS). Available at: https://pris.iaea.org/pris/home.aspx
39. Naskolko ekologichna atomnaia energetika Na samom dele tak zhe kak solnechnaia i vetrovaia. ITSOFT. Available at: https://habr.com/ru/articles/552964/
40. Ustanovlennaia moshchnost elektrostantsii. Available at: https://www.eeseaec.org/ustanovlennaa-mosnost-elektrostancij
41. Roberts, J. W. (2018). If nuclear energy is the answer, why doesn't everyone agree? Physics Education, 53, 024003. http://doi.org/10.1088/1361-6552/aa9f7c

42. Petrus, O., Zemerov, E., Pogosov, O. (2024). Technical and economic analysis of electricity supply to energy deficit regions using small modular reactors (SRM). Science and Technology Today, Series "Physical and Mathematical Sciences", 3 (31), 1035–1054. https://doi.org/10.52058/2786-6025-2024-3(31)-1035-1054
43. Advances in Small Modular Reactor Technology Developments (2022). International Atomic Energy Agency. Available at: https://aris.iaea.org/publications/SMR_booklet_2022.pdf
44. Lee, J. S., Kim, Y. S., Kim, J. H. (2022). A review of small modular reactors for power generation. Renewable and Sustainable Energy Reviews, 169, 108–109.
45. Zohuri, B. (2020). Nuclear Micro Reactors. Springer Nature, 120. https://doi.org/10.1007/978-3-030-47225-2
46. Ghimire, L., Waller, E. (2023). Small Modular Reactors: Opportunities and Challenges as Emerging Nuclear Technologies for Power Production. Journal of Nuclear Engineering and Radiation Science, 9 (4), 044501. https://doi.org/10.1115/1.4062644
47. Stadzhi, D. (2022). Matematika zelenoi energetiki khorosho no malo. Energy Business Magazine, 1–2, 1245–1246. Available at: https://e-b.com.ua/matematika-zelenoi-energetiki-xoroso-no-malo-3003
48. HOST 19431-84. Enerhetyka ta elektryfikatsiia. Terminy ta vyznachennia. (1986). Ministerstvo enerhetyky i elektryfikatsii SRSR.
49. Adoption of the Paris Agreement (2015). FCCC/CP/2015/L.9/Rev.1, 32. Available at: https://unfccc.int/resource/docs/2015/cop21/eng/l09r01.pdf
51. Maksmadiev, B. S., Ochilov, M. A., Mirzaev, Sh. N., Iuldashov, S. Sh. (2019). Types of Energy Resources and Possibilities of Development of Alternative Energy Based on Renewable Energy Sources in Uzbekistan. International Academy Journal Web of Scholar, 6 (36), 12–16. 10.31435/rsglobal_wos/30062019/6550
52. Struktura elektroheneratsii v Ukraini ta yii zviazok iz taryfamy na elektroenerhiiu (2021). Torhova Elektrychna Kompaniia. Available at: https://tek.energy/news/struktura-elektrogeneratsii-v-ukraini-ta-ii-zvyazok-iz-tarifami-na-elektroenergiyu
53. IPCC Report on Impacts, Adaptation and Vulnerability: Key Takeaways (2022). United Nations. Available at: https://www.un.org/climatechange/ipcc-wgii-report
54. Khalafian, A. A., Borovikov, V. P., Kalaidina. G. V. (2017). Teoriia veroiatnostei, matematicheskaia statistika i analiz dannykh: Osnovy teorii i praktika na kompiutere. STATISTICA. EXCEL, 320.
55. Pro skhvalennia Enerhetychnoi stratehii Ukrainy na period do 2035 roku "Bezpeka, enerhoefektyvnist, konkurentospromozhnist" (2017). Rozporiadzhennia Kabinetu Ministriv Ukrainy No. 605-p. 18.08.2017. Available at: https://zakon.rada.gov.ua/laws/show/605-2017-%D1%80#Text
56. Kozlov, I., Kovalchuk, V., Klymchuk, O., Dorozh, O., Sigal, A., Aksyonova, I., et. al. (2022). Assessing the region's energy provision. Eastern-European Journal of Enterprise Technologies, 2 (8 (116)), 13–20. https://doi.org/10.15587/1729-4061.2022.255740

57. Biliaiev, N. N., Shynkarenko, V. S., Gabrinets, V. A., Kalashnikov, I. V., Berlov, O. V. (2018). Modeling of atmosphere pollution and territorial risk assessment at emission of hazardous substances. Geo-Technical Mechanics, 140, 158–165. https://doi.org/10.15407/geotm2018.03.158
58. Zviagintseva, A. V. (2016). Veroiatnostnye metody kompleksnoi otsenki prirodno-antropogennykh sistem, 257.
59. Iaili, E. A. (2006). Nauchnye i prikladnye aspekty otsenki i upravleniia urbanizirovannymi territoriiami na osnove instrumenta riska i novykh pokazatelei kachestva okruzhaiushchei sredy, 448.
60. Savchuk, I. H. Konkordatsii koefitsiient. Slovnyk suspilnoi heohrafii. Available at: https://geohub.org.ua/node/4219

DOI: 10.15587/978-617-8360-02-3.CH5
Natalia Dunaievska, Taras Shchudlo, Ihor Beztsennyi,
Dmytro Bondzyk, Yevhen Miroshnychenko
© The Author(s) 2024. This is an Open Access chapter distributed under the terms of the CC BY-NC-ND license

CHAPTER 5

SCIENTIFIC AND TECHNICAL SOLUTIONS FOR IMPLEMENTING BIOMASS COMBUSTION AT COAL-FIRED TPP IN UKRAINE

ABSTRACT

The aim of the work is to develop a technology for co-firing of coal and biomass, which will allow to reduce emissions of CO_2, SO_2, NO_x, dust, as well as to diversify fuel sources for CHPs within the framework of ensuring compliance with standards for reducing pollutant emissions and solving problems with coal supply to power plants, and improving coal ignition conditions in fuel plants.

The article reviews biomass combustion and gasification technologies and their application for co-firing of pulverized coal with coal, and the possibility of using them in TPP boilers in Ukraine. The co-firing of pulverized coal brand G (gas) and heterogeneous biomass was experimentally investigated. A zone-by-zone thermal calculation of the boiler unit when feeding biomass with coal was performed. Using ANSYS FLUENT, the co-firing of coal with biomass was calculated for the selected solution of the biomass feeding system to the boiler fuel plant. Recommendations are provided for the application of co-firing of gas group coal and heterogeneous biomass at TPPs in Ukraine.

KEYWORDS

TPP, coal, biofuels, biomass, co-firing.

Co-firing of biomass with coal began in Europe and North America in the late 1990s. It has been proven to be a relatively rapid and cost-effective way to partially decarbonize coal-fired electricity generation in the short to medium term. Co-firing in coal-fired power plants can contribute to the achievement of the UN Sustainable Development Goals in Ukraine, such as Goal 7 "Affordable and Clean Energy" (by 2030, substantially increase the share of renewable energy in the global energy mix, strengthen international cooperation to facilitate access to clean energy research and technology, including renewable energy, energy efficiency and advanced and cleaner fossil fuel technologies), and Goal 13 "Climate Change" (integrate climate change measures into national policies, strategies and planning) [1]. Co-firing with biomass also helps extend the life of coal-fired power plants during the transition to other low-carbon types of generation. Although

most of Western Europe is gradually abandoning coal-fired power generation, which will reduce the opportunities for co-firing of biomass, coal remains an important fuel for electricity generation in Asia and Eastern Europe [2]. Co-firing activity is growing in these regions, so work on developing co-firing technologies is ongoing.

During the period of martial law, the earliest possible resumption of coal-fired TPPs became particularly important to ensure energy independence, supply heat and electricity to the population and, if possible, with simultaneous low-cost modernization with improved economic and environmental performance and given their small capacity compared to TPPs.

The authors fully support the global goal of the "green transition", enshrined in the legislation of Ukraine and the world by numerous legislative acts. But it should be noted that, as is already understood in most countries of the world and noted in reviews by the most authoritative global energy organization, the IEA [2], the world energy sector still faces a fairly long transition period of 20–30 years, when heat and electricity will be produced from both fossil and renewable fuels [3].

Despite the fact that many countries are abandoning fossil fuels, in 2023 global coal consumption reached a staggering 164 exajoules (EJ) of energy, which is a record for any year. Coal provides 26 % of global energy in 2023, more than all non-fossil fuel sources combined. The only energy source that made a greater contribution to the global energy balance was oil.

Here is how this consumption is distributed by region (**Table 5.1**).

Table 5.1 Coal consumption in different regions of the world (2023)

Region	Consumption (EJ)	Part, %
China	91.9	56.1
Asia Pacific (excluding China)	43.8	26.7
Americas	10.0	6.1
Europe	8.4	5.1
CIS	5.5	3.4
Africa	4.1	2.5
Middle East	0.4	0.2
Total	164.0	100

Source: [3]

Coal consumption has declined in many regions. For example, both North America and Europe reduced their coal energy consumption by 16 % in 2023. However, the heavy reliance on coal in the Asia-Pacific region has meant that global coal consumption has remained largely unchanged over the past 10 years. In 2023, China increased its coal consumption from 88 EJ to almost 92 EJ, accounting for 56 % of global coal consumption. This has largely contributed to Asia-Pacific becoming the global leader with a staggering 83 % of global coal consumption.

Easy access to existing infrastructure and reasonable prices has not only supported global coal consumption over the past 10 years, but have also paved the way for potential growth. Many developing countries are currently expanding their coal consumption.

For example, according to the Statistical Review of World Energy 2024, Bangladesh and Colombia experienced double-digit percentage increases in coal consumption from 2022 to 2023, compared to the previous year: 41 % and 53 %, respectively.

Coal continues to play a major role in the global energy mix, especially in developing countries, where its availability makes it the preferred energy source for them at present.

Coal-biomass co-firing technologies have been actively developing for over two decades as a partial replacement for fossil fuels in line with global trends. At the beginning of the 21st century, this technology was widely used in both Europe and North America [3]. For example, in 2015, the Netherlands built a demonstration power plant for energy conservation and deep reduction of CO_2 emissions, as well as CO_2 capture, consisting of a 1,100 MW supercritical unit + biomass combustion + closed water supply installation. The biomass utilization rate is 30 %, and the plant efficiency is over 47 %. Compared to the Netherlands, Finland built the world's largest circulating fluidized bed boiler with a capacity of 550 MW. Biomass, such as coal, sludge, wood, forest waste, etc., can be burned in any proportion in circulating fluidized bed boilers. As an example, the United Kingdom is the country with the largest use of biomass combustion technology, with an installed biomass combustion capacity of 25.336 GW by 2018 [4].

Today, due to the energy policy of these regions of complete abandonment of fossil fuels, co-firing of biomass with coal (CFBC) is undergoing a replacement stage at existing TPPs burning biomass or waste (DPAX TPP – Great Britain, AMAGER TPP – Denmark), but has found its second life in the countries of the Asia-Pacific region.

Thus, China is a large agricultural country with large biomass resources and great potential for the development and utilization of biomass energy, for which CFBC is a promising choice [5]. Utilization of agricultural waste in existing coal-fired power plants is an attractive option to reduce environmental pollution and reduce the overexploitation of fossil fuels [6]. Thanks to domestic measures to encourage and support the development of renewable energy, investment in biomass power generation is rapidly increasing, and the construction of various projects for power generation from agricultural and forestry waste has already begun. China's biomass power generation technology industry shows an overall trend of accelerated development [7]. In the first three quarters of 2019, biomass power generation in China added 3.35 million kW of installed capacity, and the total installed capacity was 21.16 million kW, an increase of 15.4 % over the previous year; The installed capacity of biomass power generation was 80.4 billion kWh, an increase of 19.4 % over the previous year [8]. By 2020, the installed capacity of coal-fired power plants in China will reach 1.1 billion kWh. If 50 % of biomass can be used for power generation in coal-fired power plants, the total capacity of coal-biomass power units can reach 550 million kWh. Based on an average blending rate of 10 %, the installed capacity of biomass power plants can reach 5.5 MW. If 50 % of biomass is used for power generation in China every year, the amount of electricity that

can be generated is about 720 billion kWh, which translates into an installed capacity of about 180 million kWh, accounting for 12 % of the national electricity generation in 2016 [9]. Large-capacity coal-fired power plants and high-efficiency coal-fired power plants are switching to co-firing of coal and biomass, which is expected to be the main carbon reduction measure at this stage in China.

Co-firing technology and efficiency are constantly developing in Indonesia to reduce coal consumption. Researchers in this technology focus on the behavior of biomass as the most complex fuel in the coal-biomass pair [10]. The type of biomass and the composition of the mixture used determine the efficiency of the boiler. The conditions of pre-mixing of biomass and coal are critical factors [11]. Biomass with high moisture content, low calorific value and poor grinding ability must be considered [12]. As a result, optimizing the quality of biomass is crucial to achieve high combustion efficiency.

As an example, the Indonesian PLN energy campaign. Co-firing was introduced as one of the strategic initiatives under the Green Booster program to accelerate the achievement of the 23 % renewable energy target by 2025 by using existing power plant infrastructure and waste management solutions. The total capacity of PLN Group's co-firing steam power plants is 18.9 GW [10]. Co-firing activities have been carried out at several PLN Group CFPP facilities since 2020 using various boiler types, namely: PC, CCS, etc. The types of biomass used include sawdust (30.8 %), palm shell (21.2 %), wood chips (15.4 %), wood pellets (11.5 %), rice husk (7.7 %), coconut shell, OPEFB, solid renewable fuel (SRF) pellets, water hyacinth and corn cobs (3.8 %).

It is recommended to improve fuel quality by hydrothermal treatment (HTT) to reduce the impact of biomass ash on such characteristics as alkalinity, high water content, and low calorific value. According to studies by Praevia and Widayat, the HTT process can increase the calorific value of biomass from 7.86 MJ/kg to 22.22 MJ/kg, which is comparable to the calorific value of coal (22.34 MJ/kg) [13].

The first studies on the influence of the chemical composition of biomass on slagging and corrosion of heating surfaces of existing boilers during the CFBC of domestic biomass and coal from Ukrainian deposits were initiated in Ukraine by the Institute of Heat and Power Technologies of the National Academy of Sciences of Ukraine [14–16]. Therefore, the use of foreign experience in CFBC and the introduction of this technology into the energy sector of Ukraine, especially in the war and post-war period, seems to the authors to be quite appropriate and economically justified.

Coal-fired TPPs in Ukraine are usually located either within or near settlements. Therefore, they are always subject to stricter emission requirements. Given the wear and tear of TPP equipment and the service life, as well as the significant costs of installing gas cleaning systems, it is not possible to expect their widespread installation of cleaning plants in the near future.

In addition, given the updated Energy Strategy of Ukraine for the period until 2050 [17], one of the urgent tasks of the Ukrainian energy sector is the need to increase the production of heat and electricity from renewable energy sources and reduce emissions of harmful substances and greenhouse gases from large combustion plants in accordance with Ukraine's commitment within the framework of the European Energy Community. Since biomass is CO2-neutral and contains

almost no sulfur and ash, it is an ideal fuel for generating energy without polluting the environment. In addition, replacing part of the coal with biomass leads to a significant reduction in the sulfur dioxide emission fee. Today, the emission of one ton of SO_2 costs about 2,500 UAH. Adding, for example, 10 % of biomass (in terms of heat) for a 300 MW power unit will reduce the sulfur dioxide emission fee by more than 4 million UAH per year.

5.1 COAL AND SOLID BIOFUEL CO-FIRING TECHNOLOGIES

5.1.1 EXISTING BIOMASS AND COAL CO-FIRING TECHNOLOGIES

Currently, there are three main technological schemes for co-firing of biomass and coal: direct, indirect and parallel combustion. The choice of the scheme depends on the design features of the boiler units, the ash composition [18] and the proportion of biomass in co-firing [19, 20].

For these schemes, **Fig. 5.1** shows the methods of co-firing of biomass at coal-fired TPPs and summarizes the main technical options for these configurations.

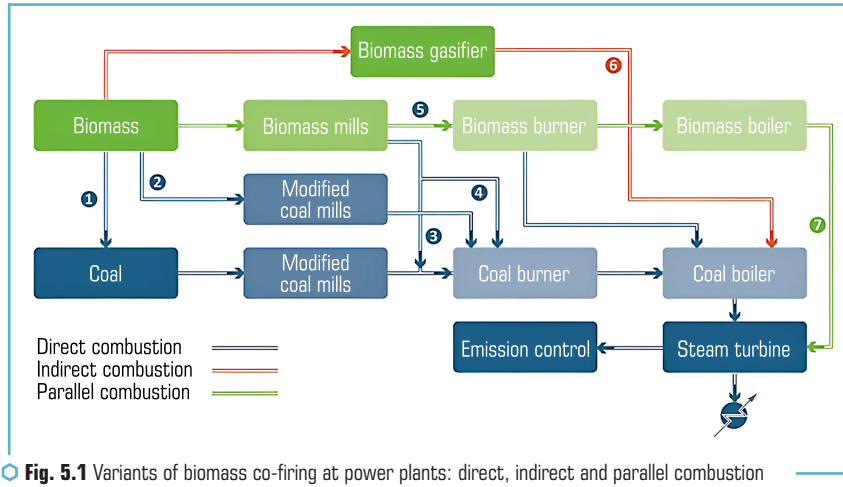

Fig. 5.1 Variants of biomass co-firing at power plants: direct, indirect and parallel combustion
Source: [17]

In direct combustion, coal and biomass are combusted in the same boiler. The biomass is premixed with the coal in the existing coal handling and transportation system, at moderate co-firing ratios (typically less than 10 % biomass in terms of energy), then co-combusted and combusted in the existing coal combustion system (Option 1 in **Fig. 5.1**). This is the most popular approach

to co-firing, as it can be implemented relatively quickly with minimal capital investment and minimal modifications. The main investment is the biomass storage and handling system. In Option 2, the biomass is comminuted in a separate, modified existing coal mill and combusted with the coal in the existing coal combustion system. The biomass can be comminuted in a new dedicated mill to increase the co-firing ratio; up to 50 % in terms of energy can be achieved.

There are then several ways to co-combust biomass. In Option 3, biomass is injected into a pipe that feeds coal to the burner. In Option 4, biomass is injected into modified coal burners. In Option 5, biomass is injected into a new dedicated biomass burner. These options involve much higher capital investment levels than Options 1 and 2. In indirect co-firing (Option 6), biomass is gasified in a separate gasifier, and the fuel gas is combusted with coal in the same coal boiler. Parallel (Option 7) combustion has separate boilers for coal and biomass, which are powered by a single turbine. This scheme allows the largest proportion of biomass to be used, and biomass types with high alkali and chlorine content can be burned [21].

Both indirect and parallel combustion allow for compositions with high biomass content and have greater fuel flexibility [17].

In the paper [22], co-firing technologies were summarized depending on the fuel: grate furnaces, fluidized bed furnaces (combustion in a fluidized bed or in boilers with a bubbling fluidized bed, or in boilers with a circulating fluidized bed) and pulverized coal combustion furnaces (**Table 5.2**).

Co-firing, depending on the technology (type of fuel), has its advantages and disadvantages.

Table 5.2 Co-firing technologies in the corresponding furnaces. Advantages and disadvantages

Fuel Type	Advantages	Disadvantages
1	**2**	**3**
Grates	– low investment costs for plants <20 MW and low operating costs; – almost any wood can be used; – suitable for biomass fuels with high moisture content (10–60 %wt); – suitable for fuels with high ash content and different particle sizes (with a limitation on the number of fine particles)	– mixtures of wood fuels can be used, but combinations of fuels with different combustion characteristics and ash melting points (e.g. mixtures of wood and straw) are sometimes not practical; – increased temperatures can cause ash melting and corrosion
Fluidized bed modifications	– wide range of fuels in terms of calorific value, moisture content and ash content, which allows fuel diversification and increasing the number of fuel types in existing power plants; – low combustion temperature in the bed, resulting in low NOx emissions; – provides the possibility of direct injection of limestone for sulfur removal, which is cost-effective (instead of flue gas desulfurization equipment);	– despite the wide range of fuels, it is not always possible to use the existing biomass supply system by pre-mixing the fuel (the cheapest option); – where the characteristics of the co-fired fuel differ too much from those of the primary fuel, a separate feeder must be installed; – slag formation and deposits on boiler walls and tubes when burning fuels with a high alkali content;

Continuation of Table 5.2

1	2	3
	– maximum combustion efficiency even with low-grade fuel; – environmental performance of FB plants with low CO, NOx emissions and high boiler efficiency (approx. 90 %); – fluidized bed technologies allow fuel conversion from coal to biomass/coal co-firing with relatively low investment	– agglomeration of the bed when burning fuels with a high alkali content; – Cl-corrosion on heat exchange surfaces (e.g. superheater tubes); – high investment costs; – low flexibility in particle size selection, high dust level in flue gases, loss of bed material with ash
Pulverized combustion	– increased efficiency due to low excess oxygen, high NOx reduction possible when using appropriate burners	– biomass particle size limited to <10–20 mm; – low moisture content required for pneumatic feeding and reduced efficiency for fuels with high moisture content

5.1.2 CURRENT BIOMASS RESEARCH

Recent research and development [23] focuses mainly on pretreatment technologies used to improve the physicochemical properties of biomass and its energy density.

The most common pretreatment technologies include washing and leaching, liquefaction, steam explosion, and densification and pelletization. Typically, pretreatment technologies are interconnected, and the final product, biomass pellets, often undergoes several processing stages. Special attention is paid to the treatment of agricultural waste. China began co-firing these materials in 2017 to reduce air pollution from unregulated waste burning. India is also interested in co-firing agricultural waste for the same reason. Thus, much of the current research is focused on the co-incineration of agricultural waste, especially straw.

Research on the pre-treatment of biomass for co-incineration is beyond the scope of this article, so let's limit ourselves to a brief comment.

Torrefaction and pelletization are commercialized, and these processes are often combined in production. Pellets from peat biomass are widely available worldwide. While open air weathering of biomass is common practice, leaching treatment is only done on a pilot scale. The steam explosion biomass preparation technology is currently in the industrial demonstration stage (April 2020) with the support of the EU Horizon 2020 program [24]. Wet torrefaction is still in the laboratory research stage.

When choosing a biomass pretreatment method, the most important aspect to consider is the overall energy efficiency. Although the higher energy density of pretreated biomass means lower storage and transportation costs, energy is also consumed in the processing processes (in particular, during grinding, loosening and compaction). However, pretreatment is necessary to overcome the problems inherent in biomass combustion.

The high costs of pelletization can be justified by the improved operability of the fuel (treatment, transportation, storage and feeding), which leads to improved boiler operation and combustion efficiency. Processed biomass has a higher energy density than raw biomass, making it suitable for long-distance transportation. While pretreatment and upgrading of biomass makes it easier to handle and improves combustion efficiency, the energy density of biomass remains lower than that of coal. In the future, research should be conducted on the evaluation of the entire process from an economic point of view, as this will invariably affect the practical implementation of biomass pretreatment on an industrial scale.

A brief summary of the experience [25], accumulated worldwide as a result of the commercial operation of co-firing at TPPs, allows to draw the following conclusions:

1) co-firing of biomass with coal, brown coal and peat in traditional steam boilers provides a unique opportunity, combining the utilization of renewable energy sources and fossil fuels, to obtain the greatest benefit from both types of fuel;

2) adding biomass to the fuel balance allows to significantly reduce carbon dioxide emissions, reduce emissions of other pollutants into the soil and air. When co-firing biomass in pulverized coal boilers, up to 10 % of the coal burned in the boiler can be easily replaced with minor equipment changes, which is extremely important, given Ukraine's limited ability to invest in equipment modernization;

3) in fluidized bed plants, significantly higher biomass fractions can usually be achieved with co-firing, along with extremely mild requirements for coal quality and crushed biomass size.

The issue of using biomass as a second fuel for Ukraine, especially now, is becoming very relevant. Replacing at least part of the coal with biomass during the period of urgent restoration of damaged generating capacities of coal-fired TPPs is one of the ways to solve the problem of shortage of fuel and energy resources, the possibility of using existing equipment of TPPs to improve the environmental performance of combustion, the involvement of renewable sources in the energy balance of the country, given the economic indicators of the implementation of direct co-firing technology in fuel boilers of various capacities can be considered the most acceptable.

The Institute of Heat and Power Technologies of the NAS of Ukraine (IHPT NASU) has been developing technologies for co-firing of biomass and anthracite since 2007, when, during cooperation with the Pittsburgh Coal Energy Technology Center (PETC) of the US Department of Energy (within the framework of the NATO Science for Peace and Security program, its foundation was laid). In the course of work to calculate the combustion process, the optimal operating parameters, synergistic effects of the mutual influence of two dissimilar solid fuels and their kinetic characteristics were determined [26-28].

From the beginning, the goal of these studies was to determine the optimal ratio between biomass and anthracite for more complete combustion of both types of fuel during a certain time of residence in the fuel of an anthracite flare boiler unit; rational regime parameters of such combustion; characteristics of a wide range of domestic biomass (pine sawdust, pulp, wheat straw pellets, rapeseed, etc.) for calculating the process of co-firing of biomass and coal. The influence of biomass impurities on the efficiency of coal combustion was studied [17] and calculation methods [29, 30] and combustion of the mixture.

In 2008, the institute conducted experiments on a pilot plant, which simulated the processes occurring in the lower radiation part of the fuel boiler and at the outlet of the burner embrasure, in order to confirm the possibility of replacing the "backlight" gas with biomass with a high content of volatile substances, which ensures the stability of the torch in the process of burning high-ash, low-reactivity anthracite, as well as to identify the regime and cost features of the process of co-burning anthracite and biomass (sawdust and pine chips - waste from woodworking production). Further, these works were developed, with the removal, for known reasons, of anthracite from the fuel base of TPP, with the involvement of gas (bituminous) coal and various types of domestic biomass in the research.

5.2 EXPERIMENTAL STUDY OF JOINT PULVERIZED COMBUSTION OF GAS COAL AND BIOMASS

To select the optimal biomass/coal ratio for heat, it is necessary to carry out joint combustion of coal and biomass under conditions close to those in fuel boilers. The installation of the Institute of Thermal Energy Technologies allows for the combustion of two solid fuels simultaneously with a flow rate of up to 30 kg/h. The temperature level in the installation can reach 1700 °C, while the flow rates of components, temperatures along the length and the composition of gases at the outlet of the installation are controlled.

The schematic diagram of a pilot installation with a thermal power in the coal combustion mode in unenriched air up to 100 kW [31] is presented in **Fig. 5.2**. It includes a vertical downflow reactor 1, a burner device 2, a slag collector 3, a rotary section with a cyclone 4, a cooling and afterburning chamber 5. The total length of the reactor is 4.8 m, the reactor section before turning into a cyclone is 3.2 m. The length of the diagnostic section from the output section of the burner device is 2.4 m.

The diagnostic section consists of 4 sections 0.6 m long, internal diameter 0.28 m. The water-cooled reactor walls are covered from the inside with a three-layer lining: the fire layer is zirconium dioxide, the heat-insulating layer is chamotte, the thermal compensation layer is asbestos fabric.

The burner device is a vertical water-cooled lined cylinder with an internal diameter of 0.2 m, a length of 0.5 m, installed through a water-cooled transition flange on the upper section of the reactor, equipped with two burners and operational and diagnostic windows. The main gas burner is installed at its end, designed for burning natural gas. In addition to air and natural gas, coal dust is supplied to it from the feeder. A natural gas channel is coaxially located, which ends with a short section with perforation for gas outlet. Coaxially with the gas is a channel for supplying air or a mixture of air and coal, which ends with a blade swirler to intensify the mixing of air with gas, and coal with gas combustion products.

The unit provides for the supply of natural gas, air (to the main and auxiliary burners, transporting air with coal and biomass, secondary air), biomass and coal dust.

At a flow temperature of 1200–1250 °C, the residence time of fuel particles was 0.75–0.8 s, which is close to the residence time of particles in the lower radiation part of pulverized coal

boilers. Previous studies [22] show that during this residence time, when burning high-ash anthracite dust, a degree of carbon conversion of X_c=0.6–0.8 is achieved, which also corresponds to the characteristics of pulverized coal boilers [23].

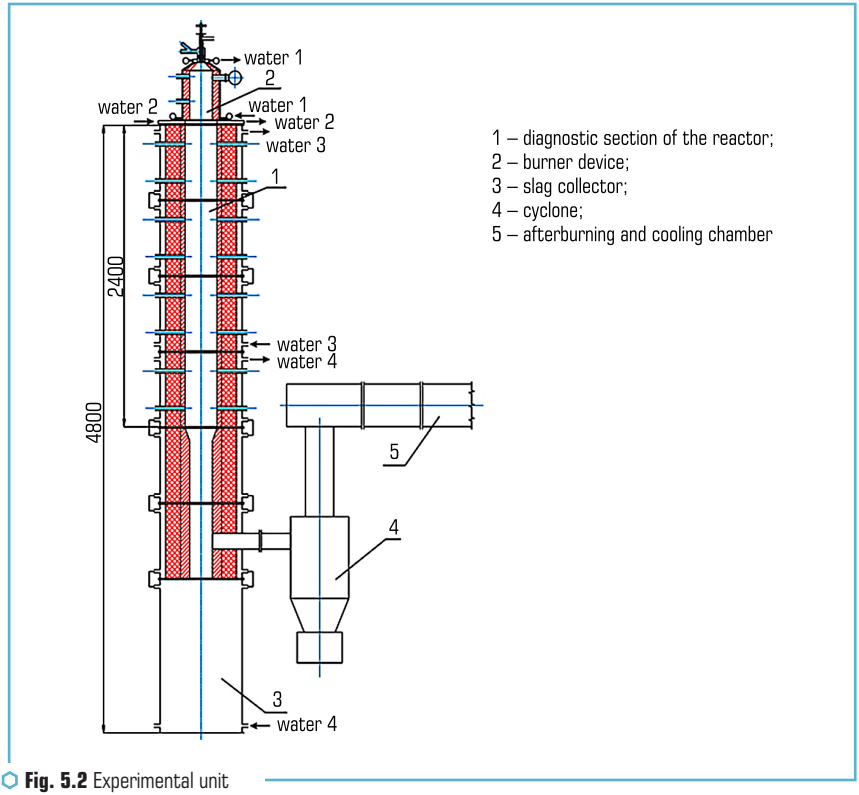

Fig. 5.2 Experimental unit

At a flow temperature of 1200–1250 °C, the residence time of fuel particles was 0.75–0.8 s, which is close to the residence time of particles in the lower radiation part of pulverized coal boilers. Previous studies [22] show that during this residence time, when burning high-ash anthracite dust, a degree of carbon conversion of X_c=0.6–0.8 is achieved, which also corresponds to the characteristics of pulverized coal boilers [23].

In view of the conversion of TPP-210A boilers to gas coal, previously designed for burning anthracite, a series of experiments were conducted on the joint flare combustion of coal dust of the gas group with three types of solid biomass – pine pellets, wheat agropellets and sunflower husk pellets [24].

Coal dust of standard station grinding was chosen for combustion. Biomass was selected from 3 types in the form of pellets, which were previously crushed to an average size of 1.6 mm. The results of sieving samples of the biomass that was burned are given in Table 5.2.

As can be seen, the particle sizes of biomass of different types are approximately the same, and the main part of the particles have a size of <1.6 mm. Technical and elemental analysis of the studied fuels are given, respectively, in **Tables 5.3** and **5.4**.

Table 5.3 Sieving of biomass prepared for combustion

Fraction, mm	Pine, %	Sunflower husk pellets, %	Agropellets, %
>1.6	0.40	0.27	0.34
1–1.6	14.58	9.84	10.38
0.63–1	21.29	20.68	18.15
0.4–0.63	24.75	28.79	22.69
0.2–0.4	23.08	24.09	25.05
0.09–0.2	10.67	12.73	15.35
<0.09	5.22	3.59	8.02

Table 5.4 Results of technical analysis of fuel samples

Sample name	Total moisture content on the working state of the fuel, W_t^r, %	Ash content on the dry state of the fuel A^d, %	Total sulfur on the dry state of the fuel S_t^d, %	Volatile substances yield V^{daf}, %	Ash fusibility			Lower calorific value, Q_i^r	
					t_A	t_B	t_C	MJ/kg	kcal/kg
Wheat pellets	9.0	12.4	0.12	84.2	1130	1180	1350	14.4	3442
Pine pellets	6.8	0.8	–	86.1	1180	1200	1215	18.1	4318
Sunflower husk pellets	10.7	5.8	0.24	80.7	>1400	>1400	>1400	16.9	4054
Gas coal	1.3	23.5	2.44	43.1	1300	1321	1360	21.47	5124

A comparison of the obtained technical characteristics of biofuels with gas coal showed that:

1) the ash content of biofuels is significantly lower than the ash content of coal;

2) the sulfur content in biomass is 5–10 times lower than in coal, which significantly reduces the formation and emissions of SO_2, respectively, environmental pollution and emission fees for TPP are reduced;

3) the content of combustible volatile substances in biomass is approximately 2 times higher than in gas coal ($V^{daf} > 80$ %), this helps the ignition of coal, but may require special measures at the preparation and transportation site;

4) the melting point of ash can vary in a wide range, which must be taken into account for each new batch of biofuel.

The experiments were conducted in three series, with each ty-pe of biomass, at different biomass heat fractions. Fuel consumption was determined by the compressor capabilities and the rarefaction in the installation. For comparison, only data from one experimental day were selected due to the maximum similarity of consumption parameters (**Table 5.5**).

Table 5.5 Results of elemental analysis of fuel samples of the combustible mass and chlorine content of fuel samples

Sample name	Chlorine on dry fuel, Cl^d, %	Elemental composition, %				
		C^{daf}	H^{daf}	O^{daf}	Ndaf	Sdaf
Wheat pellets	0.39	49.6	6.55	41.56	2.15	0.14
Pine pellets	0.10	52.93	6.64	37.67	2.76	–
Sunflower husk pellets	0.53	53.77	6.38	38.10	1.49	0.26
COAL brand G (Gas group)	0.61	86.99	5.00	5.31	1.44	1.26

Gas coal contains more than 40 % volatile substances, which ensures its stable combustion without the use of gas. At the same time, the addition of biomass, which has a lower calorific value, leads to an increase in the temperature in the reactor by 100–200 °C, which indicates an intensification of ignition even of highly reactive coal. Temperature profiles along the length of the reactor depending on the biomass fraction are shown in **Fig. 5.3**.

After testing the mode on gas coal, a certain proportion of crushed pine pellets was fed into the plant, which has the highest calorific value of the studied biomass samples. The reaction of the plant to the addition of biomass was almost the same – there was a temperature increase of 120 °C in the 2nd section and a slightly larger increase in other sections (**Fig. 5.3 *a***). The maximum temperature is observed in the range of the thermal fraction of biomass from 7–8 % to 14–15 %.

During the testing of the above experimental modes, the degree of fuel burnout in general was monitored – an important indicator of the combustion process necessary to determine the optimal proportion of biomass in the mixture with coal. It was impossible to determine the degree of combustion of biomass and coal separately, although with different reactivity, the rate of combustion of coal and biomass is different. Therefore, the degree of fuel combustion characterized the combustion process as a whole. For this, the probe at the outlet of the installation sucked off the combustion products, from which solid particles were filtered. The average degree of conversion for the two fuels was calculated based on the ash content of the sample taken. The dependence of the degree of conversion of mixtures on the biomass content in the mixture with gas coal is shown in **Fig. 5.4**.

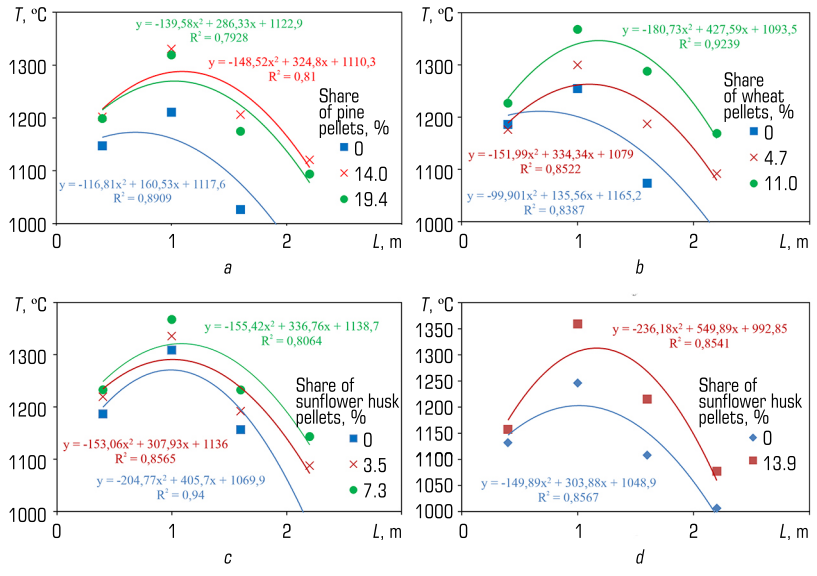

Fig. 5.3 Temperatures in the reactor in the modes of co-firing of gas coal dust and crushed pellets: *a* – pine; *b* – wheat straw; *c* – sunflower husk; *d* – sunflower husk of the 2nd series

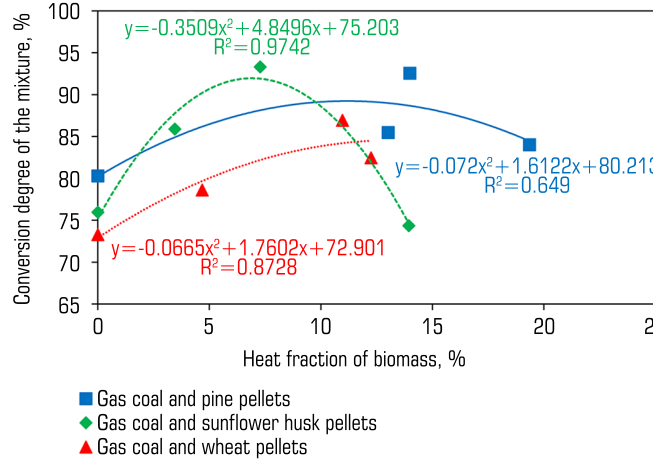

Fig. 5.4 Conversion degree of a mixture of gas coal and different types of biomass depending on the proportion of biomass in the mixture

Calculations of the conversion degree demonstrate an improvement in the completeness of the mixture burnout when adding the smallest proportion of biomass (about 5 %). With an increase in the proportion of biomass in the mixture, the burnout improved even more and reached a maximum value in the range of 8–14 %. The presence of an extremum can be explained by a change in the balance of multidirectional effects. On the one hand, adding a small amount of a more highly reactive fuel that burns faster than coal improves the ignition conditions of the latter. At the same time, oxygen is consumed for the combustion of additional volatile biomass substances, which occurs at the root of the torch, which leads to a decrease in the concentration of the oxidant in its core. When adding only 5 % of biomass, such a slight decrease does not slow down the burnout of coal particles. With an increase in the biomass fraction above 8–14 %, the effect of oxygen deficiency begins to prevail over the positive effect of early ignition of coal, which causes a decrease in the degree of conversion of the mixture relative to the maximum value. Also, the decrease in the positive effect when adding biomass above 8–14 % is affected by a decrease in the calorific value of the mixture. Due to the significantly lower calorific value of biomass, its further addition does not lead to an increase in the temperature in the torch core (**Fig. 5.3**).

The resulting effect of adding biomass on the formation of NO as a result of co-firing with coal was also assessed. An increase in the temperature in the core should lead to an increase in thermal nitrogen oxide emissions, and the low nitrogen content in biomass should reduce fuel nitrogen oxide emissions during co-firing. NO concentrations were recorded using gas analysis. The concentration of nitrogen oxide at the outlet of the installation depending on the biomass fraction is shown in **Fig. 5.5**.

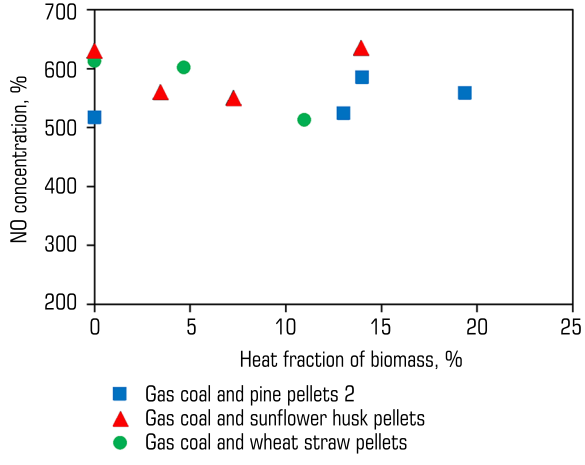

Fig. 5.5 Concentration of nitrogen oxide at the outlet depending on the biomass proportion

From the above, it can be assumed that the increase in the formation of thermal nitrogen oxides as a result of a local increase in temperature is compensated by a decrease in the output of fuel nitrogen oxides, which allows to assume a decrease in the total concentration of nitrogen oxides in the boiler unit exhaust gases.

BRIEF CONCLUSIONS

1. As a result of the conducted experimental studies, it was established that the addition of different types of biomass to gas coal leads to an increase in the temperature in the torch core by 100–200 °C. As well as to the stabilization of the torch combustion, its shift towards the burner device, which in turn indicates an improvement in the conditions for coal ignition.

2. The obtained dependences of the completeness of the burnout of a mixture of different types of biomass with gas coal on the ratio of the two fuels demonstrate an improvement in the completeness of the burnout of the mixture with an increase in the proportion of biomass. The dependence has an extremum when adding 7–14 % biomass for heat.

3. It is shown that the increase in the formation of thermal nitrogen oxides as a result of a local increase in temperature is compensated by a decrease in the yield of fuel nitrogen oxides, which suggests a decrease in the total concentration of nitrogen oxides in the boiler unit exhaust gases.

5.3 VERIFICATION OF THE OBTAINED RESULTS BY PERFORMING ENGINEERING CALCULATIONS USING THE NORMATIVE METHOD

According to the practical focus of the development, it is necessary to verify the impact of co-firing of coal and biomass by means of verification calculations of the existing boiler unit on which it is proposed for implementation. The initial concept envisaged the implementation of co-firing on anthracite boiler units, where it is possible to obtain maximum synergy from co-firing. However, given the shortage of anthracite in Ukraine caused by hostilities, and in addition, the conversion of most anthracite boilers to burning gas-group coal, experimental and computational studies were extended to coal of a different degree of metamorphism, which is currently mined in Ukraine or imported from abroad.

Co-firing calculations were performed using the example of TP-87 boiler units of Kalush TPP (fuel – coal brand "G") according to the Normative method of thermal calculation of boiler units [25]. The characteristics of coal, which is taken into account as the main fuel of the boilers, are given in **Tables 5.2** and **5.3** of paragraph 5.2.

The conditions for the calculation are determined by the operation of the boiler on a mixture of 2 fuels. The proportion is made up by thermal load: 90 % – gas coal, and 10 % crushed wood pellets from pine, or pellets from straw, or pellets from sunflower husks.

TP-87 boilers with natural circulation are made in the traditional U-shaped design. A distinctive feature of the boilers of its series is the absence of a two-light screen in the fuel chamber, which divides the fuel chamber in half, the presence of a pinch in the lower part of the fuel chamber and the equipment of vortex-type burners.

The main parameters of the boiler are given in **Table 5.6**.

The fuel chamber (fuel chamber), unlike conventional prismatic chambers, has a pinch in the lower part, formed by the fuel pipes of the front and rear screens bent inward. Some of these pipes, approximately 50 %, are curved according to the profile of the protrusion without forks, and the other part has forks in the lower and upper parts of the protrusions.

The depth of the pinch protrusions is 1890 mm on each side. The lower part of the fuel chamber is a combustion chamber (pre-firebox). The afterburning chamber is located above the pinch. Screen pipes ∅60 × 6, st. 20 with a pitch of 64 mm completely cover the front, rear and side walls of the combustion chamber and, converging at the bottom, form a fuel chamber with two inlets for removing liquid slag. The design and thermal parameters of the combustion chamber are presented in **Table 5.7**.

Table 5.6 Main parameters of the boiler operation

No.	Characteristics	Unit	Value
1	Nominal steam output	t/h	420
2	Working pressure in the steam separation chamber	MPa	14.0
3	Working pressure in the boiler drum	MPA	15.5
4	Temperature of superheated steam	°C	560
5	Feed water temperature	°C	230
6	Flue gas temperature	°C	120 (gas) 137(coal)
7	Hot air temperature	°C	400
8	Efficiency of the boiler unit at nominal load on the calculated fuel	%	92.6 (coal) 94.6 (gas)

Table 5.7 Fuel chamber characteristics

No.	Characteristics	Unit	All fuel	Preheater
1	Fuel dimensions in plan	mm	7552×14080	7552×14080
2	Calculated volume of the fuel chamber	m^3	2180	580
3	Temperature of gases at the fuel outlet	°C	1234	1785
4	Radiation heating surface	m^2	1235	411
5	Thermal voltage of the volume	kW/m^3	149	578

Thermal calculations of boilers and zone-by-zone calculations of fuel chambers of TP-87 boiler units of Kalush TPP are performed in 4 variants:

– variant 1 – nominal boiler operation mode;

– variant 2 – operation with the addition of wood pellets;

– variant 3 – operation with the addition of sunflower husk pellets;

– variant 4 – operation with the addition of grain straw pellets.

The proportion of biomass addition – according to the results of the experiments presented in paragraph 2 – 10 % of the total heat load of the boiler.

The task of the verification calculation of the fuel chamber is to determine the temperature of the gases at the outlet of the fuel chamber at the specified design dimensions. Also, within the framework of the calculation, it is necessary to confirm the conditions for the exit of liquid slag (characteristics of the burners and fuel chamber) and the absence of slagging of the screens.

A sketch of the fuel chamber is shown in **Fig. 5.6**.

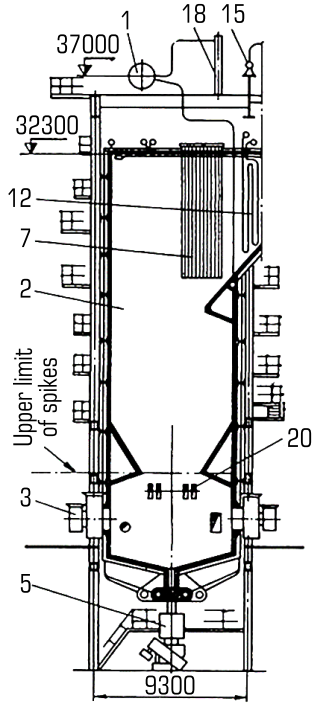

Fig. 5.6 Sketch of the fuel chamber of the TP-87 boiler

The results obtained characterize the operating mode of the TP-87 boiler fuel chamber when operating on coal brand "G" and on a mixture of coal brand "G" with the addition of 10 % of pellets in the variants of using pine pellets (var. 2), sunflower husks (var. 3) and straw (var. 4). The temperature at the fuel outlet at the nominal load ensures reliable operation of the boiler. In the case of burning coal that is slagging, it is necessary to reduce the load and conduct an additional calculation to determine the boiler operating load, which will ensure a decrease in the temperature at the outlet of the fuel chamber below 1100 °C.

In the conditions of the Kalush TPP, the boilers operate at 70–80 % of the nominal load, which ensures a decrease in the temperature at the outlet of the fuel chamber and, as a result, guarantees long-term operation of the TPP boilers without the risk of slagging of screens and superheaters.

To determine the detailed thermal characteristics of the fuel chamber, let's perform its zone-by-zone calculation.

Fig. 5.7 shows the diagram of the TP-87 boiler combustion chamber.

Table 5.8 presents the results of the zone-by-zone calculation of the boiler.

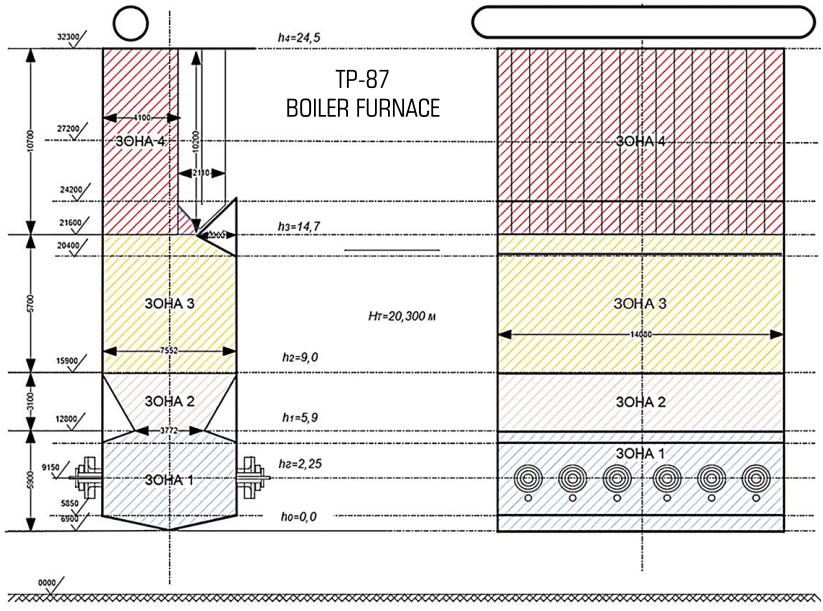

Fig. 5.7 Combustion chamber diagram with zones

Table 5.8 Zonal calculation of the fuel chamber

Name	Designation	Calculation formula or method of determination	Units of measurement	Variants			
				1	2	3	4
1	2	3	4	5	6	7	8
Zone 1							
Zone relative height	$h_1/H_т$	From the constructive calculation	–	0.323	0.323	0.323	0.323
Fuel burn-up rate at zone exit	β_{burn1}	From the normative method	m^2	0.955	0.955	0.955	0.955
Gas temperature at zone exit	ϑ_m''	Calculation according to [25]	°C	1609.95	1611.15	1606.08	1611.28
Average specific heat load of the radiation-receiving surface of the zone	Q_{rs}	$\left(B_p \cdot Q_t^L\right) / N_L$	kW/m^2	116.95	116.37	115.74	116.70
Zone 2							
Zone relative height	$h_2/H_т$	From the constructive calculation	–	0.470	0.470	0.470	0.470
Fuel burn-up rate at zone exit	β_{burn2}	From the normative method	–	0.995	0.955	0.955	0.955
Gas temperature at zone exit	ϑ_m''	Calculation according to [25]	°C	1505.7	1508.5	1504.2	1501.4
Average specific heat load of the radiation-receiving surface of the zone	Q_{rs}	$\left(B_p \cdot Q_t^L\right) / N_L$	kW/m^2	250.16	245.15	244.53	242.13
Zone 3							
Zone relative height	$h_3/H_т$	From the constructive calculation	–	0.7377	0.7377	0.7377	0.7377
Fuel burn-up rate at zone exit	β_{burn3}	From the normative method	–	0.995	0.995	0.995	0.995
Gas temperature at zone exit	ϑ_m''	Calculation according to [25]	°C	1277.4	1281.8	1278.7	1278.14
Average specific heat load of the radiation-receiving surface of the zone	Q_{rs}	$\left(B_p \cdot Q_t^L\right) / N_L$	kW/m^2	126.61	126.21	126.62	125.73

Continuation of Table 5.8

1	2	3	4	5	6	7	8
Zone 4							
Zone relative height	$h_4/H_т$	From the constructive calculation	–	1	1	1	1
Fuel burn-up rate at zone exit	β_{burn4}	From the normative method	–	0.995	0.995	0.995	0.995
Gas temperature at zone exit	ϑ_m''	Calculation according to [25]	°C	1064	1075	1072	1073
Average specific heat load of the radiation-receiving surface of the zone	Q_{rrs}	$\left(B_p \cdot Q_t^L\right) / N_L$	kW/m^2	61.62	62.51	62.90	62.54

It has been calculated that when the boiler is operating on a mixture of coal brand G (G1) and solid biofuel:

– conditions for reliable operation of the fuel chamber with a stable HID mode without the risk of slagging of the screens are ensured;

– the temperature at the outlet of the fuel chamber in all modes does not reach the level of the beginning of deformation of ash particles (t_3=1270–1300 °C).

Based on the results of the calculations, the decision of the technical council of the Kalush TPP was approved, and it was recommended to use the obtained results for further implementation of the project.

5.4 CALCULATION OF CO-FIRING OF COAL WITH BIOMASS FOR SELECTED SCHEMATIC SOLUTIONS OF THE BIOMASS FEED SYSTEM TO THE BOILER FUEL TANK

To verify the process of co-firing of coal and biomass, three-dimensional calculations were performed using the example of the TP-87 boiler (Kalush TPP).

5.4.1 INITIAL CONDITIONS FOR MODELING CO-FIRING

The modeling of the flow, heat exchange and combustion processes in the TP-87 boiler fuel tank was carried out using the generally accepted ANSYS Fluent program. For this purpose, the geometry of the calculation area shown in **Fig. 5.8** was constructed in the Gambit program, and a calculation grid was created on its basis.

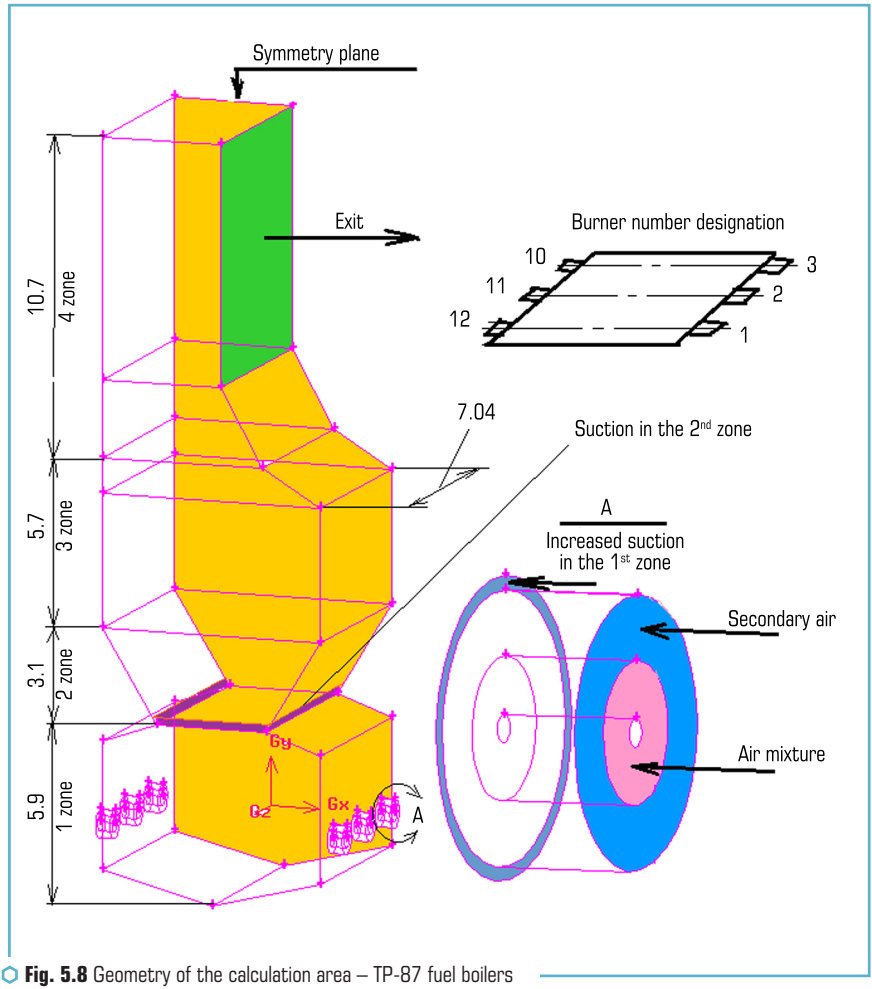

Fig. 5.8 Geometry of the calculation area – TP-87 fuel boilers

Half of a fuel boiler with 6 burners was modeled, the plane bordering the discarded part was defined in the calculations as the plane of symmetry. The calculations took into account suction, it was assumed that dust is transported to the burners by air.

When setting the boundary conditions – wall surface temperatures (pollution) T_w and their degrees of blackness ε, as well as the flow rates and temperatures of the introduced components, let's rely on the results of the zone-by-zone calculation of fuel according to the normative method. The parameters used in the simulation are given in **Tables 5.9** and **5.10**.

Table 5.9 Boundary conditions on the walls of the zones

Zone No.	T_w, K	ε
1	1790	0.68
2	1243	0.75
3	1071	0.74
4	894	0.74

Table 5.10 Input component parameters assigned to one burner

Component	Air			Coal
	Flow rate	T	Tangential component	Consumption
	kg/s	K	–	kg/s
Aeromixture	1.739	363	2.53	1.136
Secondary	6.955	643	2.63	0
Suctions of the 1st zone	0.745	313	0	0
Suctions of the 2nd zone	0.397	313	0	0

In **Table 5.10**, the parameters are given as follows – firstly, the tangential components of the velocity are indicated on the scale of the axial components, equal to unity. Secondly, the value of the coal consumption is taken directly from the boiler calculation by the normative method in the nominal mode, and the air consumption is found from the characteristics and coal consumption using the recommendations of S. L. Shagalova and I. N. Schnitzer [32] for vortex scroll-blade burners ($\alpha_b = 1.05$, $\alpha_1 = 0.26$). The suction consumption at a temperature of 313 K is taken based on the value $\alpha_f = 1.2$ ($\alpha_{1st\ zone} = 0.09$, $\alpha_{2nd\ zone} = 0.06$).

In modes with a joint supply of coal and pellets, the thermal power of the mixed fuel remained the same as when only coal was introduced, and the consumption was found based on the ratio of the thermal powers of coal and pellets as 0.9:0.1.

The parameters of gas coal and pine pellets are given in the following **Table 5.11**.

Here (taking into account the recommendations of the ANSYS Fluent program) the sulfur content is conditionally added to nitrogen. The coal particle sizes were specified according to the Rosin-Ramler distribution in the range from 5 to 200 μm with an average size of 60 μm, the distribution parameter was taken equal to 1. The pellet particles were specified as monodisperse with a variable size. The particle shape in all variants was assumed to be spherical.

Table 5.11 Characteristics of gas coal and pine pellets

Type	W^r, %	A^r, %	V^r, %	C^{daf}, %	H^{daf}, %	O^{daf}, %	N^{daf}, %	Q^r_i, M MJ/kg
Gas coal	11	19.58	25.55	80.27	5.10	12.01	2.62	22.766
Pine pellets	8.70	0.37	78.43	51.87	6.33	41.63	0.17	17.632

5.4.2 MAIN RESULTS OF MODELING IN THE MODE WITHOUT PELLET INPUT

The following figures illustrate the main results of modeling processes in the fuel in the mode without pellet input. The temperature fields in different fuel cross-sections (**Fig. 5.9**) and the fields of coke burnout and volatiles release in the fuel cross-section for burners 3–10 (**Fig. 5.10**) are shown. **Fig. 5.11–5.13** compare the results of numerical modeling with the data of zone calculations using the normative method in terms of temperature distributions along the fuel height (**Fig. 5.11**), heat flux densities in the walls (**Fig. 5.12**) and coke burnout intensity (**Fig. 5.13**). It can be noted that there is a fairly satisfactory correspondence in the temperature distribution (the difference is mainly within 100 °C) with a slightly worse agreement in terms of heat flux densities and burnout intensities.

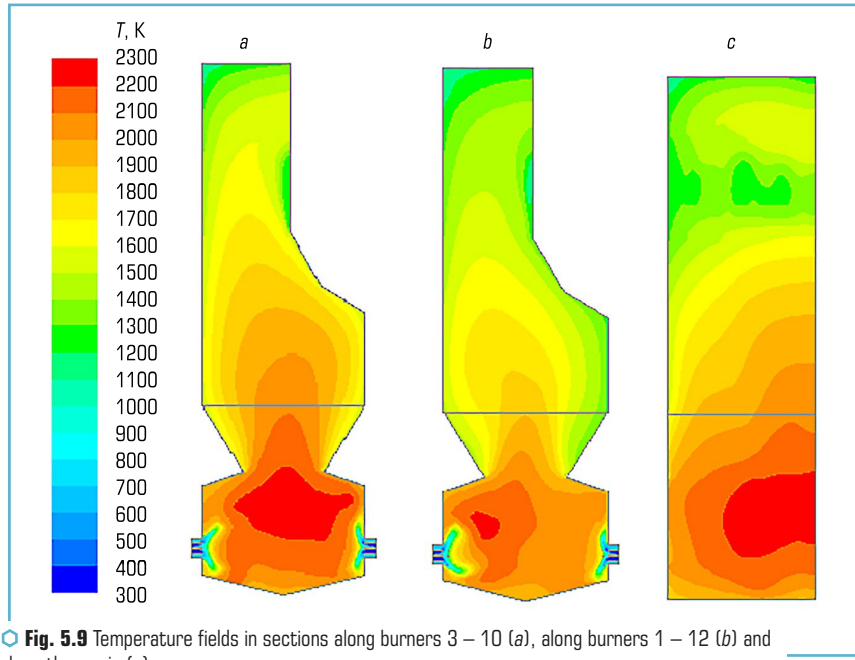

Fig. 5.9 Temperature fields in sections along burners 3 – 10 (*a*), along burners 1 – 12 (*b*) and along the z axis (*c*)

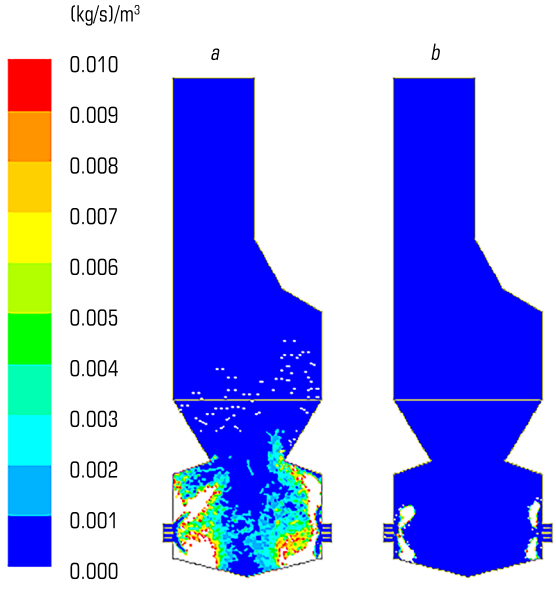

Fig. 5.10 Coke burnout intensities (*a*) and volatiles output (*b*) in the section along burners 3 – 10. White field – exceeding the upper limit of the scale

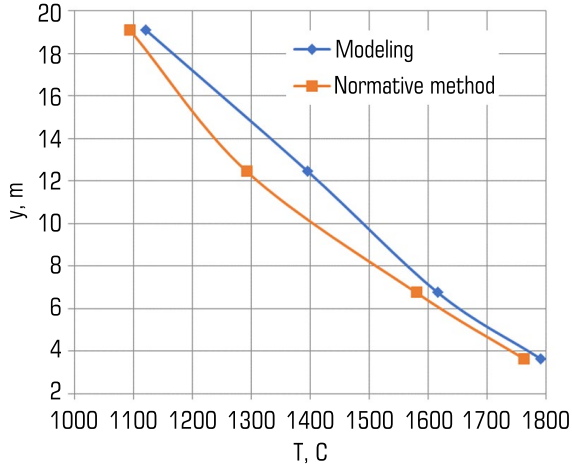

Fig. 5.11 Comparison of mass-average temperatures at the zone outlet based on the results of numerical modeling with the data of the zone-by-zone calculation using the normative method

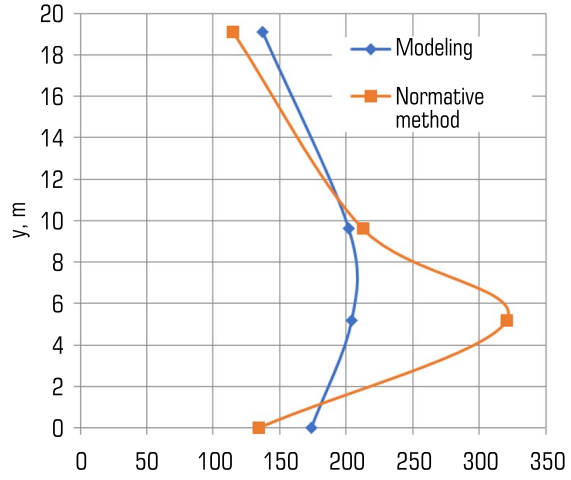

Fig. 5.12 Comparison of heat flux densities in the walls of zones according to the results of numerical modeling with the data of zone-by-zone calculations using the normative method

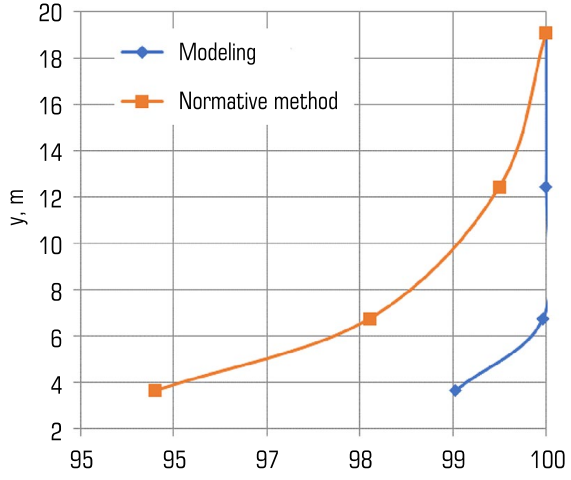

Fig. 5.13 Distribution of coke burnout intensity by fuel height according to the results of numerical modeling and according to the data of the zone calculation by the normative method

5.4.3 MAIN RESULTS OF MODELING IN THE MODE WITH THE INTRODUCTION OF PELLETS

The results of numerical modeling lead to the conclusion that the effect of the introduction of pine pellets in the amount of 10 % by heat on the processes in the fuel significantly depends on the fineness of the pellet grinding. Therefore, let's first consider this effect at the minimum of the considered pellet sizes – 60 microns.

From a comparison of these results (**Fig. 5.14**) with the data without the introduction of pellets (**Fig. 5.9**), it can be seen that the temperature level in the fuel decreased with the introduction of pellets, although the difference is small and will not affect the operation of the boiler mode and the liquid slag removal mode. This is more clearly illustrated by the values of the gas phase temperatures at the exit of the zones (**Fig. 5.15**).

A comparison of the distributions of coke coal combustion intensities in the fuel (**Fig. 5.16**) with similar results without pellet introduction (**Fig. 5.10**) shows that pellet introduction stretches the coke coal combustion zone.

As already noted, a significant impact on the combustion processes in the fuel is exerted by the size of the particles introduced, namely, with an increase in this size, the burnout intensity in the fuel of both coal fuel and the pellets themselves decreases significantly (**Fig. 5.17**).

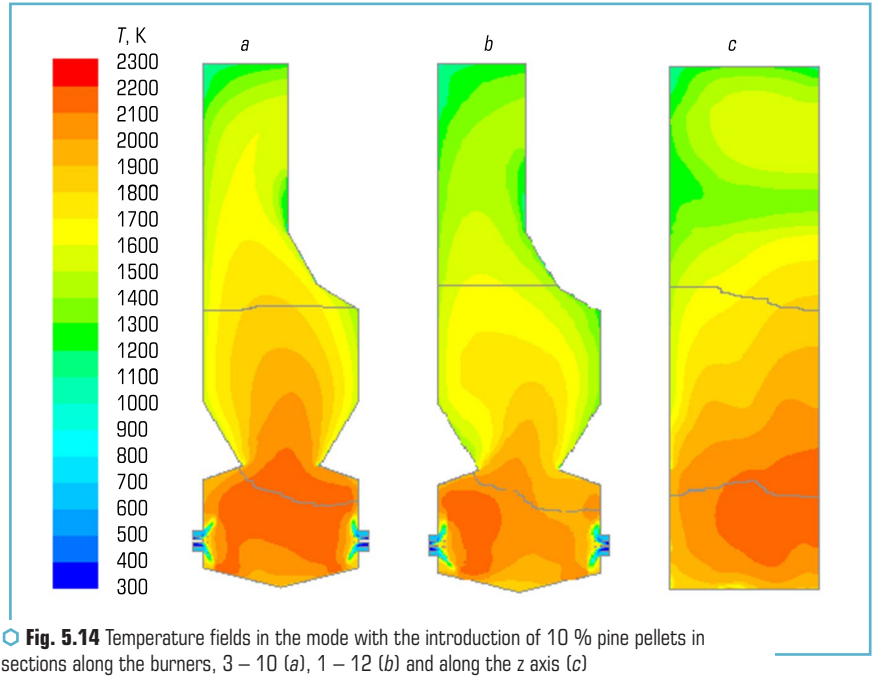

Fig. 5.14 Temperature fields in the mode with the introduction of 10 % pine pellets in sections along the burners, 3 – 10 (*a*), 1 – 12 (*b*) and along the z axis (*c*)

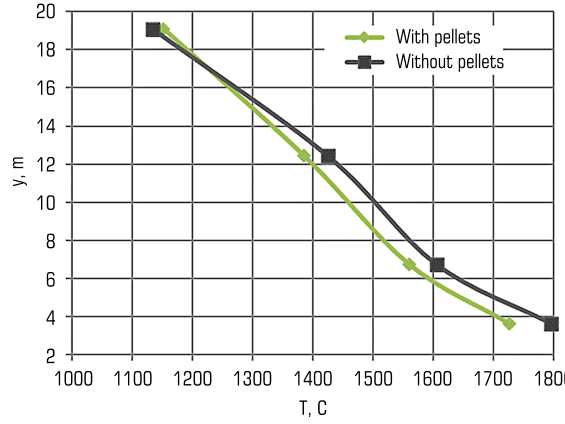

Fig. 5.15 Effect of pellet introduction on mass average temperatures at the zone outlet

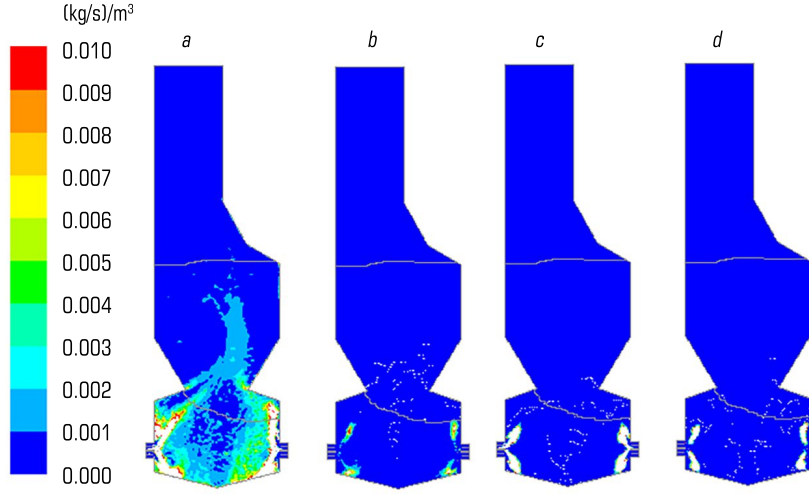

Fig. 5.16 Coke burnout intensities of coal (*a*) and pellets (*b*), as well as the intensity of volatile coal (*c*) and pellet output (d) in the cross section of burners 3 – 10. White field – exceeding the upper limit of the scale

These results should be taken into account when choosing a biomass preparation technology for use as an additive to coal fuel. However, it is necessary to take into account that the size of

the pellets in the simulation does not directly correspond to the size of the real biomass particles fed for combustion. These are conditionally spherical particles of the coke residue. While the size of biomass particles changes significantly during the process of rapid heating and pyrolysis with the release of more than 80 % of volatile substances.

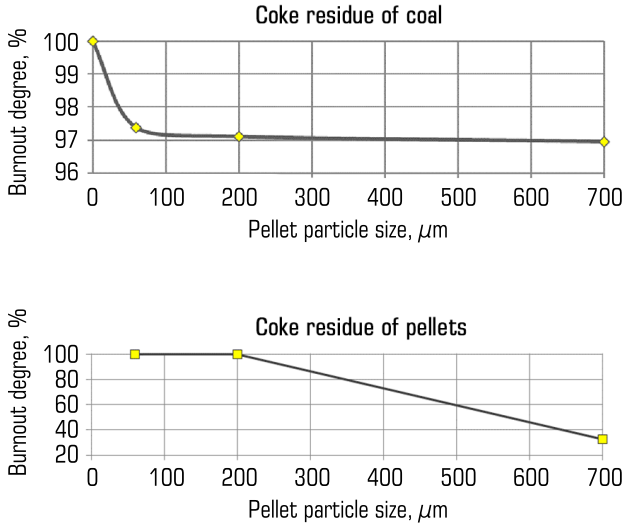

Fig. 5.17 The effect of the size of particles introduced into the pellets on the efficiency of burning coal coke and pellets

BRIEF CONCLUSIONS

As a result of modeling the co-firing of gas coal and pine biomass in the fuel of the TP-87 boiler, the following conclusions can be drawn:

1) ignition of both fuels occurs without delay;

2) addition of biomass does not worsen the conditions of liquid slag removal and the temperature conditions of slagging of the screen superheater (but the characteristics of biomass ash must be taken into account);

3) the average temperature level in the fuel decreases by 10–40 °C, which can reduce the maximum steam power of the boiler by 5 %;

4) increase in the size of biomass particles can lead to an increase in underburning (the maximum size requires verification on a real boiler).

5.5 RECOMMENDATIONS FOR THE USE OF CO-FIRING OF COAL AND BIOMASS AT UKRAINIAN TPPS

Based on the world experience of co-firing and the calculations and experiments conducted on the combustion of coal and biomass of Ukrainian origin, the following recommendations can be made for co-firing at TPPs:

1) at the moment, the optimal co-firing scheme is direct flaring of coal and biomass in one existing boiler, since such a scheme, compared to others, allows for maximum use of existing equipment and does not require much additional space;

2) to ensure reliable operation of the fuel preparation and supply system (maintaining the regulatory degree of coal grinding, as well as the temperature of the air mixture), let's recommend using a separate fuel storage, grinding and supply system for biofuel, which will ensure minimal impact of biomass on the reliability of the coal preparation system. This will also allow the use of not only wood pellets, but also sunflower husk pellets, due to the use of a mill specially designed for biomass;

3) the recommended form of biomass use at stations is pellets, which allows to reduce the costs of transporting biofuel, and also significantly increases the heat of its combustion;

4) the verification calculation of the fuel shows that with co-firing, reliable boiler operation is maintained with a stable output of liquid slag, the possibility of slagging screens requires practical study;

5) the experimentally shown stable co-firing of biomass of all three studied species (pine pellets, sunflower husk pellets, straw agropellets) for a long time (more than an hour for each of the modes);

6) the optimal proportion of biomass that improves coal combustion, but does not require significant reconstruction of the power plant is 8-12 % by heat. When using CFBC on boilers that burn gas coal, a gradual expansion of the proportion of biomass and conducting balance tests can be considered;

7) the optimal degree of grinding of different types of biomass corresponds to the maximum size of biomass particles of 1.6 mm, which allows it to ignite quickly, but does not require large grinding costs;

8) it is recommended to store pellets in closed silos that provide a 15-day fuel supply. Silos should be equipped with a temperature control system, it is recommended to maintain the temperature no higher than 45 °C. This will protect the biomass from getting wet (it has increased moisture absorption compared to coal) and spontaneous combustion;

9) when choosing biomass, it is necessary to pay attention to the characteristics of the fusibility of its ash. The melting points of ash are often lower than those of coal, which is positive when using liquid slag removal. But at the same time t_A should not be lower than the temperature of the combustion products in front of the screen superheaters +50 °C;

10) the recommended biomass feed zone is the central channel of the vortex burner. This allows to reduce the costs of boiler reconstruction and, if necessary, quickly and easily return to 100 % coal combustion.

REFERENCES

1. Tsili Staloho Rozvytku. United Nations Development Programme. Available at: https://www.undp.org/uk/ukraine/tsili-staloho-rozvytku
2. World Energy Outlook 2023 (2023). IEA. Available at: https://www.iea.org/reports/world-energy-outlook-2023
3. Kennedy, A. (2024). Visualized: Global Coal Consumption by Region. Available at: https://www.visualcapitalist.com/sp/rng01-world-coal-consumption/
4. Xu, Y., Yang, K., Zhou, J., Zhao, G. (2020). Coal-Biomass Co-Firing Power Generation Technology: Current Status, Challenges and Policy Implications. Sustainability, 12 (9), 3692. https://doi.org/10.3390/su12093692
5. Yu, B. (2018). Benefit and risk analysis of coal-fired biomass gasification coupled power generation project. Plant Maint. Eng., 20, 53–54.
6. Inside the dome. Drax. Available at: https://www.drax.com/technology/inside-the-dome/
7. Amaher Bakke. Wikipedia. Available at: https://uk.wikipedia.org/wiki/Амарер_Бакке
8. Sun, Y. (2018). Techno-economic Analysis of Biomass Co-firing in Coal-fired Boiler. [Master's Thesis; Huazhong University of Science & Technology].
9. Zhang, X., Li, K., Zhang, C., Wang, A. (2020). Performance analysis of biomass gasification coupled with a coal-fired boiler system at various loads. Waste Management, 105, 84–91. https://doi.org/10.1016/j.wasman.2020.01.039
10. Chen, H. R. (2019). Foresee 2019: Panoramic Map of China's Biomass Energy Industry in 2019 (with Market Scale, Competition Pattern and Development Prospect). Available at: https://www.qianzhan.com/analyst/detail/220/190610-a91842e0.html
11. Li Chuangjun, Deputy Director General, Introduced the Development of Renewable Energy in the First Three Quarters (2019). NEA. Available at: http://www.nea.gov.cn/2019-10/29/c_138511525.htm Last accessed: 11.03.2020
12. Zhang, Q. P. (2018). Application Analysis of Biomass and Coal-Fired Coupled Co-Combustion Power Generation Technology. Available at: http://www.china-nengyuan.com/tech/125253.html Last accessed: 11.03.2020
13. Triani, M., Tanbar, F., Cahyo, N., Sitanggang, R., Sumiarsa, D., Lara Utama, G. (2022). The Potential Implementation of Biomass Co-firing with Coal in Power Plant on Emission and Economic Aspects: A Review. EKSAKTA: Journal of Sciences and Data Analysis. https://doi.org/10.20885/eksakta.vol3.iss2.art4
14. Sidiq, A. N. (2022). Pengaruh Co-Firing Biomassa terhadap Efisiensi Boiler PLTU Batubara. KILAT, 11 (1), 21–31. https://doi.org/10.33322/kilat.v11i1.1553
15. Nudri, N. A., Wan Abdul Karim Ghani, W. A., Thomas Bachmann, R., Baharudin, B. T. H. T., Ng, D. K. S., Md Said, M. S. (2021). Co-combustion of oil palm trunk biocoal/sub-bituminous coal fuel blends. Energy Conversion and Management: X, 10, 100072. https://doi.org/10.1016/j.ecmx.2020.100072

16. Praevia, M. F., Widayat, W. (2022). Analisis Pemanfaatan Limbah Tandan Kosong Kelapa Sawit Sebagai Cofiring pada PLTU Batubara. Jurnal Energi Baru Dan Terbarukan, 3 (1), 28–37. https://doi.org/10.14710/jebt.2022.13367
17. Pro zatverdzhennia Natsionalnoho planu dii z vidnovliuvanoi enerhetyky na period do 2030 roku ta planu zakhodiv z yoho vykonannia (2024). Rozporiadzhennia Kabinetu Ministriv Ukrainy No. 761-r. 13.08.2024. Available at: https://zakon.rada.gov.ua/laws/show/761-2024-%D1%80#Text
18. Fateyev, A. I., Shendrik, T. G., Polishchuk, S. S., Dunayevska, N. I. (2018). The energy technological background of involving salty coals into energy balance of Ukraine. 1. Composition of water extracts and the prospects for their utilization. Naukovyi Visnyk Natsionalnoho Hirnychoho Universytetu, 6, 40–47. https://doi.org/10.29202/nvngu/2018/8
19. Fateyev, A. I., Shendrik, T. G., Dunayevska, N. I. (2019). The energy technological background of involving salty coals into energy balance of Ukraine. 2. Natural minerals as catalysts of thermochemical conversion of salty coals in various conditions. Naukovyi Visnyk Natsionalnoho Hirnychoho Universytetu, 6, 45–51. https://doi.org/10.29202/nvngu/2019-6/7
20. Shendrik, T., Dunayevska, N., Tsaryuk, A., Ielagin, V., Fateyev, A. (2020). Experimental development of approaches to reduce the slagging and corrosive activity of salty coal. Eastern-European Journal of Enterprise Technologies, 6 (6 (108)), 124–133. https://doi.org/10.15587/1729-4061.2020.217585
21. Shendrik, T. G., Dunayevska, N. I., Fateiev, A. I. (2024). High-temperature metal corrosion uring combustion of coal with high salt content. Fizyko-Khimichna Mekhanika Materialiv, 60 (2), 20–28.
22. Madanayake, B. N., Gan, S., Eastwick, C., Ng, H. K. (2017). Biomass as an energy source in coal co-firing and its feasibility enhancement via pre-treatment techniques. Fuel Processing Technology, 159, 287–305. https://doi.org/10.1016/j.fuproc.2017.01.029
23. Zhang, X. (2019). Support mechanisms for cofiring biomass with coal. CCC/294. London: IEA Clean Coal Centre, 60.
24. Arbaflame has signed a major contract with Engie (2019). Arbaflame. Available at: http://www.arbaflame.no Last accessed: 04.06.2019
25. Tillman, D. A., Duong, D. N. B., Stanley, N. (2012). Solid Fuel Blending. Elsevier. https://doi.org/10.1016/c2009-0-30636-4
26. Dunaievska, N., Chernyavskiy, M., Shchudlo, T. (2016). Co-combustion of solid biomass in pulverized anthracite-coal firing boilers. Ukrainian Food Journal, 5 (4), 748–764. https://doi.org/10.24263/2304-974x-2016-5-4-14
27. Dunayevska, N., Zasiadko, Y., Shchudlo, T. (2018). Thermal destruction kinetics of coal and solid biomass mixtures. Ukrainian Food Journal, 7 (4), 738–753. https://doi.org/10.24263/2304-974x-2018-7-4-17
28. Livingston, W. R., Middelkamp, J., Willeboer, W., Toseny, S., Saner, B., Madrali, S., Hansen, M. T.; Koppejan, J., Cremers, M. F. G. (Eds.) (2016). The status of large scale

biomass firing. IEA Bioenergy, 87. Available at: https://www.ieabioenergy.com/wp-content/uploads/2016/03/IEA_Bioenergy_T32_cofiring_2016.pdf

29. Nekhamin, M., Beztsennyi, I., Dunayevska, N., Vyfatnuik, V. (2020). On using the ANSYS FLUENT software for calculating the process of burning a mixture of particles from different types of solid fuels. Eastern-European Journal of Enterprise Technologies, 4 (8 (106)), 48–53. https://doi.org/10.15587/1729-4061.2020.209762
30. Baranyuk, A., Dunayevska, N., Rachinsky, A., Vorobyov, N., Merenger, P., Shevel, E. (2024). CFD Modeling of the Combustion of Ukrainian and Biomass in a Flare Boiler Unit TPP-210a. International Journal of Energy for a Clean Environment, 25 (6), 59–79. https://doi.org/10.1615/interjenercleanenv.2023051717
31. Beagle, E., Belmont, E. (2019). Comparative life cycle assessment of biomass utilization for electricity generation in the European Union and the United States. Energy Policy, 1 28, 267–275. https://doi.org/10.1016/j.enpol.2019.01.006
32. Shagalova, S., Shnicer, I. (1976). Szhiganie tverdogo topliva v topkah parogeneratorov. Leningrad: Energiya, 176.

Edited by
Tetyana Baydyk

ENERGY SYSTEMS AND RESOURCES: OPTIMISATION AND RATIONAL USE

Maksym Kovzel, Olga Nosko, Tetyana Baydyk, Masuma Mammadova, Ernst Kussul, Airam Curtidor, Yurii Sniezhkin, Zhanna Petrova, Vadym Paziuk, Viacheslav Mykhailyk, Tetiana Korinchevska, Kateryna Samoilenko, Igor Kozlov, Vyacheslav Kovalchuk, Viacheslav Miliev, Mykola Holovin, Serhii Vistiak, Olexiy Kozlov, Natalia Dunaievska, Taras Shchudlo, Ihor Beztsennyi, Dmytro Bondzyk, Yevhen Miroshnychenko

Collective monograph

Technical editor I. Prudius
Desktop publishing T. Serhiienko
Cover photo Copyright © 2024 Canva

TECHNOLOGY CENTER PC®
Published in December 2024
Enlisting the subject of publishing No. 4452 – 10.12.2012
Address: Shatylova dacha str., 4, Kharkiv, Ukraine, 61165
